The information technology of the future will contain a vast number of quantum elements with the promise of faster computers and more secure communication. The computer chips embedded into almost all technology today are made of silicon transistors and similarly will the quantum technology of tomorrow rely on mass produced quantum circuits. Circuit QED is one framework for building quantum circuits in which the information is encoded in superconducting quantum bits and operations are performed with the help of modern microwave technology. The aim of this thesis is to propose and describe devices that can be integrated into these circuits and, thus, enable new quantum technologies to emerge. A cornerstone in these devices is the so-called Josephson junction, which works as a non-linear electrical component. It is shown in this thesis, that by combining Josephson junctions and microwave resonators, novel quantum effects, such as dynamics in the ultrastrong coupling regime and quantum-classical dynamics, can be explored. Moreover, this thesis describes a proposal for a microwave detector using current-biased Josephson junctions and a recent experiment which confirms the abilities of the device. Josephson junctions also play a key role in a proposed efficient approach to classical control of quantum devices working within the cryogenic environment of the quantum system. Finally, the thesis also considers the construction of desirable controllable couplings in circuit QED. Combined, these proposed designs offer a novel perspective on the quantum information technology of the future using superconducting quantum circuits.

AARHUS
UNIVERSITY
DEPARTMENT OF PHYSICS AND ASTRONOMY

CHRISTIAN K. ANDERSEN

THEORY AND DESIGN OF QUANTUM DEVICES IN CIRCUIT QED

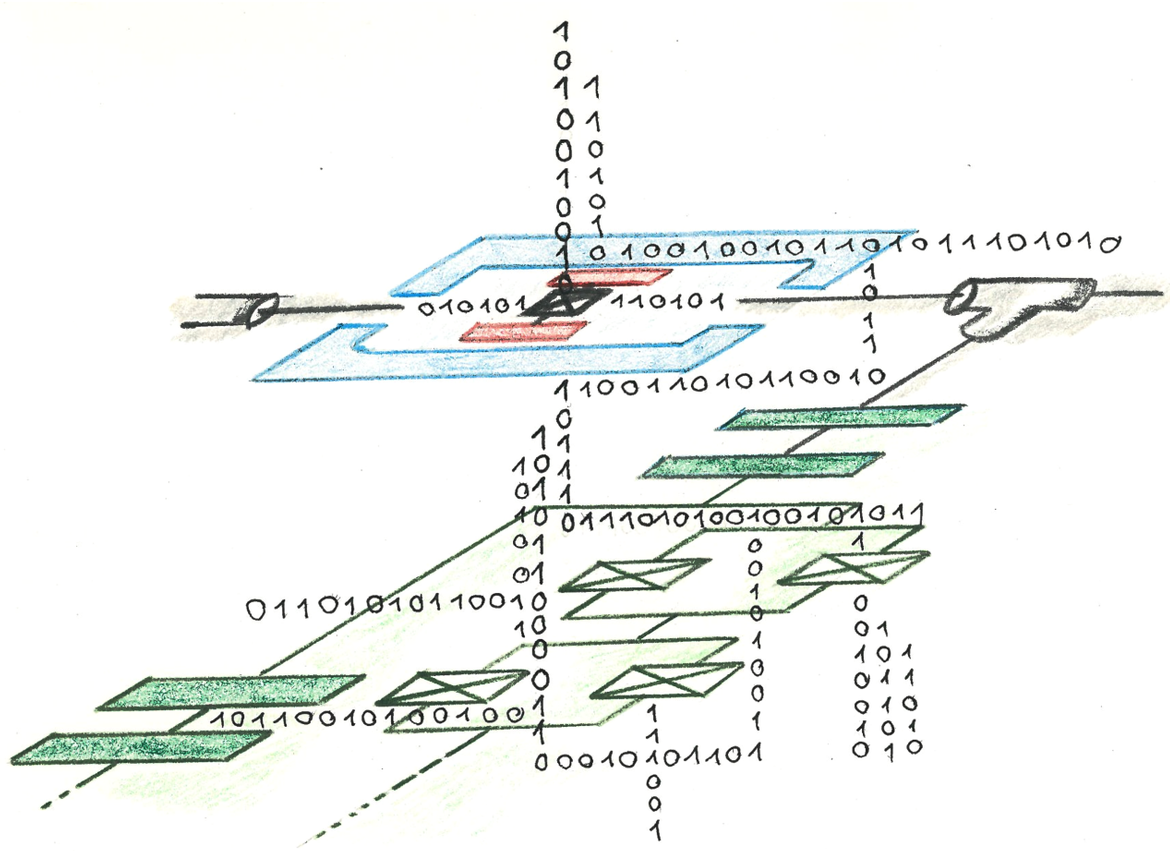

THEORY AND DESIGN OF QUANTUM DEVICES IN CIRCUIT QED

DISSERTATION

CHRISTIAN KRAGLUND ANDERSEN
PHD DISSERTATION

Theory and design of quantum devices in circuit QED

Christian Kraglund Andersen

PhD thesis
July 2016

Supervisor: Klaus Mølmer

Department of Physics and Astronomy
Aarhus University

English summary

The information technology of the future will contain a vast number of quantum elements with the promise of faster computers and more secure communication. The computer chips embedded into almost all technology today are made of silicon transistors and similarly will the quantum technology of tomorrow rely on mass produced quantum circuits. Circuit QED is one framework for building quantum circuits in which the information is encoded in superconducting quantum bits and operations are performed with the help of modern microwave technology. The aim of this thesis is to propose and describe devices that can be integrated into these circuits and, thus, enable new quantum technologies to emerge. A cornerstone in these devices is the so-called Josephson junction, which works as a non-linear electrical component. It is shown in this thesis, that by combining Josephson junctions and microwave resonators, novel quantum effects, such as dynamics in the ultrastrong coupling regime and quantum-classical dynamics, can be explored. Moreover, this thesis describes a proposal for a microwave detector using current-biased Josephson junctions and a recent experiment which confirms the abilities of the device. Josephson junctions also play a key role in a proposed efficient approach to classical control of quantum devices working within the cryogenic environment of the quantum system. Finally, the thesis also considers the construction of desirable controllable couplings in circuit QED. Combined, these proposed designs offer a novel perspective on the quantum information technology of the future using superconducting quantum circuits.

Dansk resumé (Danish summary)

Fremtidens informationsteknologi kommer til at indeholder mange kvanteelementer, hvilket vil medføre hurtigere computere og mere sikker kommunikation. De computerchips der er inde i stort set al teknologi idag er bygget af silliciumtransistore, og på samme vis vil morgendagens kvanteteknologi bygge på masseproducerede kvantekredsløb. Circuit QED er navnet på en en metode til at bygge disse kvantekredsløb, hvori kvanteinformation er gemt i superledende kvante-bits og hvor kvanteoperationer bliver udført ved hjælp af moderne mikrobølgeteknologi. Formålet med denne afhandling er at foreslå og beskrive enheder, der kan blive integreret i disse kredsløb og som dermed muliggør ny kvanteteknologi. En grundsten i disse enheder er den såkaldte Josephson junction, der virker som et ikke-liniært elektronisk element. Ved at kombinerer Josephson junctions med mikrobølgeresonatorer vil denne afhandling vise at det er muligt at udforske nye kvanteeffekter for eksempel ultrastærk kobling og kvante-klassisk dynamik. Derudover foreslåes det at en Josephson junction påtvunget en elektrisk strøm kan blive brugt som en mikrobølgedetektor og et nyligt udførst eksperiment viser at denne ide virker. Josephson junctions spiller også en afgørende rolle i en ny fremgangsmåde for klassisk kontrol af kvanteenheder, der bliver forslået i denne afhandling og som virker med samme teknologi som kvantesystemerne selv er implementeret med. Tilsidst kigger denne afhandling på hvordan forskellige ønskede koblinger i circuit QED kan kontrolleres. Tilsammen giver alle de forslåede design et nyt perspektiv på fremtidens kvanteinformationsteknologi implementeret med superledende kvantekredsløb.

Preface

In this thesis you find a presentation of research completed during my PhD studies performed at the *Department of Physics and Astronomy* at *Aarhus University*. The studies was funded by the *Faculty of Science and Technology* and further supported by the *Danish Ministry of Higher Education and Science*. The research was carried out between August 2011 and July 2016 under the supervision of Klaus Mølmer. Additionally, 5 months was spent during 2015 in the group of Alexandre Blais at University of Sherbrooke. The experimental data used for analysis in Secs. 3.2 and 4.3 was obtain by the groups of Michel Devoret at Yale and Evgeni Il'ichev at IPHT Jena respectively.

On the next pages you will find a list of publications produced during my studies. The articles [1] and [4] are less related to the main topic of this thesis and, as such, will not be covered to any extend. The same goes for [15] which is an outreach article written in Danish. The papers [11–13] fits well within the scope of the thesis, but due to constrains of length these publications will not be included even though some of the general techniques used in these publications are presented in Chapter 2. The rest of the publications will be covered during the thesis, however not all details of all the papers will be presented and I encourage the reader to consult the papers themselves for additional details. As of writing, the papers [10–12, 14] are not published yet.

I would like to thank Klaus Mølmer for his supervision during my studies. He has been a great supervisor; always ready with an impressive intuition and ready to challenge my ideas, but most importantly he has supported me greatly in developing and working out my own ideas. I am also very grateful to Alexandre Blais for the hospitality and our collaboration during my stay in Sherbrooke; his insight and expertise as well as his keen eye for details have taught me a lot. A thanks also goes to the all people I have worked with and discussed physics with over the years. There are too many people with whom I have enjoyed good

discussions about physics, but in particular I would like to mention Jerome Bourassa, Samuel Boutin, Benjamin J. Chapman, Arne Grimsmo, The Jenses, Archana Kamal, Joseph Kerckhoff, Konrad W. Lehnert, Gregor Oelsner, Shruti Puri, Malte Tichy and Andrew C.J. Wade. Finally, a very big thanks goes to Eliska Greplova for supporting me in writing this thesis, for providing the drawing for the cover and for countless of valuable input and feedback.

List of Publication

[1] Christian Kraglund Andersen and Klaus Mølmer. *Squeezing of collective excitations in spin ensembles.* Phys. Rev. A, **86**, 043831, (2012)

[2] Christian Kraglund Andersen and Klaus Mølmer. *Effective description of tunneling in a time-dependent potential with applications to voltage switching in Josephson junctions.* Phys. Rev. A, **87**, 052119, (2013)

[3] Christian Kraglund Andersen, Gregor Oelsner, Evgeni Il'ichev, and Klaus Mølmer. *Quantized resonator field coupled to a current-biased josephson junction in circuit QED.* Phys. Rev. A, **89**, 033853, (2014)

[4] Malte C. Tichy and Christian Kraglund Andersen. *Comment on "Contextuality in bosonic bunching".* Phys. Rev. Lett., **113**,138901, (2014)

[5] Christian Kraglund Andersen and Klaus Mølmer. *Circuit QED flip-flop memory with all-microwave* switching. Phys. Rev. Applied, **3**,024002, (2015)

[6] Christian Kraglund Andersen and Klaus Mølmer. *Multifrequency modes in superconducting resonators: Bridging frequency gaps in off-resonant couplings.* Phys.Rev. A, **91**,023828, (2015)

[7] Christian Kraglund Andersen, Joseph Kerckhoff, Konrad W. Lehnert, Benjamin J. Chapman, and Klaus Mølmer. *Closing a quantum feedback loop inside a cryostat: Autonomous state preparation and long-time memory of a superconducting qubit.* Phys. Rev. A, **93**,012346, (2016).

[8] G Oelsner, CK Andersen, M Rehák, M Schmelz, S Anders, M Grajcar, U Hübner, K Mølmer, and E Il'ichev. *Detection of weak microwave fields with an underdamped Josephson junction.* arXiv:1605.05935, (2016)

[9] Christian Kraglund Andersen and Alexandre Blais. *Ultrastrong coupling dynamics with a transmon qubit.* arXiv:1607.03770, (2016)

[10] Christian Kraglund Andersen, Archana Kamal, Michel H. Devoret, and Alexandre Blais. *Quantum versus classical switching dynamics of driven-dissipative Kerr resonators.* In preparation, (2016)

[11] Samuel Boutin, Christian Kraglund Andersen, Jayameenakshi Venkatraman, Andrew J. Ferris, and Alexandre Blais. *Resonator reset in circuit QED by optimal control for large open quantum systems.* In preparation, (2016)

[12] Eliska Greplova, Klaus Mølmer, and Christian Kraglund Andersen. *Quantum teleportaion with continuous measurements.* In preparation, (2016)

[13] Henrik Lund Mortensen, Klaus Mølmer, and Christian Kraglund Andersen. *Normal modes of a superconducting transmission-line resonator with embedded lumped element circuit components.* arXiv:1607.04416, (2016)

[14] Shruti Puri, Christian Kraglund Andersen, Arne Grimsmo, and Alexandre Blais. Adiabatic quantum computing with parametrically driven Kerr resonator. *In preparation*, (2016)

[15] Christian Kraglund Andersen and Andrew Christopher James Wade. Bohr vs. Einstein: Fortolkning af kvantemekanikken (*outreach article in Danish*). *Kvant*, (2013).

Contents

Chapter 1

Introduction and outline

Quantum mechanics has gone a long way since its foundation in the early 1900's. Initially, discussions in the field ware centered around the question whether quantum theory is indeed a complete theory [16, 17], but nowadays quantum mechanics is one of the best tested physical theories and it plays a fundamental role in the our everyday technologies like computers, lasers and in the medical industry.

However, since around 1990 it has been apparent that the way information is encoded in quantum mechanics is very different from the way we normally deal with information [18–21]. This fact is the motivation in the pursuit for quantum information technologies, that may revolutionize the way we think about information in the future [22].

Many physical implementations for quantum information technologies have been proposed, including NMR [23], ions [24, 25], neutral atoms [26, 27] and semiconductor quantum dots [28]. This thesis will focus on quantum information processing with superconducting quantum circuits [29–32]. As a consequence of the completeness of quantum theory, any physical degree of freedom can be treated as quantum mechanical degree of freedom if we can prepare the system in its quantum mechanical ground-state (or close to it). Electrical microwave systems typically work with electromagnetic signals with frequencies, ν, in the GHz regime, which means the energy associated with a single quantum of electrical signal is around $h\nu \sim 10^{-24}$ J, corresponding to a thermal energy at a temperature $T_q = 0.1$ K, so if we can cool our microwave device to a temperature much lower than T_q, our system will relax to its quantum mechanical ground state. At these low temperatures, many metals become superconducting (in particular niobium and aluminum), which makes them ideal as information carriers

since superconducting devices have zero Ohmic resistance of current and thus a quantum state of current will not dissipate into heat over time.

Having low loss of quantum information is however not enough for a quantum technology to perform well. Like classical digital technology that relies on bits, that is a lot of 0s and 1s, quantum technology relies on so-called qubits [33]. In quantum mechanics everything is described by wave-functions, which is much different from the classical concept of either 0 or 1, as a wave can be in superpositions and interfere with itself and other waves as well like ripples on a lake. While the general framework for quantum mechanics is more elaborate than this, we can define the simplest quantum wavefunction as

$$|\psi\rangle = a|0\rangle + b|1\rangle \tag{1.1}$$

where $|0\rangle$ and $|1\rangle$ are quantum states analogous to the classical bit values. A system described by this wavefunction is referred to as a qubit. In contrast to classical mechanics, the values a and b are not values that we can directly measure, but instead they are probability amplitudes such that $|a|^2$ is the probability to measure 0 and $|b|^2$ the probability to measure the value 1. The curious thing about quantum mechanics is that the qubit can be in both $|0\rangle$ and $|1\rangle$. However, since we as observers are classical beings we can only measure classical outcomes and, as such, once we observe a qubit we can only measure it to be in either $|0\rangle$ or $|1\rangle$.

Going back to classical bits, these are typically a high or low voltage at an electronic chip and all the devices of modern information technology are just machines that manipulate these 0s and 1s to generate a certain output (like a cat on youtube or a weather forecast). A quantum computer is a machine that can take one or more qubits and with sufficiently high probability produce an output as a classical result and which answers a specific problem for instance the prime factors of a very large number [21]. While the theoretical protocol for doing such a calculation is known, the hardware to actually run the protocol is not available. In particular it is challenging to maintain a quantum state without accidentally measuring it while at the same time performing the necessarily operations on the qubits. in that sense we have some quantum software ready, but the hardware is not yet reliable. The theory necessary for building the hardware for such quantum technologies using superconducting circuits is what this thesis covers.

In Chapter 2 the framework of circuit quantum electrodynamics (QED), which is a technical term for the circuits we will study in this thesis, will

be introduced and serve as a brief review of the field and will draw on material from [2, 3, 5–8, 12, 13]. Chapter 3 will cover work [9, 10] on arrays of Josephson junctions, a particular construction which is widely used in circuit QED. A microwave detector and the theory to describe it is presented in Chapter 4, covering [2, 3], including an overview of a recent experimental realization of the detector [8]. Chapter 5 will present ideas for classical control of a quantum computer [5, 7], while Chapter 6 will focus on ideas for engineering relevant couplings for different quantum computing architectures [6, 14]. Finally, Chapter 7 will conclude the whole thesis and discuss a brief outlook of this work and the field of circuit QED in general.

Chapter 2

Circuit QED: An introduction

Superconducting circuits of resonators and qubits, also referred to as circuit QED [29, 30], meets in principle all the criteria needed [34] for quantum computing [31, 32] as high quality qubit systems are routinely manufactured using a specific superconducting element called a Josephson junction. The low temperatures of cryogenic coolers automatically gives you a well-defined initial state, while microwave radiation and magnetic fields allow one to implement gates and measurements. The real implementation of quantum technology is, however, occurring at different abstract levels [35, 36] as both high-level algorithms need to be identified and low-level hardware needs to be precisely manufactured. This thesis and, in particular, this chapter focus on the hardware required before any hope of implementing high-level quantum algorithms are possible. Any hardware aiming at implementing a quantum computer needs to solve a list challenges that can be summarize in the following prioritized list:

1. Engineering of the optimal quantum system.
2. Readout of the relevant degrees of freedom.
3. Control of single quantum degrees of freedom.
4. Interaction between two (or more) quantum system.
5. Minimize the complexity of scaling.

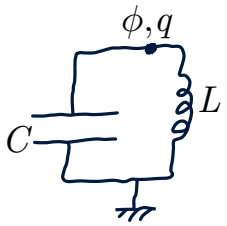

Figure 2.1: A LC-circuit with the charge, q, and phase, ϕ, as the conjugate variables.

Notice the reference to single quantum degrees instead of qubits as various quantum elements, such as continuous degrees of freedom or few-level systems, may play a role in the final architecture for a quantum computer or other quantum technologies. In this chapter, an overview of the field with the focus on the challenges above will be presented, while the rest of the thesis will present the authors contributions in (partly) solving these challenges.

2.1 Resonators and linear circuits

The simplest electrical circuit is the co-called LC-oscillator [37], made of an inductor and a capacitor as shown in Fig. 2.1. The classical equation of motion for the current and the voltage is easily written using Kirchoff's rules [38]:

$$I(t) = -C\frac{dV(t)}{dt}, \tag{2.1}$$

$$V(t) = L\frac{dI(t)}{dt}, \tag{2.2}$$

which can be expressed solely as an equation for the current,

$$\frac{d^2 I(t)}{dt^2} = -\frac{1}{LC}I(t), \tag{2.3}$$

with the solution $I(t) = A\sin\omega_0 t + B\cos\omega_0 t$ where the angular frequency of current oscillations is given as $\omega_0 = 1/\sqrt{LC}$.

Now for a capacitor, C, with a voltage V across, the stored electric energy is given by $\frac{1}{2}CV^2$ and for an inductor, L, with a current I the magnetic energy is given by $\frac{1}{2}LI^2$. Expressing the energy by the charge, the energy is simply given as [37]

$$H = \frac{1}{2C}q^2 + \frac{L}{2}\dot{q}^2, \tag{2.4}$$

or if we identify the phase ϕ such that $\dot{\phi} = V$,

$$H = \frac{1}{2C}q^2 + \frac{1}{2L}\phi^2. \tag{2.5}$$

We notice q and ϕ are conjugate variable such that this Hamiltonian is equivalent to the well-known Hamiltonian of a harmonic oscillator ($H = p^2/2m + kx^2/2$) with $m, k, x, p \to C, 1/L, \phi, q$. Thus, completely identically to the quantization of a harmonic oscillator, the bosonic ladder-operator a is introduced such that

$$[a, a^\dagger] = 1, \tag{2.6}$$

and

$$\phi = \sqrt{\frac{\hbar Z_0}{2}}(a^\dagger + a), \qquad\qquad q = i\sqrt{\frac{\hbar}{2Z_0}}(a^\dagger - a), \tag{2.7}$$

with $Z_0 = \sqrt{L/C}$ being the impedance of the resonator. The resulting quantum mechanical Hamiltonian now becomes

$$H = \hbar\omega_0\Big(a^\dagger a + \frac{1}{2}\Big) \tag{2.8}$$

as expected.

With the single LC-circuit a hand, more elaborate systems can be considered and the general approach is to write the Kirchoff equations in general way in order to extract the proper equation of motion from which normal modes can be identified and quantized. The Lagrangian formalism is indeed such a method and should be understood analogous to the Lagrangian method for classical mechanics, but with the potential energy set by the inductive elements and the kinetic energy set by the capacitive energy [37],

$$\mathcal{L} = \mathcal{K}_{\text{capacitive}} - \mathcal{U}_{\text{inductive}}. \tag{2.9}$$

A general way to express the energies is to identify the nodes of a circuit with the phase variable ϕ_i, such that the node is connected to the rest of the nodes ϕ_j by either capacitive or inductive elements. If two nodes are connected by a capacitor, C, the energy is given as

$$\mathcal{L}_C = \frac{C}{2}(\dot{\phi}_i - \dot{\phi}_j)^2 \tag{2.10}$$

and if the the two nodes are connected by an inductor, L, the Lagrangian term is

$$\mathcal{L}_L = -\frac{(\phi_i - \phi_j)^2}{2L}. \tag{2.11}$$

Does the inductive elements form a loop with an external magnetic flux through, the circuit topology must be considered in order to include the energy of the external field correctly [13, 37], but for simplicity we disregard such considerations here. Now, using the Euler-Lagrange equation,

$$\frac{\partial \mathcal{L}}{\partial \phi_i} - \frac{d}{dt}\frac{\partial \mathcal{L}}{\partial \dot{\phi}_i} = 0, \tag{2.12}$$

Kirchoffs law is regained as the equations of motion for the system.

As a quick example we consider a series of n LC-circuits, see Fig. 2.2 (a). For the phase at each node, ϕ_i, defined here as the time integral of the voltage over the i'th grounded capacitor, the equations of motion is easily seen to be

$$C\,\ddot{\phi}_j = \frac{2\phi_j - \phi_{j+1} - \phi_{j-1}}{L} \qquad \text{for } 1 \leq j \leq n-1. \tag{2.13}$$

which is also the Euler-Lagrange equation for the Lagrangian

$$\mathcal{L} = \sum_{j=1}^{n} \left(\frac{C}{2}(\dot{\phi}_j - \dot{\phi}_{j-1})^2 + \frac{(\phi_j - \phi_{j-1})^2}{2L} \right). \tag{2.14}$$

Knowing the boundary conditions for ϕ_0 and ϕ_n, we obtain $n-1$ solvable coupled equations of motion with $n-1$ normal modes as solution.

So far, we have only considered *lumped element* circuits, where all spatial properties are ignored and a circuit element diagram fully describes the system. However, we need to also consider *distributed elements*, where we allow the voltage and current to differ across a single element. This leads to a spatial mode structure and to discrete sets of eigenfrequencies.

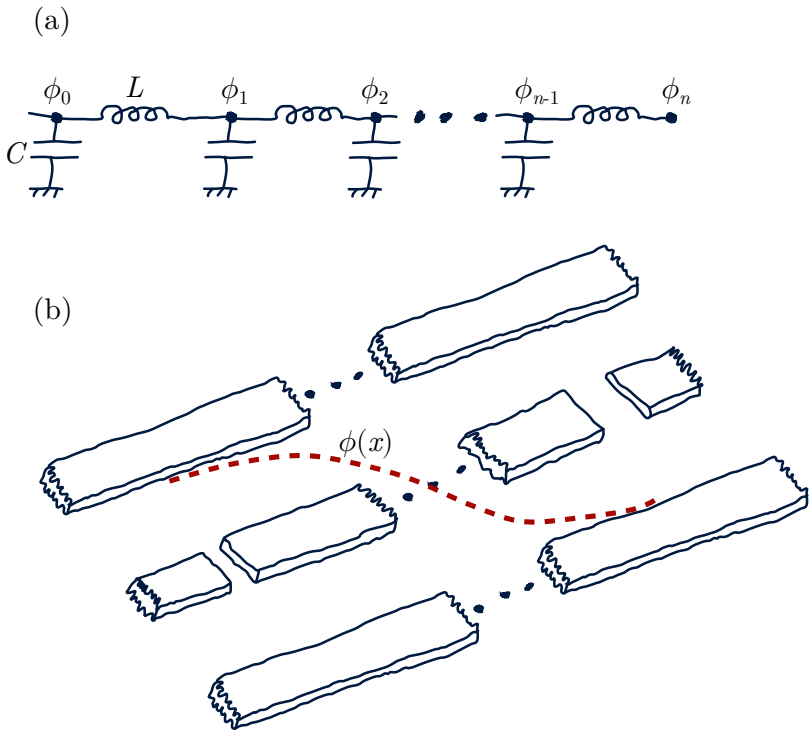

Figure 2.2: (a) A circuit of a series of n coupled LC-circuits. (b) An illustration of a transmission line resonator with the mode function, $\phi(x)$, for the fundamental mode is sketched as the red dashed line.

Any distributed element can, however, be represented by (infinitely many) lumped elements.

The most fundamental distributed element is the transmission line resonator, typically consisting of a coplanar wave-guide with breaks in the center-line working as capacitors and, thus, "mirrors" for microwave photons. In the lumped element representation, the transmission line resonator is described as an series of n LC circuits, which, in the limit $n \to \infty$, will give an appropriate description of the resonator [30]. This allows us to write the equation of motion for each node of the resonator, except the end nodes, as Eq. (2.13) with $C = C_T \Delta x$, $L = L_T \Delta x$, $\Delta x = d/n$ and, d

being the length of the resonator while C_T and L_T are the capacitance and inductance per length of the resonator. Taking the continuum limit of $\Delta x \to 0$, our sequence of discretized flux variables become a function of x, $\phi_j \to \phi(x)$, and the proper Lagrangian for the system becomes:

$$\mathcal{L} = \int_0^d dx \Big\{ \frac{C_T}{2} \big(\partial_t \phi(x,t)\big)^2 - \frac{1}{2L_T} \big(\partial_x \phi(x,t)\big)^2 \Big\}. \tag{2.15}$$

With the field now containing two continuous variables, the Euler-Lagrange equation then reads,

$$\frac{\partial \mathcal{L}}{\partial \phi(x,t)} - \frac{d}{dt} \frac{\partial \mathcal{L}}{\partial(\partial_t \phi(x,t))} - \frac{d}{dx} \frac{\partial \mathcal{L}}{\partial(\partial_x \phi(x,t))} = 0, \tag{2.16}$$

which for the transmission line resonator leads to the wave equation

$$v^2 \partial_x^2 \phi(x,t) - \partial_t^2 \phi(x,t) = 0, \tag{2.17}$$

with the wave velocity $v = 1/\sqrt{C_T L_T}$. It is natural to impose the open boundary condition $\partial_x \phi(0,t) = \partial_x \phi(d,t) = 0$ such that the normal mode expansion is written as,

$$\phi(x,t) = \sum_j \varphi_j(t) \cos k_j x, \tag{2.18}$$

with the normal-modes wave-number given by

$$k_j d = \pi j. \tag{2.19}$$

Other boundary conditions can also be set typically by capacitances at the end nodes connecting the resonator to a transmission line. The Euler-Lagrange equation can now be solved for the transmission line resonator Lagrangian, which yields $\ddot{\varphi}_j(t) = -\omega_j^2 \varphi_j(t)$ with $\omega_j = j\omega_0$. The mode operators a_j can then be introduced, such that

$$\varphi_j = \varphi_{j,0} \, (a_j^\dagger + a_j), \tag{2.20}$$

$$q_j = \frac{\partial \mathcal{L}}{\partial \dot{\varphi}_j} = C_T d \dot{\varphi}_j = i \, q_{j,0} (a_j^\dagger - a_j). \tag{2.21}$$

In the quantum regime, the resonator operators q_j and φ_j satisfy the canonical commutation relation $[\varphi_j, q_j] = -i\hbar$, such that the ladder operators a_j ($a_j^\dagger$) annihilates (creates) a microwave photon in the normal mode of

the resonator. By performing a Legendre transformation, the Hamiltonian yields (ignoring constant energy terms)

$$H = \sum_j \hbar\omega_j a_j^\dagger a_j, \tag{2.22}$$

which is equivalent to the Hamiltonian of, say, an optical Fabry-Perot cavity. Also, the voltage operator at any point in the resonator

$$\tilde{V}_j(x) = \sum_j \tilde{V}_{j,rms} i(a_j^\dagger - a_j) \sin k_j x, \tag{2.23}$$

with $\tilde{V}_{j,rms} = \sqrt{\hbar\omega_j/2C_T d}$ and similarly for any other physical quantity.

The transmission line resonator works as an engineered harmonic oscillator and it is straight forward to manipulate the state of this by applying a microwave drive to the transmission line. The resonator is capacitively connected to the applied drive, so we obtain the Lagrangian

$$\mathcal{L}_d = \frac{C_c}{2}(\dot{\phi}(0,t) - V_d(t))^2. \tag{2.24}$$

which changes the frequency of the mode slightly and also leads to the Hamiltonian

$$H_c = \sum_j -iC_c\tilde{V}_{j,rms}V_d(t)(a_j^\dagger - a_j). \tag{2.25}$$

The classical single-frequency microwave drive can be written as $V_d(t) = V_{d,0}\sin(\omega_d t)$ and if it is assume that ω_d is close to only one ω_j, only one mode is necessary to consider and in a frame rotating with ω_d the interaction Hamiltonian can be written as

$$H_c = \hbar\Delta_j\, a_j^\dagger a_j + \hbar\epsilon_d\,(a_j^\dagger + a_j) \tag{2.26}$$

with the drive $\hbar\epsilon_d = C_c\tilde{V}_{j,rms}V_{s,0}$ and the detuning $\Delta_j = \omega_j - \omega_d$. Starting in the vacuum state $|0\rangle$, the time evolution will put the resonator in a coherent state $a|\alpha\rangle = \alpha|\alpha\rangle$ at all times. The capacitative coupling, C_c not only couples an input drive, but also a continuum of modes, which will introduce a finite linewidth of the resonator mode κ. Hence, the field inside the resonator will leak out of the resonator. A measurement of the field in the transmission line wavegude therefore measures the field leaking out of the resonator.

2.2 Qubits

Superconducting resonators, both lumped and distributed, constitute in the quantum regime a quantum mechanical harmonic oscillator. However, in order to perform quantum information processing we need also non-linear elements. Without any non-linear elements, the quantum system can be described by coherent states, as shown in Sec. 2.1, which allows for an efficient classical description and any quantum advantageous disappears. The simplest non-linear system is a qubit. Therefore for circuit QED to be used for quantum information processing, we need to design a loss-less circuit that in the quantum regime only supports two eigenstates.

The main ingredient in making superconducting qubits is the Josephson junction, which can also be thought of as a non-linear inductor. The Josephson junction (JJ) consist of two superconductors separated by a thin insulation layer. It can be shown that the equation of motion for the current through the JJ is given as (known as the Josephson effect)

$$I(t) = I_c \sin(2\pi\phi(t)/\Phi_0), \tag{2.27}$$

with I_c the critical current of the Josephson junction and $\Phi_0 = h/(2e)$ the magnetic flux quantum. This equation should be compared to that of an inductor, $I(t) = \phi(t)/L$, with the voltage given as $V(t) = \partial\phi(t)/\partial t$. The energy of the electromagnetic field over the junction can then be calculated as

$$\begin{aligned} U &= \int_0^t IV dt \\ &= \frac{\Phi_0}{2\pi}\int_0^t I_c \sin(2\pi\phi(t)/\Phi_0)\frac{\partial\phi(t)}{\partial t}dt \\ &= \frac{\Phi_0}{2\pi}\int_0^{\phi(t)} I_c \sin(2\pi\phi/\Phi_0)d\phi \\ &= \frac{\Phi_0 I_c}{2\pi}(1-\cos(2\pi\phi(t)/\Phi_0). \end{aligned} \tag{2.28}$$

Therefore, the potential energy for a Josephson junction is written as $U = -E_J\cos(2\pi\phi/\Phi_0)$ with E_J referred to as the Josephson energy. With $U(\phi)$ we have the tool to make a qubit

Finally, we note that one way to assess the qubit performance is the relaxation time T_1, ie. time-scale of relaxation from the 1 state to the 0 state, and the dephasing time T_2 defined as the relaxation of the cross terms of the qubit density matrix $\rho_{10}(t)$. Notice therefore that the dephasing time is limited by the relaxation time, $T_2 \leq 2T_1$. These times will be referred to as decoherence times throughout the thesis.

2.2.1 Charge qubits

The simplest and, firstly demonstrated, superconducting qubit is the cooper-pair box [39, 40], which is just a single superconducting island connected to a superconducting reservoir via a SQUID (two Josephson junctions in parallel) and with a large charging energy set by a small gate capacitance of the island. The large charging energy, E_C, creates a big energy splitting depending on the number of charges on the island and due to SQUID coupling of the island, charges only appear in cooper pairs of charge $-2e$.

While the cooper-pair box was demonstrated to function as a qubit, its coherence time was very small in the initial design and even with the introduction of the Quantronium [41] and the use of 'sweet-spots' the coherence time was limited by charge noise, which originates from charge fluctuations on the gate capacitance. An approach to circumvent this fact is by moving to the regime of phase qubits, where the Josephson energy E_J is several orders of magnitude larger than E_C, which completely eliminated the charge noise, but the downside is that anharmonicity of the qubit becomes very small such that we essentially are left with an harmonic osciallator (however application of a control current can change this fact).

A breakthrough happened with the design of the transmon qubit [42–44], which is a cooper-pair box shunted by a large capacitor, such that $E_J/E_C \sim 50 - 100$ since $E_C = e^2/(2(C_J + C_s))$ with C_J as the junction capacitance and C_s the shunt capacitance. In Fig. 2.3 a schematic of the transmon circuit is shown and it can quickly be shown that the Hamiltonian of this circuit turns out to be

$$H = 4E_C(\hat{n} - n_g)^2 - E_J \cos(\hat{\phi}/\varphi_0) \tag{2.29}$$

with the reduced flux quantum, $\varphi_0 = \Phi_0/2\pi$. An example of the eigenenergies as a function of the gate charge n_g is shown in Fig. 2.4 [42] and we see that for sufficiently large E_J/E_C, the eigenenergies becomes insensitive to the gate charge and therefore also to charge noise. Letthe energy difference between the ground state and the first excited state be denoted as $E_{10} = E_1 - E_0$. It can then be shown [42] that the charge dispersion given as the difference between the maximum and minimum energy, $\Delta E_{10} = \max_{n_g}(E_{10}) - \min_{n_g}(E_{10})$ follows the proportionality $\Delta E_{10} \propto e^{-\sqrt{8E_J/E_C}}$, thus falling off very fast.

In the regime of $E_J/E_C \gg 1$, we can treat the Hamiltonian as an

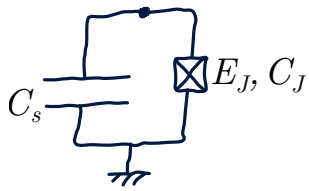

Figure 2.3: A transmon qubit consisting of a Josephson junction with the Josephson energy, E_J and Josephson capactitance, C_J. The junction is shunted by a large capacitance, C_s.

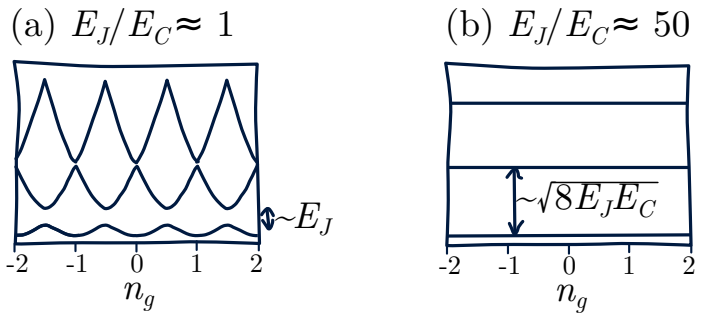

Figure 2.4: The three lowest energy levels of the charge qubits for (a) $E_J/E_C \approx 1$ and (b) $E_J/E_C \approx 50$.

harmonic oscillator with a high-order term coming from the cosine, [42]

$$H \approx \sqrt{8E_CE_J}(b^\dagger b + 1/2) - E_J - E_C(b + b^\dagger)^4. \tag{2.30}$$

To calculate the above we used that $\hat{\phi} = (8E_C/E_J)^{-1/4}(b + b^\dagger)$ and $\hat{n} = -2e\hat{q}$ similar to the way we introduced the bosonic operators for the harmonic oscialltor in Sec 2.1. This Hamiltonian have the eigenenergies [42]

$$E_n = -E_J + \sqrt{8E_CE_J}(n + 1/2) - E_C(6n^2 + 6n + 3)/12 \tag{2.31}$$

and we see that the anharmonicity is $\alpha = E_{21} - E_{10} = -E_C$, which leads to a relative anharmonicity $\alpha_r = \alpha/E_{10} = -1/\sqrt{8E_J/E_C}$, thus falling off

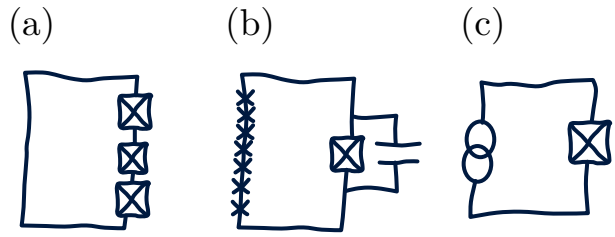

Figure 2.5: Three kinds of qubits; (a) A flux qubit, (b) a fluxonium qubit and (c) a phase qubit.

as a slow power law and hence much slower than the charge dispersion. Therefore it is advantageous to increase E_J/E_C as it will only slightly reduce qubit anharmonicity but significantly increase the coherence time of the qubit.

The transmon design has appeared in experiments in many different variations. In early experiments, the transmon was embedded into a transmission line resonator [44]. The Xmon [45], uses an X-shaped transmission line resonator as the shunt capacitor . The 3d-transmon [46] places the transmon inside a 3d-cavity with large capacitor plates acting as both the shunt capacitor and antennas for the microwave field in the cavities.

2.2.2 Other kind of qubits

There exist also different kind of superconducting qubits and here we briefly mention a few of these:

A flux qubit [47–49] consist of a superconducting loop, interrupted by three (or more) Josephson junctions, eg. as in Fig. 2.5. The Lagrangian for the flux qubit can be written as [50]

$$\mathcal{L}_{fq} = \sum_{k=1}^{3} \left[\frac{C_{J,k}}{2} \dot{\phi}_k^2 + E_{J,k} \cos(\phi_k/\phi_0) \right] \tag{2.32}$$

with k summing over the three junctions that constitute the qubit. The junction 1 and 3 are identical with $C_{J,1} = C_{J,3} = C_J$ and $E_{J,1} = E_{J,3} = E_J$, while the center junction 2, referred to as the α-junction, has $E_{J,2} = \alpha E_J$ and $C_{J,2} = \alpha C_J$ with $\alpha < 1$. Due to the loop geometry we have for the fluxes,

$$\phi_1 + \phi_2 - \phi_3 = \Phi_{\text{ex}} \tag{2.33}$$

where Φ_{ex} is the externally applied flux through the loop. Now using Eq. (2.33) we can eliminate the variable ϕ_2 and we define the variables $\phi_\pm = (\phi_3 \pm \phi_1)/2$. This way we can obtain the flux qubit Hamiltonian [50, 51],

$$H_{fq} = \frac{q_-^2}{2[(4+4\alpha)C_J]} + \frac{q_+^2}{2(4C_J)} - E_J\left[2\cos(\varphi_+)\cos(\varphi_-) + \alpha\cos\left(\frac{2\pi\Phi_{\text{ex}}}{\phi_0} + 2\varphi_-\right)\right] \tag{2.34}$$

with q_i being the conjugate variable to ϕ_i and $\varphi_i = 2\pi\phi_i/\Phi_0$. This Hamiltonian can be diagonalized numerically and at the flux sweet-spot $\Phi_{ex} = \Phi_0/2$ the energy-splitting between the two lowest eigenstates are much smaller than E_J, while the third state is far away in the energy spectrum, i.e. we have a well-defined qubit in the φ_--mode. For flux qubits we often have E_J much larger than the charge energy and in the vicinity of the sweet-spot, the Hamiltonian is often written as

$$H_{fq} = \Delta\sigma_z + \varepsilon(\Phi_{\text{ex}})\,\sigma_x \tag{2.35}$$

with the energy gap, Δ, and the flux dependent tunneling amplitude, $\varepsilon(\Phi_{ex})$, to emphasize a rotation of the qubit basis when tuning the qubit by the external flux.

A qubit type similar to the flux qubit is the fluxonium [52, 53]. Here, a flux-loop is made of of single small (and thus very anharmonic) Josephson junction shunted with a capacitance and a superinductor [54, 55], that is a very high impedance loss-less inductance typically constructed by a large array of Josephson junctions, see Chapter 3 [9, 10] and Fig. 2.5. The Hamiltonian for the fluxonium is given as

$$H = 4E_C\hat{n}^2 + E_L(\hat{\phi}/\varphi_0)^2 - E_J\cos((\hat{\phi} - \Phi_{ex})/\varphi_0). \tag{2.36}$$

The fluxonium has the advantage of being charge insensitive as the transmon but with a very large anharmonicity. Furthermore, the very large impedance suppresses so-called quasi-particle contributions to the relaxation yielding very large relaxation times, T_1 [56].

The phase qubit [57, 58] is similar to the charge qubit but it has $E_J/E_C \sim 10^4$, which (as mentioned) makes it almost fully harmonics. To compensate, a current, I_b, is applied to the junction and therefore the phase qubit is also often referred to as a current-biased Josephson junction (CBJJ). The potential is now given as

$$U(\phi) = -E_J(\cos(\phi/\varphi_0) + I\phi_0/\varphi_0) \tag{2.37}$$

with $I = I_b/I_c$. Now for I close to 1, the potential becomes again very anharmonic and thus the CBJJ works as a phase qubit, however noise in the current limits the coherence time of the qubit.

The last interesting qubit mentioned in the chapter is qubits encoded in the subspace of a resonator field of a high Q cavity [59–61]. The simplest idea is to create a way to create cat states of a harmonic oscillator, $|\mathcal{C}_\pm\rangle = (|\alpha\rangle \pm |-\alpha\rangle)/\sqrt{2}$, where the "cat" refers to the analogy to Schrödinger's cat being in the superposition of two very classical states, namely being dead and alive, $|\text{cat}\rangle = (|\text{dead}\rangle + |\text{alive}\rangle)/\sqrt{2}$. The cat states of an oscillator is less morbid, and is only a superposition of the classical-like coherent states, $|\alpha\rangle$. In the limit of $\alpha \gg 1$, the two cat states can be used as a subspace for encoding quantum information. Similarly, the coherent states themselves can be used as a basis [12, 14] or one can define 'multi-legged' cat states as a basis [60].

2.3 Circuit QED – light-matter interaction

Having a linear circuit (resonator) and a qubit, the two can be coupled together. This is in particular interesting as the qubit is acting as an artificial atom, having only a discrete number of energy level and the resonator is similarly considered to play the role of light interacting with atoms [62]. For atoms and light, cavity quantum electrodynamics is the study of light-matter interaction at the level of a single atom interacting with a single photon both confined in a high-Q cavity and is often described by the Jaynes-Cummings (JC) Hamiltonian,

$$H_{\text{JC}} = \hbar\omega\, a^\dagger a + \frac{\hbar\omega_a}{2}\sigma_z + \hbar g(a^\dagger\sigma_- + a\sigma_+), \tag{2.38}$$

where ω is the cavity frequency, ω_a the atomic frequency and g the electric dipole coupling. In this expression, a ($a^\dagger$) is the photon annihilation (creation) operator and σ_i Pauli matrices for the atomic levels. Reducing the atom to a single qubit, is often a very good approximation due to the anharmonicity of the atomic transitions. The interaction between the superconducting qubit and the resonator would now constitute a manufactured system with a controllable quantum light-matter interaction, one of the main points of interest in the field of quantum optics and physics in general. The combination of a microwave resonator with a superconducting qubit is referred to as circuit QED [29, 30]. In particular, various experiments with superconducting circuits [30] have shown strong

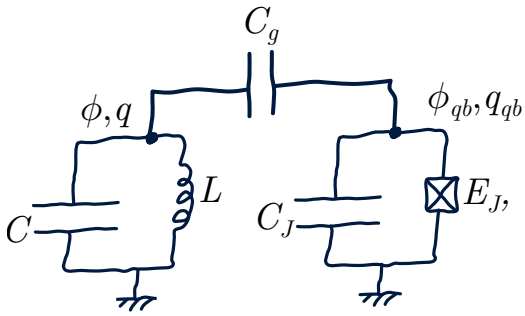

Figure 2.6: A lumped element circiut of a LC-resonator and a transmon qubit. The resonator is characterized by the capacitor C and the inductor L and its dynamics is described by the conjugate variables ϕ and q. The transmon is the system of a Josephson junction with the energy E_J and the capacitor C_J descriped by ϕ_{qb} and q_{qb}. The transmon and the resonator is coupled by the capacitor C_g.

coupling between a superconducting qubit and a microwave mode of a coplanar wave guide resonator [29, 63]. Strong coupling (which is the regime of g much bigger than the qubit decoherence rates, $1/T_1, 1/T_2$, and the cavity linewidth, κ) with superconducting circuits has allowed for experiments preparing and manipulating various quantum properties and states of the resonator and qubit [59, 64–66]. While circuit QED incorporates any kind of superconducting qubit, we will here only focus on circuit QED with transmon qubits.

We consider the circuit in Fig. 2.6 and get the Lagrangian

$$\mathcal{L} = \frac{C}{2}\dot{\phi}^2 - \frac{1}{2L}\phi^2 + \frac{C_J}{2}\dot{\phi}_{qb}^2 + E_J \cos\frac{\phi_{qb}}{\varphi_0} + \frac{C_g}{2}(\dot{\phi} - \dot{\phi}_{qb})^2, \tag{2.39}$$

where C_J here include the junction capacitance in the shunt capacitance. Using this Lagrangian we can easily find the conjugate variables

$$q = \frac{\partial \mathcal{L}}{\partial \dot{\phi}} = C\dot{\phi} + C_g(\dot{\phi} - \dot{\phi}_{qb}), \tag{2.40}$$

$$q_{qb} = \frac{\partial \mathcal{L}}{\partial \dot{\phi}_{qb}} = C_J\dot{\phi}_{qb} + C_g(\dot{\phi} - \dot{\phi}_{qb}). \tag{2.41}$$

Using this equation we can express the time-derivative of ϕ and ϕ_{qb} by the q's and we arrive at this Hamiltonian for the system

$$\begin{aligned} H = &\frac{C}{2}\Big(\frac{C_g + C_J}{C_\Sigma^2} q + \frac{C_g}{C_\Sigma^2} q_{qb}\Big)^2 - \frac{1}{2L}\phi^2 \\ &+ \frac{C_J}{2}\Big(\frac{C_g}{C_\Sigma^2} q + \frac{C + C_J}{C_\Sigma^2} q_{qb}\Big)^2 - E_J \cos\frac{\phi_{qb}}{\varphi_0} \\ &+ \frac{C_g}{2}\Big(\frac{C_J}{C_\Sigma^2} q - \frac{C}{C_\Sigma^2} q_{qb}\Big)^2 \qquad (2.42) \\ = &\frac{1}{2C_{eff}} q^2 + \frac{1}{2L}\phi^2 + \frac{C_g}{C_\Sigma^2} q q_{qb} \\ &+ \frac{1}{2C_{J,eff}} q_{qb}^2 - E_J \cos\frac{\phi_{qb}}{\varphi_0} \qquad (2.43) \end{aligned}$$

with

$$C_\Sigma^2 = CC_g + CC_J + C_g C_j, \qquad (2.44)$$

$$C_{eff}^{-1} = \frac{C(C_g + C_J)^2 + C_J C_g^2 + C_g C_J^2}{2C_\Sigma^4}, \qquad (2.45)$$

$$C_{J,eff}^{-1} = \frac{CC_g^2 + C_J(C + C_J) + C_g C^2}{2C_\Sigma^4}. \qquad (2.46)$$

We now go the the quantum regime and we introduce the bosonic degree of freedom, a for the ϕ-q-variables and we replace q with $-2e\hat{n}$. This yields the well-known transmon-circuit QED Hamiltonian [42]

$$H = \hbar\omega a^\dagger a + 4E_c\hat{n}^2 - E_J \cos\frac{\phi_{qb}}{\Phi_0} - 2e\beta\,\tilde{V}_{rms}\,\hat{n}(a^\dagger + a), \qquad (2.47)$$

where the new parameters are defined as

$$\omega = \frac{1}{\sqrt{C_{eff}L}}, \qquad E_C = \frac{e^2}{2C_{J,eff}}, \qquad (2.48)$$

$$\tilde{V}_{rms} = \sqrt{\frac{\hbar\omega}{2C_{eff}}}, \qquad \beta = \frac{C_g}{C_\Sigma^2/C_{eff}}. \qquad (2.49)$$

Now we can calculate the coupling strength between the resonator and the two nearby levels, j and $j+1$, of the transmon by

$$\hbar\,|g_{j,j+1}| \equiv 2e\beta\,\tilde{V}_{rms}\,|\langle j+1|\hat{n}|j\rangle|, \qquad (2.50)$$

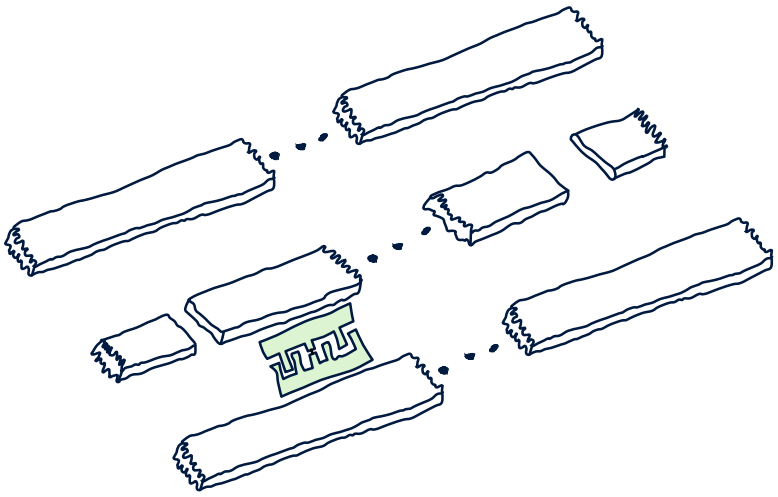

Figure 2.7: A transmission line resonator with a transmon qubit embedded into the line. This is equivalant to the circuit in Fig. 2.6.

where the matrix elements of $\hat{n}$ can be approximated in the limit $E_J/E_C \gg 1$ by

$$|\langle j+1|\hat{n}|j\rangle| = \sqrt{\frac{j+1}{2}}\left(\frac{E_J}{8E_C}\right)^{1/4}. \tag{2.51}$$

The matrix elements of $\hat{n}$ between j and $j+k$ $(k>1)$ all vanish in the transmon limit, $E_J/E_C \gg 1$. Thus, a generalized Jaynes-Cummings Hamiltonian can be written for the resonator and the transmon,

$$H = \hbar\omega a^\dagger a + \sum_j E_j|j\rangle\langle j| + \hbar\sum_j \Big(g_{j,j+1}|j\rangle\langle j+1|\,a^\dagger + g^*_{j,j+1}|j+1\rangle\langle j|\,a\Big), \tag{2.52}$$

with the transmon energies given in Eq. (2.31). Truncating to $j=0,1$ simplifies the transmon to a qubit. This truncation does not influence the physics if $\omega \sim \omega_{10} \equiv (E_1-E_0)/\hbar$ and ω is sufficiently different from ω_{21}.

In many physical realizations of circuit QED the resonator is however not made by lumped elements but rather by transmission line resonators

[42, 44], see Fig. 2.7. This does not change anything in the derivation above as long as we assume that only a single mode of the resonator is close in frequency to the qubit degree of freedom. We do however need to replace $\tilde{V}_{rms}$ with $\tilde{V}(x)$ as given by Eq. (2.23). Furthermore, for transmission line resonators often have an impedance of $Z_0 = \sqrt{L/C} \sim 50\,\Omega$ and since ω needs to in the GHz-regime, this puts $C \gg C_g, C_j$ for typical parameters. With this assumption $C_{eff} \approx C$, such that the resonator frequency is more or less unchanged by the qubit coupling and for the qubit $C_{J,eff} \approx C_J + C_g$ and $\beta \approx C_g/(C_J + C_g)$.

A final implementation are superconducting 3d cavities with a transmon coupling to the resonator field through a large antenna capacitor [46, 67, 68]. We will not talk about these in detail, but only note that these system are typically operated in the dispersive regime.

In Chapter 3 we will come back to the question of light–matter interaction, as it will be investigated how the interaction can be engineered to increase the strength of the light-matter interaction.

2.3.1 The dispersive regime

In the off-resonant limit of the qubit and the resonator [42, 69] such that detuning is much larger than the coupling, $|\Delta_{10}| \gg g$ (with $\Delta_{ij} = \omega_{ij} - \omega$ and $g = g_{0,1}$), the small parameter $\lambda = g/\Delta_{10}$ makes it possible to simplify the circuit QED Hamiltonian, Eq. (2.52). A unitary transformation can be made on the Hamiltonian as [70, 71],

$$H_D = e^{-\lambda X} H e^{\lambda X} = H + \lambda[H, X] + \mathcal{O}(\lambda^2), \tag{2.53}$$

and truncating to two levels of the transmon with choosing $X = a^\dagger \sigma_- - a\sigma_+$, $\sigma_- = |0\rangle\langle 1|$ and $\sigma_+ = \sigma_-^\dagger$, we get

$$H_D \approx \hbar\omega a^\dagger a + \hbar\frac{\omega_{10} + \chi}{2}\sigma_z + \chi\, a^\dagger a \sigma_z \tag{2.54}$$

with $\chi = g^2/\Delta_{10}$. This Hamiltonian can be interpreted as a qubit-state dependent frequency shift of the resonator (or equivalently, a photon number dependent frequency shift of the qubit), which under unitary time evolution leads to a qubit state conditional phase evolution of the resonator state. This evolution can directly be used for state preparation of the resonator state or as a gate between the resonator and the qubit. For instance, in Sec. 5.1 the conditional photon number in a resonator is used to make a conditional gate on the qubit. In Sec. 2.4 we will come back to how the same mechanism can be used for readout.

It is also important to note, that it is not only the coupling between the resonator and the qubit changes under the transformation above, but also any loss and dephasing channels. Before any transformation, the full quantum dynamics is governed by the master equation [72]

$$\dot{\rho} = \frac{-i}{\hbar}[H, \rho] + \kappa\mathcal{D}[a]\rho + \gamma\mathcal{D}[\sigma_-]\rho + \frac{\gamma_\phi}{2}\mathcal{D}[\sigma_z]\rho, \tag{2.55}$$

with $\mathcal{D}[X]\rho = X\rho X^\dagger - (X^\dagger X\rho + \rho X^\dagger X)/2$, κ the resonator relaxation rate, γ the qubit relaxation rate and γ_ϕ the pure dephasing rate of the qubit. Now, when the unitary transformation is performed and if the cavity is assumed to be in the vacuum, the qubit density matrix reduces to [70, 71]

$$\dot{\rho} = \frac{-i}{\hbar}[H, \rho] + \gamma_\downarrow\mathcal{D}[\sigma_-]\rho + \frac{\tilde{\gamma}_\phi}{2}\mathcal{D}[\sigma_z]\rho, \tag{2.56}$$

with $\tilde{\gamma}_\phi = \gamma_\phi(1 - 2g^2/\Delta_{10}^2)$, $\gamma_\downarrow = \gamma(1 - g^2/\Delta_{10}^2) + \gamma_p$ and the Purcell decay $\gamma_p = \kappa g^2/\Delta_{10}^2$. If the resonator is not empty both $\gamma_\downarrow$ and $\tilde{\gamma}_\phi$ increases linearly in photon number $\bar{n}$, also known as dressed dephasing [71] which also adds a spontaneous excitation term $\gamma_\uparrow\mathcal{D}[\sigma_+]\rho$ to the master equation.

2.4 Readout

Once a quantum system has been engineered, a readout is needed. In optical systems, photon counters and cameras can measure light emitted from a quantum system. As already mentioned, circuit QED systems work with microwaves in the GHz regime, where a single photon contain insufficient amount of energy to be measured using conventional approaches. Instead, a so-called IQ-mixer can down-convert a classical microwave signal to a frequency of ∼100 MHz using a large local oscillator fiel. The down-conversion process happens at room temperature and therefore also mixes the signal with a thermal field. The signal must therefore be stronger than the thermal background at room-temperature, which means only strong microwave signals can be measured. The down-converted signal has two output ports, I and Q, which is the in-phase and out-of-phase component of the signal as compared to the phase of the local oscillator. These output can be analyzed using a standard analog to digital converters [29, 73]. In the language of quantum optics, this measurement of I and Q corresponds to a measurement of the microwave quadratures $X \propto (a^\dagger + a)$ and $Y \propto i(a^\dagger - a)$ respectively, thus, constitutes a heterodyne measurements. A homodyne measurement can also be obtained by mixing the signal with a local oscillator at the same frequency [73–75].

The challenge is now to have weak quantum signals amplified sufficiently to be observable at room temperature. There exist off-the-shelf microwave amplifiers, eg. the so-called HEMT amplifier working at a temperature of 4 K, but such an amplifier also adds noise corresponding to a thermal state of 4 K, which contains a much larger energy than a single microwave photon [29, 74]. Therefore we need a quantum limited amplifier adding only noise arising from Heisenbergs uncertainty relation [76]. It is straight forward to see this quantum limit; for an amplifier that takes the mode a as input and b as an amplified output [76–78],

$$b = \sqrt{G}a + \mathcal{N} \tag{2.57}$$

with G being the power amplification factor and $\mathcal{N}$ being an operator that must be added in order to have $[b, b^\dagger] = 1$. This way we get

$$[\mathcal{N}, \mathcal{N}^\dagger] = 1 - G. \tag{2.58}$$

From this we can calculate a bound on the noise in b by calculation its variance,

$$(\Delta b)^2 = G(\Delta a)^2 + \frac{1}{2}\langle\{\mathcal{N}, \mathcal{N}^\dagger\}\rangle \geq G(\Delta a)^2 + |G-1|/2. \tag{2.59}$$

which is the quantum limit of amplification (also know as the Caves limit) [76–78].

Having only linear elements will never lead to amplifications, so in order to create an amplifier in circuit QED, Josephson junctions need to be embedded into a circuit [79, 80] which creates a so-called Josephson parametric amplifier (JPA), for example, by shunting a $\lambda/4$-resonator with a Josephson junction [81]. Expanding the cosine of the Josephson junction potential energy gives a 4th order term, yielding the Hamiltonian (by only keeping energy conserving terms) [81]

$$H = \omega a^\dagger a + \frac{K}{2} a^\dagger a^\dagger a a. \tag{2.60}$$

The Heisenberg-Langevin equation for the operator a is

$$\dot{a} = -i\omega a - iKa^\dagger a a - \frac{\kappa}{2}a + \sqrt{\kappa}a_{in}(t) \tag{2.61}$$

with κ the linewidth set by the input coupling to the JPA and $a_{in}(t)$ being the input field with $[a_{in}(t), a_{in}^\dagger(t')] = \delta(t'-t)$. We can now make the substitutions $a \to (a+\alpha)e^{-i\omega_p t}$ and $a_{in} \to (a_{in}+\alpha_{in})e^{-i\omega_p t}$ with α and

α_{in} complex numbers such that $\alpha_{in}e^{-i\omega_p t}$ represents a classical pump field with the frequency ω_p. The equation of motion for the coherent state amplitude, α, of the JPA is now [81]

$$\dot{\alpha} = -i\Delta\alpha - \frac{\kappa}{2}\alpha - iK|\alpha|^2\alpha + \sqrt{\kappa}\alpha_{in}, \tag{2.62}$$

with $\Delta = \omega - \omega_p$. Now we can find steady state by $\dot{\alpha} = 0$ and taking the norm squared of this equation yields terms of $n = |\alpha|^2$:

$$\kappa|\alpha_{in}|^2 = \Delta^2 n + 2\Delta K n^2 + K^2 n^3 + \frac{\kappa^2}{4}n, \tag{2.63}$$

which calculates the drive power needed for a given target photon number. We may take the inverse to obtain $n(\alpha_{in})$, however, we are not ensured that this function will be single-valued. As a matter of fact, there will always be a set of parameters, Δ, K and κ, where $n(\alpha_{in})$ is multivalued and we can write the highest and lowest n's in this bistable regime as

$$n_{c,\pm} = \frac{2\Delta}{3K}\left(1 \mp \sqrt{1 - \frac{3(\Delta^2 + \kappa^2)/4)}{4\Delta^2}}\right). \tag{2.64}$$

This expression for $n_{c,\pm}$ can now be inserted into Eq. (2.63) to get the critical drive power to be in the bistable regime, α_c. However, if α_{in} is smaller but very close to α_c, we have a photon number that depends critically on the input amplitude – this fact is what can cause parametric amplification.

The linear equation of motion for a is now given as [81]

$$\dot{a} = -i\Delta a - 2iK|\alpha|^2 a - \frac{\kappa}{2}a - iK\alpha^2 a^\dagger + \sqrt{\kappa}a_{in} \tag{2.65}$$

and since this equation is linear, we can solve it in Fourier space, $a(t) = (2\pi)^{-1/2}\int d\delta e^{-i\delta t}a_\delta$, such that

$$0 = -i\Big(\Delta + 2K|\alpha|^2 + \delta\Big)a_\delta - \frac{\kappa}{2}a_\delta - iK\alpha^2 a^\dagger_{-\delta} + \sqrt{\kappa}a_{in,\delta} \tag{2.66}$$

Solving this equation we get (where γ_x and γ_y can be expressed from the solution)

$$a_\delta = \gamma_x\frac{a_{in,\delta}}{\sqrt{\kappa}} + \gamma_y\frac{a^\dagger_{in,-\delta}}{\sqrt{\kappa}} \tag{2.67}$$

and now we can use the boundary condition, $a_{out} = \sqrt{\kappa}a - a_{in}$, to write

$$a_{out,\delta} = g_{s,\delta} a_{in,\delta} + g_{i,\delta} a^{\dagger}_{in,-\delta} \tag{2.68}$$

with the signal amplitude gain, $g_{s,\delta}$ and the idler gain, $g_{i,\delta}$ given from Eq. (2.67). It can readily be checked that [81]

$$G_{\delta} \equiv |g_{s,\delta}|^2 = |g_{i,\delta}|^2 + 1 \tag{2.69}$$

such that the JPA saturates the bound for the quantum limited amplifier given in (2.59). We also observe that the imaginary part of $g_{s,\delta}$ vanish by choosing the correct phase of α. Therefore, if we consider $\delta = 0$ (degenerate case) where G_{δ} is maximized, we easily see that for the out-of-phase quadrature, $y_{out} \propto i(a_{out} - a^{\dagger}_{out})$, of the signal will vanish, thus only a single quadrature is amplified, which is also referred to as phase-sensitive or phase-non-preserving amplifier [77]. Therefore, when the strong signal is detected by the classical detector at room-temperature, only one quadrature is available and, thus, the detection is a homodyne detection [73, 82–85].

The JPA above was designed by embedding a junction inside a resonator and pumping with a strong microwave drive at the input port, see Fig. 2.8. The same effect can also be achieved by other means, most importantly by using a flux-modulated SQUID [86, 87]. When the SQUID is embedded into an LC-resonator, the frequency is tunable by the flux through the SQUID. Now, by applying a parametrically modulated flux trough the SQUID, Φ_{pump}, as a frequency $\omega_p = 2\omega$ we obtain an equivalent equation of motion for a as in Eq. (2.65) such that the degenerate amplification appears in the same way. This setup has the advantage that the signal is not mixed with the strong pump.

An alternative approach compared to the degenerate amplifier is the non-degenerate amplifier, that treats both in-phase and out-of-phase quadratures on equal footing. The Josephson parametric converter (JPC) works as such an amplifier [88–90]. The JPC consist of a three mode Josephson device shown in Fig. 2.8 with two modes, a and b, as the longitudinal and transverse mode, while a third mode, c, lives as an anti-symmetric mode across all four junctions. Under the strong classical pumping of the third mode the Hamiltonian reduces to

$$H = \omega_a a^{\dagger} a + \omega_b b^{\dagger} b + i g_{ab} (ab\, e^{i(\omega_a + \omega_b)t + \phi} + \text{h.c.}). \tag{2.70}$$

Now having the signal coupling into a as the input and the field leaking of of b as the output, this will generate a parametric amplification given that

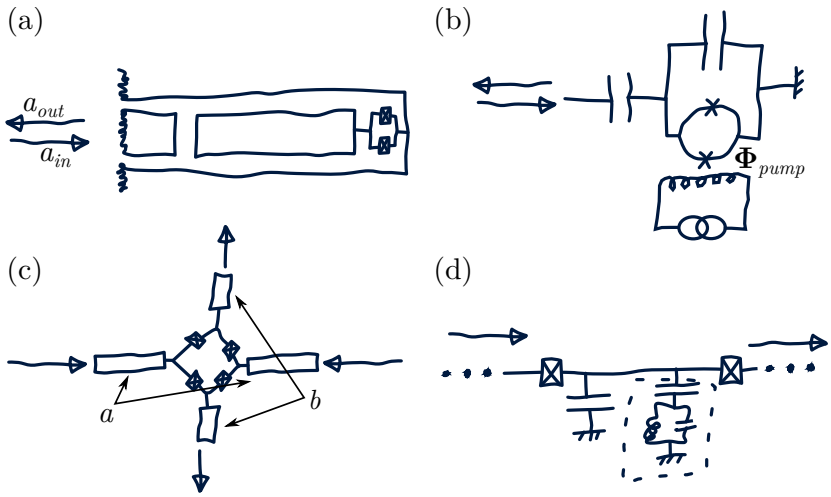

Figure 2.8: (a) A JPA made by embedding a SQUID into a $\lambda/$-resonator. The input and output is on the same port. (b) A lumped element JPA pumped by an external flux Φ_{pump}. (c) A JPC made of a Josephson ring inside two crossing resonators. (d) A JTWPA with Josephson junctions in a waveguide and embedded resonance circuits to phase match the transmitted signal.

g_{ab} is sufficiently large. The same physical process can also be achieved in so-called Josephson traveling wave amplifiers [91–93] (JTWPA), where a Josephson junction embedded wave guide creates a broadband gain medium for non-degenerate amplification. This technique can create a very large gain by embedding the nonlinear wave-guide with capacitively coupled LC-circuits as in Fig. 2.8 in order to resonantly phase match the amplified signal [91].

Finally it should be mentioned that even though all of the above measurement techniques work as a amplitude measurement and not as a single-photon detector, there is progress towards single-photon detectors for microwave photons, but due to the quantum-limit for amplifiers these must rely on different physics than the Kerr effect. One approach is to let a single photon be absorbed by artificial Λ system, which then can be read out with high fidelity [94]. Another approach is to use a three level system as a single photon transistor, such that a single photon phase-shifts

a probe field, however, such a setup is limited to a signal to noise ratio below 1 [95], but having directional elements that break the symmetry, such that multiple phase shifters element-wise can increase the signal [96]. Furthermore, an option is to let the single photon be absorbed by a phase qubit, which is characterized by a fast high fidelity readout mechanism [97–100]. A variation of the latter is the topic of Chapter 4 [2, 3] and a first experiment shows great promise [8].

2.4.1 Qubit readout

While having an approach to read microwave signals is important, a method to encode a qubit state into a microwave signal is required if we want to perform a measurement on a qubit. The standard approach is to perform a dispersive readout [29, 73, 74] of a qubit by having the qubit in an off-resonant resonator, such that the system is described by the Hamiltonian

$$H = \omega a^\dagger a + \frac{\omega_q}{2}\sigma_z + \chi\sigma_z a^\dagger a, \tag{2.71}$$

or written in a frame rotating according to the Hamiltonian $H_0 = \omega a^\dagger a + \frac{\omega_q}{2}\sigma_z$,

$$H_I = \chi\sigma_z a^\dagger a. \tag{2.72}$$

By applying a resonant coherent drive with amplitude ϵ_r to the cavity, $H_I \to H_I + \epsilon_r(a + a^\dagger)$. The mean-field coherent state amplitude of the cavity field now follows the equation

$$\frac{d}{dt}\alpha = -i\chi\langle\sigma_z\rangle\alpha - \frac{\kappa}{2}\alpha - i\epsilon_r, \tag{2.73}$$

with κ being the linewidth of the resonator. The steady state solution ($d\alpha_{ss}/dt = 0$) yields (assuming the qubit to be in an eigenstate)

$$\alpha_{ss} = \frac{-i\,\epsilon_r\kappa - 2\epsilon_r\chi\langle\sigma_z\rangle}{\frac{\kappa^2}{2} + 2\chi^2}. \tag{2.74}$$

For homodyne detection as presented above, we measure the quadrature $X_c = (a + a^\dagger)/2$, such that $\langle X_c\rangle_\beta = \mathrm{Re}(\beta)$ and for the steady state we obtain

$$\mathrm{Re}(\alpha_{ss}) = \frac{-2\epsilon_r\chi\langle\sigma_z\rangle}{\frac{\kappa^2}{2} + 2\chi^2}. \tag{2.75}$$

Therefore, we see that a measurement of X_c is a measurement of σ_z. The denominator of the expression above is strictly positive so that we can conclude that the sign of $\langle\sigma_z\rangle$ determines the sign of the homodyne signal. Therefore, if the signal, $J(t) = \sqrt{\kappa}\langle X_c\rangle_t + dW(t)/dt$ [101] with dW being the quantum noise with $\langle dW\rangle = 0$, is integrated over time, we get the integrated signal

$$M = \int_0^{T_m} \sqrt{\kappa} J(t)\, dt = \int_0^{T_m} \kappa\langle X_c\rangle_t\, dt + \Delta W_{T_m}, \tag{2.76}$$

with ΔW_{T_m} being the integrated Gaussian noise. The resulting sign of this average determines the state of the qubit: negative sign of the current implies excited state $|1\rangle$, while positive corresponds to ground state $|0\rangle$. Also note that H_I commutes with σ_z, such that the state of the qubit does not change during the readout, ie. the qubit readout is a quantum non-demolition measurement, so increasing T_m will always increase the measurement fidelity as long as we disregard qubit decay. In a real experiment, the qubit state will however spontaneously decay, hence, as fast readout as possible is desirable. To obtain a fast readout, it can be seen that a larger κ can optimize κ and find the maximal signal is achieved if $\kappa = 2\chi$. For this value, the average signal $\langle\sqrt{\kappa}J\rangle$ only depends on ε_r, which we can pick to fix a given photon number $n_r = |\alpha_{ss}|^2$ and we find $\epsilon_r = \kappa\sqrt{n_r}/8$. So in the end, we see that we need many photons in the resonator and a large linewidth to have a fast readout. Unfortunately, the dispersive regime breaks down if $n_r \gtrsim n_{crit} = \chi/(4\Delta)$ [70], with the qubit-resonator detuning $\Delta = \omega_q - \omega$, so in the end, κ is the only method to make the readout even faster.

A very large κ also requires a very large χ, which may be hard to obtain physically. Even more detrimental is the fact that a large κ leads to a Purcell decay as discussed above. However, recently an active area of research is the so-called Purcell filters [102–105]. In general [103], it holds that the contribution to the relaxation for a qubit that sees an environment with the admittance Y (inverse of the load impedance of the environment [106]) goes as

$$T_1^{\text{Purcell}} \propto 1/\text{Re}(Y(\omega_q)) \tag{2.77}$$

with ω_q as the qubit frequency. Thus if $\text{Re}(Y(\omega_q)) \to \infty$, the contribution to T_1 from the environment will vanish. In its simplest form the Purcell filter is made by a transmission line stub connected to the output of the resonator. This stub acts as a $\lambda/4$ impedance transducer, but only

at a single frequency, ω_f. Now, if $\omega_f = \omega_q$, the filter will short out the environment of the transmission line and thus create an effectively vanishing density of states in the environment at the qubit frequency, leading to vanishing Purcell-decay of the qubit through the filtered channel.

There are also other means of readout. For instance, the qubit could be coupled to a non-linear Kerr resonator instead of a linear one [107, 108]. As derived above, we find that for a driven dissipative Kerr resonator there exist a critical photon number,

$$n_{c\pm} = -\frac{2\Delta K}{3K^2}\left(1 \mp \sqrt{1 - \frac{3(\Delta_a^2 + \kappa^2/4)}{4\Delta_a^2}}\right). \tag{2.78}$$

We can then solve the input field, α_{in} corresponding to the critical point and for drives strong than that drive, there will be two steady state solutions of the photon number for certain parameters. If $\Delta = \Delta_{a,c} \equiv \sqrt{3/4}\kappa$, we obtain a point of inflection in the steady state value of photon number, while if we increase Δ beyond Δ_c we obtain two unique solutions, $n_{c\pm}$. For driving strengths that between the two corresponding field values, Eq. (2.78) has one unstable and two stable solutions. The resonator bifurcated such that very weak initial perturbation is sufficient to make the resonator field attain different stationary solutions that depends on this initial perturbation. The perturbation can be be introduced as a dispersive shift from the qubit and in this case, a high fidelity QND detection of the qubit state results [107, 108]. Due to the bifurcating nature of the resonator, this readout is referred to as a Josephson Bifurcation Amplifier (JBA).

Another protocol is the high power readout drives the resonator with a very high power, such that $\epsilon_r \gg \Delta$ [109, 110]. In this regime the resonator act as if the qubit was not even present in the resonator, but the transition from a dispersive shifted frequency to the bare frequency happens at different drive strengths for the different qubit states, thus, a high fidelity readout is possible. This readout is however not QND.

Finally, ideas to optimize the dispersive readout using a squeezed microwave drive is possible, but requires either coupling the qubit longitudinally to the resonator, $H_I = \chi\sigma_z(a + a^\dagger)$, [111] or to a two resonator mode in the quantum mechanically free subspace $H_I = \chi\sigma_z(a_1^\dagger a_1 - a_2^\dagger a_2)$ [112].

2.5 Gates

2.5.1 Single qubit gates

Once a qubit has been designed it is essential to find a method for control of the qubit. In the language of quantum information, this is referred to as quantum gates. Let us consider a transmon qubit, but we add a capacitative coupling to an open microwave line with the time-dependent voltage at the capacitor, $V_\Omega(t)$. This adds the Lagrangian

$$\mathcal{L}_\Omega = \frac{C_c}{2}(\dot{\phi}_{qb} - V_\Omega(t))^2 \tag{2.79}$$

to the qubit Lagrangian, with C_c being the (small) capacitor that couples to the input line. Going to the quantum Hamiltonian in the transmon regime ($E_J/E_C \gg 1$), this added Lagrangian transforms into (we neglect energy shift for the qubit and the self-energy of the input field, V_Ω)

$$H_\Omega = -i\frac{C_c}{\sqrt{2}}\left(\frac{E_J}{8E_C}\right)^{1/4} V_\Omega(t)(b - b^\dagger), \tag{2.80}$$

with b being the bosonic operator for the transmon in the regime of $E_J/E_C \gg 1$ as introduced in Sec. 2.2. Now, for simplicity the voltage can be taken as $V_\Omega(t) = V_\Omega^0 \sin(\omega_d t) = iV_\Omega^0(e^{i\omega_d t} - e^{-i\omega_d t})/2$. Now, we can truncate the transmon to only two states and go to a frame rotation with $H_0 = \omega_d \sigma_z/2$ and the resulting Hamiltonian becomes

$$H = \frac{\Delta}{2}\sigma_z + \frac{\Omega}{2}\sigma_x \tag{2.81}$$

with $\Delta = \omega_{qb} - \omega_d$ and

$$\Omega = \frac{C_c V_\Omega^0}{\sqrt{2}}\left(\frac{E_J}{8E_C}\right)^{1/4}. \tag{2.82}$$

The result is that the coherent drive of $V_\Omega(t)$ is transformed into a Rabi drive on the qubit. The drive can also change phase, $\sin(\omega_d t) \to \sin(\omega_d t + \phi)$ and the Rabi drive can change into $\sigma_x \to \alpha\,\sigma_x + \beta\,\sigma_y$ with $\alpha^2 + \beta^2 = 1$ and $\tan(\phi) = \beta/\alpha$. This option of choosing the phase of the drive becomes very important for gates in transmon qubits. As already presented, the transmon is as a matter of fact a multi level system with an anharmonicity to the third level given a $\alpha = -E_c$ and not a true two-level system. Therefore, adding a Rabi drive as a above will cause leakage into the

third level and the anharmonicity sets a limit for how fast a single qubit gate can be [42, 113, 114]. However, by using the Derivative Removal by Adiabatic Gate (DRAG) this leakage can be suppressed [115]. If we apply a time-dependent pulse with two quadratures $\Omega_x(t)$ and $\Omega_y(t)$ being the two out-of-phase components of the drive, it can be shown that choosing

$$\Omega_y = \frac{\dot{\Omega}_x(t)}{\alpha}, \qquad \Delta = \frac{-\Omega_x^2}{2\alpha} \tag{2.83}$$

we eliminate leakage into the third level by the order Ω_x^3/α^3, thus as expected the anharmonicity sets an absolute limit on the Rabi drive strength. The DRAG has experimentally been demonstrated to produce single qubit gates with an error per gate of $< 10^{-4}$ [116, 117].

2.5.2 Tunable frequency gates

To have a complete universal set of gates, a two-qubit gate is also needed beside the single-qubit gate presented above. The simplest approach [118, 119] to make such a two qubit gate is to capacitively couple two transmons to a single resonator, such that the qubits, 1 and 2, couple with the Hamiltonian $H_c^i = g_i(\sigma_-^i a^\dagger + \sigma_+^i a)$. Now, in the dispersive regime, the effective Hamiltonian becomes

$$H = \frac{\omega_1}{2}\sigma_z^1 + \frac{\omega_2}{2}\sigma_z^2 + (\omega a + \chi_1\sigma_z^1 + \chi_2\sigma_z^2)a^\dagger a + J(\sigma_+^1\sigma_-^2 + \sigma_-^1\sigma_+^2) \tag{2.84}$$

with $J = g_1 g_2(\Delta_1^{-1} + \Delta_2^{-1})/2$ where the detuning is given as $\Delta_i = \omega_i - \omega$. Since the transmon can be tunable, the frequencies can be set such that $|\omega_1 - \omega_2| \gg J$, which will yield the exchange interaction between the qubits off-resonant and nothing will happen. Then, changing the tuning such that $\omega_1 = \omega_2$ and waiting a time $\tau = \pi/(4J)$ will implement an $\sqrt{i\text{SWAP}}$-gate, which for instance will map $|10\rangle$ to $(|10\rangle + |01\rangle)/\sqrt{2}$.

A more robust way of implementing a two-qubit gate using the tunability of the transmons are the Controlled-Phase gate [120, 121]. The Hamiltonian are the same as for the resonant exchange gate, but instead of tuning the two qubits into resonance, one of the qubits is adiabatically tuned towards the avoided crossing between the state $|20\rangle$ and $|11\rangle$, such that the state $|11\rangle$ will acquire an additional phase compared to the states $|00\rangle$, $|10\rangle$ and $|01\rangle$ which will only acquire a trivial phase from the eigenenergies of the states. Thus, by picking the time spent at the avoided crossing, the gate can map $|11\rangle$ to $-|11\rangle$, while acting as identity on the rest of the computational basis.

2.5.3 Fixed frequency gates

The two-qubit gates presented above all rely on tunable qubits, but in order to reduce the decoherence of the qubits and to simplify the control microwaved controlled gates acting on fixed frequency qubits may be advantageous. One approach for such a gate it the so-called Cross-resonance gate [122, 123], which can be derived from considering the Hamiltonian

$$\frac{\omega_1}{2}\sigma_z^1 + \frac{\omega_2}{2}\sigma_z^2 + J\sigma_x^1\sigma_x^2 + \Omega_1\cos(\omega_d^1 t + \phi)\sigma_x^1. \tag{2.85}$$

Now, it can be shown, that if $\omega_d^1 = \omega_2$, the effective Hamiltonian in a rotation frame becomes

$$H = \frac{\Omega_1 J}{2(\omega_2 - \omega_1)}\big(\cos(\phi)\sigma_z^1\sigma_x^2 + \sin(\phi)\sigma_z^1\sigma_y^2\big) \tag{2.86}$$

such that this gate can be combined with a Z-rotation of qubit 1 and a X rotation of qubit 2 to constitute a CNOT-gate.

The resonators so far have only played the role as a medium to mediate the coupling between two qubits. However, the resonator can also play an active role to drive a two-qubit gate. An example of such a gate is the resonator induced phase gate [124, 125]. Consider the Hamiltonian

$$H = \frac{\omega_1}{2}\sigma_z^1 + \frac{\omega_2}{2}\sigma_z^2 + (\omega a + \chi\sigma_z^1 + \chi\sigma_z^2)a^\dagger a + (\epsilon_r(t)a^\dagger + \epsilon_r^*(t)a), \tag{2.87}$$

with $\epsilon_r(t) = \epsilon_r^0(t)e^{-i\omega_d t}$. Under a unitary transformation this can be written as

$$H = \frac{1}{2}(\omega + 2\chi(a^\dagger a + |\alpha|^2))(\sigma_z^1 + \sigma_z^2) - \frac{2\chi^2|\alpha|^2}{\delta_r}\sigma_z^1\sigma_z^2, \tag{2.88}$$

with α as the solution to the differential equation $\dot{\alpha} = -i\delta_r\alpha - i\epsilon_r^0(t)$ and $\delta_r = \omega - \omega_d$. Now, by picking $\epsilon_r^0(t)$ the evolution can be tailored to generate a controlled phase gate.

2.5.4 Flux-driven gates

The last type of gates that are common in the field of circuit QED is gates activated by an ac-driven flux [6, 126, 127]. This type of gates is also the theme of Chapter 6, thus, here we will only mention the general idea.

For instance, we can imagine that we have two off-resonant qubits coupled by the interaction Hamiltonian

$$H_I = J(\sigma_+^1\sigma_-^2 + \sigma_-^1\sigma_+^2). \tag{2.89}$$

Since the qubits are off-resonant, this interaction Hamiltonian will not cause any dynamics. However, if we change the coupling to be parametrically modulated, $J \to J\cos(\omega_p t)$, with eg. $\omega_p = \omega_1 - \omega_2$, then the coupling will suddenly be resonant. This can both be used directly between the qubits [126, 127] or by using a resonator as a mediator of the coupling, as in [6] and Chapter 6. Having a flux activated gate may offers some advantages: (i) Using the flux to modulate the coupling, there is no need for additional control lines to each individual qubits and we avoid the dephasing associated with the conventional frequency tuning of qubits. (ii) When our qubits are idle, they are far detuned with respect to each other and to any bus resonator, and hence they are immune to cross talk and Purcell-enhanced decay.

2.6 Control with superconducting microwave devices

In circuit QED, coherent operations can be performed fast and with high fidelities (see Sec. 2.5) and different strategies for state initialization [128–131] and readout (see Sec. 2.4) have been demonstrated. For control, these components can be combined into a measurement based feedback loop. A generic setup of such a feedback loop is shown in Fig. 2.9 (a) with a quantum system controlled by microwave sources and an amplifier chain feeds the output into a classical controller at room temperature. This can be used for both a digital feedback procedure or for an analog scheme. The digital scheme could eg. be used to deterministically generate an entangle state by performing a joint measurement of two qubits and then apply a conditional pulse to prepared the desired state [132]. More complicated ideas can easily be visualized and in the general idea is to have one or many qubit state readouts control which of a descrete set of feedback operations is to be applied. Feedback be by an analog signal can eg. be used stabilize a Rabi-oscillation of a single qubit by monitoring the dephasing [84] and relies on feeding back a (post-processed) continuous measurement record onto the system.

However, the pursuit of large-scale quantum information processing is necessarily accompanied by a massive, further increase in quantum and classical system complexity for initialization, measurement, and control. As complexity increases, the inefficiencies inherent in the standard approach to measurement and control using external, room temperature apparatuses will become increasingly burdensome. Circuit QED components are

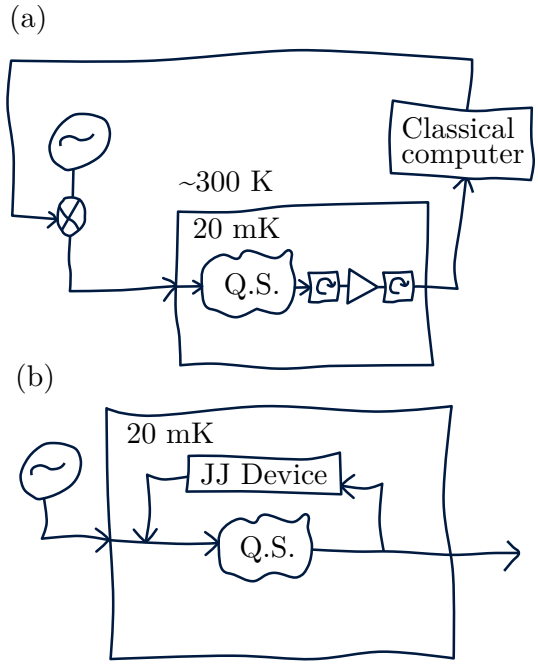

Figure 2.9: (a) A measurement based feedback scheme of a quantum system (Q.S.) where the signal processing happens at room temperatur (∼300 K) (b) Similar feedback system, but here all feedback and control are performed by a Josephson junction (JJ) device.

operated below 100 mK, and measurement signals used for readout and conditional control are sent through an expensive and meter-scale amplification chain up to room temperature. Similarly, controlling the quantum components requires transmitting signals from room temperature through ∼60 dB of cold attenuation to the <100 mK-stage [133]. Thus, the current approach to inter-temperature communication between quantum and classical hardware involves significant inefficiencies in size and power. Hence, controlling many qubits with feedback loops closed outside of the cryogenic environment poses a significant challenge [134] since each qubit-readout requires its own signal analyzer and a corresponding signal generator to apply the desired feedback. Another possible approach that sidesteps these inefficiencies would be to perform much of the measurement and signal

processing at the same temperature and with the same technology as the quantum hardware, as in in Fig. 2.9 (b). This approach may be used for both autonomous initialization and manipulation of qubits and is of particular interest for the implementation of quantum error correction codes [135]. In general terms, a quantum error correction protocol performs a measurement on a set of qubits to determine if an error occurred in the encoded quantum information and then, through feedback, corrects this error (or simply saves the error for later correction as in the so-called surface code [136]). Ideally, such error corrections codes should work autonomously in order to scale up quantum computing protocols.

Chapter 5 will cover two proposals for implementing Josephson junction based control elements [5, 7]. Another Josephson based microwave device is the JPC already mentioned in Sec. 2.4, which not only works as an amplifier, but also as a frequency converter. Similarly, the JPC can be operated as a loss-less circulator which can be used to redirect quantum signal inside the cryostat [137]. In [138] another idea for a circulator is presented using active flux modulation of Josephson elements. A similar idea was used in [139] as a microwave switch, but only working as an either fully reflective or transmissive element. In [140], on the other hand, a fast switch was presented which works as two output switch, based in the tunable frequency of Josephson junction embedded resonators.

Chapter 3

Arrays of Josephson junctions

Nonlinearities are essential resources required for many non-classical effects in quantum optics and for quantum information processes [33]. Without any non-linearity, everything would consist of harmonic oscillators in coherent states, which poses very little interesting physics, see also Sec. 2.1. A particular example of a nonlinear effect that appears in both the quantum and classical optics is the Kerr effect, which shift optical properties proportionally to the field intensity, also known as a Kerr resonator, given by the Hamiltonian

$$H = \sum_k \hbar\omega_k \, a_k^\dagger a_k + \sum_{k,j} \hbar K_{k,j} \, a_k^\dagger a_k \, a_j^\dagger a_j, \tag{3.1}$$

with a_k ($a_k^\dagger$) the annihilation (creation) operator for photons in mode k, ω_k is the bare resonator frequencies and $K_{j,k}$ the Kerr coefficients responsible for shifting the photon-energy of mode j proportionally to the intensity of the field in mode k (and visa versa). This Hamiltonian is particularly interesting as it naturally appears in superconducting resonators embedded with Josephson junctions [10, 13, 80, 81, 141]. Engineered superconducting circuits have shown a large range of non-linearities, which is typically achieved by accurately manufacturing Josephson junctions with varying ratio between the Josephson and charging energy, E_J and E_C introduced in Sec. 2.2, and by connecting several Josephson junctions in series [10, 55, 81, 142]. Therefore, experiments with Josephson junction arrays may readily explore any regime of nonlinearity. This Chapter focuses on the

usage of arrays of Josephson junctions as a non-linear element to study particular effects in quantum optics and is built on [9, 10].

Consider an array of N Josephson junctions: We assume the junctions forming the array to have a large Josephson energy such that, to a good approximation, they behave as weakly nonlinear inductances. These junctions are then characterized by their Josephson inductance L_J and junction capacitance C_J. Following Refs. [67, 141], the nonlinearity of the array junctions will be perturbatively reintroduced at a later step. Moreover, we take into account so-called *parasitic capacitance* to ground C_0 of the islands formed between the array junctions. This gives us the Lagrangian for the array:

$$\mathcal{L}_{array} = \sum_{n=1}^{N} \left[\frac{C_J}{2}(\dot{\phi}_n - \dot{\phi}_{n+1})^2 + \frac{C_0}{2}\dot{\phi}_n^2 - \frac{1}{2L_J}(\phi_n - \phi_{n+1})^2 \right], \tag{3.2}$$

where ϕ_n is the node flux of the nth island of the array. We also need to include the capacitance of the end points of the array, which is done by the Lagrangian term

$$\mathcal{L}_{end} = \frac{C_s}{2}\dot{\phi}_1^2 + \frac{C_e}{2}\dot{\phi}_{N+1}^2, \tag{3.3}$$

where we have C_s as the capacitance at the start of the array and C_e as the capacitance to ground at the far end of the array. In total we obtain the full Lagrangian

$$\mathcal{L} = \mathcal{L}_{array} + \mathcal{L}_{end} \tag{3.4}$$

$$= \dot{\vec{\phi}}^T \frac{\boldsymbol{C}}{2}\dot{\vec{\phi}} - \vec{\phi}^T \frac{\boldsymbol{L}}{2}\vec{\phi}. \tag{3.5}$$

In Eq. (3.5), the symmetric matrices $\boldsymbol{C}$ and $\boldsymbol{L}$ are defined along with the vector $\phi = \{\phi_1, \phi_2, \ldots, \phi_{N+1}\}^T$, such that they generate the Lagrangian in Eq. (3.4).

Standing waves across the array now constitute a set of normal modes for the array. Formally we find these standing mode by diagonalizing the matrix $\boldsymbol{\Omega}^2 = \boldsymbol{C}^{-1}\boldsymbol{L}$. The matrix $\boldsymbol{\Omega}^2$ express the Euler-Lagrange equation for this linear system and diagonalizing this matrix results in equations of motions for uncoupled normal modes. The eigenvalues of the matrix, $\boldsymbol{\Omega}^2$ are the resonances in the system squared. We refer to these eigenvectors of $\boldsymbol{\Omega}^2$ as $\vec{v}_k$, such that the flux across the array is given as $\vec{\phi}(t) = \sum_k \phi_k(t)\vec{v}_k$ with the time-dependence written explicitly. We can define the effective

capacitances and inductances for these modes by

$$C_k = \vec{v}_k^T \boldsymbol{C} \vec{v}_k, \qquad L_k^{-1} = \vec{v}_k^T \boldsymbol{L} \vec{v}_k. \tag{3.6}$$

The eigenfrequencies are now, by construction, given by $\omega_k = 1/\sqrt{L_k C_k}$.

Having found the normal modes we can apply a canonical quantization scheme to find a quantum model for the arrays [37]. This is done by first rewriting the Lagrangian into diagonal form, which is identical to that of a N uncoupled LC-circuits,

$$\mathcal{L} = \sum_k \frac{C_k}{2} \dot{\phi}_k(t)^2 - \frac{1}{2L_k} \phi_k(t)^2. \tag{3.7}$$

This Lagrangian now yields the conjugate variables

$$q_k = C_k \dot{\phi}_k^2, \tag{3.8}$$

such that the quantum operators $\hat{\phi}_k$ and $\hat{q}_k$ with the commutator relation $[\hat{\phi}_k, \hat{q}_k] = i\hbar$ can be introduced. The Hamiltonian for the system is then readily obtained as

$$H = \sum_k \frac{\hat{q}_k^2}{2C_k} + \frac{\hat{\phi}_k^2}{2L_k}, \tag{3.9}$$

which we can recast into the form

$$H = \sum_k \omega_k a_k^\dagger a_k \tag{3.10}$$

by the introduction of the ladder operators such that

$$\hat{\phi}_k = \sqrt{\frac{\hbar \omega_k L_k}{2}} (a^\dagger + a), \tag{3.11}$$

$$\hat{q}_k = i \sqrt{\frac{\hbar \omega_k C_k}{2}} (a^\dagger - a). \tag{3.12}$$

The real physical phase variable of the array is now described by the vector, $\hat{\phi} = \sum_k \hat{\phi}_k \vec{v}_k$, with $\vec{v}_k$ as the eigenvectors of the Euler-Lagrange equations found above.

To finalize the derivation of the system Hamiltonian, we now include the array junction nonlinearities following the approach of Refs. [67, 141]. Since the potential of a Josephson junction is actually equal to $U(\phi) =$

$-E_J\cos(\phi/\varphi_0)$ (with $\varphi_0 = \hbar/(2e)$), we have implicitly assumed that $\phi \ll \varphi_0$ such that we can approximate $\cos x \approx 1 - x^2$. Taking advantage of the weak nonlinearity of the junctions, it is sufficient to include only the fourth order expansion of the cosine potential, $x^4/24$, which gives rise a non-linear potential, $\mathcal{U}_{nl}$, for the flux variable given by

$$\mathcal{U}_{nl} = -\frac{1}{24L_J\varphi_0^2}\sum_{n=0}^{N}\left(\phi_n - \phi_{n+1}\right)^4. \tag{3.13}$$

We will now introduce the variable

$$\Delta\phi_k(n) = v_k[n] - v_k[n+1], \tag{3.14}$$

with $v_k[n]$ denoting the nth entry in the vector $\vec{v}_k$, such that we can rewrite the potential in terms of the quantum mode operators,

$$\mathcal{U}_{nl} = -\sum_{k_1,k_2,k_3,k_4}\frac{\prod_{j=1}^{4}\hat{\phi}_{k_j}}{24L_J\varphi_0^2}\sum_{n=1}^{N}\prod_{j=1}^{4}\Delta\phi_{k_j}(n). \tag{3.15}$$

Generally such a term will lead to Kerr terms as in Eq. 3.1 as well as beam-splitter terms, $a_k^\dagger a_l + a_l^\dagger a_k$. The beam-splitter terms are, however, only important between modes of small frequency difference or if the system is strongly pumped by some external field with certain frequencies that brings the beam-splitter terms into resonance. We are mainly interested in the few photon regime of the lowest modes, which are all well-separated in frequency, so we will only consider the self-Kerr and the cross-Kerr terms [141], which we can express with the Hamiltonian

$$H_{nl} = \sum_{kl} K_{kl}a_k^\dagger a_k a_l^\dagger a_l\,, \tag{3.16}$$

where the Kerr-coefficients are found by inserting Eq. (3.12) into Eq. (3.15) and rearranging the terms such that we obtain Eq. (3.16) with

$$K_{kl} = -\frac{2-\delta_{kl}}{4L_J\varphi_0^2}\frac{\hbar\omega_k L_k}{2}\frac{\hbar\omega_l L_l}{2}\sum_{n=1}^{N}\Delta\phi_k(n)^2\Delta\phi_l(n)^2, \tag{3.17}$$

with δ_{kl} being the Kronecker-delta. As a last important detail, we should mention that the non-linear contribution, due to the commutator terms when reordering all the operators, also drags the eigenfrequencies down such that the actual mode frequencies become

$$\omega_k' = \omega_k + \sum_l K_{kl}. \tag{3.18}$$

This extra contribution is very important as it shifts the frequency of each mode significantly for multi-mode structures with large non-linearities. The Hamiltonian for the array is therefore expressed as

$$H = \sum_k \hbar\omega'_k a_k^\dagger a_k + \sum_{kl} \hbar K_{kl} a_k^\dagger a_k a_l^\dagger a_l \,, \tag{3.19}$$

which is the exactly Eq. (3.1).

3.1 Quantum and classical dynamics

Kerr resonators can be described by the Hamiltonian Eq. (3.1) and can exhibit both classical and quantum behaviour. It is fundamentally interesting to study what happens in the cross over from a classically well-described system to a quantum system and for practical applications it is worth to systematically investigate when a device behaves classically or quantum mechanically. Therefore, as a particular effect we study here the switching dynamics in the bistable regime of the Kerr resonator [10], which is very interesting eg. for the JBA readout protocols [107, 108] or for quantum controllers [7, 143]. We will initially consider only a single mode Kerr resonator ($\hbar = 1$ from now on and for convenience we change the sign of K in this section)

$$H = \omega_r a^\dagger a - K a^\dagger a\, a^\dagger a. \tag{3.20}$$

Assuming zero temperature, the system will relax to the vacuum state, but to have dynamics in the system, we add a coherent drive. To account for a Markovian relaxation, the time-evolution of the Kerr resonator with an applied coherent drive, $H_d = \varepsilon(t)\, a^\dagger + \varepsilon^*(t)\, a$, can be calculated using the quantum master equation

$$\begin{aligned} \dot\rho &= \mathcal{L}[\rho] \\ &= -i[H{+}H_d, \rho] + \kappa\Big(a\rho a^\dagger - \frac{1}{2}(a^\dagger a\rho + \rho a^\dagger a)\Big), \end{aligned} \tag{3.21}$$

where ρ is the density matrix for the oscillator and $\mathcal{L}[\cdot]$ denotes the Liouvillian super-operator. The resonator linewidth is set by κ which is responsible for the fluctuations and dissipation in the system. The pure relaxation time of the resonator is $T_\kappa = 1/\kappa$. The system is usually treated in a frame rotating at the drive frequency, ω_d, such that we make the replacements $\varepsilon(t) \to \varepsilon$ and $\omega_r \to \Delta = \omega_r - \omega_d$ in the Hamiltonian, making it time-independent.

An approximate approach to solve the time-evolution is by using a semi-classical trajectory approach [144]. To arrive at the semi-classical equation of motion we start by writing the Heisenberg-Langevin equation for the annihilation operator, a [72]:

$$\dot{a} = -i\big[a\,,\, H + H_d\big] - \frac{\kappa}{2}a + \sqrt{\kappa}a_{in}(t) \tag{3.22}$$

with the input field, $a_{in}(t)$, accounting for the quantum fluctuations satisfying the commutation relation $[a_{in}(t), a_{in}^{\dagger}(t')] = \delta(t-t')$. In case system is linear ($K = 0$) the resonator state is always a coherent state, ie. $\langle a(t)\rangle = \alpha(t)$ and $\langle a^{\dagger}a\rangle = |\alpha(t)|^2$ with $\alpha(t)$ being a complex number characterizing the coherent state amplitude at time t. The semi-classical approximation relies on the replacement of field operators with complex numbers and was also used in Sec. 2.4 for the description of the read-out processes. This semi-classical replacement reduces Eq. (3.22) to an equation of motion for the phase-space variable α,

$$\dot{\alpha} = -i\Delta\alpha + 2i\,K|\alpha|^2\alpha - i\varepsilon - \frac{\kappa}{2}\alpha + \sqrt{\kappa}\,\zeta(t), \tag{3.23}$$

corresponding to an equation for the coherent state amplitude of the system. In Eq. (3.23) we have $\zeta(t) = (dW_1(t) + i\,dW_2(t))/\sqrt{2}$ as a stochastic Weiner process with $\langle dW_i\rangle = 0$ and $\langle dW_i^2\rangle = dt$ that on average corresponds to the input field being the quantum vacuum state [72]. Notice that the quantum noise from $\zeta(t)$ enters the equation of motion in the same way as thermal noise enters for Brownian motion of a classical particle, hence κ acts as an effective thermal energy. A particular realization of $\zeta(t)$ is referred to as a semi-classical trajectory. Averaging over a large number of trajectories perfectly reproduce the master equation for a linear quantum system, while for increasing non-linearity quantum effects starts to play a larger role [145]. Therefore, for sufficiently large non-linearities, the semi-classical trajectories will fail to capture the system dynamics accurately.

3.1.1 Numerical Analysis

To understand the quantum effects that arise in the dynamics of the Kerr resonator, we perform numerical simulations of the driven system and analyze the relaxation towards the steady state. The dynamics of the semi-classical trajectories is such that a single trajectory initially latches to a low photon-number state but after some time it jumps to, and continues to fluctuate around, a high photon-number state. This

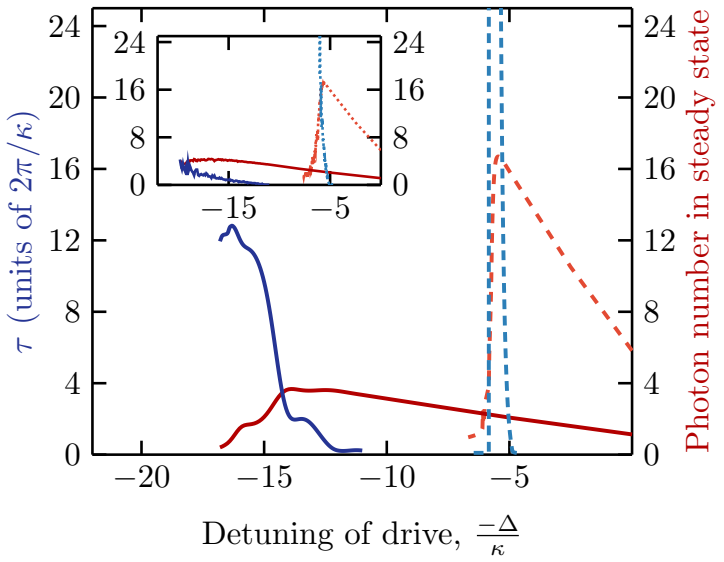

Figure 3.1: Steady state photon number as a function of drive detuning $(-\Delta)$. The red lines are steady state photon number, indicated on the right axis. The bue curves are the time scales obtained from an exponential fit displayed on the left axis. The dashed curves are for $K = 0.2\kappa$ and the solid curves are for $K = 2\kappa$. The main figure displays the master equation simulations and the inset shows the results of the semi-classical simulations. In all simulations $\varepsilon = 6\kappa$ were used.

switching dynamics continues with a waiting time between such switches being approximately Poisson distributed. Then, using an exponential fit to the average over many trajectories we can extract the time scale to reach steady state. From the master equation simulation, Eq. (3.21), we observe an oscillatory behaviour that relaxes on a time scale T_κ followed by an exponential relaxation towards steady state. We readily extract the relaxation time scale, τ, for the master equation simulations from the exponential behaviour. In Fig. 3.1, we present the results of quantum master equation simulations obtained for two kinds of Kerr resonators as well as the corresponding semi-classical results: (i) strongly nonlinear

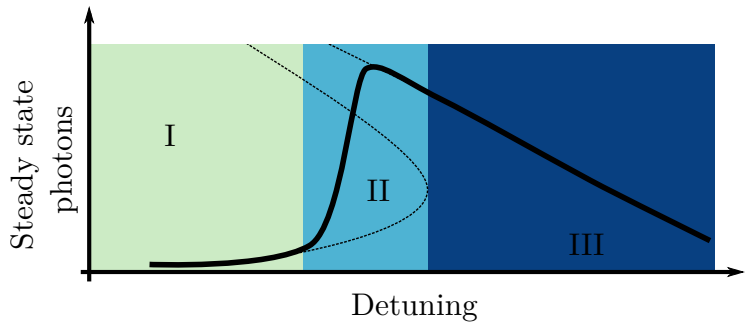

Figure 3.2: Sketch of the steady state photon number as a function of the drive detuning similar to the lighter lines of Fig. 3.1. The solid lines are the steady state of the master equation. The dashed lines shows the steady state solution to the semi-classical equation of motion. In region I and III the resonator relaxes directly to steady state in the time scale $T_\kappa = \kappa^{-1}$, while region II corresponds to the switching region where the dynamic is slowed down.

($K = 2\kappa$) and (ii) weakly nonlinear ($K = 0.2\kappa$). The observed behaviour can be broadly categorized into three regions, as sketched in Fig. 3.2.

In region I, the resonator relaxes to a state with a low photon number on a time scale of T_κ. Region III is conceptually comparable to region I, except that the system relaxes into a high photon number state. In region II the time scale to reach steady state becomes larger and significantly exceeds T_κ. In particular we notice a divergence in τ for $K = 0.2\kappa$ around the maximum photon number of the steady state. This divergence is similarly observed for any smaller nonlinearity as long as the system is in the bistable regime, that is, when the system poses a range of detuning with two solution found in Sec. 2.4. The slow-down in region II can partly be understood from a semi-classical point of view as indicated in Fig. 3.1 where quantum and the semi-classical simulations match for the small Kerr coefficient. In the semi-classical trajectories we clearly see that switching between the two stable classical solution is responsible for slowdown in the average behaviour [145, 146]. However, for larger nonlinearity, $K = 2\kappa$, we see a much richer structure of the time scale in the full quantum simulations indicating that the semi-classical is not sufficient to describe the nonlinear quantum dynamics. A hint that this is not surprising comes

from the fact that the steady state for the large nonlinearity shows a Q-parameter, $Q = (\langle(\Delta a^\dagger a)^2\rangle - \langle a^\dagger a\rangle)/\langle a^\dagger a\rangle$, around -0.4, which indicates a sub-Poissonian statistics. Similarly we observe the Wigner function to have negative values. These indications emphasize the non-classical nature of the state state of the system and as such, the state cannot be fully described within a classical framework [72].

3.1.2 Quantum and semi-classical calculations

We now want to analytically calculate the switching rates found numerically in the previous subsection. For a Hilbert-space of arbitrary size N, we have N^2 eigenstates of the Liouvillian, but only the zero-eigenvalue state, ρ_{ss}, is a physical state (it is the only positive definite eigenstate) and it corresponds to the steady state the system. Any density matrix can, however, be constructed by linear combinations $\rho = \sum_n c_n \rho_n$, where ρ_n are the eigenstates of the Liouvillian ($\mathcal{L}[\rho_n] = n\,\rho_n$). The steady state ρ_{ss} always appear in this superposition with a constant pre-factor of $c_{ss} = 1$ in order to preserve trace. Furthermore, all dynamics can be inferred from the eigenstates and the eigenvalues of the Liouvillian [147]. For $\rho_n \neq \rho_{ss}$ we have $|\mathrm{Re}(n)| \neq 0$. Since the real part of n is non-zero, the trace of ρ_n will vanish (or diverge) under the Liouvillian time-evolution and it acquires an exponential on the diagonal given by $\exp(nt)$ but since the time evolution is trace-preserving we see that $\mathrm{Tr}(\rho_n) = 0$.

We consider the eigenstate with the smallest real part, ρ_χ and use an inner product for matrices given by $\langle A, B\rangle = \mathrm{Tr}(A^\dagger B)$, and it turns out that $\langle \rho_{ss}, \rho_\chi\rangle \neq 0$. Using a Gram-Schmidt process ,

$$\tilde{\rho}_\chi = \rho_\chi - \frac{\langle \rho_{ss}, \rho_\chi\rangle}{\langle \rho_{ss}, \rho_{ss}\rangle}\rho_{ss}, \tag{3.24}$$

this new matrix, $\tilde{\rho}_\chi$, is by construction orthogonal to the steady state, $\langle \tilde{\rho}_\chi, \rho_{ss}\rangle = 0$. The matrix $\tilde{\rho} = \tilde{\rho}_\chi/\mathrm{Tr}(\tilde{\rho}_\chi)$ is now normalized, $\mathrm{Tr}(\tilde{\rho}) = 1$, but it is still not positive definite. Nevertheless, we can now express any density matrix as

$$\rho(t) = \beta_0(t)\rho_{ss} + \beta_1(t)\tilde{\rho} + \sigma(t), \tag{3.25}$$

with $\sigma(t)$ only contributing to ensure the positive definiteness of the full density matrix. We assume that $\beta_0(t) = (1 - \tilde{\beta}_0 e^{-\lambda t})$. To estimate the rate at which we approach the steady state in the long time limit, we can now calculate the time scale λ by inserting Eq. (3.25) into the master equation,

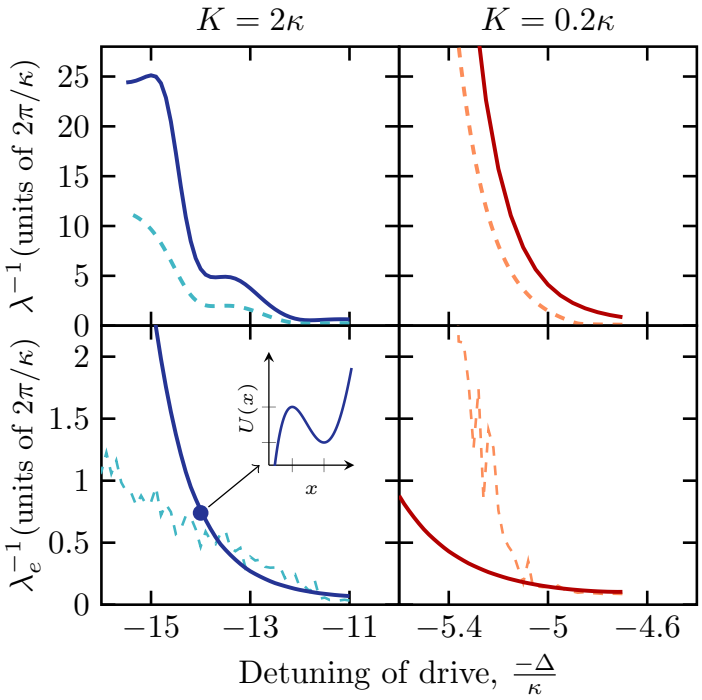

Figure 3.3: The upper two panels displays with the solid lines the relaxation time-scale calculated from a full quantum model by Eq. (3.26), while the lower two panels shows relative increase in the switching time-scale from an effective potential calculated by Eq. (3.30). The dashed lines are the time scales extracted from Fig. 3.1 with the upper panels being the master equation simulations and for the lower panels we show the time scale from the semi-classical trajectories. We have used $\varepsilon = 6\kappa$. The inset of the lower left panel displays an example of the quasi potential $U(x)$ for the parameters marked by the blue dot. The ticks in the insets x-axis are at 0 and x_0 with corrosponding ticks on the y-axis.

Eq. (3.21),

$$\dot{\beta}_0(t) = \langle\, \rho_{ss}, \mathcal{L}[\rho(t)] \,\rangle. \tag{3.26}$$

The quantum induced switching rate can now be expressed as $\lambda = \dot{\beta}_0(t)/(1-\beta_0(t))$. Omitting $\sigma(t)$ makes this expression only account for the

dynamics induced by the steady state and the smallest eigenvalue. These are the two dominant contributions in the long time limit. Equation (3.26) is now simple to evaluate and in the upper panels of Fig. 3.3 we show how the this expression predicts the time scale $\tau = \lambda^{-1}$ and the dashed lines shows τ from Fig. 3.1. The calculated time scales from Eq. (3.26) matches the numerically found time scale shown in Fig. 3.1 (shown as dashed lines in Fig. 3.3) very well, however, we see a numerically larger value from Eq. (3.26). We can understand this from the fact that we neglected $\sigma(t)$ and in general $\sigma(t)$ have contributions from all eigenvalues of the Liouvillian which includes contributions with a larger negative real part than χ. Therefore the dynamics associated with $\sigma(t)$ must be faster than λ. Thus, we have seen that we qualitatively can understand the switching behavior from a quantum mechanical description.

On a different note, a semi-classical picture of bistability-switching can be understood in terms of so-called quasi potentials. A quasi potential is an effective potential that describes the same equation of motion as the semi-classical model. The quantum fluctuations associated with the quantum noise $\zeta(t)$ in Eq. (3.23) is transformed into an effective temperature and the thermal escape rate from the minima of quasi potential should correspond to the switching rate [148, 149].

To estimate the semi-classical escape we consider the semi-classical equation, Eq. (3.23) with $\zeta(t) = 0$. The general approach is to rephrase the complex equation into a real equation for a generalized position variable, x. The equation of motion for a classical particle moving in a potential, $U(x)$, is given by $\dot{p} = -\partial U(x)/\partial x$. Integrating this equation results in an effective potential and applying Kramers escape law [150, 151] with an effective temperature set by the resonator linewidth, κ, yields the quantum escape rate. We solve Eq. (3.23) with $\zeta(t) = 0$ and denote the low-amplitude solution α_0 and the unstable solution α_u. Now, we define a rotation angle $\varphi = \tan^{-1}(-\mathrm{Im}(\alpha_u - \alpha_0)/\mathrm{Re}(\alpha_u - \alpha_0))$ such that the quantity $x_0 = e^{i\varphi}(\alpha_u - \alpha_0)$ is a real number and the axis on the line from 0 to x_0 constitutes our position variable. To obtain the quasi potential we rephrase the equation of motion, Eq. (3.23), into

$$\begin{aligned} dU(x) =& (-i\Delta - \kappa/2)(x + e^{i\varphi}\alpha_0) - ie^{i\varphi}\varepsilon \\ & - 2iK(x + e^{-i\varphi}\alpha_0^*)(x + e^{i\varphi}\alpha_0)^2, \end{aligned} \tag{3.27}$$

by rotating the equation and making the displacement of α by $e^{i\varphi}\alpha_0$. Because the two states α_0 and α_u are steady states it follows that $dU(0) = dU(x_0) = 0$. We note that x here constitutes the generalized position and,

similarly, the imaginary part of the equation of motion accounts for the dynamics of the momentum p. This yields

$$\mathrm{Im}(\, dU(x)\,) = \dot{p} = -\frac{\partial U(x)}{\partial x}. \tag{3.28}$$

Integrating this equation results in a one-dimensional quasi-potential,

$$U(x) = \int \mathrm{Im}(\, -dU(x)\,)\, dx, \tag{3.29}$$

with a minimum at 0 and maximum at x_0. The escape rate over the barrier using the Kramers escape law [150, 151] can be written as [148, 149]

$$\lambda_e = \lambda_0 \exp\Big(-\frac{\Delta U}{\kappa}\Big), \tag{3.30}$$

with $\Delta U = U(x_0) - U(0)$ denoting the activation energy. Note that effective temperature is set by the resonator linewidth, κ since it enters as a pre-factor for $\zeta(t)$ in Eq. (3.23). The rate λ_0 is the attempt frequency and it is extracted from the quadratic term of the potential, $\frac{\lambda_0^2}{2\kappa}x^2$. We also readily verify that for increasing drive, ϵ, the barrier height is decreased leading to a faster escape rate. In the inset of Fig. 3.3 we display an example of the quasi potential obtained by this calculation.

The lower panels of Fig. 3.3 show how larger drive detuning increases the time scale of the relaxation towards steady state and we compare directly with the semi-classical simulations (dashed lines) also shown in the inset of Fig. 3.1. We observe that for the semi-classical simulations and the escape rate from Eq. (3.30) match well for the smaller detuning, but when approaching the bifurcation border between region I and II, we see a larger discrepancy. This is understandable since we only calculate the rate going from the low amplitude state to the high amplitude state, which will not be the relevant rate close to the bifurcation point where back-and-forth dynamics are dominating. Therefore, for the weakly nonlinear case, the escape rate calculations matches in the region away from the bifurcation point.

To summarize this section we have investigated the time scales relevant for a Kerr-resonator to relax into steady state. The regions in Fig. 3.2 are each characterized by different behaviour and, most significantly, we see in region II that the time scale for relaxation towards steady state becomes very large. The increase in the time scale is an effect highly relevant when conducting experimental characterization of Kerr resonator as all

experiments are inherently dynamical processes and, thus, assumptions of being in steady state may be incorrect. We also found that while a semi-classical calculation is predicting the dynamics of the weakly nonlinear system, it fails to capture the rich structure of the time scale for relaxation, τ, seen for large nonlinearities and near the bifurcation. Such a break-down of the semi-classical description emphasize a transition into a quantum regime, previously not observed. This is important to note since all Josephson Bifurcation Amplifiers (JBA) also described in Sec. 2.4 have only been described by this semi-classical picture [108]. Therefore it is crucial to know when this description fails and even more interesting is the fact that experiments (see next section) has made it possible to systematically probe this regime where the semi-classical picture breaks down.

3.2 Analysis of an experiment with Josephson junction arrays

As we have seen in the previous section, the time scale for reaching the steady state of a Kerr resonator might be very long compared to the decay rate and can only be accounted for by a full quantum model. Therefore, experiments set to probe the properties of a Kerr resonator might arrive to false conclusions if they assume that the experiment only observe semi-classical properties of the steady state. In this section we go beyond the a steady state analysis by comparing experimental data of a Kerr resonator in the large nonlinearity regime to fully dynamical quantum simulations.

Figure 3.4 shows the experimental system which consist of an array of 80 Josephson junctions capacitively coupled to a transmission line in a hanger geometry [55]. The fundamental frequency of the resonator is 4.357 GHz with an internal quality factor of 37000 and external quality factor of 5000. The experimental setup is limited by circulators and a low-pass filter to measure signals with frequencies < 12 GHz. This means that only the fundamental mode of the Kerr resonator can be read out directly. A continuous drive applied to the higher modes of the array, however, shifts the frequency of the fundamental mode due to the cross-Kerr coupling giving a mechanism to readout the dynamics of modes above 12 GHz. This technique is employed to map the full dispersion relation of the distributed modes of the array in Ref. [55]. The first excited mode was identified to be at 11.9 GHz. To probe the photon number in this first excited mode as a function of the drive detuning, similar to the results

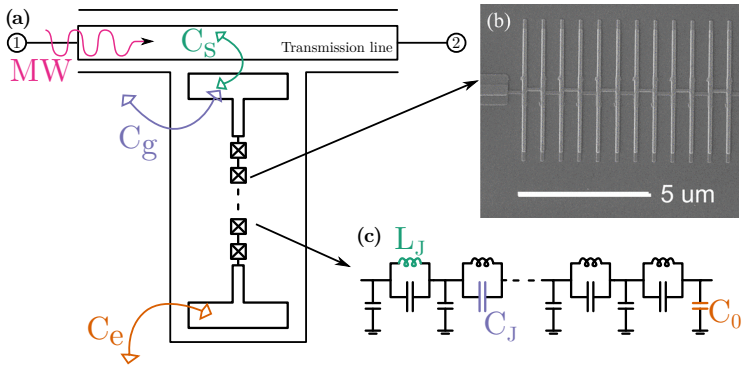

Figure 3.4: An array of Josephson junctions is coupled to a transmisson in a geometric shown in (a). The capacitance C_s is the capicitance from the array's end-capacitor to the tranmission line and C_g is the caacitance to ground, while C_e is the other end-capacitors capacitance to ground. In (b) we see a (rotated) SEM image of the junction array, while (c) show a lumped element describtion of the linear part of the array. Here we are consider the array to be an array of LC-circuits with the capacitance C_J and inductance L_J and with an extra parasitic capacitance, C_0, to ground.

shown in the previous section, a continuous coherent drive is applied close to the first mode's frequency. Now, while keeping this drive always-on, a readout drive is applied close to the fundamental frequency and scanned the detuning of the readout to find the resultant frequency shift from the minimum of the transmission spectra. Fig. 3.5 shows the experimental data obtained for the different drive powers, that shows a line shape similar to those predicted in the previous section.

To compare the experiments to numerical simulations we need to know the Kerr coefficients for each mode, but this would be very hard to measure without direct access to each mode. Instead we model the resonator from first principles. The inductance of the array can be measured at room-temperature, thus we can infer that we have an inductance per junction of $L_J = 1.9$ nH. We can find the effective plasma frequency, ie. the frequency to which the high order modes converges towards, to be 18.2 GHz. Using the knowledge of the number of junctions, the fundamental mode frequency and the effective plasma frequency we find $C_0 = 0.066$ fF, $C_J = 26.54$ fF,

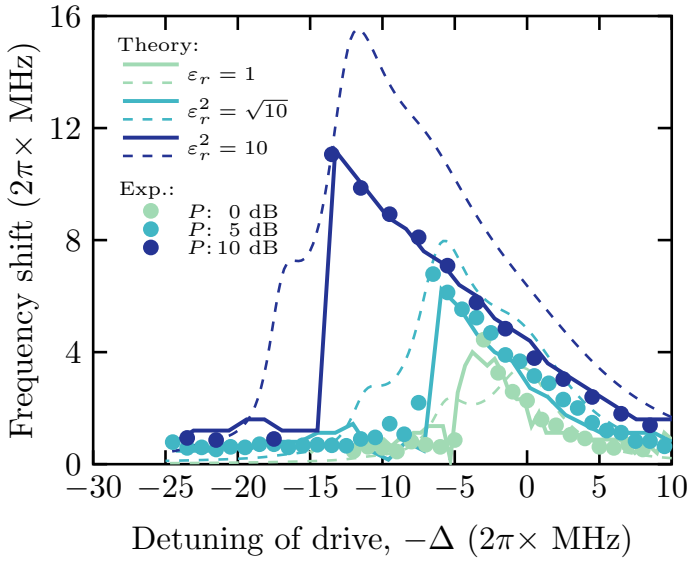

Figure 3.5: The lines represent the numerical simulations while the dots represent the experimental data. The legend indicates the power, P, of the drive applied both in the experiment and in the simulations, normalized to 0 dB for the weakest drive display here. For the numerics we have used power proportional to the experimentally applied power and we give the normalized units in the legend such that $\varepsilon_r \equiv \varepsilon/\varepsilon_0$ with $\varepsilon_0/(2\pi) = 1.83$ MHz. The solid lines are a full stochastic two-mode simulation, while the dashed lines are the Kerr shifts calculated from a steady state assumption using Eq. (3.31). For the simulation we have used $K = 2\pi \times 5.7$ MHz, $\kappa = 2\pi \times 2.9$ MHz and $\kappa_0 = 2\pi \times 1.0$ MHz.

$C_g = 10.4$ fF, $C_s = 3$ fF and $C_e = 10.84$ fF, all of which are close to the design parameters found by simulations [55]. With these parameters we calculate the first mode to have $K = 2\pi \times 5.7$ MHz which is around a factor of 2 bigger than the line-width of $\kappa = 2\pi \times 2.9$ MHz.

Driving the Kerr-resonator increases the photon number, $\langle a^\dagger a \rangle$, and we aim to infer this photon number from the experimentally obtained frequency shift of fundamental mode. A straight-forward way of connecting the photon number and the frequency shift so would be to calculate the

steady state photon number, $\langle a^\dagger a\rangle_{ss} = \mathrm{Tr}(\rho_{ss} a^\dagger a)$, and directly put this into the cross-Kerr term of the Hamiltonian. This approach leads to a shift of the readout given by

$$\Delta_{readout} = K_{cross}\langle a^\dagger a\rangle_{ss}. \tag{3.31}$$

From the bottom-up calculation of the array we find the Kerr coefficient of the fundamental mode to be $K_0 = 2\pi \times 0.5$ MHz and thus we can calculated the cross-Kerr as $K_{cross} = -4\sqrt{K_0 K}$. The result of this calculation is shown as the dashed line in Fig. 3.5. We see that only some features of the experiment are predicted by the steady-state approach; for instance, the detunings are approximately correctly predicted. The structure of the line-shape, on the other hand, is very poorly predicted and the plateaus to the left of the maxima are completely missing from the experimental data. This is not surprising given the knowledge we have from the previous section. The shoulders appear in region II of Fig. 3.2 and represent a multiphoton transition to a state with population in both a high photon number state and a low photon number state. However, the measurement induced dephasing project the system onto only a low-amplitude or a high-amplitude state. Furthermore, we note that we are probing using the fundamental mode, so we extract information in a time scale of $T_{\kappa_0} = 1/\kappa_0 \approx 3/\kappa$. This is much faster than the prolonged time required to relax into the steady state in this regime, so as a consequence the system always dephases to the same state and no dual peaked transmission spectrum is observed. Moreover, we notice that even in region III, where no switching is present, the dephasing even changes the effective steady state of the system which we understand as a measurement induced dephasing or, equivalently, a cross-Kerr interaction between the probe and the field effectively increasing κ compared to the detuning. Summarizing, it is clear that the steady state depicted by the dashed line in Fig. 3.5 does not capture the dynamics of the experiment and a more complete description is called upon.

We can describe the dynamics more accurately using a full two-mode model, that includes the fundamental mode, a_0. We therefore consider the following Hamiltonian in addition to Eq. (3.1),

$$H_0 = \Delta_0\, a_0^\dagger a_0 + \epsilon_0(a_0^\dagger + a_0) + K_{cross}\, a^\dagger a\, a_0^\dagger a_0 - K_0 a_0^\dagger a_0 a_0^\dagger a_0. \tag{3.32}$$

We can now simulate the system dynamics by the two-mode stochastic master equation for heterodyne measurement [101] of the transmitted

signal:

$$\begin{aligned}\dot{\rho} = &-i[H + H_0, \rho] + \kappa(a\rho a^\dagger - \frac{1}{2}(a^\dagger a\rho + \rho a^\dagger a)) \\ &+ \kappa_0(a_0\rho a_0^\dagger - \frac{1}{2}(a_0^\dagger a_0\rho + \rho a_0^\dagger a_0)) \\ &+ \sqrt{\kappa_p}\Big(dZ a_0\rho + dZ^*\rho a_0^\dagger - \mathrm{Tr}(dZ a_0\rho + dZ^*\rho a_0^\dagger)\,\rho\Big). \end{aligned} \tag{3.33}$$

The stochastic variable is now given by $dZ = dW_a + idW_b$, where dW_i again are stochastic Weiner processes with $\langle dW_i\rangle = 0$ and $\langle dW_i^2\rangle = dt$. The transmitted signal can be calculated as

$$J_T(t) = \Big(\sqrt{\kappa}\,\mathrm{Tr}(\rho(a_0 + a_0^\dagger)) + \frac{dW_a}{dt}\Big)^2 + \Big(\sqrt{\kappa}\,\mathrm{Tr}(\rho(a_0 - a_0^\dagger)i) + \frac{dW_b}{dt}\Big)^2. \tag{3.34}$$

Modelling the measurement process as a heterodyne is equivalent to an IQ measurement, of the down-converted transmission signal, as discussed in Sec. 2.4, where the $X \propto (a_0^\dagger + a_0)$ and $Y \propto i(a_0^\dagger - a_0)$ quadrature plus the real and imaginary part of dZ respectively corresponds to I and Q of the downconverted current and we can reconstruct the measurements from the experiment. In Fig. 3.5 we see numerical simulations using the parameters of experiment. We observe that we can accurately predict the experiment using this fully dynamical stochastic quantum description.

3.3 Ultrastrong coupling to a qubit

We have seen how the array can play a role as a nonlinear element with interesting quantum dynamics. This section will investigate how to couple the array to a transmon qubit (see Sec. 2.2), to get even more interesting dynamics [9]. Here, the array partly plays the role a mediator of the dynamics and partly of an effective readout tool for this dynamics.

As discussed in 2.3, a superconducting qubit and a microwave resonator can implement a controllable interaction between light and matter. In general terms, understanding light-matter interaction is one of the primary goals in quantum optics. The simplest case to consider is the coupling of a single atom to a single mode of light [62] often described by the Jaynes-Cummings (JC) Hamiltonian ($\hbar = 1$),

$$H_{\mathrm{JC}} = \omega_r\, a^\dagger a + \frac{\omega_a}{2}\sigma_z + g(a^\dagger\sigma_- + a\sigma_+), \tag{3.35}$$

where ω_c is the cavity frequency, ω_a the atomic frequency and g the electric-dipole coupling. In this expression, a ($a^\dagger$) is the photon annihilation (creation) operator and σ_i are the Pauli matrices for the atomic levels. The JC Hamiltonian describes the exchange of a single quanta between the field and the atom leading to Rabi oscillations with angular frequency $2g$. The JC Hamiltonian is however only an approximation of the Rabi Hamiltonian,

$$H_{\text{Rabi}} = \omega_r\, a^\dagger a + \frac{\omega_a}{2}\sigma_z + g(a^\dagger + a)\sigma_x. \tag{3.36}$$

The JC Hamiltonian can be derived from the Rabi Hamiltonian by imposing the rotating wave approximation (RWA). The RWA is valid when the period for exchanging a single excitation is much longer than the period of self-oscillations for both the atom and the light, ie. $g \ll \omega_a, \omega_r$. To arrive at the RWA, a unitary transformation, $\mathcal{U} = e^{-iH_0 t/\hbar}$, is performed with the Hamiltonian $H_0 = \hbar\omega_r\, a^\dagger a + \hbar\frac{\omega_{qb}}{2}\sigma_z$. This transformation leads to time-dependent operators, $a \rightarrow a\, e^{-i\omega_r t}$ and $\sigma_- \rightarrow \sigma_-\, e^{-i\omega_a t}$. The interaction terms of the Rabi Hamiltonian therefore rotate with $\omega_r \pm \omega_a$ and in the RWA it is assumed that $\Omega_\Sigma = \omega_r + \omega_a$ is much larger than any other dynamics, such that terms with Ω_Σ do not contribute to the interaction when averaging over time. Therefore we can safely neglect the term $a^\dagger\sigma_+ + a\sigma_-$ and we arrive at the JC.

While more challenging to realize, there has recently been much attention to the situation where the RWA is no longer valid. This regime is known as the ultrastrong coupling regime and it differs remarkably from the JC regime [152–159]. Most significantly, while the ground state of H_{JC} is simply the product of the atomic ground state and vacuum of the field, the ground state of the Rabi Hamiltonian is an entangled atom-field state with a non-zero average photon number.

Superconducting quantum circuits form a promising platform to realize and study this novel light-matter coupling regime. In particular, realization of the ultrastrong coupling regime with flux qubits (see Sec. 2.2), acting as the atom, coupled to a microwave resonator have been theoretically studied [50] and experimentally implemented [160–163]. These experiments have primarily probed the spectral properties of the ultrastrong regime, since the fast coupling and short coherence times limits the possibilities for probing the dynamics. A next step is to probe the dynamics of the this regime. With the system starting in its ground state, an approach is to non-adiabatically tune the coupling strength g from the ultrastrong coupling regime to the strong coupling regime. The system will readjust

to this change by emitting photons as it relaxes back to its new ground state. Observing these photons would constitute a clear signature of the non-trivial nature of the ultrastrong coupling ground state. With system frequencies around 10 GHz [50, 160, 161, 163], this however requires changes in system parameters of the order of 10 pico-seconds. In practice, this therefore appears to be extremely challenging.

Using an arrays of Josephson junctions [55] described in the this Chapter as replacement of the standard coplanar waveguide resonator, see Sec. 2.3, we will in this section show how we address the ultrastrong coupling regime with a transmon qubit. Assuming that the resonators effective capacitance is much larger than the capacitances of the transmon, it can be shown that $g/\omega_r \propto \sqrt{Z_0}$ with Z_0 being the impedance of the resonator [42]. Therefore, to obtain a large coupling and enter a regime with $g \sim \omega_r, \omega_a$, we need to increase the impedance of the resonator [50, 164]. The experiment of previous section implements an inductance with a dissipationless impedance around $Z_0 \sim 4\,\mathrm{k}\Omega$ [54, 55]. This impedance is much larger than typical coplanar waveguides with $Z_0 = 50\,\Omega$, and as such we expect thatcoupling a transmon to such a superinductor may increase the coupling strength significantly. Moreover, by using a low-frequency mode of the array, it is possible to realize ultrastrong coupling with only a moderately large coupling strength. In this situation, fast changes of system parameters are possible and allow for the observation of signatures of the ultrastrong coupling in the dynamics of the combined system. This dynamic can then be probed by taking advantage of the presence of multiple modes of the array and their cross-Kerr interaction [55], see also Secs. 3.1 and 3.2.

We consider the circuit of Fig. 3.6 which consists of a transmon qubit [42] coupled to an array of N Josephson junctions [55]. The transmon qubit is characterized by the Josephson energy E_J and the capacitance C_s, which for simplicity we take to include both the shunt capacitance and the junction capacitance. As for the introduction of the array in the beginning of this Chapter, we assume the junctions forming the array to have a large Josephson energy such that, to a good approximation, they behave as weakly nonlinear inductances. These junctions are then characterized by their Josephson inductance L_J, the junction capacitance C_J and capacitance to ground C_0 of the islands formed between the array junctions. The capacitance C_q couples the qubit to the array and will largely control their interaction strength. Finally, C_i is a capacitance to an external control field which will be used to probe the system and C_e is the capacitance to ground of the last array island. The Lagrangian of this

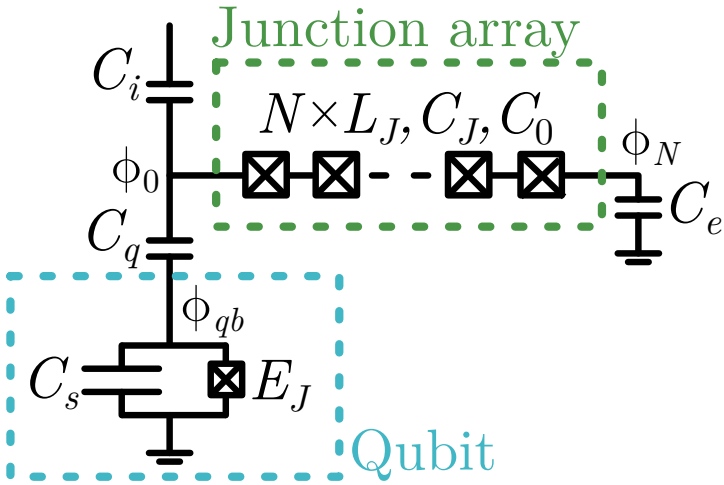

Figure 3.6: A circuit representation of the system. We have an array of N Josphson junctions treated as a series of inductors with the inductance L_J and a series of capticances, C_J. For each junction we also have a parasitic capacitance to ground, C_0. At the end-points we have the couplings C_i and C_e. The array is coupled to a tranmon qubit, characterised by the capacitance C_s and the Josephson energy E_J, through the coupling capacitance C_q.

system reads [37],

$$\begin{aligned}\mathcal{L} = &\sum_{n=0}^{N-1} \frac{C_J}{2}(\dot{\phi}_n - \dot{\phi}_{n+1})^2 - \frac{1}{2L_J}(\phi_n - \phi_{n+1})^2 + \frac{C_0}{2}\dot{\phi}_n^2 \\ &+ \frac{C_i}{2}\dot{\phi}_0^2 + \frac{C_e}{2}\dot{\phi}_N^2 + \frac{C_q}{2}(\dot{\phi}_0 - \dot{\phi}_{qb})^2 \\ &+ \frac{C_s}{2}\dot{\phi}_{qb} + E_J \cos\left(\phi_{qb}/\varphi_0\right) \qquad (3.37) \\ = &\dot{\vec{\phi}}^T \boldsymbol{C} \dot{\vec{\phi}} - \vec{\phi}^T \boldsymbol{L} \vec{\phi} + E_J \cos\left(\phi_{qb}/\varphi_0\right), \qquad (3.38)\end{aligned}$$

where we have defined the vector $\vec{\phi} = \{\phi_0, \phi_1, \ldots, \phi_N, \phi_{qb}\}^T$ and the matrices $\boldsymbol{C}$ and $\boldsymbol{L}$ such that Eq. (3.38) reproduces Eq. (3.37).

Following a derivation similar to the derivation of the array Hamiltonian

(3.19), the Hamiltonian of the full system takes the form,

$$\hat{H} = H_{qb} + \sum_k \tilde{\omega}_k \, a_k^\dagger a_k + \sum_{kl} K_{kl} a_k^\dagger a_k a_l^\dagger a_l + \sum_k g_k (b^\dagger - b)(a_k^\dagger - a_k) + \sum_{k \neq l} G_{kl} (a_k^\dagger - a_k)(a_l^\dagger - a_l), \tag{3.39}$$

with H_{qb} the transmon Hamiltonian which (for $E_J/E_C >> 1$) is $H_{qb} = \omega_a b^\dagger b - E_C(6b^\dagger b + 12 b^\dagger b b^\dagger b)$. The mode frequencies are $\tilde{\omega}_k = 1/(Z_k \tilde{C}_k)$ where $Z_k = \sqrt{\tilde{L}_k/\tilde{C}_k}$ is the characteristic impedance of mode k [141] ($\tilde{L}_k$ and $\tilde{C}_k$ are renormalized array mode capacitances, see below). The ladder operator b is here introduce as in Sec. 2.2. While the above form is useful in simplifying analytical expressions, all numerical calculations in this paper are based on the exact diagonalization of

$$H_{qb} = 4E_C \hat{n}^2 - E_J \cos\left(\phi_{qb}/\varphi_0\right), \tag{3.40}$$

When $E_J/E_C \gg 1$, we write the Rabi-like coupling strengthsas [42],

$$g_k = \left(\frac{8E_J}{E_C}\right)^{\frac{1}{4}} \sqrt{\frac{1}{2Z_k}} e \, \tilde{\boldsymbol{C}}^{-1}_{[k,qb]}. \tag{3.41}$$

where $\tilde{\boldsymbol{C}}$ is the matrix $\boldsymbol{C}$ reexpressed in the eigenbasis of the array [9]. This basis is found from considering the $N{+}2{\times}N{+}2$ matrix $\boldsymbol{\Omega}^2 = \boldsymbol{C}^{-1}\boldsymbol{L}$ and then calculate the eigenvectors, $\vec{v}_k$, of the $N{+}1{\times}N{+}1$ upper block matrix of $\boldsymbol{\Omega}^2$ that does not relate to $\vec{\phi}_{qb}$. We will refer to these $\vec{v}_k$ as the array modes and together with the qubit mode, $\vec{\phi}_{qb} = \{0, 0, \ldots, 0, \phi_{qb}\}^T$, they form a complete basis set which we use to reexpress the capacitance and inductance matrices to obtain $\tilde{\boldsymbol{C}}$ and $\tilde{\boldsymbol{L}}$ respectively, see also [9]. We now have $\tilde{C}_k$ on the diagonal of $\tilde{\boldsymbol{C}}$ as the mode capacitance of the kth mode of the array similar to Eq. (3.6). In addition to a qubit-mode coupling, Eq. (3.39) also contains a mode-mode coupling

$$G_{kl} = \sqrt{\frac{1}{2Z_k}} \sqrt{\frac{1}{2Z_l}} \, \tilde{\boldsymbol{C}}^{-1}_{[k,l]}/2, \tag{3.42}$$

which we can neglect due to the large frequency difference between each mode, $G_{kl} \lesssim 0.01(\tilde{\omega}_l - \tilde{\omega}_k)$. We could also get rid of this term by re-diagonalizing the Hamiltonian which would renormalize g_k and $\tilde{\omega}_k$. Finally, the Kerr-coefficients are found from Eq. (3.17).

Before moving on, let us note that the distinction between the resonator and the transmon in the system Hamiltonian may seem artificial. After all, the split into a transmon degree of freedom and array degrees of freedom is unnecessary to calculate the eigenfrequencies of the combined system. This distinction is, however, useful since one of the modes of the total system, the qubit mode, inherits the most from the transmon's small junction nonlinearity. This can be made more apparent by replacing this junction with a SQUID loop. For symmetric loop junctions, this leads to the replacement $E_J \to E_J \cos(\Phi_x/2\varphi_0)$, with Φ_x the external flux, in the qubit Hamiltonian H_{qb}. In this situation, the qubit mode is widely flux tunable while the array modes have, following our treatment, no explicit dependence on flux. This also affects the qubit-array coupling which, in the transmon regime, now takes the form

$$g_k(\Phi_x) \approx \cos(\Phi_x/2\varphi_0)^{1/4}\, g_k(\Phi_x = 0), \tag{3.43}$$

with $g_k(\Phi_x = 0)$ given by Eq. (3.41). As a consequence the transmon is now defined as the degree of freedom that we can tune by the external flux and it is clearly distinct from the resonator.

To investigate how strongly we couple the transmon to the resonator, the focus will be on the lowest mode of the resonator, $k = 0$, as this mode is expected to have the largest zero-point fluctuations of the field compared to its resonant frequency. This is captured in figure of merit g_0/ω_0, and as already mentioned it can be estimated that $g_0 \propto \sqrt{Z_0}$ (from now on we write ω_k, however, still referring to $\tilde{\omega}_k$). In order to have a high Z_0 the array must have a large junction inductance, L_J, and a small capacitance to ground per junction, C_0. Furthermore, the coupling strength, g_0, is intuitively expected to depend directly on the coupling capacitor, C_q. However, a change in both C_0 and C_q does not only change g_0, but in general also change E_C, ω_k and g_k. By fixing E_C and ω_k with capacitances, C_0 with C_q as a variable, the rest of the array capacitances and transmon parameters can, however, be identified numerically.

We perform a numerical search for the largest coupling strength, g_0, for a given set of C_0 and C_q with a fixed ω_0 and E_C. This search does not guarantee the globally maximal coupling strength, but it is sufficient to identify parameters that yield a transmon in the ultrastrog coupling regime. The resonator frequency is fixed at $\omega_0 = 2\pi \times 2$ GHz in order to have the coupling strength small enough that we can perform non-adiabatic operations on the mode, which is of crucial importance for the observation of ultrastrong dynamics. For the transmon, the charging energy, which also

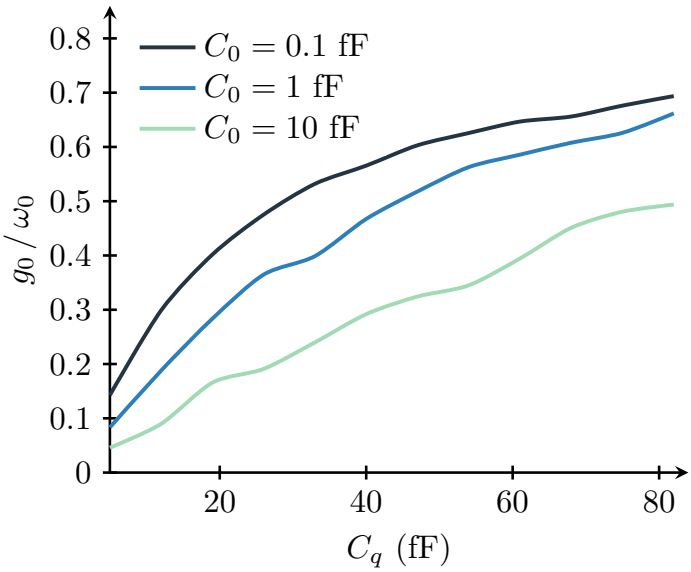

Figure 3.7: The coupling strength, g_0, in units of ω_0 as a function of the coupling capacitance C_q. Each value have been found numerically in order to maximize g_0. From top to bottom we increase the parasitic capacitance C_0 with 0.1 fF at the top followed by $C_0 = 1$ fF and finally $C_0 = 10$ fF. In every case we have $L_J = 1.5$ nH and we have solved C_s, C_i, C_e and N to keep $\omega_0 = 2\pi \times 2$ GHz and $E_C = 2\pi \times 300$ MHz fixed. Furthermore we have used $E_J/E_C = 50$.

set the anharmonicity, is fixed at $E_C = 2\pi \times 300$ MHz and the Josephson energy is set to $E_J/E_C = 50$. The resulting numerically optimized coupling strength is displayed in Fig. 3.7. The coupling strength is indeed observed to be larger when C_0 is small and the general trend is that a larger C_q leads to larger coupling.

The rest of this section uses a particular set of parameters chosen in order to have both a large coupling strength far within the ultrastrong coupling regime and with a significantly large cross-Kerr coupling between

the resonator modes. With this in mind, we take as parameters:

$$N = 145, \qquad L_J = 1.5 \text{ nH}, \tag{3.44a}$$
$$C_0 = 0.1 \text{ fF}, \qquad C_q = 85 \text{ fF}, \tag{3.44b}$$
$$C_i = 26 \text{ fF}, \qquad C_J = 30 \text{ fF}, \tag{3.44c}$$
$$C_e = 72 \text{ fF}, \qquad C_s = 63 \text{ fF}, \tag{3.44d}$$

which lead to

$$\omega_0/2\pi = 2 \text{ GHz}, \qquad g_0/\omega_0 = 0.61, \tag{3.45a}$$
$$\omega_1/2\pi = 8.8 \text{ GHz}, \qquad g_1/\omega_1 = 0.11, \tag{3.45b}$$
$$\omega_2/2\pi = 14.45 \text{ GHz}, \qquad g_2/\omega_2 = 0.04, \tag{3.45c}$$
$$K_{00}/2\pi = -0.03 \text{ MHz}, \qquad K_{22}/2\pi = -2.46 \text{ MHz} \tag{3.45d}$$
$$K_{02}/2\pi = -0.54 \text{ MHz}, \qquad \omega_a/2\pi = 5.7 \text{ GHz}, \tag{3.45e}$$

with ω_a the transmon qubit frequency at $\Phi_x = 0$. Furthermore we take the resonator decay rate $\kappa = 2\pi\times 50$ kHz, corresponding to the losses observed in Ref. [55]. The qubit decay rate and the pure dephasing rate are taken as $\gamma = \gamma_\phi = 2\pi\times 50$ kHz, values that are routinely observed for flux tunable transmons [66]. With these choices, the 0th mode is well within the ultrastrong coupling regime while the 1st mode is on the edge of that regime. Moreover, the 2nd mode is both outside the ultrastrong coupling regime and is far-detuned from the qubit. As a result, the dispersive coupling of that mode to the qubit is vanishingly small. On the other hand, as desired the 2nd mode has a significant cross-Kerr coupling to the 0th mode allowing for photon population readout, which we will discuss in Sec. 3.3.2.

3.3.1 Ultrastrong dynamics

We now turn to an approach to probe the dynamics in the ultrastrong coupling regime. Before going into detail with a protocol to probe this dynamics, we fist introduce the numerical tool that will be required to simulate the dynamics. Because of the open nature of the system, these simulations are based on the master equation. However, since the rotating wave approximation breaks down in the ultrastrong coupling regime, the standard quantum optics master equation leads to unphysical results. For this reason, we instead use the master equation derived in the dressed

basis [165],

$$\begin{aligned}\dot{\rho} = \frac{-i}{\hbar}[H,\rho] &+ \sum_{j,k\neq j} \Gamma_\phi^{jk}\mathcal{D}[|j\rangle\langle k|]\rho \\ &+ \sum_{j,k>j} (\Gamma_\kappa^{jk} + \Gamma_\gamma^{jk})\mathcal{D}[|j\rangle\langle k|]\rho \\ &+ \mathcal{D}\Big[\sum_j \Phi^j |j\rangle\langle j|\Big]\rho, \end{aligned} \tag{3.46}$$

with $\mathcal{D}[O]\rho = O\rho O^\dagger - \frac{1}{2}(O^\dagger O\rho + \rho O^\dagger O)$. In this expression, the dephasing rates are expressed in terms of the eigenstates of the instantaneous Hamtiltonian, $|j\rangle$, and they take the form

$$\Phi^j = \sqrt{\frac{\gamma_\phi}{2}}|\langle j|b^\dagger b|j\rangle|^2. \tag{3.47}$$

Similarly, the dephasing induced relaxation rates are given as

$$\Gamma_\phi^{jk} = \frac{\gamma_\phi}{2}|\langle j|b^\dagger b|k\rangle|^2, \tag{3.48}$$

and the rescaled relaxation rates as

$$\Gamma_\gamma^{jk} = \gamma\,|\langle j|b^\dagger + b|k\rangle|^2, \tag{3.49}$$

$$\Gamma_\kappa^{jk} = \kappa\,|\langle j|a^\dagger + a|k\rangle|^2. \tag{3.50}$$

The master equation, Eq. (3.46), is constructed to ensure that the system will relax into the ground state of the coupled system, which importantly can be very different from the ground state of the Jaynes-Cummings Hamiltonian.

As already mentioned, an important feature of the JC Hamiltonian is that its ground state is that of the uncoupled system. As a result, the nature of this ground state does not change with system parameters. In other words, if prepared in its ground state, a system described by the JC Hamiltonian will remain in the vacuum state under parametric modulations.

In contrast, the ground state, $|j=0\rangle$, of the Rabi Hamiltonian can be approximated as [165]

$$|j=0\rangle \approx \left(1 - \frac{\lambda^2}{2}\right)|00\rangle - \Lambda|11\rangle + \xi\sqrt{2}|02\rangle \tag{3.51}$$

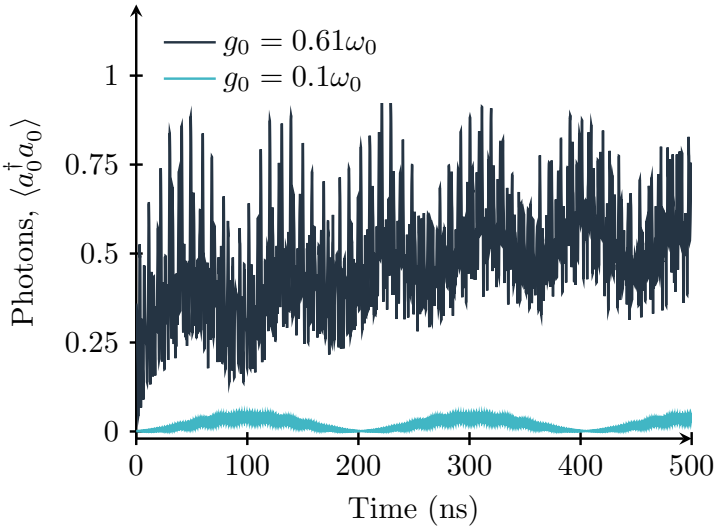

Figure 3.8: Photon in the resonator as a function of time. We have used a resonator with $\omega_0 = 2\pi \times 2$ GHz and a transmon with $E_C = 2\pi \times 300$ MHz and $E_J/E_C = 50$. The coupling strength was set to $g_0(\Phi_x = 0) = 0.61\omega_0$ for the darker line and $g_0(\Phi_x = 0) = 0.1\omega_0$ for the lighter line. We modulate the external flux $\Phi_x/(2\varphi_0) = 0.35\pi \cos(\omega_d t)$ with $\omega_d = 2\pi \times 1.5$ GHz.

to second order in $\Lambda = g/(\omega_a + \omega_r)$ and with $\xi = g\Lambda/2\omega_r$. On the right-hand-side of this expression, the first index in the states refers to the qubit and the second to the photon number. Equation (3.51) makes it clear that the ground state of H_{Rabi} depends on the system parameters and, moreover, has a finite average photon number. Since the master equation Eq. (3.46) relaxes the system back to $|j = 0\rangle$, these photons do not decay out of the cavity and are consequently difficult to observe.

Here we propose to take advantage of the dependence of $|j = 0\rangle$ on the system parameters to observe a signature of these photons. Indeed, a non-adiabatic change of the system parameters should lead to a change of the average photon population under H_{Rabi} while it should have no effect under H_{JC}. As alluded to earlier, this photon population can then be probed by taking advantage of the cross-Kerr coupling between array modes. For the photon population to change under parametric modulations, this

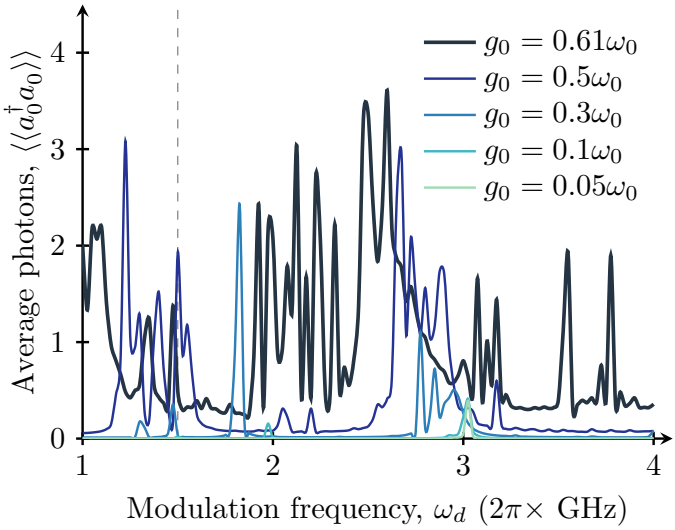

Figure 3.9: Time averaged mean value of the photon number from time-evolutions similar to Fig. 3.8 with parameters the same, but with different modulation frequencies and coupling strengths. The lines from light to dark indicates stronger coupling, g_0, as indicated by the legend.

modulation must, however, be non-adiabatic. This is possible in this system and with the parameters used here because of the small mode frequency ω_0 and therefore the reasonably small g_0 required to reach ultrastrong coupling.

Our approach is now to apply an ac-flux through the transmon SQUID as a method to change the qubit frequency and induce non-adiabatic dynamics, with the flux given as

$$\Phi_x(t) = \Phi_X^a \cos(\omega_d t). \tag{3.52}$$

For modulated SQUIDs it is often assumed that $\cos(\Phi_x(t)) \approx 1 - \Phi_x(t)^2$, however here the important contribution is not the parametric modulation of $\Phi_x(t)$ but the change in the ground state and as such we are not restricted by any small-angle approximation and we can choose the modulation amplitude, Φ_X^a, to be very large, which has also been shown to be experimentally possible [166]. Because of this change in system parameters,

the overlap between the instantaneous ground state at a given time, $|0(t)\rangle$, and the nth excited state as later time $t' > t$, $|n(t')\rangle$ is in general non-zero,

$$\langle 0(t)|n(t')\rangle \neq 0, \tag{3.53}$$

a result that holds only when the RWA is not valid. This implies that we may indeed dynamically excite the system from the ground state by a change of the system parameters. An analogy can be drawn to multi-passage Landau-Zener transitions [167]. These transitions appear when the parameters of a two-level system is changed in a non-adiabatic fashion through an avoided crossing. A similar effect is observed here with a non-adiabatic change in the ground state. The transmon-array system has, however, a complex level structure where the Landau-Zener results cannot be explicitly applied.

In Fig. 3.8 we see an example of this dynamics using the system parameters of Eqs. (3.44) and (3.45) and a modulation frequency of $\omega_d = 2\pi \times 1.5$ GHz. The darker line shows the photon number as a function of time within the ultrastrong regime and it can be observed that the system is being excited with resonator photons over time. We emphasize that the drive frequency, ω_d, does not directly correspond to any other system frequency, hence, the observed generation of photons can be understood as the transfer of photons from non-zero photon number in the ground state into real photons of in higher excited states. For comparison, the lighter line in Fig. 3.8 shows the same simulation but for a weaker coupling of $g = 0.1\omega_0$ and as expected almost no photon are generated in this case.

To further investigate the ultrastrong dynamics, Fig. 3.9 displays the time-averaged photon number as a function the modulation frequency, ω_d, for different drive strengths. Again, we observe that for the small coupling strengths very few photons are generated and only at specific frequencies. In the ultrastrong coupling regime photons are generated for a large range of frequencies. For the strongest coupling of $g = 0.61\omega_0$ we see photons for any frequency, which supports the conjecture that the photons are not generated by a simple resonant exchange interaction at a static system frequency but due to the non-adiabatic change of the ground state.

3.3.2 Readout of the photon number

It turns out that the states generated by the ultrastrong coupling dynamics are similar to thermal states, which means that $\langle a + a^\dagger \rangle \approx 0$ even when we have a strictly non-zero photon number, $\langle a^\dagger a \rangle > 0$. A direct homodyne

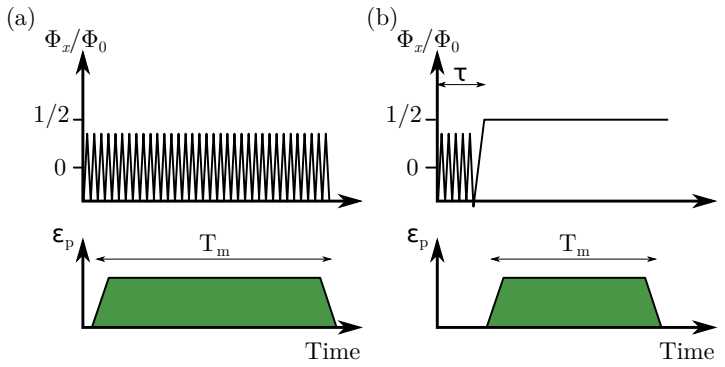

Figure 3.10: Cross-Kerr readout schemes to probe the photons generated by the ultrastrong coupling dynamics. In (a) we apply the modulation of the transmon continuously while probing a higher mode of the Kerr resonator. In (b) we only modulate for a time τ followed by a probing of a higher mode.

detection would therefore not reveal any signal to first order. Still, higher order correlation functions are possible to measure, using linear detectors [73], which would allow for a full reconstruction of the resonator field. Such a measurement will usually require the averaging of a very large number of measurements.

A more convenient method is therefore to measure the photon population in the ultrastrongly coupled mode $k = 0$ by taking advantage of the cross-Kerr coupling between modes $k = 0$ and 2. This coupling was already used experimentally to characterize a junction array [55], as presented in Sec. 3.2. Ignoring the other array modes, this coupling takes the form

$$H_K = K_{02} a_0^\dagger a_0 \, a_2^\dagger a_2, \tag{3.54}$$

with $K_{02} = -4\sqrt{K_{00}K_{22}}$. Photon population in mode 0 will shift the second mode frequency by $K_{02}a_0^\dagger a_0$, a shift that can be resolved by probing mode 2.

The general approach is now to apply a coherent drive, $H_p = \varepsilon_p(a_2 + a_2^\dagger)$, on resonance with the probe mode via the input port C_i (see Fig. 2.6). The signal reflected from this port is then continuously monitored. Similarly to dispersive qubit readout [30], the photon number, $\langle a_0^\dagger a_0 \rangle$, can be determined

by homodyne measurement of the field amplitude a_2. The integrated homodyne signal can be expressed as

$$M_{\varepsilon_p} = \sqrt{\kappa_2} \int_{\tau}^{\tau+T_m} [a_{\rm out}(t) + a_{\rm out}^{\dagger}(t)]\, dt \tag{3.55}$$

with T_m the integration time and τ the initial time of the integration. In this expression, $a_{\rm out}(t) = \sqrt{\kappa_2} a_2(t) + a_{\rm in}(t)$ is the output field [72], with $a_{\rm in}$ the input noise of the vacuum respecting $[a_{\rm in}(t),\, a_{\rm in}^{\dagger}(t')] = \delta(t'-t)$, and κ_2 the decay rate of mode $k=2$. The ability for such a measurement to distinguish the state from the system with no flux modulation, ie. no ultrastrong dynamics, is captured by the signal-to-noise ratio (SNR). Following Ref. [77, 112], the SNR can be expressed as

$$\mathrm{SNR}_{T_m} = \frac{|\langle M_{\varepsilon_p}\rangle - \langle M_0\rangle|}{\sqrt{\langle \tilde{M}_{\varepsilon_p}^2\rangle + \langle \tilde{M}_0^2\rangle}}, \tag{3.56}$$

with $\tilde{M}_{\varepsilon_p} = M_{\varepsilon_p} - \langle M_{\varepsilon_p}\rangle$ and M_0 corresponds to the same measurement without flux-modulation, $\Phi_x = 0$.

As illustrated in Fig. 3.10, two approaches are considered. In the first approach, depicted in panel (a), the probe field is monitored while continuously modulating the qubit flux. For simplicity, the nonlinearity of the probe mode is ignored and the photon number $a_0^{\dagger}a_0$ is taken to be a classical number. Then, the equation of motion for a_2 reads

$$\dot{a}_2 = -iK_{02}\langle a_0^{\dagger}a_0\rangle a_2 - \frac{\kappa_2}{2} a_2 - i\varepsilon_p + \sqrt{\kappa_2} a_{\rm in} \tag{3.57}$$

which as the steady state solution

$$a_2^{\rm s} = \frac{\sqrt{\kappa_2} a_{\rm in} - i\varepsilon_p}{iK_{02}\langle a_0^{\dagger}a_0\rangle + \kappa_2/2}. \tag{3.58}$$

To obtain a simple estimate for the SNR, we use the values of $\langle a_0^{\dagger}a_0\rangle$ oscillating between 0.2 and 0.8 shown in Fig. 3.8 and integrate the signal taking $\tau = 100$ ns to go beyond the initial ring up dynamics. For the parameters presented above, together with $\varepsilon_p = 2\pi \times 2$ MHz and $\kappa_2 = 2\pi \times 0.35$ MHz, this yields a SNR larger than 1 for an integration time $T_m \approx \kappa_2^{-1}$. A larger SNR can be obtained by longer integration times, however, the ultrastrong dynamics will eventually dephase due the dephasing rates Φ^j. Using Eq. (3.58) the value of $\langle a_0^{\dagger}a_0\rangle$ is estimated and we recover, as desired, the numerical time-averaged results shown in Fig. 3.9. In this analysis we

neglected the self-Kerr nonlinearity, $K_{22} = 2\pi \times -2.4$ MHz, but in general similar results for the cross-Kerr probing can be obtained by including the nonlinearity in the analysis [10] (see Sec. 3.2).

An alternative method to map the dynamics shown in Fig. 3.8 is sketched in Fig. 3.10(b). In this approach, the qubit flux is modulated for a time τ around $\Phi_x = 0$ with an amplitude of $\Phi_x = 0.35\Phi_0$. After this initial period of ultrastrong dynamics, the flux is rapidly increased to $\Phi_x = \Phi_0/2$ in a time span of one full period of oscillation, $2\pi/\omega_d \approx 0.66$ ns. At that point, the qubit has a vanishingly small transition frequency and is uncoupled from the array, see Eq. (3.43). Now, with the coupling to the qubit absent, the population of mode a_0 simply decays to the vacuum state at a rate κ_0. Again, it is worth emphasizing that due to the choice of a small resonator frequency and, thus, low coupling, this change in flux is fast enough to maintain the photon number in the a_0 mode. Using the same parameters as in Fig. 3.8, we numerically integrate Eq. (3.56) and find, taking into account array damping, a maximal $\mathrm{SNR}_{T_m} \approx 0.5$ for a measurement time $T_m \approx 6$ μs. For larger measurement times, the signal will be dominated by noise because the photon population of the a_0 mode have decayed. This estimate is obtained from numerical integration including cross-Kerr coupling given by Eq. (3.54) and self-Kerr nonlinearities for both modes. As above, from the measured signal, the detuning of the probe mode a_2 from its bare frequency ω_2 can now be inferred. Using the inferred probe detuning, the photon population in mode $k = 0$ can then be estimated. Therefore, by treating the average photon number as an unknown parameter, standard parameter estimation techniques [101] can be used and the dynamics generated during the ultrastrong coupling is observed. We expect that a measurement of the dynamics can be obtained by only a few experimental runs for each value of τ.

In conclusion we have shown that using a high impedance resonator constructed by an array of Josephson junctions we can bring a transmon within the ultrastrong coupling regime. We performed a full Lagrangian analysis of the array and transmon circuit and using experimentally realistic parameters we identify a coupling up to 0.7 of the resonator frequency. A very large coupling strength makes in general any dynamics hard to observe, since a change in any parameter most be made faster than the coupling strength or ideally even as a sudden change in order to observe any non-adiabatic dynamics. Choosing a low-frequency resonator and by using the tunability of the transmon qubit we identify dynamics specific to the ultrastrong coupling regime. This dynamics appeared by modulating the transmon frequency non-adiabatically, which resulted in photons appearing

in the resonator mode. These photons would not have appeared within the rotating wave approximation and as such it constitute a unique feature of the ultrastrong coupling regime. Finally, we presented a method how the cross-Kerr coupling of the array can be used to efficiently probe the dynamics.

3.4 Conclusion

In this Chapter we have considered the use of Josephson junction arrays in quantum optics scenarios. First we showed the due to the nonlinear nature of the array, interesting non-classical dynamics appeared in the bistable regime. This is surprising as switching dynamics so far were considered well-described by the quasi-potential approach also presented here. This conclusion may be very useful in characterization of state-of-the-art Josephson devices as arrays of Josephson junctions play a major role in experiments and theory proposals including various readout schemes [80, 83, 168], see Sec. 2.4, quantum controllers [7, 137, 138], as also presented in Sec. 2.6, and even qubit architectures such as the fluxonium [53]. This analysis was followed by an analysis of a recent experiment [55] probing the properties of a Josephson junction array. From the experimental data it is clear the the full quantum dynamics must be taken into account to fully characterize nonlinear quantum elements.

Moreover, it was proposed to couple the array to a single transmon qubit. The effectively large impedance of the array now enhances the coupling to the qubit significantly and we enter the ultrastrong coupling regime. Designing the array with a low frequency, this ultrastrong coupling is obtained for moderate values of the coupling. This is an important advantage of our proposal. Indeed, with this choice, it was shown that realistic modulations of the qubit parameters are sufficient to results in dynamics of the system that is distinctive of the ultrastrong coupling regime. Moreover, we have shown how this dynamic and the corresponding photon population can be probed by taking advantage of the multi-mode structure of the array. These results show the possibility to probe the complex dynamics of the ultrastrong coupling regime, opening a new window on this unconventional regime of quantum optics.

Finally it may be speculated in which regard Josephson junction arrays additionally can serve to improve experiments in the field of circuit QED. An example could be for the use in hybrid systems [169], where the coupling different charge based systems could be increased by using a Josephson

junction array. For example in [170], a semiconductor charge qubit was coupled to a superconducting waveguide resonator. The resulting coupling strength was measured to be $g_0 = 2\pi \times 11$ MHz. Additional parameters for the system was a qubit decay rate of $\gamma_1 \approx 2\pi \times 100$ MHz, dephasing of $\gamma_\phi = 2\pi \times 250$ MHz and a resonator decay rate of $\kappa = 2\pi \times 3.3$ MHz. With these parameters the qubit-resonator system has a cooperatively of $C = g^2/(\kappa\gamma_1) = 0.36$, which is just below 1 and, thus, the system is only on the edge of the strong coupling regime. Using an array instead of a coplanar waveguide as above, we find $g \approx 2\pi \times 50$ MHz, which will yield a cooperatively $C \approx 7$, which is far into the strong coupling regime.

Chapter 4

A detector for microwave fields

Readout of superconducting devices is, as introduced, one of the dominating challenges of circuit QED. Often, different readout schemes are developed to solve a specific task, eg. reading the state of a superconducting qubit. The dominating physical measurement is the amplitude measurement of a downconverted microwave signal processed at room temperature. Such a measurement is equivalent to a homodyne detection as explained in 2.4. This is very different from the optical domain, where detectors react to the presence of a single photon as the energy associated with only one photon can be amplified to an observable effect.

With present technology, a general purpose detector for single microwave photons is not possible due to the low energy associated with photons in the microwave regime. However, a few ideas for workarounds exist. For this purpose, a qubit is a natural component to consider if you are interested in single photon dynamics as qubits inherently work in the single excitation regime. For instance one could imagine a photon detector working by absorbing a photon by qubit and then reading out the qubit state [94, 171]. The phase qubit is therefore of particular interest as the qubit supports a built-in readout process [57, 58]. The phase qubit is, as presented in Sec. 2.2, a current biased Josephson Junctions (CBJJ) operated in the regime of only two bound states. Recent works using a CBJJ have made progress towards a single microwave-photon detector [97–100]. This chapter will expand on the progress with both novel theory [2, 3] and a brief presentation of a recent experiment [8].

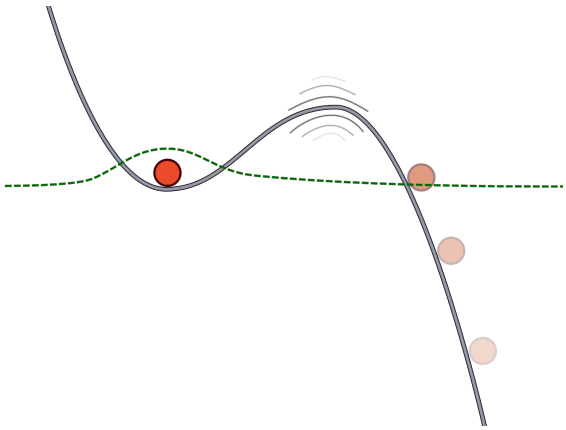

Figure 4.1: The superconducting phase variable in a current-biased Josephson junction behaves as a quantum particle trapped in a tilted washboard potential. The dashed (green) line is a sketch of the ground state wavefunction in one of the trapping wells. The probability that the phase particle tunnels out of the potential is increased if the barrier is modulated, e.g., by variation of the tilt due to a time dependent microwave field.

A current biased Josephson Junctions (CBJJ) is a device of particular interest since the phase variable associated with the junction acts as a particle trapped in a washboard potential. The properties of the CBJJ is, however, generally directly modified by even a weak probe field and may therefore directly measure an incident microwave field. This idea is presented in Fig. 4.1; the phase particle is trapped in a washboard potential well and by modifying the barrier height, the particles motional states are subject to tunneling into the continuum. A particle in the continuum will accelerate corresponding to a voltage drop over the device. The switching can occur due to thermal activation [172] and due to macroscopic quantum tunneling [173]. However, when the CBJJ is at a temperature of 20 mK, which is the case in the dilutions fridges of current quantum experiments, contribution from thermal activation can safely be neglected. This implies that the system can be described as an ordinary quantum particle and general methods from quantum mechanics can be applied to qualitatively and quantitatively study several features associated with its dynamics.

In this chapter we will work towards using the tunneling events in a

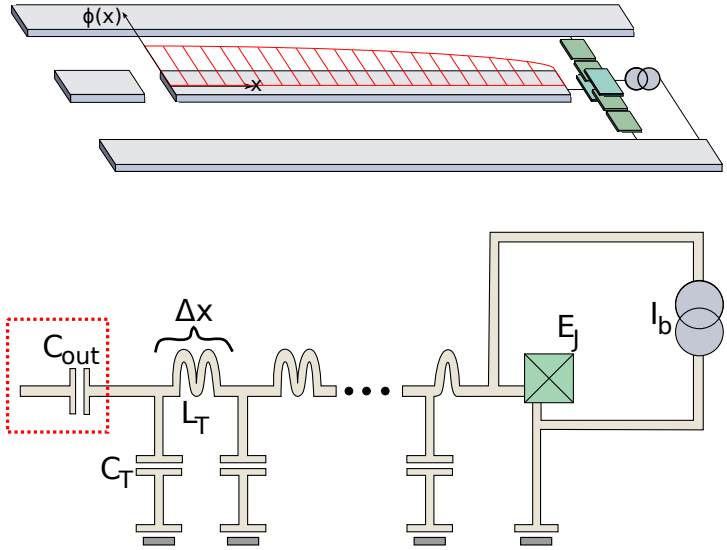

Figure 4.2: A schematic (top) and a circuit diagram (bottom) of the system. In the upper picture the fundamental normal mode of the flux is sketched. In the circuit diagram, the transmission waveguide resonator is described as a chain of capacitors and inductors. The resonator is shunted by a current biased Josephson junction. In the dashed (red) box, we couple capacitively to fields outside of the device.

CBJJ as a photon detector in the few photon regime by coupling the CBJJ to a $\lambda/4$-resonator (see Fig. 4.2). The general idea is to use the device both as a collector of photons and as a detector, sensitive to a single or a few quanta in the resonator through a classical measurable response in the form of a voltage switch over the Josephson junction. The major difference in the approach discussed in this Chapter compared to [99, 100] is that the detection here is not due to the resonance interaction between a single CBJJ (a phase qubit) and a photon. Instead the photon interacts with the resonator and due to the strong interaction between the resonator and the CBJJ, the tunneling properties of the CBJJ depend now directly on the photon number inside the resonator. This difference makes the appropriate theoretical treatment much different. A phase qubit requires

only two states to be properly described, but for a CBJJ coupled (possibly off-resonantly) to the field of a resonator, many levels may be relevant. Furthermore, the switching dynamics can no longer be described as a simple incoherent decay from the two qubit levels, but must be described as resonator-field dependent process. Moreover, the current device may result in several operational advantages: (i) Having the detector operating as a qubit, it can inherently only measure one photon, but using the current setup, a threshold for any number of photons in the field can be set allowing for a wider spectrum of applications. (ii) The bandwidth of the detector is more directly controlled since engineering a capacitive coupling to a resonator is straight forward. (iii) For the CBJJ to work well as a qubit, the bias current must be tuned to a specific value. For our setup, the resonator frequency only depends weakly on the bias current. (iv) A phase qubit is often dominated by a very large decoherence rate, which limits its detector efficiency. (v) A resonator is more convenient to incorporate in a modular fashion in larger circuits. For instance one can imagine an additional qubit being dispersively coupled to the resonator such that this device now also works as a qubit readout device.

4.1 Tunneling in current-biased Josephson junctions

We will now first focus on the junction Hamiltonian,

$$H_{JJ} = -\frac{\hbar^2}{2M}\frac{\partial^2}{\partial\varphi^2} - E_J(\cos\varphi + I\varphi), \tag{4.1}$$

and we develop a time-dependent phenomenological theory for the tunneling dynamics of a CBJJ. In previous works [97–100], the CBJJ was treated as a simple two-level system with an incoherent decay out of the exited state. While this model works well in the regime where the CBJJ interacts coherently with a single photon, it is not sufficient for what we are about to consider. First of all we will incorporate a time-dependent bias current and thus a time-dependent decay rate and secondly the switching to the voltage state is caused by the modulation of the junction potential by the rf-current in the coupled resonator and junction system and not just by resonance between an applied microwave and a qubit. Following the development of a tunneling theory in this section, the next section will include a general treatment to derive the full Hamiltonian of the resonator and CBJJ. This directly allows us to asses the performance of such a device as a detector of weak incident microwave fields.

The detection events of the detector can be described as the tunneling of a phase particle out of the well in the washboard potential of the CBJJ. In general, tunneling is a widely observed phenomenon in quantum mechanics and for tunneling through stationary barriers, scattering theory and good approximations based on the JWKB method are available [174], however for the dynamical situation these methods are not always applicable. While the Schrödinger equation is indeed uniquely defined in any time dependent potential, the handling of the scattering continuum components of the wave function outside the tunneling barrier is impeded by the demand for precise calculations on a very large interval of the coordinate variable. This also applies for the CBJJ. As a particular example consider, a weak field-induced modulation, resonantly coupling the ground state of the well to discrete excited states subject to stronger tunneling as the tunneling barrier height is reduced for these state. This situation can be treated as a perturbation and the CBJJ theory yields good agreement with experimental results [57, 175]. However, the wave-function may be subject to a strongly modified potential and is in this case not amenable to the perturbative description. Instead, we shall formally describe the tunneling process by wave packet propagation in a time dependent imaginary potential (TDIP), such that tunneling, observed as switching of the CBJJ into the voltage state, is treated as a dynamical loss process. In this way we both determine the time dependent probability for the tunneling to occur and we appropriately describe the evolution of the wave function conditioned on no tunneling event being detected.

4.1.1 Tunneling of the Josephson junction phase

The Josephson junction phase ϕ behaves as the position of a particle and is dynamically fully described by the time dependent Schrödinger equation,

$$i\hbar\frac{\partial}{\partial t}\psi(\phi,t) = H_{JJ}(t)\psi(\phi,t), \tag{4.2}$$

where the Hamiltonian operator $H_{JJ}(t)$ contains a, possibly time-dependent, potential and an effective kinetic energy term. Following the early work by Gamow, one can describe tunneling in static potentials by eigenfunctions of a time-independent, but possibly unbound, Hamiltonian [174]. The eigenfunctions may then be chosen with outgoing, radiating boundary conditions and then used as a wave function basis. This process effectively redefines the scalar product on the system Hilbert space, and the original Hamiltonian is then not Hermitian. This in turn leads to the emergence of

complex eigenvalues. The dynamically lost norm associated with the imaginary part of the energy eigenvalues represents the probability of tunnelling [176, 177]. Effective non-Hermitian Hamiltonians also emerge in quantum optics and quantum measurement theory, where they govern the evolution of a quantum system conditioned on the absence of absorption or loss events. In these theories, the decreasing norm of the state vector provides the probability for the evolution to occur without these events happening, while one may simulate the complete dynamics including random detection events by suitable application of "quantum jump" operators [101, 178].

At any given time the tunneling probability is governed by the wave function obtained by propagation our non-Hermitian Hamiltonian, i.e., the state conditioned on the detection of no previous switching events. An approach for finding the complex eigenvalues is by directly implementing a non-Hermitian Hamiltonian with respect to the original Hilbert space of square integrable wave functions, for example by the introduction of a complex absorbing potential (CAP). A properly designed CAP may thus describe the same physics as the Gamov vectors, i.e., the evolution of the unnormalized states may yield identical or very similar wave function behaviour in the spatial and temporal range of interest.

There is a rich literature (see [179] and references herein) on the identification of suitable CAPs, but since we shall be dealing with the further complexity of tunneling through a time dependent potential, we shall merely propose a simple, physically motivated *ansatz* for our time dependent imaginary potential (TDIP), $V_{im}(\phi, t)$, and solve the time-dependent Schrödinger equation

$$i\hbar\frac{\partial}{\partial t}\psi(\phi,t) = H_{JJ}(t)\psi(\phi,t) - iV_{im}(\phi,t)\psi(\phi,t). \tag{4.3}$$

For the CBJJ, we have the mass set by the capacitive charging energy, $M = C(\Phi_0/2\pi)^2$, where C is the capacitance of the junction and $\Phi_0 = \frac{h}{2e}$ is the flux quantum. The CBJJ potential is

$$U_0(\phi,t) = -E_J(I(t)\phi + \cos\phi) \tag{4.4}$$

where $E_J = \frac{I_c\Phi_0}{2\pi}$ is the Josephson energy and $I(t) = \frac{I_b(t)}{I_c}$, with I_b being the bias current applied to the junction. When I_b exceeds the critical current I_c, the potential tilt dominates the harmonic variation with ϕ, and the phase becomes classically unbound. We further include the interaction of the CBJJ with a time dependent microwave field via the potential term

expressed for convenience as,

$$U_{mw}(\phi,t) = -E_J\eta\phi\sin\Big(\omega_{mw}t\Big) \tag{4.5}$$

where η is proportional to the field amplitude. The CBJJ is thus described by the time-dependent Schrödinger equation

$$i\hbar\frac{\partial}{\partial t}\psi(\phi,t) = \Big(-\frac{\hbar^2}{2M}\frac{\partial^2}{\partial\phi^2} + U(\phi,t)\Big)\psi(\phi,t) \tag{4.6}$$

with $U(\phi,t) = U_0(\phi,t) + U_{mw}(\phi,t)$. This time dependent potential is sketched in Fig. 4.1, indicating also the tunneling process, responsible for the switching of the Josephson junction.

An imaginary absorbing potential, extending beyond the outer turning point of a potential barrier would seem a natural candidate to remove the tail of the wave function as tunneling develops. Since we want the potential to remove the projection of our wave function on the running states in that region, it is useful to apply approximate solutions for their position (phase) and time dependence in our ansatz for the TDIP. From [180] we have an approximate expression for the running state of the Josephson junction phase variable $\phi > \phi_{turn}$, initially at time τ in the ground state, in the linear potential region beyond the outer classical turning point of the potential barrier ϕ_{turn},

$$\begin{aligned}\psi_{out}(\phi,t,\tau) =& \sqrt{\frac{\Gamma}{\sqrt{2\phi'}\Phi_0\omega_p(\tau)}}e^{i\frac{\hbar\omega_p{\phi'}^{3/2}}{6\sqrt{2}E_J}} \\ &\times e^{-\left(i\frac{\omega}{\omega_p}+\frac{\Gamma}{2\omega_p}\right)((t-\tau)\omega_p-\sqrt{2\phi'})}\end{aligned} \tag{4.7}$$

with $\phi' = \phi - \phi_0$, where ϕ_0 is the initial equilibrium position (bottom of the well) and $\hbar\omega$ is the energy difference between the bottom of the well and the energy of the lowest quasi-bound state. We have further introduced the frequency parameter $\omega_0 = \sqrt{\frac{2\pi I_c}{C\Phi_0}}$ and the plasma frequency $\omega_p = \omega_0(1-I^2)^{1/4}$. The wavefunction (4.7) is defined for $t\omega_p > \sqrt{2\phi}$, and we assume a bias current less than the critical current, $I < 1$. The rate parameter Γ in (4.7) which attains a definite value in a static potential, will be briefly discussed below.

Our aim is to remove the projection of our time dependent wave function $|\psi(t)\rangle$ on a suitable set of running states of the form (4.7), $P_{out}|\psi\rangle = \sum_{\psi_{out}}|\psi_{out}\rangle\langle\psi_{out}|\psi\rangle$. We model this operation by a time-dependent complex potential, obtained as an integral over different running

states, emitted within the past interval of time Δt,

$$V_{im}(\phi, t) = \beta \int_{t-\Delta t}^{t} |\psi_{out}(\phi, t, t')|^2 \, dt'. \tag{4.8}$$

The parameter β serves both as an adjustable strength parameter and as a convenient normalization for the temporal integration. We assume a constant value of Γ and Δt, with $\Delta t^{-1} \ll \Gamma \ll \omega_p$,, and we evaluate the integral (4.8) only for values ϕ larger than the outer turning point, ϕ_{turn}, of the potential. The dependence on Γ drops out, and we obtain

$$V_{im}(\phi, t) = \begin{cases} \frac{\beta}{\sqrt{2\phi}\,\Phi_0 \omega_p(t)} & \text{for } \phi > \phi_{turn}(t) \\ 0 & \text{for } \phi < \phi_{turn}(t). \end{cases} \tag{4.9}$$

Here, we recall the time-dependence of the plasma frequency as the effective bias-current is changing with time.

Unlike normal CAPs used in time-independent problems, this potential is modeled to absorb the running state components (4.7) pertaining to the time dependent Hamiltonian, and our ansatz imaginary potential indeed attains finite values only beyond the time dependent outer classical turning point of the real potential. We emphasize that (4.9) is only an ansatz, but it ensures that the depletion of the wave function norm is properly associated with the probability that the particle has tunneled through the barrier.

As discussed in [2], zero temperature and Markovian noise effects of the junction resistance, R, can be included by a non-linear imaginary potential term, $-i\zeta\Big(\phi - \langle\phi\rangle_t\Big)^2$, where $\zeta \propto \frac{1}{RC}$ and $\langle\phi\rangle_t = \int_{-\infty}^{\infty} \phi \, |\psi(\phi, t)|^2 \, d\phi$ is the mean value of ϕ at time t. When added to the Hamiltonian this term penalizes large variations of ϕ around its mean and decoheres the spatial wave function, which in turn leads to friction for the phase variable ϕ. This effect is what set the T_1 time for phase qubits. It also leads to a loss of norm, albeit on a typically slower scale than the tunneling dynamics. We shall include this term in our calculations on the CBJJ, but we shall renormalize the wave function with respect to the loss it induce, so that we unambiguously associate the wave function loss of norm with the tunneling dynamics. To summarize, we treat the entire problem by solving the

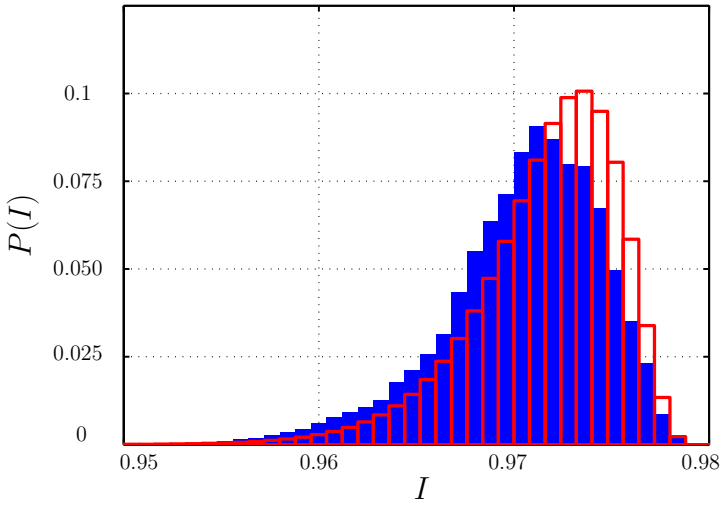

Figure 4.3: Blue (solid) bars show the switching current distribution simulated with an absorbing potential. Red (hollow) bars are calculated by Eq. (4.11). We have chosen C and R such that $\omega_0 = 0.0183\ E_J/\hbar$ and $\zeta = 8.4 \times 10^{-4} E_J$. The bias current is increased linearly from $I = 0.2$ at a slow rate $dI/dt = \frac{6\times10^{-7}\,E_J}{5\hbar}$. Results are shown for $I > 0.95$.

non-linear Schrödinger equation

$$\begin{aligned} i\hbar\frac{\partial}{\partial t}\psi(\phi,t) = \Big(&- \frac{\hbar^2}{2M}\frac{\partial^2}{\partial\phi^2} + U(\phi,t)\Big)\psi(\phi,t) \\ &- iV_{im}(\phi,t)\,\psi(\phi,t) \\ &- i\zeta\Big(\phi - \langle\phi\rangle_t\Big)^2\psi(\phi,t) \end{aligned} \tag{4.10}$$

and renormalize with respect to the loss of norm caused by the last term.

In a time-independent potential, the tunneling rate of the Josephson junction phase variable has been determined by Caldeira and Leggett [181, 182],

$$\gamma_{CL} = \frac{\omega_p}{2\pi}\sqrt{\frac{120\pi\cdot 7.2\Delta U}{\hbar\omega_p}}\,e^{-\frac{7.2\Delta U}{\hbar\omega_p}\left(1+\frac{0.87}{\omega_p RC}\right)} \tag{4.11}$$

where $\Delta U = 2E_J\big(\sqrt{1-I^2} - I\mathrm{acos}(I)\big)$ is the barrier-height, and where effects due to the friction are also taken explicitly into account. This analytic expression available for CBJJs qualify them as ideal candidates to test our general tunneling description.

The gradually decreasing norm, $||\psi(t)||^2$ of our numerically determined wave packet is interpreted as the probability that the phase variable has not tunneled until time t. The probability for a current switching event in the next infinitesimal time interval dt, is thus simply given by the loss of norm in that interval, and conditioned on no previous event, the switching rate of the CBJJ reads

$$\gamma_t = -\frac{d||\psi(t)||^2}{dt}/||\psi(t)||^2. \tag{4.12}$$

It is convenient in experiments to determine the switching current distribution, i.e., the probability distribution $P(I)$ for switching events to occur at different values of the bias current I, while this is being ramped up slowly, $I(t) = I_0 + \frac{dI}{dt}\cdot t$.

Our wave packet propagation yields the surviving (non-switching) population $||\psi(t)||^2$ as function of time, and we directly obtain the corresponding switching current distribution, obeying

$$\begin{aligned} P(I)\Delta I &= -\frac{d||\psi(t)||^2}{dt}\Delta t \\ &= -\frac{d||\psi(t)||^2}{dt}\Big(\frac{dI}{dt}\Big)^{-1}\Delta I, \end{aligned} \tag{4.13}$$

evaluated at the time t such that $I = I(t)$ and Δt being the infinitesimal time interval in which I increases by ΔI.

Under the assumption of a slowly ramped bias current, the rate γ_{CL} found by Caldeira and Leggett leads to a switching current density, expressed as a product of the current tunneling rate with the survival probability until the value I is reached during the ramp,

$$P_{CL}(I) = \Big(\frac{dI}{dt}\Big)^{-1}\gamma_{CL}(I)\, e^{-\int_{I_0}^{I}\left(\frac{dI}{dt}\big|_{I=I'}\right)^{-1}\gamma_{CL}(I')dI'}. \tag{4.14}$$

In Fig. 4.3 we see, that our calculation, matches the result of the quasi-static switching current distribution, (4.14), reasonably well as a function of the bias current. Furthermore, we present in [2] a more general study of TDIP applied to more complicated dynamics. The method introduced here used a time dependent imaginary potentials to describe

the switching behaviour of a current biased Josephson junction and it is readily implemented with standard wave packet solvers and with realistic parameters. We emphasize that our treatment builds on an ansatz for a time dependent imaginary potential (TDIP), and a number of possibilities may be explored for quantitative improvement of the potential chosen, however, this potential is sufficient for generalizing the model to arbitrary circuits involving a CBJJ.

4.2 Resonator and CBJJ as a detector

In the previous section we derived a method for treating the tunneling dynamics of a CBJJ. To calculate the dynamics of the circuit displayed in Fig. 4.2, we need to obtain the Hamiltonian for the system. Thus, we consider the corresponding classical system for which we can directly write up the Lagrangian. With the Lagrangian at hand we can identify the canonical variables and perform a canonical quantization and a Legendre transform to obtain the quantum mechanical Hamiltonian. The approach followed here is similar to the approaches of [37, 81] and while some steps are omitted here for simplicity, the full analysis can be found in [3].

In Fig. 4.2 (bottom panel), we show a lumped element representation of our system. We will choose the bias line to be a closure branch of the system, while the rest constructs the spanning tree. The resonator is here depicted as a series of n LC circuits, which in the limit $n \to \infty$ will give an appropriate description of the resonator as detailed in Sec. 2.1. Thus, the dynamics of the resonator is described by the wave equation

$$\frac{1}{C_T L_T}\partial_x^2\phi(x) - \partial_t^2\phi(x) = 0. \tag{4.15}$$

The end point of the circuit is shunted with a bias current, I_b, which we model as a high inductance line, with the inductance L_S, pre-charged with a large flux, $\tilde{\Phi}_S$, such that $\tilde{\Phi}_S/L_S = I_b$. The equation of motion is then

$$C_J\,\ddot{\phi}_n = \frac{\phi_n - \phi_{n-1}}{L_T\Delta x} - \frac{2e}{\hbar}E_J\sin\Big(\frac{2e}{\hbar}\phi_n\Big) + \frac{\tilde{\Phi}_S - \phi_n}{L_s} \tag{4.16}$$

$$\underset{L_S\to\infty}{=} \frac{\phi_n - \phi_{n-1}}{L_T\Delta x} - \frac{2e}{\hbar}E_J\sin\Big(\frac{2e}{\hbar}\phi_n\Big) + I_b. \tag{4.17}$$

We are now able to write the proper Lagrangian for the system, such that the Euler-Lagrange equations give the above equations of motion:

$$\mathcal{L} = \int_0^d dx \Big\{ \frac{C_T}{2} \big(\partial_t \phi(x)\big)^2 - \frac{1}{2L_T} \big(\partial_x \phi(x)\big)^2 \Big\} + \frac{C_J \big(\partial_t \phi(d)\big)^2}{2} + E_J \Big(\cos\Big(\frac{2e}{\hbar}\phi(d)\Big) + I\,\frac{2e}{\hbar}\phi(d)\Big), \tag{4.18}$$

with $I = I_b/I_c$, where the critical current is defined as $I_c = \frac{2e}{\hbar} E_J$.

The phase across the Josephson junction, ϕ_J, is given as a function of the bias current,

$$\frac{2e}{\hbar}\phi_J = \sin^{-1} I, \tag{4.19}$$

which will also contribute with a predefined flux in the transmission resonator. If we neglect contributions from the Josephson capacitance, C_J, the Euler-Lagrange equation at $x = d$ yields

$$\frac{1}{L_T}\partial_x \phi(d) = \frac{2e}{\hbar} E_j \Big(\sin\frac{2e}{\hbar}\phi(d) + I\Big). \tag{4.20}$$

Generally the flux bias will not be constant, but it leads us to the ansatz for solutions of the equation of motion given by

$$\phi(x) = \sum_j \phi_j \, \cos k_j x + \phi_0. \tag{4.21}$$

In writing Eq. (4.21), we have assumed that there is no incident field at the capacitor, C_{out}, leading to the open boundary condition $\partial_x \phi = 0$ at $x = 0$. The open boundary condition is equivalent to the assumption of a vanishing current, while the time-derivative of $\phi(0)$ yields the voltage at C_{out}, determined by the field inside the resonator. The values of k in Eq. (4.21) must be chosen to match the boundary condition following from the linearized Euler-Lagrange equation at $x = d$ [Eq. (4.20)].

Using the steady state result for the junction phase $\phi_0 = \phi_J$, with the approximation that the phase difference between the phase across the junction and the steady state phase is small, that is $\sum \phi_j \cos k_j d \ll 1$, we can derive the following approximate identity

$$\Big(\sin\frac{2e}{\hbar}\phi(d) + I\Big) = \frac{2e}{\hbar} \sum_j \phi_j \cos k_j d \, \cos\frac{2e}{\hbar}\phi_0, \tag{4.22}$$

and we obtain the linearised equation for each independent mode

$$k_j d \tan k_j d = \frac{L_T d}{L_J} \cos\frac{2e}{\hbar}\phi_J, \tag{4.23}$$

with $L_J = (\hbar/2e)^2/E_J$. This equation can be solved numerically or approximated by

$$k_j d = \frac{\pi(1+2j)}{2(1+\frac{L_J}{L_T d\cos\phi_J})}, \tag{4.24}$$

valid for $L_J \ll L_T d\cos\frac{2e}{\hbar}\phi_J$. We recall that our approximate solutions are only valid when neglecting the Josephson capacitance, C_J. In the following we shall reinstate a contribution from C_J and evaluate its influence on the modes defined in (4.21).

4.2.1 Single-mode approximation

Having Eq. (4.21) as a solution for the normal modes we can choose to look at a single-mode field

$$\phi(x) = \phi\cos kx + \phi_0 \tag{4.25}$$

and substitute this solution into the Lagrangian

$$\begin{aligned}\mathcal{L} = {}& \dot{\phi}^2\Big(\int_0^d \frac{C_T\cos^2 kx}{2}dx + \frac{C_J\cos^2 kd}{2}\Big)\\ &+ \dot{\phi}_0^2\frac{C_T d + C_J}{2}\\ &+ \dot{\phi}\dot{\phi}_0\Big(\int_0^d C_T\cos kx\,dx + C_J\cos kd\Big)\\ &- \phi^2\int_0^d \frac{k^2\sin^2 kx}{2L_T}dx\\ &+ E_J\Big(\cos\frac{2e}{\hbar}(\phi\cos kd+\phi_0) + \frac{2e}{\hbar}I(\phi\cos kd+\phi_0)\Big).\end{aligned} \tag{4.26}$$

Next, we expand the cos-term of the potential as $\cos(A+B) = \cos A\cos B - \sin A\sin B$ followed by an expansion to fourth order of $(\frac{2e}{\hbar}\phi\cos kd)$ allowing also for Kerr-effects in the device. We can reduce the expressions in the Lagrangian significantly by introduction of the quantities

$$C_E = \frac{C_T d}{2}\Big(1+\frac{\sin 2kd}{2kd}\Big) + C_J\cos^2 kd \tag{4.27}$$

$$C_0 = C_T d + C_J \tag{4.28}$$

$$C_c = C_T d\,\frac{\sin kd}{kd} + C_J\cos kd \tag{4.29}$$

$$L_E^{-1} = \frac{(kd)^2}{2L_T d}\Big(1-\frac{\sin 2kd}{2kd}\Big). \tag{4.30}$$

This constitutes the Lagrangian

$$\begin{aligned}\mathcal{L} =& \dot{\phi}^2\frac{C_E}{2} - \phi^2\frac{1}{2L_E} + \dot{\phi}\dot{\phi}_0 C_c \\ &+ \dot{\phi}_0^2\frac{C_0}{2} + E_J\Big(\cos\frac{2e}{\hbar}\phi_0 + \frac{2e}{\hbar}I\phi_0\Big) \\ &- E_J\Big(\frac{(2e)^2\phi^2\cos^2 kd}{2\hbar^2} - \frac{(2e)^4\phi^4\cos^4 kd}{24\hbar^4}\Big)\cos\frac{2e}{\hbar}\phi_0 \\ &- E_J\frac{2e}{\hbar}\phi\cos kd\Big(\sin\frac{2e}{\hbar}(\phi_0-\phi_J)\cos\frac{2e}{\hbar}\phi_J \\ &\qquad - \frac{(2e)^2\phi^2\cos^2 kd}{6\hbar^2}\sin\frac{2e}{\hbar}\phi_0\Big),\end{aligned} \tag{4.31}$$

from which we will derive the Hamiltonian. We introduce the conjugate variables to ϕ and ϕ_0,

$$q = \frac{\partial\mathcal{L}}{\partial\dot{\phi}} = C_E\dot{\phi} + C_c\dot{\phi}_0 \tag{4.32}$$

$$q_0 = \frac{\partial\mathcal{L}}{\partial\dot{\phi}_0} = C_0\dot{\phi}_0 + C_c\dot{\phi}, \tag{4.33}$$

and we perform a Legendre transformation to get the Hamiltonian

$$\begin{aligned}H =& \frac{q_0^2}{2(C_0 - C_c^2/C_E)} - E_J\Big(\cos\frac{2e}{\hbar}\phi_0 + \frac{2e}{\hbar}I\phi_0\Big) \\ &- \frac{C_c}{C_0C_E - C_c^2}qq_0 + \frac{q^2}{2(C_E - C_c^2/C_0)} \\ &+ \frac{\phi^2}{2L_E} + E_J\frac{(2e)^2\cos^2 kd}{2\hbar^2}\phi^2\cos\frac{2e}{\hbar}\phi_0 \\ &- E_J\frac{(2e)^4\cos^4 kd}{24\hbar^4}\phi^4\cos\frac{2e}{\hbar}\phi_0 \\ &- E_J\frac{2e}{\hbar}\phi\cos kd\Big(\sin\frac{2e}{\hbar}(\phi_0-\phi_J)\cos\frac{2e}{\hbar}\phi_J \\ &\qquad - \frac{(2e)^2\phi^2\cos^2 kd}{6\hbar^2}\sin\frac{2e}{\hbar}\phi_0\Big).\end{aligned} \tag{4.34}$$

In the quantum regime the resonator operators q and ϕ satisfy the canonical commutation relation $[\phi, q] = -i\hbar$, which allows us to introduce the ladder operator a ($a^\dagger$) that annihilates (creates) a photon in the normal

mode of the resonator. For convenience we now define the operators as

$$\phi = i\sqrt{\frac{\hbar\omega L_E}{2}}(a - a^\dagger) \tag{4.35}$$

$$q = \sqrt{\frac{\hbar}{2\omega L_E}}(a + a^\dagger) \tag{4.36}$$

with the angular frequency $\omega = 1/\sqrt{L_E(C_E - C_c^2/C_0)}$. This definition differs from the standard approach in Sec. 2.1, however, it simplifies the Hamiltonian in this section.

Now, we introduce the variable $\varphi = \frac{2e}{\hbar}\phi_0$ as well as its conjugate variable q_φ satisfying $[\varphi, q_\varphi] = -i\hbar$. We define $M = (C_0 - C_c^2/C_E)/(2e)^2$ and substitute Eq. (4.35) and (4.36) into the Hamiltonian, while keeping only energy conserving terms for the cavity field mode and ignoring constant energy shifts and get

$$\begin{aligned} H = {} & \frac{q_\varphi^2}{2M} - E_J(\cos\varphi + I\varphi) \\ & + (\hbar\omega + \hbar\,\eta\cos\varphi)\, a^\dagger a \\ & + \hbar\,\kappa\cos\varphi\, a^\dagger a^\dagger a a + \hbar\lambda\, q_\varphi q \\ & + (\hbar\mu + \hbar\chi\, a^\dagger a)\, \sin(\varphi - \varphi_J)\, \phi. \end{aligned} \tag{4.37}$$

This Hamiltonian is the main result needed to calculate the dynamics of our system and, thus, to assess if the system may function as a microwave detector. We recognize the Hamiltonian for a single Josephson junction and a single resonator mode coupled by linear and non-linear terms. The constants in the Hamiltonian are given as

$$\eta = \frac{E_J}{2}\frac{(2e)^2}{\hbar^2}\cos^2 kd\, L_E\omega \tag{4.38}$$

$$\kappa = -\frac{E_J}{4}\frac{(2e)^4}{\hbar^3}\cos^4 kd\, L_E^2\omega^2 \tag{4.39}$$

$$\lambda = -\frac{2e}{\hbar}\frac{C_c}{C_0C_E - C_c^2} \tag{4.40}$$

$$\mu = -\frac{E_J}{\hbar}\frac{2e}{\hbar}\cos kd\, \cos\varphi_J \tag{4.41}$$

$$\chi = \frac{E_J}{4\hbar}\frac{(2e)^3}{\hbar^2}\cos^3 kd\, L_E\omega\, \cos\varphi_J. \tag{4.42}$$

For a $\lambda/4$-resonator with no junction, $\cos kd$ would naturally be 0, but due to the CBJJ the field has a non-zero value at $x = d$. However, $\cos kd$ is

still expected to be small, due to the weak field in the resonator, so the magnitude of the strengths in frequency units supposedly follow the order $\mu\sqrt{\frac{\hbar\omega L_E}{2}} > \eta > \sqrt{\frac{\hbar\omega L_E}{2}}\chi > \kappa$, while $\lambda\sqrt{\frac{\hbar}{2\omega L_E}}$ does not directly relate to the other quantities. It should also be noted that weak terms which include $\cos\varphi$ but no field coupling terms, a or $a^\dagger$, are neglected as they merely change the Josephson energy, E_J, by a small amount.

4.2.2 Validity of the single-mode approximation

The Hamiltonian (4.37) assumes the near-resonant coupling to only one active resonator mode. The single-mode approximation is valid when the energy difference between modes is much larger than the coupling strengths, but in superconducting circuits, $\mu\sqrt{\frac{\hbar\omega L_E}{2}}$ may be comparable to the mode frequencies, and a more careful analysis is needed.

To illuminate the discussion, we will write the Hamiltonian as

$$H = H_{JJ} + H_{a,JJ} \tag{4.43}$$

with H_{JJ} equal to the two first terms of Eq. (4.37) and $H_{a,JJ}$ equal to the rest of the terms involving the fundamental mode a of the resonator. Now, we include a second resonator mode b, and we write the Hamiltonian

$$H = H_{a,JJ} + H_{JJ} + H_{b,JJ} + H_{a,b} \tag{4.44}$$

with $H_{b,JJ}$ similar to $H_{a,JJ}$ and $H_{a,b}$ representing the direct coupling terms between the two modes caused by the spatially dependent terms in Eq. (4.18).

We assume that the lowest state of the coupled system is approximately a product state,

$$\Psi_0 = \psi_a^0\,\psi_{JJ}^0\,\psi_b^0 \tag{4.45}$$

while the first excited states for the Hamiltonian in Eq. (4.44) may be expanded on,

$$\Psi_1 = \psi_{a,JJ}^1\,\psi_b^0, \tag{4.46}$$

and

$$\tilde{\Psi}_1 = \psi_a^0\,\psi_{b,JJ}^1, \tag{4.47}$$

where $\psi_{a,JJ}^1$ and $\psi_{b,JJ}^1$ are the first excited eigenstates of $H_{JJ} + H_{a,JJ}$ and $H_{JJ} + H_{b,JJ}$, respectively.

The validity of the single mode approximation is determined by the coupling of the ground state Ψ_0 and the excited state Ψ_1 to $\tilde{\Psi}_1$,

$$g_{1a,1b} = \int \tilde{\Psi}_1^*(H_{b,JJ} + H_{a,b})\Psi_1 \tag{4.48}$$

$$g_{0,1b} = \int \tilde{\Psi}_1^*(H_{b,JJ} + H_{a,b}\Psi_0. \tag{4.49}$$

The system will be driven close to the resonance between Ψ_0 and Ψ_1, and if the conditions

$$|g_{1a,1b}| \ll |\Delta_{1a,1b}| \qquad\qquad |g_{0,1b}| \ll |\Delta_{0,1b}| \tag{4.50}$$

are satisfied, where $\Delta_{x,y}$ is the energy difference between states x and y, the coupling can be neglected and the single-mode approximation is justified.

In the calculations in Sec. 4.2.5 we find numerically the conditions in Eq. (4.50) to be almost satisfied. With parameters used later in the text we find $|g_{1a,1b}/\Delta_{1a,1b}| \lesssim 0.1$. This will lead to a pertubation of the energy of Ψ_1 by $\sim \hbar\Delta_{0,1a}/100$, and to a population in $\tilde{\Psi}_1$ of 1%. The calculations in Secs. 4.2.4 and 4.2.5 are performed using the single-mode approximation, and they may hence slightly overestimate the efficiency of the device at the level of 1%. For higher excited states and higher order resonator modes, we find a decreasing ratio between the coupling strengths and the energy differences, but further theoretical analyses into this matter will be needed to clarify the influence of more modes and levels.

Note as well, the the validity of the single-mode approximation is based on the parameters used for the numerics in Sec. 4.2.5 and, as such, is not necessarily valid for all sets of parameters. Indeed, the experiment presented in Sec. 4.3 uses parameters where the single-mode approximation is less valid and we attribute parts of the derivation between experiment and theory to this fact.

4.2.3 Off-resonance and multi-mode interaction

In the previous subsection, in order to simplify the problem, we ignored multi-mode interaction from the term $\dot{\phi}\dot{\phi}_0$, which transforms into coupling of all q_j's. Another way to simplify the problem is to choose the parameters of the resonator such that the energy splittings are much smaller than the energy splittings in the Josephson junction. Then we safely ignore ϕ_0 as a dynamical variable and replace it with the static value ϕ_J and from (4.36)

we get $q_j = C_j \phi_j$ with

$$C_j = \frac{C_T d}{2}\Big(1 + \frac{\sin 2k_j d}{2k_j d}\Big). \tag{4.51}$$

We can also use the Euler-Lagrange equation (4.23), and obtain the effective inductance

$$L_j^{-1} = \frac{(k_j d)^2}{2L_T d}\Big(1 + \frac{\sin 2k_j d}{2k_j d}\Big). \tag{4.52}$$

Defining $\omega_j = 1/\sqrt{L_j C_j}$ and following the derivation of Eq. (4.37) we then get the Hamiltonian

$$H = \sum_j \left(\hbar\omega_j a_j^\dagger a_j + \hbar\kappa_{jj} a_j^\dagger a_j^\dagger a_j a_j\right) + \sum_{i\neq j} 2\hbar\kappa_{ij} a_i^\dagger a_i a_j^\dagger a_j \tag{4.53}$$

with

$$\kappa_{ij} = -\frac{E_J}{4\hbar}\frac{(2e)^4}{\hbar^2}\cos^2 k_i d \cos^2 k_i d\, L_E^2 \omega^2 \cos\varphi_J. \tag{4.54}$$

This Hamiltonian is formally equivalent to the JPA Hamiltonian with κ_{00} being the fundamental JPA Kerr non-linearity [81, 141]. Unlike the usual set-up for a JPA, however, we now have an easy way of tuning the non-linearity since $\kappa_{ij} \propto \cos\varphi_J$ can be controlled by the bias current.

4.2.4 Spectral Analysis

After having derived the single-mode Hamiltonian (4.37), we can choose the realistic parameters [183–185]. We assume a Josephson Junction with a zero-coupling critical current $I_c = 2\,\mu$A and a Josephson capacitance $C_J = 1500$ fF together with a $50\,\Omega$-impedance resonator with a bare resonance at 7 GHz. For these parameters we get $\mu\sqrt{\frac{\hbar L_E \omega}{2}}/\omega \approx 3.5$ for $I = 0.9$, which means that we have ultra-strong coupling between the two system, hence we cannot approximate the system by a Jaynes-Cummings-type Hamiltonian.

In Fig. 4.4 we have numerically diagonalized Eq. (4.37) for parameters chosen as described above. In the diagonalization procedure, the junction phase variable is described on a grid in a box of length 2.5π leaving only one well in the potential of Eq. (4.1) and the states are now identified as localized wave-packets quasi-bound in the well. We see a band-like structure of highly dressed modes given by the number of photons in the

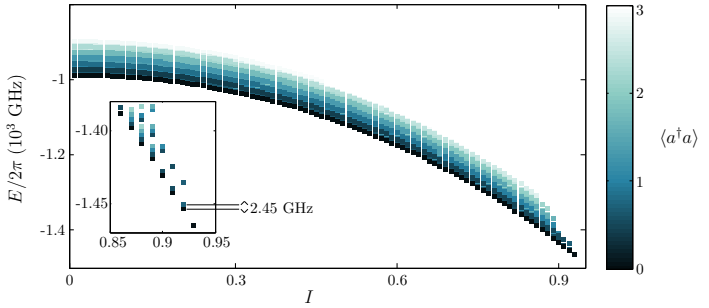

Figure 4.4: Eigenenergies of the Hamiltonian (4.37) for different values of the dimensionless bias current I. The color represents the meanvalue of $a^\dagger a$. The parameters are chosen to represent a Josephson junction with a critical current of 2 μA and a capacitance of 1500 fF. The 50 Ω-impedance resonators bare frequency is chosen to be 7 GHz. Eigensolutions with a mean occupation number in the resonator mode above 3 are not included. In the inset is a zoom of the lowest bands near the end of the bands. Marked with lines in the inset are the eigenenergies in the lowest band at $I = 0.92$, highlighting the energy difference between the only two bound state of the lowest band.

resonator and we observe that the higher bands gradually disappear when the bias current is increased. In the end, only the empty cavity with the junction in the ground state survives as a bound state. However, even this state is not bound for $I = 0.94$, which implies that the coupling to the resonator effectively changes the critical current of the junction, as one would expect.

It is also interesting to look at the wave function, Ψ, for the eigenstates. We expect the resonator field mode and junction phase to be highly correlated due to the ultra strong coupling terms, however we can still define the phase distribution,

$$P(\varphi) = \int d\phi \, |\Psi(\phi, \varphi)|^2, \tag{4.55}$$

which we have depicted in Fig. 4.5 for the first two eigenstates at $I = 0.92$. Since the numerical calculations are done in a Fock basis for the resonator degree of freedom, we use the partial trace, $\langle\varphi| \operatorname{Tr}_{res}(|\Psi\rangle\langle\Psi|) |\varphi\rangle$,

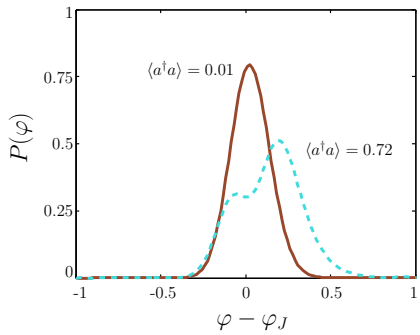

Figure 4.5: Probability distribution for the Josephson junction phase variable, φ, calculated with the parameters as in Fig. 4.4 and $I = 0.92$. This choice of physical parameters yields the following values for the parameters in Eqs. (4.38)-(4.42), $(\eta, \kappa, \lambda\sqrt{\frac{\hbar}{2\omega L_E}}, \mu\sqrt{\frac{\hbar\omega L_E}{2}}, \chi\sqrt{\frac{\hbar\omega L_E}{2}}) = (5.78, 0.03, 0.90, 29.7, 0.08) \times 2\pi$ GHz. The solid (red) line is the calculated ground state, while the dashed (blue) line is first excited state. The mean value of $a^\dagger a$ for the two states is also indicated in the figure.

to calculate the probability distribution. As an interesting feature we see that, even though the ground state is nearly symmetric, the first excited state is very asymmetric. The population in the one-photon state of the resonator effectively lowers the barrier of the potential from Eq. (4.1) [see also Eq. (4.65)], which in turn pushes the probability distribution for φ towards the continuum.

Coupling of the eigenstates by an external field

We are now interested in driving transitions between the eigenstates of the system. Such a coupling can be realized by coupling the system to the field in an outside resonator through a capacitor with the capacitance C_{out} at $x = 0$ (see dashed box in Fig. 4.2).

Adding the capacitor gives rise to a Lagrangian term

$$\mathcal{L}_{out} = \frac{C_{out}}{2}\left(\dot{\phi}_{out} - \dot{\phi}(0)\right)^2 \tag{4.56}$$

which yields terms quadratic in both $\dot{\phi}(0)$ and $\dot{\phi}_{out}$, but typically C_{out} is much smaller than any other capacitive element so we neglect these terms.

In this approximation the canonical variables are not changed. We can therefore write

$$\dot{\phi}(0) = \frac{C_0 - C_c}{2(C_c^2 - C_E C_0)} q + \frac{C_E - C_c}{2(C_c^2 - C_E C_0)} q_0 \tag{4.57}$$

$$\dot{\phi}_{out} = \sqrt{\frac{\hbar \omega_{out}^2 Z_{out}}{2}} (b + b^\dagger), \tag{4.58}$$

with Z_{out} being the impedance of the outside resonator and ω_{out} its frequency. Now b ($b^\dagger$) annihilates (creates) a photon in the the outside resonator.

In order to estimate the coupling strength of the coupling between the device and the outside field we look at the spectra from the Hamiltonian and choose a value of I such that we only have two states in the lowest band. We will now denote these as $|0\rangle$ and $|1\rangle$. From this, we get a term for the Hamiltonian

$$H_{out} = \Omega |0\rangle\langle 1| (b + b^\dagger) + \text{H.c.} \tag{4.59}$$

with the coupling strength

$$\Omega = \alpha \left(\beta_1 \langle 0 | q_\varphi | 1 \rangle + \beta_2 \langle 0 | a + a^\dagger | 1 \rangle \right) \tag{4.60}$$

and the quantities defined by

$$\alpha = C_{out} \sqrt{\frac{\hbar \omega_{out}^2 Z_{out}}{2}} \tag{4.61}$$

$$\beta_1 = 2e \frac{C_E - C_c}{2(C_c^2 - C_E C_0)} \tag{4.62}$$

$$\beta_2 = \sqrt{\frac{\hbar}{2 L_E \omega}} \frac{C_0 - C_c}{2(C_c^2 - C_E C_0)}. \tag{4.63}$$

In writing Eq. (4.59) we have neglected coupling to higher bands as well as coupling to unbound states, but if we choose ω_{out} to be resonant with the splitting in the lowest band, this should be a good approximation. Now, if we use the same parameters as before and we set $C_{out} = 5$ fF at a bias current $I = 0.92$ with a frequency of the outside field resonant with the energy-spltting, $\hbar\omega_{out} = E_1 - E_0$, we get a coupling strength of $|\Omega| = 2\pi \times 29$ MHz. This coupling will also mediate a decay from $|1\rangle$ assuming no external field is applied with a time-scale set by the coupling strength.

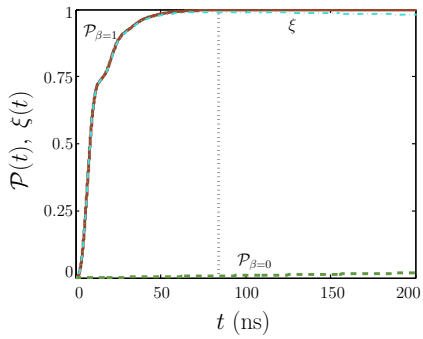

Figure 4.6: Accumulated probability for a switching event and the detector efficiency for $I = 0.92$. The switching probability for $\beta = 1$ is shown as the solid (red) line, and for $\beta = 0$ as the dashed (green) line. The detector efficiency is shown as the dashed-dotted (blue) line. The dotted vertical line marks the maximal efficiency point. The parameters chosen are those of a Josephson junction with a critical current at 2 μA, a capacitance at 1500 fF and a Josephson resistance at 300 Ω, thus Eqs. (4.38)-(4.42) yield the same numerical values as in Fig. 4.5. The 50 Ω-impedance resonator bare frequency is 7 GHz, and we assume $C_{out} = 5$ fF.

4.2.5 Time-dependent analysis

With a time-independent description in place, we turn to the question of time evolution of the system. If the system is prepared in an eigenstate of the Hamiltonian the time evolution is at a first glance trivial, however if the system is prepared with a bias current close to the critical current, there is a finite chance of tunneling through the potential barrier causing a voltage switch across the junction [2, 180, 186, 187], as was discussed in Sec. 4.1 [185].

Following the description in last section, we treat the tunneling loss process by propagating the wave function of the phase variable in a time-dependent imaginary potential (TDIP),

$$i\hbar\frac{\partial\Psi}{\partial t} = (H - iV_{im}(t))\Psi, \tag{4.64}$$

and we also include a Markovian friction term to take the junction resistance into account. In the simulations we have used a Josephson resistance at

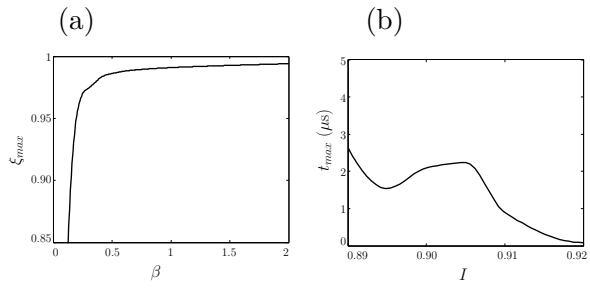

Figure 4.7: In (a) we show the maximal detector efficiency for $I = 0.92$ as a function of β, while in we display the detection time required to reach the maximal efficiency as a function of I. In all figures ω_{out} is equal to the energy splitting between the two lowest bound states. The rest of the parameters are the same as Fig. 4.6.

300 Ω.

We use here an ansatz for the TDIP evaluated at each time-step as a function of the resonator field mode variable, ϕ. Taking the mean of resonator operators in each time-step provides an effective potential for the phase particle

$$U_{eff}(\varphi) = \hbar\omega\bar{n} - E_J\Big(\cos\varphi(1 + \frac{\hbar\eta}{E_J}\bar{n} + \frac{\hbar\kappa}{E_J}\langle a^\dagger a^\dagger aa\rangle) + \varphi(I + \frac{\hbar\mu}{E_J}\langle\phi\rangle + \frac{\hbar\chi}{E_J}\bar{n}\langle\phi\rangle)\Big), \tag{4.65}$$

with $\bar{n} = \langle a^\dagger a\rangle$ being the mean photon number in the resonator field mode at a given time. By taking the mean values we neglect an amount of correlations between the tunneled phase-particle and the resonator, however the tunneling and detection time is much faster than the characteristic time scale of these correlations. With this potential, we can determine the time dependent classical turning point and,thus, a useful expression for $V_{im}(\varphi)$.

In the following we assume that our device is initialized in the ground state and that the resonator is driven with a constant weak classical field, so that

$$(b + b^\dagger)(t) \to \beta \sin\omega_{out}t \tag{4.66}$$

with β a constant of order 1 [188]. We thus neglect the operator character of the incident field and the decay from the resonator mode into field modes outside the resonator. Equation (4.59) then yields

$$H_{out}(t) = \alpha\beta\Big(\beta_1 q_\varphi + \beta_2(a + a^\dagger)\Big)\sin\omega_{out}t. \tag{4.67}$$

In Fig. 4.6 we present the calculated probability that a switching event has happened, calculated as

$$\mathcal{P}(t) = 1 - ||\Psi(t)||^2 \tag{4.68}$$

evaluated at the time t and we define the detector efficiency as in [100], $\xi(t) = \mathcal{P}_{\beta=1}(t) - \mathcal{P}_{\beta=0}(t)$. The norm $||\Psi(t)||^2$ is expected to decrease due to the propagation in the TDIP and the tunneling rate can be calculated from the derivative $\gamma = -d||\Psi(t)||^2/dt$. We see that for $\beta = 1$ we approach unit probability within roughly 80 ns, which we may compare with the Rabi time $t_r = \pi/|\Omega| \approx 21$ ns, which implies that around 4 Rabi oscillations are made before a tunneling event is certain. We recall, however, that the Rabi oscillations are modified due to the non-linear nature of the detector. Nevertheless, the first oscillation can be observed in Fig. 4.6 as a shoulder on the probability graph around half the Rabi time.

We have also marked the most efficient point in Fig. 4.6, that is the maximum of $\xi(t)$. We will denote this efficiency ξ_{max} and the time where it occurs t_{max}. For the parameters in Fig. 4.6 we get $\xi_{max} = 0.991$ with $t_{max} = 82$ ns. Figure 4.7 now shows the maximal efficiency as a function of both I and β. In each case the driving frequency, ω_{out}, is equal to the energy splitting of the two lowest bound states. This restricts these simulations to $I \leq 0.92$, as we do not have more than one bound state above this bias-current. As expected, the maximal efficiency increases as the field strength, β, increases as seen in Fig. 4.7 (a). However, once we are above $\beta = 0.5$, ξ_{max} saturates. Note that, in our description, a change in β is equivalent to a change in C_{out}. We can change the current, I, to a lower bias-current, which opens for the possibility of even higher quantum efficiency, but in Fig. 4.7 (b) we see that it comes at a price of significantly larger detection time. For the large detection times required for $I < 0.91$, we might not be able to safely neglect resonator decay as we have done in these calculations.

4.2.6 Summary of the theoretical treatment

We have derived the Hamiltonian for a $\lambda/4$-resonator shunted by a current-biased Josephson junction (CBJJ). This device was expected to work as a

very sensitive microwave detector near the quantum limit, as it combines the techniques of a JPA to amplify the incoming signal, with the voltage switch of a CBJJ to detect the signal. Numerical calculations show that we indeed get a very high detector efficiency of the device.

Using the theory in Sec. 4.1 [2] to describe the switching of a CBJJ, the calculations take into account both the complex tunneling dynamics of a CBJJ as well as relaxation in the junction, however we have neglected losses in the resonator. The method to describe the tunneling uses a time-dependent imaginary potential (TDIP), which is shown to be a good approximate method. We derived the Hamiltonian using a standard method for quantization of electric circuits [37] and we obtained a coupled resonator-like degree of freedom and CBJJ-like degree of freedom. Furthermore, to make sure that resonator losses may be neglected, we seek short optimal detection time, which we get by going to the highest bias current, $I = 0.92$, where two bound states still remain in the full system. Here, we get a quantum efficiency pf 0.991 at a detection time of 82 ns. Tuning the bias current to a higher value will reduce the efficiency, as bound excited states are lost. The calculations have been done based on a single-mode approximation, thus an experimental implementation might suffer from a small leakage into higher modes of the resonator and thus the efficiency will be slightly reduced or a slightly longer detection time will be required.

4.3 Experimental realization

In the previous section we used a quantum trajectory treatment to analyze the performance of such a system comprised of a $\lambda/4$ coplanar waveguide (CPW) resonator shunted to ground via a Josephson junction. In [8], an experiment was presented using a fabricated superconducting circuit that consists of two $\lambda/4$ waveguides, both shunted to ground via a Josephson junction. The chip layout together with an SEM-image of one of the Josephson junctions is shown in Fig. 4.8.

The two resonators are coupled to a microwave waveguide with a coupling capacitance estimated to be $C_c = 10$ fF by a full electromagnetic finite element simulation. The resonators are designed to have a fundamental resonance at about 2.5 GHz. The sample is fabricated with Nb-AlOx-Nb junctions [189] with an aimed critical current density of 200 A/cm^2. Thus, the output (gap) voltage of the Josephson junctions takes a value of 2.6 mV and no additional amplifiers are necessary for the detection of switching events. The sample is placed in a dilution refrigerator with a

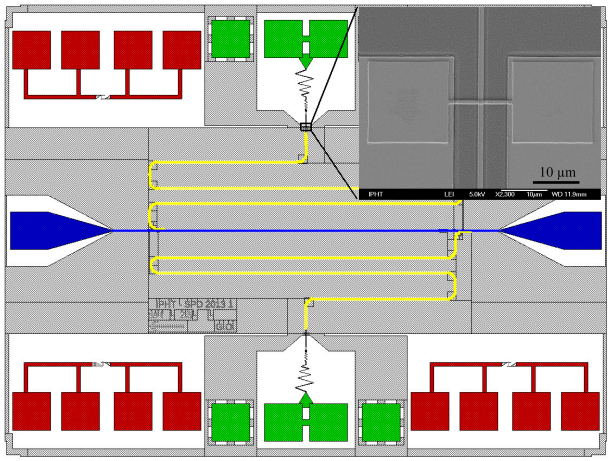

Figure 4.8: The 8×6 cm sized sample is displayed as a coloured design picture consisting of a central conduction line (blue), capacitively coupled to two $\lambda/4$ resonators (yellow). The resonators are shunted in their current antinodes via Josephson junctions as shown in the insert SEM image. Each junctions has four DC-connections (green) for current bias and voltage output. In the corners of the chip similar circuitry (red) are introduced to test and pre-calibrate the Josephson junctions.

base temperature of about 15 mK.

By measuring the transmission amplitude of the central waveguide at different frequencies, the two resonances are found at $\omega_1/2\pi = 2.506$ GHz and $\omega_2/2\pi = 2.44$ GHz with similar quality factors about 1000 and by applying a dc-bias current to the connected Josephson junction we are able to measure its resonance frequency ω_1 shift to lower values as expected for phase CBJJs. A microwave driving signal $V_{in} \sin \omega_p t$ in the waveguide with V_{in} the input voltage amplitude at the coupling capacitance yields a resonator driving amplitude of $\Omega_d = C_c V_{in} V_r / 2\hbar$ where $V_r = \sqrt{\hbar\omega_1 / C_E}$ the zero point voltage of the resonator. With this drive experiments can be performed by ramping the bias current. The switching behaviour is recorded with the switching current distributions as functions of the applied microwave frequency and amplitude similar to the calculated distributions of Sec. 4.1.

To detect a given amplitude of the rf-signal, the bias current must attain a specific value such that the additional rf-current suffices to switch the junction to the finite voltage state. Due to the non-linear Josephson inductance, this bias current shifts the resonator frequency, and hence the optimal input coupling is achieved at the shifted resonance condition of the resonator. When decreasing the frequency for the large amplitude driving, we obtain a standard deviation with a minimum, that lies below the one of the undisturbed junction. This is because the strong driving allows excitation directly into continuum representing the voltage stage in addition to the switching by tunnelling which is also discussed in [2, 3].

Finally, from the experimental data, we extract the dependence of the maximal shifts of the mean switching currents as function of the driving amplitude and corresponding photon number in the resonator, see Fig. 4.9. It should be emphasized that for the device to work as a detector of single photons, we need to tailor the design such that the maximal sensitivity appears at the frequency of the photons.

The upper panel of Fig. 4.9 displays a linear dependence of the maximal shift of the mean switching currents and the driving amplitude. This indicates that it is, indeed, not just resonance between the applied microwave and the qubit but rather the modulation of the junction potential by the rf-current in the coupled resonator and junction system that causes the voltage switching and leads to the detection as discussed in previous section.

The incident field leads to a reduction in the switching current, that we can measure with the uncertainty σ, which motivates the assignment of the sensitivity parameter, $S = (I_0 - I_1)/(\sigma + (I_0 - I_1))$ that we plot as function of the mean photon number $N = 4\Omega_d^2/\kappa^2$ [190] in the lower panel of Fig. 4.9. We find a reasonable value of 0.5 in the low photon limit. While a sensitivity of 0.5 does not hold any particular meaning by it self, we can understand a sensitivity of 0 as having no dependence of the input field, while a sensitivity of 1 as two switching distributions with no overlap and hence perfect distinction between field and no field. For clarification, the insert in the lower plot of Fig. 4.9 shows the shifted histogram of the switching currents at the lowest driving power in comparison to the undisturbed one. The presence of a driving signal shifts the distribution but due to the broad distribution we cannot distinguish the events in the overlap region.

Similarly, we can use the theory of developed in Sec. 4.2 to calculate the effective potential from which we can directly find a switching rate [191] both when applying a weak field and without any drive. Using these

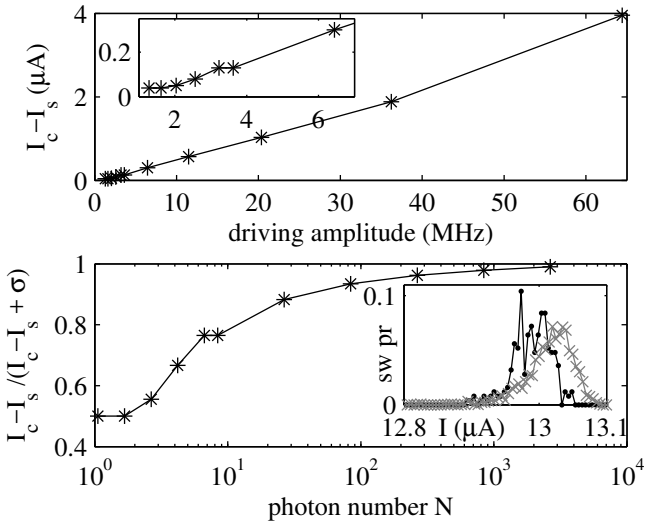

Figure 4.9: (Upper plot) Maximal shift of the mean switching current at different driving amplitudes. The insert shows a zoom of the region close to zero driving. (Lower plot) Reconstructed sensitivity of our detector as extracted maximal shift of the histograms divided by the shift plus the standard deviation of the switching current of the undisturbed junction. The insert shows the histograms maximal shifted histogram for the lowest applied driving power (black, dots) compared to the undisturbed histogram (grey, crosses).

rates we can calculate results equivalent as to the inset of Fig. 4.9. These theoretical calculations are shown in Fig. 4.10. While the theory produces a narrower distribution ($\sigma = 10$ nA) we find a behaviour that qualitative reproduces the experimental data and we calculate a sensitivity of 0.65 in the single photon regime. The broader distribution of the experiment is most likely due to the multi-mode structure of the resonator. In Sec. 4.2 we explicitly neglected higher modes as both the resonator and the CBJJ were far detuned from these. However, in the experiment, the CBJJ is also far detuned from the probed mode and, thus, we expect the CBJJ to interact equivalently with several modes. This effectively introduces another decay-channel of the resonator, not taken into account in the theory and leads to a broader switching distribution. More notably, we find that the theory directly reproduces a spiked structure of the switching current distribution

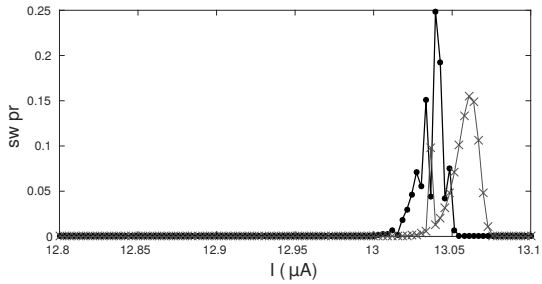

Figure 4.10: Theoretically calculated histograms for an average field in the combined resonator+CBJJ of a single photon coherent state (black, dots) compared to the undisturbed histogram (grey, crosses).

for the driven detector also seen in the inset of Fig. 4.9, which confirms that this structure indeed is related to the coupling between the resonator and the current-biased Josephson junction. The theory also predicts that for a device with smaller critical current we may achieve a higher sensitivity. The detection works also for strong microwave signals nicely and after a calibration at a fixed frequency detuning, we can conclude that the device can be used to infer the intensity of the drive signal.

4.4 Conclusion – and is this detector useful?

In conclusion, we developed the theory for a device, that may be used for the determination of classical field amplitudes in the microwave domain. Furthermore, a first experiment achieves a sensitivity of 0.5 in the single photon limit. This value is in agreement with the expected signal level of single photons and optimizing the design may improve this sensitivity. For example the width of the switching currents may be decreased as the values achieved in [184], and with these values a sensitivity of the order of unity can be expected at the single photon level, similar to the simulations in Sec. 4.2. Also the input coupling of the cavity may be optimized and the resonator can be matched to fit the impedance of standard transmission lines and thus avoid reflections, similarly to the experiment performed in [94]. In further experiments the usability of an optimized device as single photon detector can be tested.

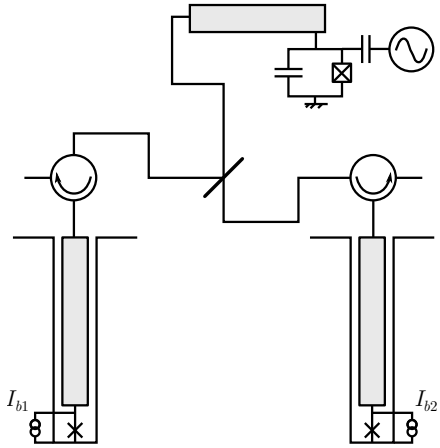

Figure 4.11: Measurement scheme using the current detector in a Hanbury Brown and Twiss type experiment. We have two detectors controlled by the bias currents I_{b1} and I_{b2}. The detectors are probed by the signal leaking from a low-Q cavity (in gray) coupled to a single qubit. The qubit is controlled by a coherent drive.

The current experiment do, however, have a few drawbacks compared to an all-purpose single photon detector in the microwave regime. As mentioned, the detector basically detects photons stored in the resonator and as such it only measure photons within a linewidth of the resonator frequency. As identified by the theory in Sec. 4.2, the resonators life time must be larger than the tunneling time of the CBJJ, set by the effective coupling of the resonator to the CBJJ. This imposes a Q-factor around 1000 to be minimal and thus the device will have a bandwidth of only a few MHz. This is however not so different from the bandwidth of quantum limited amplifier described in Sec. 2.4. A more detrimental drawback is the initialization time and the related dead time of the detector. The detector works by having the bias current slowly ramped up from 0. This ramping takes seconds in order to avoid non-adiabatic excitations in the CBJJ. Similarly, once the detector switches, it must be reset by setting the current back to 0 and waiting $\sim$ms for the quasiparticles to leave the CBJJ. This implies a very low repetition rate for experiments using this detector.

While the current experimental device is far from a perfect photon detector we may, however, consider setups where the present detector may be preferable to the homodyne or heterodyne detection schemes commonly used in circuit QED. Such an experiment could be a microwave analogy of a Hanbury Brown and Twiss (HBT) experiment [192]. In an HBT experiment, a source of light is split on a beam splitter and correlations between measurements of the two output fields reveals photon statistics of the input field. With photon detectors at the outputs, the two-time correlation function between the two signal is denoted $G^2(\tau) = \langle \mathcal{I}_1(t)\mathcal{I}_2(t-\tau)\rangle$, with $\mathcal{I}_i(t)$ being the intensity at detector i. Now, if the input field is a single photon field (as opposed to a coherent field) the correlation function vanishes for simultaneous detection, ie $G^2(0) = 0$, which would not be true for a coherent field. This effect for single photons is known as antibunching. A microwave analogy of such an experiment was performed in [193] using linear amplifiers and a heterodyne detection scheme. The linear signal does obviously not directly contain the signatures of antibunching, but recording many ($\sim 10^5$) time trajectories, statistics of the classical signals reveal the G^2-function of the single photons [73]. A similar experiment could be performed with this newly developed detector using a set-up presented in Fig. 4.11. Here a single qubit is driven with a weak drive while being coupled to a very lossy cavity. This leads to a fast Purcell decay of the single photons, which approach the beam splitter and enter into only one of the detectors. The circulators ensure that the single photons do not bounce back into the qubiit. Meanwhile, the biased current of both detectors is slowly ramped up as in the experiment presented in Sec. 3.2 and the joint switching current distribution $P_Q(I_{b1}, I_{b2})$ can be recorded. This should be compared $P_C(I_{b1}, I_{b2})$ recorded in an experiment with a coherent drive with a single photon on average instead of the single photon source. Similarly we have a joint distribution function $P_0(I_{b1}, I_{b2})$ measured with no input signal. Then we find the relation $G^2(0) \propto \langle (P_Q - P_0)/(P_C - P_0)\rangle_{I_{b1}=I_{b2}}$ and thus we can directly observe the antibunching of microwave photons, an effect that previously was only indirectly inferred [193]. However, due to the long initialization and dead times of the detector this, the measurement time to obtain sufficient data to calculate the G^2 function would still be comparable to the total time using linear detectors as in [193]. Therefore, the detector does not allow a more efficient way of obtaining non-classical photon statistic, but its merits lies in a more direct physical observation of the non-classical effects.

Chapter 5

Cryogenic devices for control in circuit QED

Recently, optical devices with in cavity QED have made a tremendous progress towards ultra-low-power all-optical logical elements [145, 194–200], all of which merits as impressive classical control elements and may become crucial for the control of quantum technologies in the optical domain. Similarly, implementations for quantum switches [201, 202] and single-microwave-photon transistors [203, 204] have been proposed for circuit QED, mimicking and even surpassing the progress realized with optics. A photonic device with few-photon memory states would also be able to temporarily store and process the classical read-out from quantum information experiments [121, 133, 205] and possibly use this classical information in feedback protocols. As discussed in Sec. 2.6, such cryogenic memory devices could potentially alleviate part of the the complicated stages of amplification to signal levels detectable outside the cryogenic environment and benefit, e.g., the application of error correction schemes such as the surface code [136]. In more developed quantum technologies the combination of low-power parallelizable Josephson based elements and classical microwave controllers and computers will naturally be employed side-by-side. As of now, however, only few-qubit systems are implemented and which technical difficulties will become most detrimental is not clear. Therefore, every new approach that possible reduce technical overhead is vital.

In this chapter we will investigate two ideas for a memory device built entirely using superconducting resonators and Josephson junctions.

First, we will focus on the use of a bifurcated Kerr-resonator as our classical memory and we will show that this device allows for efficient autonomous measurement based all-cryogenics feedback [7]. The second part will present an all-microwave flip-flop memory device [5] working using specially engineered qubit couplings.

5.1 Feedback control of a qubit with a Kerr resonator

In this section, we present a proposal [7] in which a nonlinear, superconducting microwave resonator [80] effectively reads-out and feeds back to a superconducting transmon qubit (here taken to be a 3d-transmon [46]). The nonlinear resonator acts like a Josephson bifurcation amplifier (JBA) [107, 108, 168] in that the circuit's Kerr-nonlinearity is driven and latches into one of two bistable states, depending on the state of the qubit and, thus, constitute a qubit measurement. However, the Kerr-resonator does not play the standard JBA role, as communicating this state to the room temperature equipment (and experimenters) is not critical. Rather, a state stored in the Kerr-resonator is fed back directly to implement conditional qubit operations. The bistable states of the Kerr resonator are now classical memory-states and may be maintained even if the qubit subsequently decays.

The control of a single qubit is, hardware-wise, not particularly burdensome, and as such, it is anticipated that natural advantages of control elements working within the cryogenic environment may be most practical in multi-qubit systems. However, since no general approach exists even for single qubit control within the cryogenic environment, two specific demonstrative cases in single qubit-control will be presented in this section, see also [7]. In the first case, the nonlinear controller is used to initialize the qubit in a definite eigenstate. And in the second case, the qubit's state is read into the controller's classical memory, where it is stored for an indefinite period of time, and then used to reinstate the measured state after the qubit has decayed.

5.1.1 Qualitative description of the scheme

The proposed setup is sketched in Fig. 5.1. The two critical components are a two-port Kerr-resonator [80] and a 3d-cavity containing a superconducting qubit [46]. These are interconnected via two transmission lines and a tee-

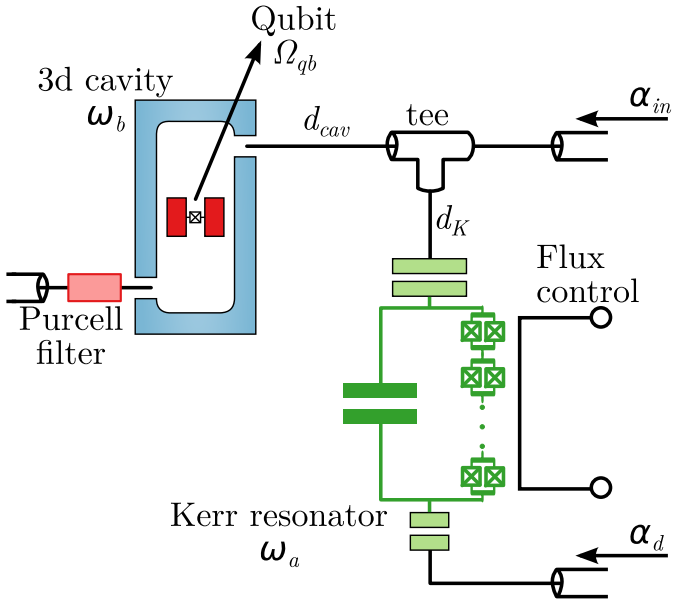

Figure 5.1: A qubit-cavity system is connected to a Kerr-resonator through a tee-junction. The qubit with a transition frequency Ω_{qb} is embedded in the 3d-cavity with a resonance at ω_b and the coupling port for the 3d-cavity is placed a distance d_{cav} from the tee-junction. The Kerr-resonator, which consists of an array of SQUIDs that allows for a tunable frequency ω_a, is placed a distance d_K from the tee-junction. The Kerr-resonator is driven by a strong drive α_d, while both the Kerr-resonator and the 3d-cavity are driven by the field α_{in}. Both drives are operated at the same frequency ω_d.

junction. The microwave network has three connections to the external environment. The two most important are the transmission lines emanating from the bottom, weakly coupled port of the Kerr-resonator, and from the tee-port. A less critical port from the 3d-cavity uses a Purcell filter [102–105] to control the photon number in the 3d-cavity and helps optimize performance. We will only discuss this port briefly as the essential scheme can be understood without it. Dynamical control of the network is achieved by two microwave drives, labelled by the incoming amplitudes α_d and α_{in}, and a flux control line that controls the center frequency of the Kerr-

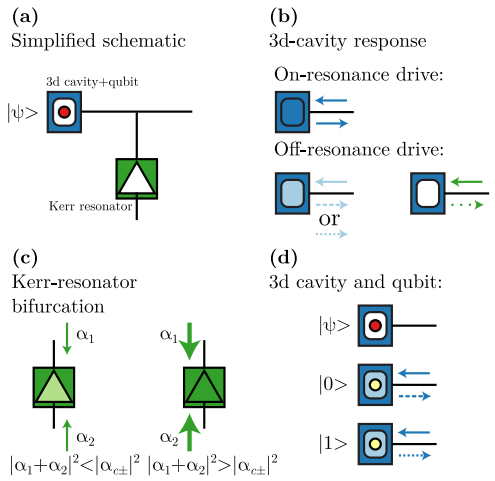

Figure 5.2: (a) A simplified schematic of Fig. 5.1. The rectangle with a rectangular cut-out represents the 3d-cavity, the circle the qubit (in state $|\psi\rangle$), and the rectangle with a triangle cut-out the Kerr-resonator. Object colors are coarse representations of the center frequency of each component. (b) An empty 3d-cavity is driven by a resonant microwave drive, microwave power is built up in the 3d-cavity, and the drive is reflected. When the same cavity is driven by a slightly-off- or far-off-resonant drive, less or no power is built up inside the cavity. The reflected signal will now have a phase that depends on the sign of the detuned incident field. (c) When the total power incident on the Kerr-resonator is sufficiently low the power built up is relatively low but increases disproportionally when a certain pair of critical powers, $|\alpha_{c\pm}|^2$, are exceeded. (d) The qubit inside the 3d-cavity will shift the center frequency of the cavity by a small, but significant amount. When the power is built up in the 3d-cavity, the center frequency of the qubit shifts proportionally.

resonator.

The basic operations that the network exploits are depicted schematically in Fig. 5.2. When a resonant mode, like an empty 3d-cavity in Fig. 5.2 (b), is driven by a slightly off-resonant microwave signal, microwave power builds up in the mode and the signal is reflected with a

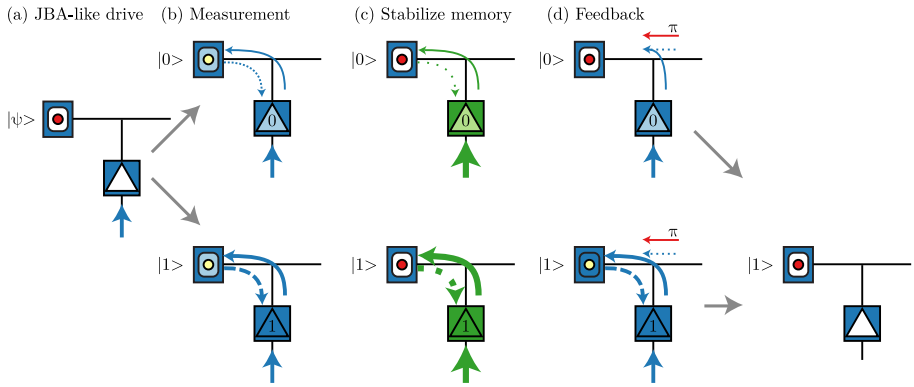

Figure 5.3: Protocol for measurement, classical memory storage, and feedback to a qubit. a) With the qubit in an initial state $|\psi\rangle$, the Kerr-resonator and drive are tuned to be co-resonant with the 3d-cavity (all three are colored blue). (b) Measurement operation as described in the text. (Note: the signal emitted by the Kerr-resonator is typically phase shifted as well, which we disregard in this section for simplicity.) (c) Stabilizing the classical memory state by tuning the Kerr-resonator and drive, and increasing drive power. (d) Using the classical memory state to apply a conditional π-pulse to the qubit, stabilizing it in the $|1\rangle$ state.

certain phase shift.

While the center frequency of the 3d-cavity is fixed, the Kerr-resonator's center frequency is highly dynamic. Firstly, applying an external flux bias through the Kerr-resonator's dc SQUIDs via the flux control line will shift the center frequency [80]. Secondly, the amount of power circulating inside the Kerr-resonator also decreases the center frequency. This power-induced shift is a highly non-linear function of the externally-applied near-resonant microwave drives (see also Sec. 2.4), and Fig. 5.2 (c) depicts the critical function for the purpose of this scheme. If the total incident power of red-detuned microwave drives is below a pair of detuning-dependent critical drive powers, $|\alpha_{c\pm}|^2$, the frequency shift will be negligible and little power is built up in the Kerr-resonator. If the incident power exceeds these critical values, though, the center frequency decreases significantly and it causes a stronger internal power to build up inside the resonator. If the incident power lies between the two critical values, the Kerr-resonator's

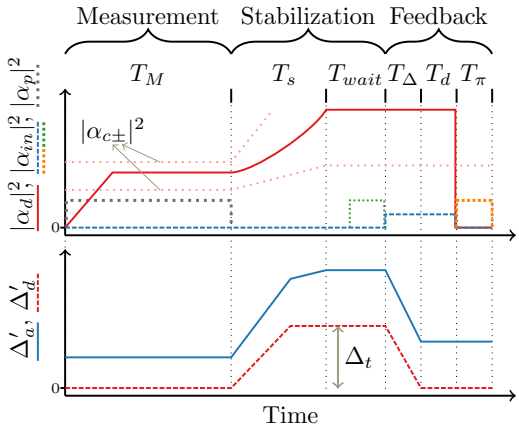

Figure 5.4: The upper panel sketches the power of the input drives, while the lower panel illustrates the detuning between the Kerr-resonator and the 3d-cavity, $\Delta'_a = \omega_a - \omega_b$ (solid blue line) and between the drive and the 3d-cavity $\Delta'_d = \omega_d - \omega_b$ (dashed red line). During the first time-step, T_M, we apply a measurement driven by α_d (solid red line) and an drive at the 3d-cavity, α_p (dashed gray line), which is followed by a stabilization time T_s, where the drive is changed far away from the critical input powers indicated by $\alpha_{c\pm}$ (thinly dotted light red line). Simultanously the Kerr-resonator and the input-drive are tuned away from the 3d-cavity by Δ_t. After a waiting time T_{wait}, we tune the Kerr-resonator back into resonance with the 3d-cavity. During T_Δ, α_{in} (dashed blue line) is applied to the upper port. Finally, a π-pulse (dotted orange and green (optional) lines) of duration T_π is applied.

center frequency and internal power are bistable and hysteric.

In Fig. 5.2 (d) we depict the inclusion of a qubit, which changes the behavior of the 3d-cavity. The qubit-cavity coupling is in the dispersive regime, as introduced in Sec. 2.3, which implies that the qubit state, either $|0\rangle$ or $|1\rangle$, shifts the center frequency of the 3d-cavity. Conversely, the center frequency of the qubit is shifted in proportion to the amount of power built up in the 3d cavity.

Figure 5.3 depicts a protocol that uses these functions to measure the qubit, store the result in a classical memory, and apply conditional feedback to stabilize the $|1\rangle$ state. In Fig. 5.3 (a), the qubit is initially in an arbitrary state $|\psi\rangle$, the Kerr-resonator is tuned using the flux control line to be near-resonant with the 3d-cavity, and the Kerr-resonator is driven through its bottom, weakly-coupled port. Some amount of drive power passes through the Kerr-resonator and drives the 3d-cavity, Fig. 5.3 (b). The signal reflected by the 3d-cavity is partially lost in the remaining tee-port (this loss is not depicted) and partially reflected back to the Kerr-resonator. The phase of this reflected signal depends on the qubit state and interferes with the Kerr-resonator drive. Specifically, a $|1\rangle$ ($|0\rangle$) qubit state will reflect a signal that interferes constructively (destructively) with the Kerr-resonator drive and pushes the total incident power above (below) the Kerr-resonators critical values. A disproportionally high (low) internal power then builds up in the Kerr-resonator. Thus, the Kerr resonator measures the qubit state and stores the result in its internal power level. A high or low power level represents a 1 or 0 classical "memory" state, respectively.

Figure 5.4 accompanies Fig. 5.3 and depicts the detunings and amplitudes of the external controls used in the protocol. The measurement of the qubit state occurs over a time T_M. During this interval, the Kerr resonator/3d-cavity detuning $\Delta_a' \equiv \omega_a - \omega_b$ is small, while the drive/3d-cavity detuning $\Delta_d' \equiv \omega_d - \omega_b$ is zero with ω_a, ω_b and ω_d as the frequency of the Kerr-resonator, the 3d-cavity and the drive respectively. Furthermore, we depict in Fig. 5.4 a drive applied at the Purcell-protected port, α_p, which adds additional signal of the qubit state to the Kerr-resonator but does not change the qualitative scheme depicted in Fig. 5.3. Also shown in Fig. 5.4 is the drive field of the Kerr-resonator, α_d, which is slowly increased to a value between the two critical values, α_c, between which the Kerr-resonator is bistable (see Sec. 2.4).

The memory state of the Kerr resonator can be protected against subsequent changes in the qubit state by increasing the drive power and detuning the drive frequency and Kerr-resonator center frequency in tandem, as indicated by the changed color in Fig. 5.3 (c). Although the phase of the drive reflected by the 3d-cavity is now almost independent of the qubit state, the total power incident on the Kerr-resonator remains relatively high or low depending on the most recent memory result. The classical memory state has been effectively stored and may be retained indefinitely. The external controls applied during stabilization is depicted in Fig. 5.4. First, during a stabilization time, T_s, the detuning of the Kerr-resonator and the drive

amplitude are increased, which further separates the two critical values. This ensures that neither fluctuations in the field nor subsequent qubit dynamics will induce changes in the classical memory state. To further decouple the classical memory from the qubit, the Kerr-resonator and drive are detuned from the 3d-cavity by a large amount, Δ_t simultaneously with the stabilization. At this point, the memory may be held for an extended time T_{wait}.

Finally, Fig. 5.3 (d) depicts how the qubit may be deterministically prepared in the $|1\rangle$ state, regardless of the initial state $|\psi\rangle$. The Kerr-resonator and drive are tuned back toward the 3d-cavity's frequency, resuming their values from the measurement step (Fig. 5.3 (b)). This is depicted in Fig. 5.4 in which the detunings are brought back to their original values. If the Kerr-resonator memory state is 0, the power incident on the 3d-cavity through the Kerr-resonator is weak and can be eliminated by superimposing it with another weak and phase shifted drive through the remaining tee-port, depicted in Fig. 5.3 (d) and by the dashed blue line in Fig. 5.4. In this case, no power is built up in the 3d-cavity and the qubit center frequency remains un-shifted. If the Kerr-resonator's memory state is 1, however, the drive incident on the 3d-cavity is relatively large and some power will build up in the cavity (despite the phase-shifted drive through the remaining tee-port) and shift the qubit center frequency. We are therefore left with a qubit whose center frequency is either shifted or not, depending on the classical memory state. If a third microwave pulse tuned to apply a π-rotation at the original qubit frequency is now applied at the tee-port (Fig. 5.3 (d) and the dotted orange line of duration T_π in Fig. 5.4), a $|0\rangle$ qubit will be rotated to $|1\rangle$, but a $|1\rangle$ qubit will be off-resonant and will remain in $|1\rangle$. Thus, a qubit in the $|1\rangle$ state is prepared deterministically.

The protocol closes an autonomous feedback loop at cryogenic temperatures but from the point of view of an operator at room temperature, it constitutes an open loop protocol, as was sought in Sec. 2.6. This is conceptually similar to quantum reservoir engineering schemes [130, 206–208], in the way that it changes the effective ground state and does not rely upon any conditional room temperature operations common to conventional feedback schemes [84, 131, 132]. The protocol, however, relies upon the performance of a coupling to a dissipative meter system and, thus, it falls conceptually in-between conventional feedback and quantum reservoir engineering schemes.

We can further demonstrate that the classical memory may be usefully retained for an arbitrary amount of time. For example, the setup proposed

here can return the classical state stored in the memory to the qubit, even after the qubit has undergone T_1 decay to $|0\rangle$ (and assuming no spontaneous excitation to $|1\rangle$ for demonstration purposes), i.e. $T_{wait} \gg T_1$. Just before we bring the Kerr-resonator back onto resonance, we apply a π-pulse on the bare qubit frequency bringing the qubit into the excited state, dotted green line in Fig. 5.4. After this pulse, we apply the same input field and tuning sequence as above. A resonant π-pulse will now prepare the qubit in the excited state if and only if that was the state measured earlier.

5.1.2 Quantitative analysis of the full system

The Kerr resonator may be implemented as an array of SQUIDs in parallel with a capacitance [80] (the description of such an array is similar to Chapter 3). The SQUIDs provide the inductance for the equivalent LC-circuit and they permit tuning of the resonance of the Kerr resonator by a magnetic flux. While a single SQUID provides a Kerr-nonlinear behavior, an array will dilute the non-linearity and allow a much higher photon number in the Kerr resonator [81]. The resonator loss rates associated with the two coupling capacitors in Fig. 5.1 are κ_d and κ_a and we assume a classical input field α_d coupled with strength $\sqrt{\kappa}_d$ to the resonator mode. In a frame rotating with the drive frequency, ω_d, the classical field amplitude in the resonator solves the non-linear equation,

$$\dot{\alpha} = -i\Delta_a\alpha - iK|\alpha|^2\alpha - \frac{\kappa_a + \kappa_d}{2}\alpha - \sqrt{\kappa_d}\alpha_d, \tag{5.1}$$

where K denotes the Kerr-nonlinearity, which originates from the non-linear inductance of the SQUID-array. The equation's steady state was solved in Sec. 2.4 and yields the critical photon numbers $n_{c\pm} = |\alpha_{c\pm}|^2$,

$$n_{c\pm} = -\frac{2\Delta_a K}{3K^2}\left(1 \mp \sqrt{1 - \frac{3(\Delta_a^2 + (\kappa_a + \kappa_d)^2/4)}{4\Delta_a^2}}\right), \tag{5.2}$$

also shown in Eq. (2.64). In the bistable regime, the Kerr-resonator will latch into one of the two stable solutions and a small perturbation in the initial conditions can determine which one. The Kerr resonator will even remain in this state when the perturbation is switched off. In our case, the perturbation is introduced in the upper input port to the Kerr-resonator from the 3d-cavity controlled by the qubit state in Fig. 5.1.

The Kerr-resonator and the qubit in the 3d-cavity are described by the Hamiltonians [67, 81]:

$$H_K = \hbar\omega_a a^\dagger a + \hbar\frac{K}{2}a^\dagger a a^\dagger a, \tag{5.3}$$

$$H_{cav} = \hbar\omega_b b^\dagger b + \hbar\frac{\Omega_{qb}}{2}\sigma_z + \hbar\chi\, b^\dagger b\,\sigma_z, \tag{5.4}$$

with resonator eigenfrequencies $\omega_{a,b}$, a qubit frequency Ω_{qb} and a dispersive interaction between the qubit and the 3d-cavity field with the strength χ. Here σ_z denotes the qubit operator such that $\sigma_z|1\rangle = |1\rangle$ and $\sigma_z|0\rangle = -|0\rangle$. The operators a ($a^\dagger$) and b ($b^\dagger$) describes the annihilation (creation) operators for the Kerr-resonator and the 3d-cavity respectively.

The Kerr-resonator and the qubit-cavity are connected by one-dimensional waveguides. The position dependent phase operator, $\phi(x,t)$, (time integral of the voltage) and charge density, $q(x,t)$, along the waveguides obey wave-equations and they can be expanded on left and right propagating wave solutions [209, 210],

$$\overleftrightarrow{\phi}(x,t) = \sqrt{\frac{\hbar Z_0}{4\pi}}\int_0^\infty \frac{d\omega}{\sqrt{\omega}}\overleftrightarrow{a}_\omega e^{-i(\omega t \pm k_\omega x)} + h.c. \tag{5.5}$$

$$\overleftrightarrow{q}(x,t) = -i\sqrt{\frac{\hbar Z_0}{4\pi}}\int_0^\infty d\omega\,\sqrt{\omega}\,\overleftrightarrow{a}_\omega e^{-i(\omega t \pm k_\omega x)} + h.c. \tag{5.6}$$

such that

$$\phi(x,t) = \overleftarrow{\phi}(x,t) + \overrightarrow{\phi}(x,t). \tag{5.7}$$

In the above equations we have assumed that the wave-guide impedance Z_0 is constant and the same for all lines. We choose the origin of the position variable to be at the tee-junction. The left (right) arrow denotes the field moving towards (away from) the 3d-cavity and down (up) towards (away from) the Kerr-resonator.

The waveguides are joined by a tee-junction, and Kirchoff's equations yield [106]

$$\phi_{out}(t) = \frac{1}{3}\phi_{in}(t) + \frac{2}{3}\overrightarrow{\phi}_K(0,t) + \frac{2}{3}\overrightarrow{\phi}_{cav}(0,t) \tag{5.8}$$

for the reflected component, ϕ_{out}, in terms of the waves incident on the junction, ϕ_{in}. Now $\phi_{out}(t)$ depends, in particular, on the fields from the Kerr-resonator, $\overrightarrow{\phi}_K$, and from the 3d-cavity, $\overrightarrow{\phi}_{cav}$.

Let q_b denote the charge degree of freedom at the 3d-cavity and similarly let q_a denote the charge at the Kerr-resonator, such that we obtain the boundary conditions [209]

$$\vec{\phi}_K(d_K, t) = \overleftarrow{\phi}_K(d_K, t) + Z_0 \beta_a q_a(t), \tag{5.9}$$

$$\vec{\phi}_{cav}(d_{cav}, t) = \overleftarrow{\phi}_{cav}(d_{cav}, t) + Z_0 \beta_b q_b(t), \tag{5.10}$$

where d_K and d_{cav} denote the lengths of the waveguides from the junction to the Kerr-resonator and the 3D cavity respectively. The quantities β_a and β_b are unit-less geometric constants that depend on the relation between the effective coupling capacitance and the total capacitance of each subsystem. The charge variables q_a and q_b, are given by the cavity mode operators $(a, a^\dagger)$ and $(b, b^\dagger)$, respectively. Through the so-called black-box quantization [67] we assume the Hamiltonian of the qubit-cavity system to be of the form Eq. (5.4). Following this description, q_b now also includes a contribution from the qubit and this exactly leads to the well-known Purcell-decay of the qubit. We will omit the qubit dynamics for now, but it will be considered in Sec. 5.1.3.

An input-output relation similar to Eq. (5.10) can also be written for the lower output port of the 3d-cavity shown in Fig 5.1. However, unlike the upper port, we will attach a Purcell filter to the output port. The sole purpose of this additional decay-channel for the 3d-cavity is to allow a very strong interaction between the Kerr-resonator and the 3d-cavity without exciting the 3d-cavity beyond the dispersive regime [211]. The extra cavity decay does therefore not by itself improve the qubit readout, but it allows for a much stronger coupling between the Kerr-resonator and the 3d-cavity. So as long as the total decay rate of the 3d-cavity remains in the same order of magnitude as the dispersive coupling to the qubit, we can increase the coupling to the Kerr-resonator by increasing the decay through the Purcell-fitered channel by the same amount.

We will assume a narrow frequency band of the travelling fields, $k_\omega \approx k$, and we restrict the analysis to the situation of wave propagation times much shorter than other dynamical time scales of the systems. This allows elimination of the wave-guide observables, $\phi(x, t)$ and $q(x, t)$, and we obtain

the Heisenberg-Langevin equations for the a and b operators

$$\begin{aligned}\dot{a} &= -i\omega_a a - iKa^\dagger aa - \frac{\kappa_a+\kappa_d}{2}a \\ &\quad + \sqrt{\kappa_a\kappa_b}be^{i(\phi_b-\phi_a)} - \sqrt{\kappa_a}a_{in}e^{-i\phi_a} - \sqrt{\kappa_d}a_d, \qquad (5.11)\\ \dot{b} &= -i\omega_b b - i\chi\sigma_z b - \frac{\kappa_b+\kappa_p}{2}b \\ &\quad + \sqrt{\kappa_a\kappa_b}ae^{i(\phi_a-\phi_b)} - \sqrt{\kappa_b}a_{in}e^{-i\phi_b} - \sqrt{\kappa_p}a_p. \qquad (5.12)\end{aligned}$$

where the 3d-cavity and the Kerr resonator are coupled with the strength $\sqrt{\kappa_a\kappa_b}$. In Eqs. (5.11) and (5.12), we have also included an extra input and decay channel for the Kerr resonator corresponding to the lower input port of Fig.1 and for the 3d-cavity through the upper port (κ_b) and the Purcell filtered lower port (κ_p). The operators a_{in} and a_d are the input field operators, while the phases $\phi_a = d_K k$ and $\phi_b = d_{cav}k$ come from the propagation through the transmission lines to the Kerr-resonator and the 3d-cavity.

Having Eqs. (5.11) and (5.12) we can in principle solve the full dynamics of the system, but since a and b are operators and the mean value of a might be on the order of $\sim$10, we would need to expand the Hilbert space on a large number of Fock states to solve the full quantum dynamics. We, therefore, employ a stochastic mean-field description by making the c-number substitutions:

$$\begin{aligned} a &\to \alpha e^{-i\omega_d t}, & b &\to \beta e^{-i\omega_d t},\\ a_{in} &\to \alpha_{in} e^{-i\omega_d t}, & a_d &\to \alpha_d e^{-i\omega_d t},\\ a_p &\to \alpha_p\, e^{-i\omega_d t}, & \sigma_z &\to \langle\sigma_z\rangle. \end{aligned}$$

For convenience we have transformed our equations to a frame rotating at the frequency of the external drive, ω_d, which will make the detunings $\Delta_a = \omega_a - \omega_d$ and $\Delta_b = \omega_b - \omega_d$ appear in the equations of motion. We can make the complex field variables represent random samplings of the quantum Wigner quasiprobability distributions if we include stochastic terms, representing the quantum noise associated with the dissipation terms in (5.11) and (5.12), [72].

Following the prescription in [72], we obtain fluctuating complex noise

contributions

$$\xi_a(t) = \sqrt{\frac{1}{2}(\kappa_a+\kappa_d)(\bar{N}+\frac{1}{2})}dW_{a,1} + i\sqrt{\frac{1}{2}(\kappa_a+\kappa_d)(\bar{N}+\frac{1}{2})}dW_{a,2}, \tag{5.13}$$

$$\xi_b(t) = \sqrt{\frac{1}{2}(\kappa_b+\kappa_p)(\bar{N}+\frac{1}{2})}dW_{b,1} + i\sqrt{\frac{1}{2}(\kappa_b+\kappa_p)(\bar{N}+\frac{1}{2})}dW_{b,2}, \tag{5.14}$$

where $dW_{i,n}$ denote independent Wiener processes with $\langle dW_{i,n}\rangle = 0$ and $\langle dW_{i,n}^2\rangle = dt$ and $\bar{N}$ is the mean photon number in the thermal bath coupled to the resonators.

Adding these terms to the deterministic mean value equations, we obtain the equations of motion for α and β,

$$\begin{aligned}\dot{\alpha} = &-i\Delta_a\alpha - iK|\alpha|^2\alpha - \frac{\kappa_a+\kappa_d}{2}\alpha + \sqrt{\kappa_a\kappa_b}\beta e^{i(\theta_b-\theta_a)} \\ &- \sqrt{\kappa_a}\alpha_{in}e^{-i\theta_a} - \sqrt{\kappa_d}\alpha_d + \xi_a(t),\end{aligned} \tag{5.15}$$

$$\begin{aligned}\dot{\beta} = &-i\Delta_b\beta - i\chi\langle\sigma_z\rangle\beta - \frac{\kappa_b+\kappa_p}{2}\beta + \sqrt{\kappa_a\kappa_b}\alpha e^{i(\theta_a-\theta_b)} \\ &- \sqrt{\kappa_b}\alpha_{in}e^{-i\theta_b} - \sqrt{\kappa_p}\alpha_p + \xi_b(t),\end{aligned} \tag{5.16}$$

The replacement of the full quantum operator equations by noisy mean field equations has been succesfully applied in a wide range of quantum optics problems, and due to the weak Kerr non-linearity we expect this description to correctly describe the mean value of the resonator field as long as the qubit is in one of the eigenstates of σ_z. We refer to [145] and Sec. 3.1 for a recent comparison of full quantum and noisy mean field calculations. Since we operate in the regime of $K \ll \kappa$, we find that the mean field approach only fails very close to the bifurcation point.

As one sees from Eq. (5.16), the qubit state influences the driving of the 3d-cavity, which in turn affects the driving of the Kerr-resonator. In the regime where the qubit-dependent feedback drives the Kerr-resonator into two different stable states, this will lead to a projective measurement of the qubit, and storage of the outcome in the Kerr-resonator. The tunability of both Δ_a, α_d and α_{in} now enables the implementation of the schemes described above.

5.1.3 Numerical simulations

So far we have treated the qubit as a semi-classical object with two states, $|0\rangle$ and $|1\rangle$, each of which shifts the frequency of the 3d-cavity. In reality

the qubit is described by the quantum mechanical density matrix, $\rho_{qb} = \sum_{i,j=0,1} \rho_{i,j}|i\rangle\langle j|$, and its dynamics are described by a master equation.

However, we choose to describe the Kerr-resonator as well as the 3d-cavity by stochastic complex fields, where a single trajectory is determined by the particular instance of $dW(t)$ restricting ourselves to classical-like states. Similarly we can unravel the master equation for the qubit into a non-Hermitian Schrödinger equation [101, 212]

$$\frac{d}{dt}|\psi\rangle = -i\frac{\Delta_{qb} + 2\chi|\beta|^2}{2}\sigma_z|\psi\rangle - \frac{\gamma}{2}|1\rangle\langle 1|\,|\psi\rangle + (\Omega_d(t)\sigma_+ + \Omega_d^*(t)\sigma_-)|\psi\rangle, \tag{5.17}$$

where $\Delta_{qb} = \Omega_{qb} - \omega_d$ and $\Omega_d(t)$ describe a drive at the qubit frequency. The non-Hermitian Schrödinger equation is designed such that the norm of the wavefunction, $|\psi\rangle$ decays, due to the excited state decay rate $\gamma = 1/T_1$. When the norm becomes smaller than a random number R, drawn uniformly between 0 and 1, we apply the jump operator σ_- to the state and then we renormalize $|\psi\rangle$. This procedure reproduces the average density matrix evolution of the qubit.

A superposition state of the qubit generally yields expectation values $\langle\sigma_z\rangle = \langle\psi|\sigma_z|\psi\rangle$ that differ from the eigenvalues ± 1, but after the bifurcation readout of the qubit, we expect the state of the coupled system to be in a completely mixed state with different field states pertaining to the excited and ground state qubit, $\rho = P_0|0\rangle\langle 0| \otimes \rho_{a,0} + P_1|1\rangle\langle 1| \otimes \rho_{a,1}$, with $\rho_{a,0\,(1)}$ being the 0 (1) memory state of the Kerr-resonator. Here P_n denote the probabilities for the qubit to be in state 0 and 1, and due to the QND interaction, these probabilities do not change during the readout. Thus, we can simulate the two classical qubit cases separately, and on average generate the full master equation evolution.

Now, we can investigate the performance of the proposed scheme by numerically solving Eqs. (5.15), (5.16) and (5.17), but with the qubit in an eigenstate as described above leaving $\langle\sigma_z\rangle = \pm 1$. For the numerical simulation we need realistic parameters, so we choose a detuning between the qubit and the resonator at $\Delta_{qb} = 2\pi \times 1.2$ GHz. Furthermore we assume that the coupling between the two systems are at $g = 2\pi \times 122$ MHz, which yields a dispersive shift at $\chi = g^2 E_c/(\hbar\Delta_{qb}(\Delta_{qb} - E_c/\hbar)) = 2\pi \times -2.5$ MHz [42] with the anharmonicity of the qubit given by $E_c/\hbar = 2\pi \times 300$ MHz. We set the decay-rate for the 3d-cavity to $\kappa_b = 2\pi \times 1$ MHz and $\kappa_p = 2\pi \times 4$ MHz. For the Kerr-resonator we assume $K = 2\pi \times (-0.4)$ MHz, $\kappa_a = 2\pi \times 5$ MHz and $\kappa_d = 2\pi \times 0.3$ MHz with a detuning of the center frequency from

the drive initially at $\Delta_a = 3.5 \times (\kappa_a + \kappa_d)$. Finally, for the qubit we assume the intrinsic decay-rate $\gamma_{qb} = 2\pi \times 5$ kHz and from the cavity we get an additional Purcell-rate of $\gamma_p = \kappa_b \frac{g^2}{\Delta_{qb}^2}$, which yields $\gamma = \gamma_{qb} + \gamma_p = 2\pi \times 15.3$ kHz corresponding to a qubit lifetime of $T_1 = 10$ μs.

For the bifurcation readout our goal is a large difference in the Kerr-resonator photon number conditioned upon the qubit state. We find that a measurement time of $T_M = 400$ ns is sufficient to obtain a significant difference between the signals for the different qubit states compared to the noise of the input field. A shorter measurement time would be dominated by noise and yield a poor readout fidelity. During the first 80 ns, we slowly increase the drive towards $\alpha_d = 33.02\sqrt{\kappa_d}$, which is just below the larger $\alpha_{c\pm}$. The Purcell protected port was driven by $\sqrt{\kappa_p}\alpha_p/(2\pi i) = 8$ MHz, with the i indicating a $\pi/2$-phase shift of the drive compared to the rest of the drives. The next step is the stabilization where we linearly increase Δ_a by a factor of 1.7 and α_d by a factor of 1.8. This increases the difference in amplitude between the two critical drives of the Kerr resonator and puts α_d further away from both – as a consequence the probability of a spontaneous jump between the two solutions vanishes. To ensure that we remain on the right branch of the bifurcation curve T_s cannot be too small and we choose $T_s = 150$ ns. The stabilization time T_s might be chosen smaller if we apply a non-linear tuning scheme for Δ_a and α_d, but with the linear increase we numerically find that smaller times introduce significant errors.

The next step is the frequency tuning of the Kerr-resonator along with the drive. To ensure that we are indeed very far-detuned from the 3d-cavity after the detuning, we choose $\Delta_t = 2\pi \times 30$ MHz and to avoid exciting the Kerr-resonator while tuning the frequency, we cannot exceed $d\Delta_a/dt = \kappa/\frac{1}{\kappa}$, with $\kappa = \kappa_a + \kappa_d$. This limits the detuning time to $T_\Delta = 100$ ns. This detuning between the Kerr-resonator and the 3d-cavity is also occurring during T_s simultaneous with the increase in Δ_a (see Fig. 5.4). The waiting time T_{wait} can be chosen according to our applications. We then wait for a driving time $T_d = 15$ ns before the π-pulse with Rabi-frequency $\Omega_d = 2\pi \times 7$ MHz and $T_\pi = \pi/(2\Omega_d) = 35.7$ ns.

State preparation and stabilization

For the state preparation scheme we want to have the waiting time, T_{wait}, as small as possible in order to quickly initialize the state into the excited state. Since $1/(\kappa_b + \kappa_p) = 31$ ns, the 3d-cavity is (almost) empty after the

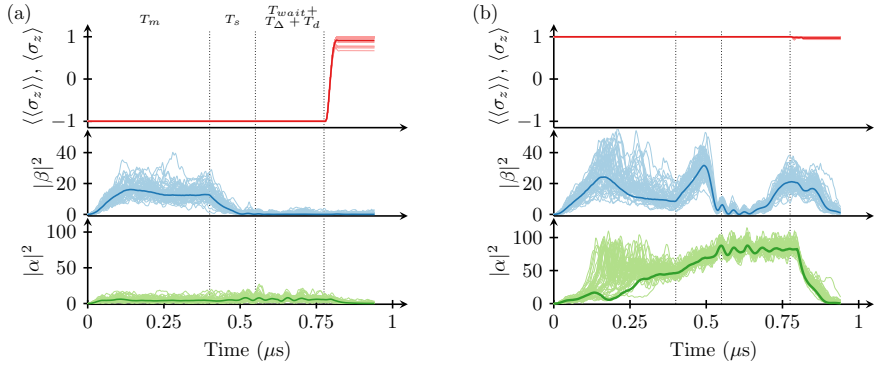

Figure 5.5: Numerical simulations of the state preparation with parameters described in the text without qubit decay. In (a) we start with the qubit in $|0\rangle$ and bring the state into $|1\rangle$ with 95.7% fidelity while in (b) we start with the qubit in the $|1\rangle$-state, where it remains with 98.5% fidelity. The upper panel of each figure displays the mean value of σ_z, the middle panel displays the photon population in the 3d-cavity and the lower panel the population in the Kerr-resonator. In each panel we plot both the mean values for 50 trajectories (thin lines) and the average over 200 trajectories (thick line). The vertical dotted lines indicate the different time intervals similar to Fig. 5.4 and explained in the text.

two tuning steps, so we can choose a very small waiting time $T_{wait} = 25$ ns. After T_{wait} we tune the resonator and drive frequency back again and we also apply the input field α_{in}, which is of equal amplitude but opposite phase of the 0 state of the Kerr-resonator obtained when the qubit was measured to be in its ground state. When we are back on resonance such that $\omega_d = \omega_b$, we apply the π-pulse and we obtain numerically a pulse fidelity of 98%. The imperfection arises from the field fluctuations in the 3d-cavity and due to the fluctuating field emitted from the Kerr-resonator. These fluctuations are the same fluctuations that limit the readout fidelity. We apply square π-pulses in our simulations, and a study of pulse-shaping is beyond the scope of the present work, but we note that more elaborate pulse shapes may prevent leakage of population into higher excited states of the weakly anharmonic transmon qubits [115] and to mitigate some

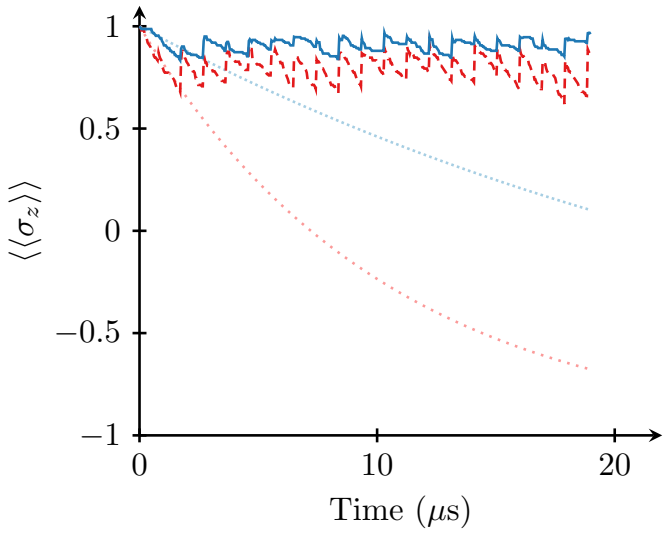

Figure 5.6: Stabilization of the qubit by running the same scheme as in Fig. 5.5 but 20 times after each other. The parameters are all listed in the text. The dashed (red) line is the average of 400 trajectories, while the dotted (light red) line is an exponential Purcell-enhanced decay with the decay-rate of the qubit, $1/\gamma = 10$ μs. The solid (blue) curve shows the same but with a decay-rate of $1/\gamma = 30$ μs acheived with an additional Purcell-filter as explained in the text and the densely dotted (light blue) curve shows the corresponding exponential decay.

types of quantum fluctuations [213].

In Fig. 5.5 we show the evolution of $|\beta|^2$ and from the numerical simulation we achieve $|\beta|^2 \approx 0.5 n_{crit}$ during the readout, where $n_{crit} = \Delta^2/(4g^2)$ is the critical photon number at which the dispersive regime breaks down [211]. The effective detuning of the qubit due to higher order effects is reduced by around 10% at $0.5 n_{crit}$ (included in numerical calculations). We cannot improve the scheme by increasing the drive power, as we are already close to the maximum photon number where the dispersive coupling offers a valid description. We even notice that just after the bifurcation, the photon number is momentarily increased beyond

the dispersive regime. While this is not important for the readout since we have already transferred the state to the resonator, we need to take into account the so-called dressed dephasing [71] (see also Sec. 2.2), which adds an additional decoherence channel for the qubit proportional to the photon number in the 3d-cavity. This effect will effectively decrease the lifetime of the qubit state and since the typical time where each trajectory remains above n_{crit} is 25 ns, we expect a 1%-2% additional error from the additional dephasing. In [71] it is also shown that above a saturation point around $0.5n_{crit}$, dispersive readout cannot be improved, however higher power leads to a faster bifurcation and more stability of the bifurcated states, so the optimal power of our scheme is expected to be much higher than just the optimal power for pure dispersive readout. If there is still a demand for lower photon number, around $0.1\text{-}0.2n_{crit}$, our scheme will still work, but with a fidelity of only around 85%-90%.

Figure 5.5 demonstrates the ability of our scheme to deterministically prepare the qubit in the exited state from any unknown state. For simplicity we have not included qubit decay in these simulations. Starting in the excited state yields a succes probability of 98.1% and if the qubit starts in the ground start we achieve a success probability of 96.1%. The error originates partly from the imperfect π-pulse and partly from the fact that the readout-fidelity is only around 98%.

Qubit decay is included with a finite qubit lifetimes of 10 μs (red line) and 30 μs (blue line) in the simulations shown for 20 runs in Fig. 5.6 with the same parameters as in Fig. 5.5. The time averaged state fidelity is 89.9% and it can be increased to 93.5% by averaging only at the instants of the protocol, where the preparation scheme is completed and the fidelity is known to be highest. The main limitation for the stabilization is the assumed qubit lifetime. For example, installing an additional Purcell-filter on the upper output port (possibly between the 3d-cavity and the tee-junction) increases the qubit lifetime to around 30 μs and leads to an average fidelity with the excited state of 95.4% (and 96.8% by only averaging after each protocol ends) in our calculations.

Qubit readout and memory

To demonstrate that the classical memory state can be stored and reused in a feedback scheme at a later point in time, we will bring back the measured qubit state after a very long time. This scheme relies upon qubit decay into the ground state, but in practice qubits within a 3d-cavity tend to have a residual thermal excited-state population beyond what is expected

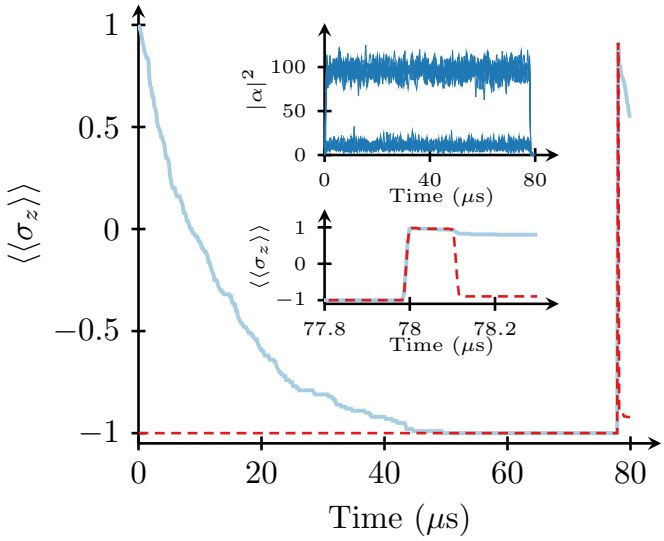

Figure 5.7: Demonstration of the memory recovery scheme with parameters described in the text. The main figure shows the mean value of the qubit operator σ_z averaged over 200 trajectories for each. The solid light blue line assumes $|1\rangle$ as the initial state, while the dashed red line starts in $|0\rangle$. The π-pulse is applied after 78 μs, where we obtain a fidelity with the original state of 98.6% for $|1\rangle$ and 96.0% for $|0\rangle$. The upper inset shows Kerr-resonator excitations for 20 randomly chosen realizations and we see two clearly distinct stable states. The lower inset displays a zoom of the region around the recovery of the state.

from the cryogenic temperature [214]. This analysis is thus an idealisation to demonstrate the memory properties of the Kerr-resonator. We now apply a very long T_{wait}, and just before applying the tuning sequence, we apply a π-pulse to bring the qubit into the excited state. The final steps are then the same as in the state-preparation scheme. We have chosen T_{wait}, such that we start the tuning after 78 μs. In Fig. 5.7 we illustrate the performance of this memory scheme. From 400 trajectories, we obtain a fidelity for reading out $|1\rangle$ and bringing the qubit back into

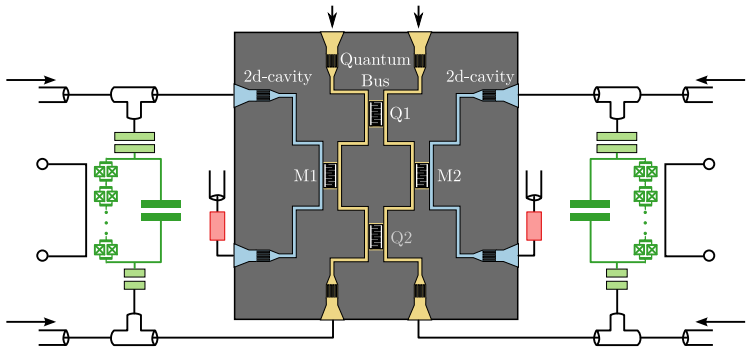

Figure 5.8: Schematics to stabilize a Bell-state. The circuit components are the same as in Fig. 5.1, but instead of 3d-cavities, we use waveguides on a 2d-chip. The state of interest is encoded into the data qubits, Q1 and Q2, while M1 and M2 are measurement qubits and they serve the same purpose as the qubit in Fig. 5.1. To perform the stabilization of Q1 and Q2, we apply quantum gates between these and M1 and M2. This can be achieved through the two quantum buses (in yellow). Control channels from the Kerr-resonators to each quantum bus allow the feedback to correct errors in the data qubits.

$|1\rangle$ of 98.6%, consistent with the state preparation scheme for the excited state. Similarly for $|0\rangle$ we find a fidelity of 96.0%. The memory scheme is limited by the imperfect π-pulses as discussed in the previous subsection, thus we have a smaller fidelity for the $|0\rangle$ state. There is also a small ($<$1%) remnant excitation from the qubit after T_{wait}.

5.1.4 A short outlook: Multi qubit feedback

We have proposed a new type of feedback scheme that aims at closing the feedback loop within the cryogenic environment of circuit QED experiments using Kerr-resonator to a 3d-cavity connected with a qubit. The goal is to control the qubit without having any knowledge of the qubit state outside the cryostat. As an application of this type of feedback we have simulated three applications with experimentally realistic parameters, but all these results are only single qubit applications. It is natural to extend the system to include more qubits or more resonators. For example, to

mitigate the need for qubit dissipation for the reinitialization protocol described in Sec 5.1.3 and to suppress residual qubit excitation, a second Kerr-resonator can be used to prepare the qubit in the ground state, just before the memory state, stored in the first Kerr-resonator, is fed back to the qubit.

Moreover, controlling many qubits with closed feedback outside of the cryogenic environment poses a significant challenge [134] as discussed in Sec. 2.6. For systems with 1000 qubits or more, reading out all at once may be infeasible even with state-of-the-art multi-channel analyzers. Therefore, the initialization of all qubits may seem an overwhelming task. In contrast, the all-cryogenic state-preparation presented in this work is inherently parallel, as each qubit has it own memory that holds the measured qubit state and autonomously controls the input state. The only additional requirement to prepare any number of qubit in, e.g., the ground state is that enough power is provided and appropriate power dividers are installed to drive all qubits sytems.

A more elaborate extension allows stabilization of e.g. a Bell-state of two qubits against phase-flip and bit-flip errors using a quantum error correcting code. A possible setup for this employs two data qubits in which the Bell-state is encoded and two additional measurement qubits to detect the errors. Performing two-qubit gates between the data and the measurement qubits, see Sec. 2.5, followed by a readout of the two measurement qubits will detect any errors in the encoded state [133, 136]. A subsequent feedback on the data qubit will stabilize the state. In Fig. 5.8 we have sketched how such a scheme might be implemented using a 2d-chip with multiple qubits [205]. Two units, each consisting of a Kerr-resonator, a 2d-cavity and a measurement qubit, allow us to perform the desired two-qubit gates and the additional coupling between the quantum buses and the Kerr-resonators will be sufficient to effectively stabilize the desired Bell-state in a completely autonomous manner. Extending this scheme to a seven qubit code is in principle possible and would allow autonomous stabilization of any logical qubit state with a limited amount of external control lines.

This Bell-state stabilization represents a minimal implementation of the so-called surface code [136]. In general, the surface code can be extended to any number of qubits, and the outcome of the measurements identifies whether an error occurred or not at a given point in the code. If an error is found, it is not necessary to correct it immediately, but errors can be tracked and corrected at the end of the full protocol [136].

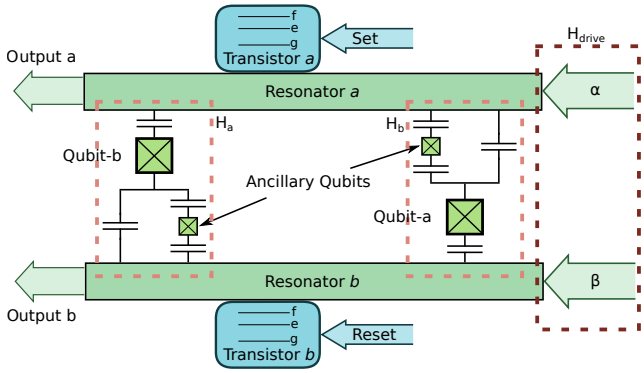

Figure 5.9: We schematically illustrate a system with coupled qubits and microwave resonators implementing the Hamiltonians described in the text. Qubit-a and qubit-b are resonant with microwave resonators a and b, respectively. The states of the two ancialla qubits in the set-up adiabatically follow the states of the resonators and qubits-a an -b, and mediate the desired coupling between the systems. The classically driven resonators are coupled to the e-f transitions of three-level transmons. When Set- and Reset-signals are applied on the g-e transitions, the transmons serve as transistors and control the resonator field.

5.2 All-microwave flip flop memory in the single photon regime

The previous section considered using a Kerr-resonator as a simple classical memory. The Kerr-resonator does, however, not compose a logical memory as such, since there is no direct way of switching the memory state. While this could be circumvented by using a more elaborate setup [143], here we will go beyond the use of bistable Kerr-resonators. The aim is to engineer a classical Set-Reset flip-flop system, which is the simplest possible memory system, using few Josephson junctions and linear resonators. The Set-Reset flip-flop consists of two inputs and two outputs and the output logical states depend on the history of input signals: When a signal pulse arrives at Set the a-output is set to 0 and the b-output is set to 1, until a signal pulse arrives at Reset, and the a-output is set to 1 and the b-output is set to 0. The switching between the logical states of a qubit implements a

microscopic flip-flop-device and Refs. [198, 204, 215] propose to extend the qubit to a three-level system constituting a photonic transistor for the field modes and thus implementing a few photon input and output device. Superconducting qubits are, however, hampered by fast relaxation and logical memories that rely on qubit-states coupled to microwave-field modes are currently limited to memory times on the order of 10 μs. This suggests to investigate the use of more complex systems of coupled superconducting components. Therefore, we aim for a classical flip-flop memory device that may be controlled by ultra-weak, few-photon microwave pulses, and to this end we shall apply a combination of microwave resonators and qubits and obtain memory lifetimes much longer than the ones of the individual components.

5.2.1 Description of the device

Our goal is to create a flip-flop system, where the two logical memory states are associated with the coherent excitation of one or the other of two weakly driven microwave resonators. A damped cavity subject to continuous driving assumes a coherent steady state excitation (see Sec. 2.1), and using the framework and properties of existing components in circuit QED, we propose in Fig. 5.9 a bistable device that switches between such states when subject to few-photon Set and Reset pulses. The essential mechanism controlling the coherent state amplitudes in the resonators is the frequency shift or splitting of the resonator modes when they are coupled to two- and three-level systems.

In Fig. 5.9, two three-level transmons, ta and tb, are shown in the top and bottom of the figure. They are strongly coupled to microwave resonators with resonance frequencies ω_a, ω_b via their first and second excited (e, f) states, while the transition between the ground (g) and first excited states is reserved for control by external set- and reset field pulses. The transistor coupling Hamiltonian is given by ($\hbar = 1$)

$$H_t = g_{ta} \left|f\right\rangle_{ta}\!\left\langle e\right| a + g_{tb} \left|f\right\rangle_{tb}\!\left\langle e\right| b + \text{H.c.}, \tag{5.18}$$

where a and b are the annihilation operators for photons in resonator a and resonator b. Both resonators are driven by classical external fields,

$$H_{drive} = \alpha(a + a^\dagger) + \beta(b + b^\dagger), \tag{5.19}$$

and we choose $\alpha\,(\beta) = \sqrt{\langle n_{a\,(b)}\rangle}\kappa_{a\,(b)}/2$, where $\langle n_{a\,(b)}\rangle$ are the target steady-state photon numbers and $\kappa_{a\,(b)}$ are the photon-loss rates of the resonators.

Consider first the interaction between resonator a and transistor ta. If ta is in the state g, H_t vanishes and the resonator mode is only subject to H_{drive} and cavity damping which results in a steady state coherent field in the resonator. If a π-pulse on the g-e transition excites ta into state e, H_t induces a vacuum Rabi-splitting of the resonator frequency of magnitude g_{ta}, and if this is larger than other coupling strengths and decay rates in the system, it will make H_{drive} in (5.19) off-resonant. The resonator field will then decay into the vacuum state. Decay of ta back to g will, however, bring the resonator back on resonance with the driving field, and the coherent state will reappear: although it is stored in the resonator field, the memory of the π-pulse excitation is governed by the transistor excited state lifetime.

The π-pulses need, in this scheme, to be injected by separate lines connected to ta and tb. There are no requirements on how the pulses are created as long as the pulse-areas correspond to a fast π-rotation on the g-e transition. We note, however, that symmetrically shaped single-photon wave packets [216–218] would meet the desire of having as few photon as possible.

To extend the time over which the cavity field memory states recall the excitation of both ta and tb, we propose the elaborate system design in Fig. 5.9 where the resonators are coupled to each other via two qubits. The two ancillary qubits shown are adiabatically eliminated but they are crucial to mediate the desired effective interaction Hamiltonian,

$$\begin{aligned} H_a &= \chi_a\, a^\dagger a\, (b^\dagger \sigma_{b,-} + b\sigma_{b,+}), \\ H_b &= \chi_b\, b^\dagger b\, (a^\dagger \sigma_{a,-} + a\sigma_{a,+}), \end{aligned} \tag{5.20}$$

where $\sigma_{a\,(b),-}$ and $\sigma_{a\,(b),+}$ are the lowering and raising operators for qubit-a and qubit-b in the figure.

With the Hamiltonian H_a we achieve that a non-vanishing field in resonator a gives rise to a strong Jaynes-Cummings coupling between resonator b and qubit-b. We already discussed how such a coupling causes a splitting of the resonator frequency, so as a consequence of the excitation in resonator a the driving of resonator b now becomes off-resonant and inefficient. The set-up is symmetric, and a field in resonator b similarly controls the strength of the coupling between resonator a and its qubit and hereby prevents its resonant driving. The switching pulses still work as described above: e.g., a switching π-pulse exciting transistor ta stops the driving of resonator a. The field in resonator a decays on a time scale of $1/\kappa_a$, allowing the field to build up in resonator b, and now, even after

ta has decayed (assuming a lifetime $T_{ta,1} > 1/\kappa_a$), resonator a cannot be excited because of H_b and the coherent state in resonator b. The coherent state in resonator b is maintained until a Reset pulse on tb shifts this resonator off resonance, the field decays, and now the coherent state builds up in resonator a and prevents excitation of resonator b also after tb has returned to its ground state.

Summing up, the memory states are a driven coherent state in one resonator and the vacuum state in the other and vice versa. By a nonlinear cross-coupling between the resonators mediated by qubits, the field in one resonator prevents the excitation of the other one and preserves the memory states for times longer than both the resonator and qubit lifetimes. The Set and Reset pulses applied to the transistor ta (tb) works by putting resonator a (b) off resonance. This causes the field to decay and the other field to grow and, thus, the system switches between the memory states. The scheme is robust against decay and decoherence, since the switching and the preservation of the memory states relies on the interaction induced vacuum-Rabi splitting, and while dephasing or noise on the qubits may change the coupling strengths and introduce damping effects in (5.20), the precise interaction is not crucial, as their role is not to mediate but to prevent excitation of the resonator fields.

5.2.2 Contruction of the Hamiltonian

In Eq. (5.20), H_a and H_b describe a coupled system of two resonators and two transmon qubits. We consider here the construction of

$$H_a = \chi\, a^\dagger a\, (b^\dagger \sigma_{b,-} + b\sigma_{b,+}). \tag{5.21}$$

by the circuit illustrated in Fig. 5.10, where a and b are annihilation operators for two driven resonators and $\sigma_{b,\pm}$ are the ladder operators for Qubit-b. As we shall show in the following, incorporation of a capacitively coupled ancillary qubit component, Qubit-anc, leads to the highly nonlinear coupling terms in Eq. (5.21) (H_b is obtained in a similar manner).

We write the Lagrangian of the system and, at first, we neglect contributions from the resonators, such that we obtain

$$\begin{aligned}\mathcal{L} = {} & \frac{2C_{J,b}\dot{\phi}_b^2}{2} + \frac{2C_{J,anc}\dot{\phi}_{anc}^2}{2} + \frac{C_{12}(\dot{\phi}_b - \dot{\phi}_{anc})^2}{2} + \frac{C_{a1}\dot{\phi}_b^2}{2} \\ & + \frac{C_{b1}\dot{\phi}_b^2}{2} + \frac{C_{b2}\dot{\phi}_{anc}^2}{2} + E_{J,b}\cos\phi_b + E_{J,anc}\cos\phi_{anc},\end{aligned} \tag{5.22}$$

where the shunted capacitors parallel to the junctions are absorbed into $2C_{j,b}$. We can now find the conjugate variables,

$$q_b = \frac{\partial \mathcal{L}}{\partial \dot{\phi}_b} \qquad\qquad q_{anc} = \frac{\partial \mathcal{L}}{\partial \dot{\phi}_{anc}}, \tag{5.23}$$

and transform into the two-transmon Hamiltonian

$$\begin{aligned} H \ &= 4E_{C,b}n_b^2 - E_{J,b}\cos\phi_b + 4E_{C,anc}n_{anc}^2 \\ &\quad - E_{J,anc}\cos\phi_{anc} + 4E_I n_b n_{anc} \end{aligned} \tag{5.24}$$

with $q_k = -2en_k$ and

$$E_{C,b} = e^2\frac{C_{12} + C_{b2} + 2C_{J,anc}}{2C_\Sigma^2} \tag{5.25}$$

$$E_{C,anc} = e^2\frac{C_{12} + C_{a1} + C_{b1} + 2C_{J,b}}{2C_\Sigma^2} \tag{5.26}$$

$$E_I = e^2\frac{C_{12}}{C_\Sigma^2}, \tag{5.27}$$

where $C_\Sigma^2 = C_{12}(C_{a1} + C_{b1} + 2C_{J,b} + C_{b2} + 2C_{J,anc}) + (C_{b2} + 2C_{J,anc})(C_{a1} + C_{b1} + 2C_{J,b})$.

The coupling to the resonators is assume to happen at anti-nodes of the voltage mode functions, and by including contributions to the gate charge from second-order voltage fluctuations [201] we can replace the charge number, n_k by $n_k - n_{g,k}$, where the gate-charges are given by

$$n_{g,b} = \frac{C_{b1}V_{b,0}}{2e}i(b - b^\dagger) \pm \frac{C_{a1}V_{a,0}}{2e}i(a - a^\dagger) \tag{5.28}$$

$$n_{g,anc} = \frac{C_{b2}V_{b,0}}{2e}i(b - b^\dagger), \tag{5.29}$$

with the root mean square of the voltage fluctuations in each resonator given by $V_{j,0} = \sqrt{\omega_j/(2C_j)}$, with C_j being the capacitance of resonator j. In the limit of $E_J \gg E_C$, the Hamiltonian $H_k = 4E_{C,k}n_k^2 - E_{J,k}\cos\phi_k$ is approximated by $H_k = \sqrt{8E_C E_J}a_k^\dagger a_k - E_C(a_k + a_k^\dagger)^4/12$, with a_k being a bosonic operator. With these operators we can express the charge as $n_k = -i(E_J/8E_C)^{1/4}(a_k - a_k^\dagger)/\sqrt{2}$. If the anharmonicity of the transmon is sufficient, we can restrict ourselves to the two lowest energy levels and replace a_k by a Pauli lowering operator $\sigma_{k,-}$. The $\pm$-sign in Eq. (5.28) is obtained if we assume that C_{b1} and C_{b2} connect to the resonator b

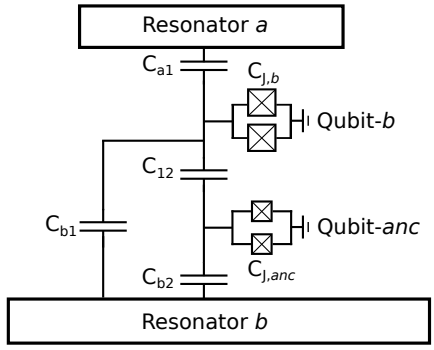

Figure 5.10: Schematic figure of two resonators coupled via two transmon qubits. Qubit-b is coupled to resonator a, resonator b and Qubit-anc, while Qubit-anc is only coupled to resonator b and Qubit-b. After ellimination of Qubit-anc, we obtain H_a of the main article. Unlike the simplified Fig. 1 in the main article, we have here displayed all circuit elements required to generate the qubits.

at integer (half-integer) wavelength separation with the same (opposite) coupling amplitude. This is possible with meandering resonators and is particular manageable using the arms of the Xmon design of the transmon [45].

This now allows us to recast the Hamiltonian in the qubit basis of each transmon and using the rotating wave approximation we end up with the Hamiltonian

$$\begin{aligned} H = &\frac{\Omega_b}{2}\sigma_{z,b} + \frac{\Omega_{anc}}{2}\sigma_{z,anc} + \omega_a a^\dagger a + \omega_b b^\dagger b \\ &+ g_{ab}(a^\dagger b + b^\dagger a) + g_{12}(\sigma_{b,+}\sigma_{anc,-} + \sigma_{anc,+}\sigma_{b,-}) \\ &+ g_{a1}(a^\dagger \sigma_{b,-} + \sigma_{b,+} a) + g_{b1}(b^\dagger \sigma_{b,-} + \sigma_{b,+} b) \\ &+ g_{a2}(a^\dagger \sigma_{anc,-} + \sigma_{anc,+} a) + g_{b2}(b^\dagger \sigma_{anc,-} + \sigma_{anc,+} b), \end{aligned} \tag{5.30}$$

where $\Omega_k \approx \sqrt{8E_{C,k}E_{J,k}}$ and the coupling strength are given by

$$g_{ab} = \pm(8E_{C,b} + 4E_I)\frac{C_{b1}C_{a1}}{4e^2}V_{0,a}V_{0,b} \tag{5.31}$$

$$g_{12} = 4E_I\beta_{anc}\beta_b \tag{5.32}$$

$$g_{a1} = -8E_{c,b}\beta_b\frac{C_{a1}V_{0,a}}{2e} \tag{5.33}$$

$$g_{a2} = -4E_I\beta_{anc}\frac{C_{a1}V_{0,a}}{2e} \tag{5.34}$$

$$g_{b1} = -4E_I\beta_b\frac{C_{b2}V_{0,b}}{2e} \mp 8E_{c,b}\beta_b\frac{C_{b1}V_{0,b}}{2e} \tag{5.35}$$

$$g_{b2} = -4E_I\beta_{anc}\frac{C_{b1}V_{0,b}}{2e} - 8E_{c,anc}\beta_{anc}\frac{C_{b2}V_{0,b}}{2e}. \tag{5.36}$$

with the the overlap functions $\beta_k \approx (E_{J_k}/8E_{C,k})^{1/4}/\sqrt{2}$.

We now tune the frequencies of the qubits close to resonance, $\Omega_{anc} \approx \omega_a$ and $\Omega_b \approx \omega_b$ and we transform to a rotating frame interaction picture with respect to $H_0 = \frac{\Omega_b}{2}\sigma_{z,b} + \frac{\Omega_{anc}}{2}\sigma_{z,anc} + \omega_a a^\dagger a + \omega_b b^\dagger b$. Here, second order time-dependent perturbation theory yields the interaction Hamiltonian $H_I = \frac{1}{\Delta}[\Xi^\dagger, \Xi]$ with $\Xi = a(g_{ab}b^\dagger + g_{a1}\sigma_{b,+}) + \sigma_{anc,-}(g_{b2}b^\dagger + g_{12}\sigma_{b,+})$ and $\Delta = \Omega_a - \Omega_b$. This gives us the Hamiltonian

$$\begin{aligned} H = &\Big(g_{b1} - \frac{g_{a1}g_{ab}}{\Delta} + \frac{g_{12}g_{b2}}{\Delta}\sigma_{anc,z}\Big)(b^\dagger\sigma_{b,-} + \sigma_{b,+}b) \\ &+ \Big(g_{a2} + \frac{g_{b2}g_{ab}}{\Delta} - \frac{g_{12}g_{a1}}{\Delta}\sigma_{b,z}\Big)(a^\dagger\sigma_{anc,-} + \sigma_{anc,+}a) \\ &- \frac{g_{a1}^2}{\Delta}a^\dagger a\sigma_{b,z} + \frac{g_{b2}^2}{\Delta}b^\dagger b\sigma_{anc,z}. \end{aligned} \tag{5.37}$$

At this point we want to saturate Qubit-*anc* at a value conditioned upon the occupation in resonator a. To achieve this we implement a slight detuning $\delta = \omega_a - \Omega_{anc}$ between resonator a and the ancillary qubit, which allows for a adiabatic elimination, such that we only have one qubit degree of freedom as in H_a.

We choose δ such that it is much larger than the effective coupling between the resonator and the qubit given by $g_{eff} = g_{a2} + \frac{g_{b2}g_{ab}}{\Delta} + \frac{g_{12}g_{a1}}{\Delta}$, and we assume a classical field amplitude α for resonator a. This gives us an effective damped Rabi-model where the steady state ancillary qubit inversion reads,

$$(\rho_{ee} - \rho_{gg})\Big|_{ss} = -1 + \zeta^{(1)}|\alpha|^2 - \zeta^{(2)}|\alpha|^4, \tag{5.38}$$

Table 5.1: Component parameters and the resulting effective coupling strengths. We provide two different sets of parameters corresponding to the implementation of H_a and H_b (with $a \leftrightarrow b$) in the main article, respectively. For both sets of parameters we assume a mean photon number of 8 in the resonantly driven resonator. Note that $\Delta = \pm 2\pi \times 1.5$ GHz, has opposite signs for the two parameters sets - this leads to a reduction of the cross-Kerr coupling between the two resonators. T_1 for the adiabatically eliminated qubit-*anc* is set to 50 ns.

	$\omega_a = 2\pi \times 7$ GHz $\omega_b = 2\pi \times 5$ GHz	$\omega_a = 2\pi \times 5$ GHz $\omega_b = 2\pi \times 7$ GHz
$C_{J,1}$	45 fF	32 fF
$C_{J,2}$	11 fF	15 fF
C_{a1}	0.90 fF	3.31 fF
C_{b1}	0.86 fF	1.70 fF
C_{b2}	9.18 fF	8.84 fF
C_{12}	3.70 fF	3.48 fF
δ	$2\pi \times 31.4$ MHz	$2\pi \times 27.5$ MHz
$E_{J,b}/E_{C,b}$	83	93
$E_{J,anc}/E_{C,anc}$	24	18
$E_{c,b}$	$2\pi \times 202$ MHz	$2\pi \times 266$ MHz
$E_{c,anc}$	$2\pi \times 545$ MHz	$2\pi \times 456$ MHz
g_{ab}	$2\pi \times 0.05$ MHz	$2\pi \times -0.464$ MHz
g_{12}	$2\pi \times 199.3$ MHz	$2\pi \times 197.6$ MHz
g_{a1}	$2\pi \times -13.1$ MHz	$2\pi \times -46.6$ MHz
g_{a2}	$2\pi \times -1.0$ MHz	$2\pi \times -2.53$ MHz
g_{b1}	$2\pi \times -18.3$ MHz	$2\pi \times 19.3$ MHz
g_{b2}	$2\pi \times -188.9$ MHz	$2\pi \times -195.5$ MHz
$\chi^{(1)}$	$2\pi \times 0.9799$ MHz	$2\pi \times 1.0043$ MHz
$\chi^{(2)}$	$2\pi \times 0.0109$ MHz	$2\pi \times 0.0121$ MHz
$\chi^{(ab)}$	$2\pi \times 0.92$ MHz	$2\pi \times -0.85$ MHz

where $\zeta^{(1)} = g_{eff}^2/(\gamma^2+2\Delta^2)$ and $\zeta^{(2)} = 2g_{eff}^4/(\gamma^2+2\Delta^2)^2$ can be evaluated with γ equal to the relaxation rate of the ancillary qubit. This solution is reached much faster than the timescale of the field evolution in the resonators, and therefore we can safely utilize this steady state solution as the state of the qubit.

The task is now to choose parameters such that the switching condition is fulfilled [201],

$$g_{b1} \approx \frac{g_{a1}g_{ab}}{\Delta} + \frac{1}{2}\frac{g_{12}g_{b2}}{\Delta}, \tag{5.39}$$

and at the same time to maximize the effective coupling,

$$\chi = \frac{g_{12}g_{b2}}{\Delta}(\zeta^{(1)} - \zeta^{(2)}a^\dagger a), \tag{5.40}$$

where we have returned to describe the resonator occupation by its operator expression. This is indeed possible, and we find $\chi^{(1)} = \frac{g_{12}g_{b2}}{\Delta}\zeta^{(1)}$ and $\chi^{(2)} = \frac{g_{12}g_{b2}}{\Delta}\zeta^{(2)}$ large enough that (5.21) gives rise to a strong coupling between resonator b and qubit-1 when resonator a is excited. The optimal quantities and the resulting coupling strengths are found numerically and displayed in Table 5.1. Controlling the capacitances precisely as specified in Tabel 5.1 may be difficult; however, once fabricated, one can tune Δ, until Eq. (5.39) is fulfilled [42, 219, 220]. Note as well that all effective couplings g_{eff} and $\chi a^\dagger a$ are much smaller the qubit anharmonicities, while the actual g's are much smaller than Δ, justifying our approximations.

As a last remark, we notice that Eq. (5.37) includes two dispersive terms. We ignore the term between Qubit-b and resonator a, since they are rarely simultaneously excited and since g_{a1} is small. The last term in (5.37) does, however, give rise to a cross-Kerr term,

$$H_{cross} = \chi^{(ab)}a^\dagger a b^\dagger b, \tag{5.41}$$

with $\chi^{(ab)} = \frac{g_{b2}^2}{\Delta}\zeta^{(1)}$. With the opposite choices for the detuning in the implementation of H_a and H_b (see Table 1), this term is effectively reduced.

Using realistic numbers for the implementation the cross Kerr term yields $\chi^{(ab)} = 2\pi \times 0.07$ MHz, and we can achieve an effective coupling strength between resonator b and its qubit of around $\tilde{g}_b = \chi_a\langle a^\dagger a\rangle = 2\pi\times 7.1$ MHz, for $\langle a^\dagger a\rangle = 8$, $\langle b^\dagger b\rangle = 0$, while for resonator a we can achieve $\tilde{g}_a = \chi_b\langle b^\dagger b\rangle = 2\pi \times 7.6$ MHz with $\langle b^\dagger b\rangle = 8$, $\langle a^\dagger a\rangle = 0$. In order to have a strong coupling, $\tilde{g}_i^2/\kappa\gamma \gg 1$, we use a lifetime of the qubits $T_{qa\,(qb),1} = 1/\gamma = 12\,\mu$s and a decay-rate of the cavities of $\kappa = 2\pi \times 0.1$

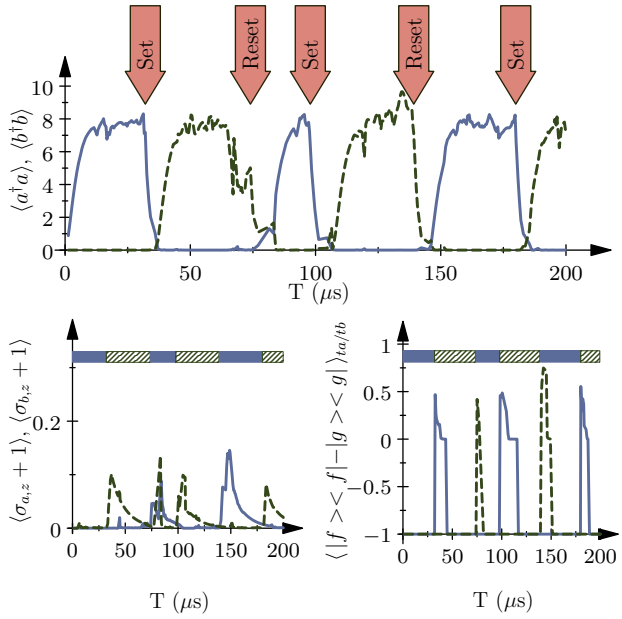

Figure 5.11: Upper panel: A single quantum trajectory with Set and Reset pulses applied at the times indicated. The solid (blue) curve is $\langle a^\dagger a\rangle$ and the dashed (green) curve is $\langle b^\dagger b\rangle$. Lower left panel: Population of qubit-a (solid blue curve) and qubit-b (dashed green curve). Lower right panel: Expectation value of $|f\rangle_{ta}\langle f| - |g\rangle_{ta}\langle g|$ (solid blue curve) and $|f\rangle_{tb}\langle f| - |g\rangle_{tb}\langle g|$ (dashed green curve). The bar in the top of both lower panels indicates that resonator a (blue) or resonator b (green hatched) is excited. The parameters used in the simulations are shown in Table 5.1. We use a decay-rate of the cavities at $\kappa = 2\pi \times 0.1$ MHz and a lifetime of qubit-a and -b of 12 μs. For both transitors we assume $g_{ta\,(tb)} = 2\pi \times 30$ MHz and lifetimes of 20 μs.

MHz. With these parameters, the power needed to drive the resonators is a mere 2×10^{-17} W, thus, this device constitute an ultra-low energy microwave device. Also, with these resonator-parameters we must require a transistor qubit lifetime, $T_{ta,(tb),1}$ of around 20 μs.

5.2.3 Quantum trajectory simulations

The average time-evolution of the system is governed by the quantum master equation [72]

$$\begin{aligned}\frac{\partial\rho}{\partial t} = i[\rho, H] + \sum_{k\in\{a,b\}} \Bigg[& \frac{\kappa_k}{2}\left(2\,k\rho k^\dagger - k^\dagger k\rho - \rho k^\dagger k\right) \\ & + \frac{\gamma_t}{2}\left(2\,\sigma_{tk,-}\rho\sigma_{tk,+} - \sigma_{tk,+}\sigma_{tk,-}\rho - \rho\sigma_{tk,+}\sigma_{tk,-}\right) \\ & + \frac{\gamma}{2}\left(2\,\sigma_{k,-}\rho\sigma_{k,+} - \sigma_{k,+}\sigma_{k,-}\rho - \rho\sigma_{k,+}\sigma_{k,-}\right)\Bigg] \end{aligned} \tag{5.42}$$

with κ_a, κ_b, γ_t and γ being the decay rate of the cavities, the exited states of the transistor transmons and the qubits. We will assume $\kappa_a = \kappa_b = \kappa$. Instead of directly solving Eq. (5.42), which will yield an average over the bistable behaviour of the device, we apply Monte Carlo wave function (MCWF) simulations similar to how the qubit was treated in Sec. 5.1, [101, 212], ie we evolve $\frac{d}{dt}|\psi(t)\rangle = -\Big(\sum_\mu c_\mu^\dagger c_\mu/2 + iH\Big)|\psi(t)\rangle$, interrupted by the application of quantum jumps $|\psi\rangle \to c_\mu|\psi\rangle$, where c_μ are the jump operators for all decay channels. In Fig. 5.11 we present a quantum trajectory simulation of the device. The upper panel of Fig. 5.11 shows that the flip-flop operates as we expect.

In the lower left panel of Fig. 5.11 we see that while resonator a is populated and H_a is 'active', qubit-b remains in the ground state, while when resonator b is populated qubit-b undergoes excitation dynamics during the switching process. This excitation in qubit-b is not important since the Hamiltonian, H_b, responsible for keeping resonator a empty and resonator b excited does not contain qubit-b operators. The lower right panel of Fig. 5.11 shows the corresponding transient evolution of the transistor population of states $|g\rangle$ and $|f\rangle$, triggering the filling and emptying of the resonators.

The trajectory in the upper panel of Fig. 5.12 shows that in the absence of Set- and Reset-pulses, the flip-flop undergoes spontaneous state changes, and we estimate the rate of such erroneous switches to be about one every 600 μs. We have further quantified the behaviour over many realizations in the lower panel of Fig. 5.12, where we have used $N = 30$ trajectories to generate the ensemble averaged mean photon number in the a-resonator when no Set- and Reset-pulses are applied. Fitting the relaxation of this mean value, we find a memory time of 347.7 μs with an uncertainty around 50 μs, which is over 2 orders of magnitude longer than the bare cavity

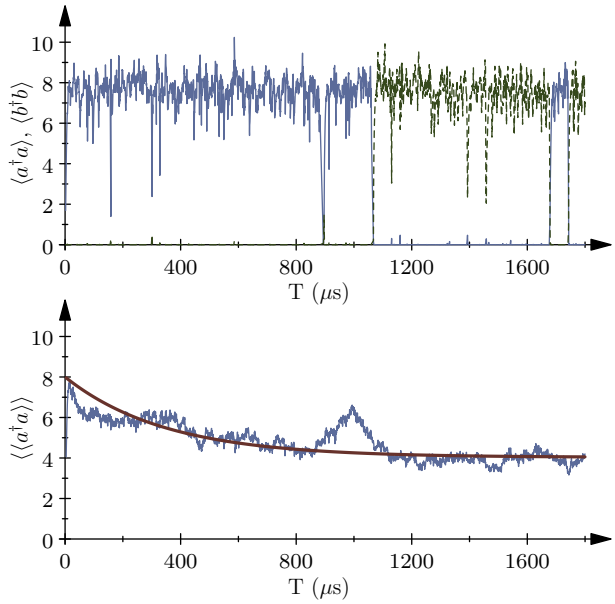

Figure 5.12: Upper figure: A single trajectory with no switching pulses applied. The solid (blue) curve is $\langle a^\dagger a\rangle$ and the dashed (green) curve is $\langle b^\dagger b\rangle$. Lower figure: An ensemble averaged mean of $\langle a^\dagger a\rangle$ over 30 trajectories (thin light blue) and an exponential fit (thick dark red) with the decay-time 347 μs. The parameters used are the same as in Fig. 5.11.

lifetime at 1.5 μs and also much longer than the qubit lifetime of 12 μs. Note at this point, that if an error occurs, already after a subsequent Set- and Reset-pulse the device returns to the desired memory state.

In Fig. 5.13 we supplement the trajectories in Fig. 5.11 to illustrate further features of the device. In the upper left trajectory we see that after the first Set-pulse empties resonator a, when the transistor has decayed, resonator b is occupied by less than two photons, which implies that in this trajectory we have a high probability for an unintended switch back to resonator a, which indeed happens. The system however recovers only after the next Reset-pulse. The upper right figure shows an unintended switch of the device around $t = 75\,\mu$s, and in the lower left figure we show a trajectory where both kinds of error occur. The lower right figure shows the ideal performance of the device, this time with a high frequency of

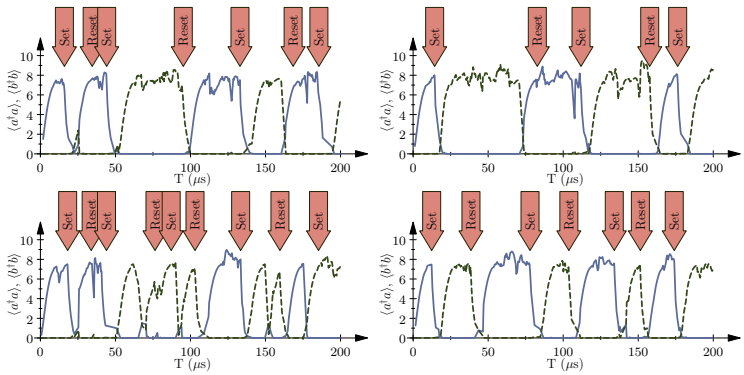

Figure 5.13: (Color online) Single trajectories with Set and Reset pulses applied at the times shown. Parameters are identical to Fig. 5.11.

switching pulses indicating a wider range of robustness. Accumulating the statistic of 30 simulations we find that the probability to have no error during 200 μs of evolution with 4–10 Set- and Reset-pulses is around 54 %, accounting both for the finite memory time ($\sim 347\,\mu$s) and errors occurring during switches. Longer memory times and better transistor qubits will increase this probability significantly.

5.2.4 Estimates of performance

To supplement our numerical simulations of the functioning of the device, we estimate the memory time of the flip flop in the resonator a state as

$$\frac{1}{T_{mem}} = \sum_n e^{-\langle n_a\rangle} \frac{\langle n_a\rangle^n}{n!} \frac{(2\beta)^2}{\kappa^2 + (\chi_a^{(1)} n - \chi_a^{(2)} n^2)^2}\,\kappa \tag{5.43}$$

which is the feeding rate of photons in the off-resonant resonator b weighted over Poisson distributed number states occupying resonator a. This yields $T_{mem} = 340\,\mu$s for the parameters used, which is in qualitative agreement with our simulations. Using Eq. (5.43) we have calculated the memory time for different values of the mean excitation of resonator a. When varying $\langle n_a\rangle$, we change κ in order to keep the ratio $\kappa/\langle n_a\rangle$ constant. Estimates from (5.43) for different values of $\kappa T_{ta,1}/\langle n_a\rangle$ are shown as curves in Fig. 5.14 (a). The numerically simulated memory times for $\kappa T_{ta,1}/\langle n_a\rangle = 1.5$ are calculated from exponential fits similar to that of Fig. 5.12. We see that our rough estimate of Eq. (5.43) qualitatively

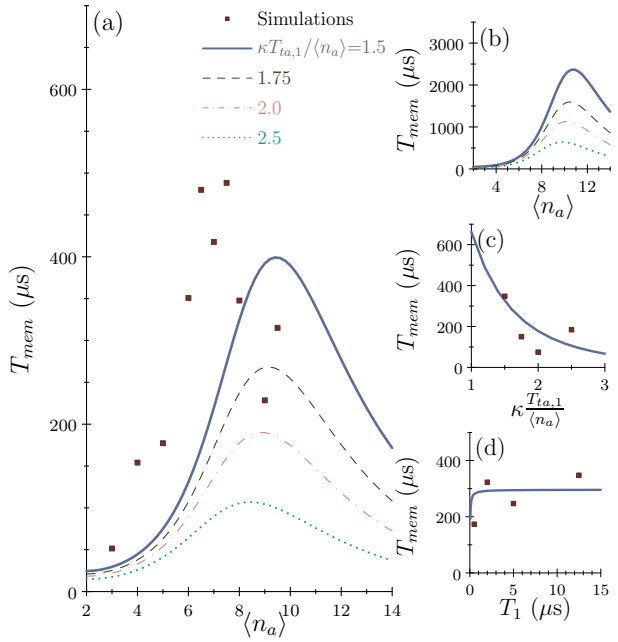

Figure 5.14: Memory time simulated using parameters specified in Fig. 5.11 and calculated using Eq. (5.43) and in (d) using the qubit excitation estimate as well. All simulated results contain an uncertainty on the order of 10 μs. In (a) we vary the target photon number in the resonators while keeping the fraction $\kappa T_{ta,1}/\langle n_a\rangle$ constant at the values specified. In the simulations represented by the square symbols, we use $\kappa T_{ta,1}/\langle n_a\rangle = 1.5$. In (b) we show the analytical estimates as in (a) with the same parameters except $T_{ta,1} = 40\,\mu$s. In (c) we vary κ while keeping $\langle n_a\rangle = 8$ and $T_{ta,1} = 20\,\mu$s and in (d) we study the memory time for different values of the qubit-a and -b lifetimes.

reproduce the simulated behaviour. The maximum memory time is fairly well predicted, but the optimal photon number is slightly shifted compared to the simulations. This may be due to an underestimation of the effect of κ. To achieve a better Set-Reset-performance, $\kappa T_{ta,1}/\langle n_a\rangle$ must be increased, but we see that this decreases the memory time. In 5.14 (b), however, we see that with a better transistor qubit we can improve the

memory time significantly, even with high values of $\kappa T_{ta,1}/\langle n_a \rangle$. In Fig. 5.14 (c) we compare simulations with the estimate of (5.43) as a function of $\kappa T_{ta,1}/\langle n_a \rangle$ by varying κ.

In Fig. 5.14 (d) we show how the use of worse qubits influence the memory time. For a quantitative analysis of the qubit contribution, we approximate the master equation, neglecting contributions from H_b, by coupled equations for the steady-state qubit population in the excited and ground state, $P_{\uparrow/\downarrow}$, and the accompanying field amplitude of each resonator, $\alpha_{\uparrow/\downarrow}$ and $\beta_{\uparrow/\downarrow}$ [221] (see full calculation of this in [5]),

$$\frac{P_\uparrow}{P_\downarrow} = \frac{\frac{4\chi_a^2}{\gamma^2}(|\alpha_\downarrow|^4 + |\alpha_\downarrow|^2)|\beta_\downarrow|^2}{1 + \frac{4\chi_a^2}{\gamma^2}(|\alpha_\uparrow|^4 + |\alpha_\uparrow|^2)(|\beta_\uparrow|^2 + 1)}. \tag{5.44}$$

We estimate the qubit contribution to the memory time by adding $P_\uparrow \gamma$ to $1/T_{mem}$. Our simulations confirm the qubit effect and the sharp decrease in the memory time when T_1 becomes less than ~ 1 μs. Since we are approaching the edge of the strong coupling regime we cannot expect the photon blockade to function well here. To summarize, the dominant contribution to the erroneous flipping between the states originates from the finite probability of having zero photons according to the Poisson distributed population of the resonators. If qubit-a and qubit-b have very short lifetimes, their relaxation will also contribute significantly to the erroneous state changes.

5.2.5 Flip-flop outlook

This section has proposed a scheme for implementing a flip-flop system operating in the few microwave photon regime of circuit QED. The development is inspired by optical cavity QED, but due to the absence of the long-lived and phase stable states offered by atoms, we use a two-resonator Hamiltonian, where the excitation of one resonator blocks the excitation of the other one. Using realistic parameters we show that with single photon pulses we can switch between two stable states and that the systems memory time far exceeds that of its intrinsic components. This type of memory system is a significant step towards classical microwave logic in circuit QED. In contrast to other strategies, this device exploits strong vacuum Rabi-splitting and operates in the regime of few photons.

The primary limitations of our proposal are set by the life-time of the qubits, but one can expect future superconducting qubits with much

longer life-times, which translates directly into an improvement of the performance of the present device.

As a possible extension, avoiding the difficulties of creating π-pulses, one might imagine that resonator a (b) is not resonant with the e-f transition of ta (tb). Then a cw-signal with driving amplitude Ω_d detuned from the g-e transition by $\Delta_{SR} = \omega_d - \omega_{ge} = \omega_{ef} - \omega_a$ will generate a second order coupling of $\tilde{g}_{ta} = g_{ta}\Omega_d/\Delta_{SR}$. If $\tilde{g}_{ta}$ is much larger than any other coupling strength or decay rate resonator a will decay to the ground state during the duration of the driving signal and we retrieve the same functionality as before. This type of pulses, which typically will consist of $\sim$100 photons, might originate from an elongated dispersive readout of a superconducting qubit.

5.3 Conclusion

In this chapter we have presented two ideas for classical control with circuit QED elements. The systems that we propose involves more components than a typical circuit QED device, but the added complexity serves a purpose and improves the system characteristics beyond what is currently achievable with single components. It is worthwhile for a wide range of possible applications to see the complexity not as a disadvantage but, rather, as an opportunity to pursue circuit strategies along with the efforts to improve the performance of individual components.

As already mentioned, room-temperature-based feedback control requires interfacing very different and remote technologies and gross energy inefficiency is unavoidable between qubits operating at fW power scales and W-scale room-temperature equipment. In contrast, the components of our proposed scheme are proximate in a cold, low-noise environment. A qubit and the controllers presented then feature only a factor of $\lesssim 10^2$ difference in operating power. There is, however, no single correct approach to the design of these low-power qubit controllers. For comparison, we can directly draw an analogy to popular autonomous approaches today in superconducting microwave systems using continuous pumping schemes, inspired by quantum optics techniques [206–208]. Here, microwave transitions in a single component (usually a circuit QED qubit or qubits) are designed so that a continuous microwave pump drives the qubit(s) into a desired state. These schemes are often understood in terms of an internal feedback loop in which a cavity and the qubit states respond to each other. These approaches are similar in power consumption and require

not signal-processing at room temperature. However, it may be hard to realize to scale these controllers as the component are inherently coupled – for example remove the cavity from a circuit QED qubit and it becomes a very different device. Also, a strong coupling of a quantum circuit to a cavity leads to a highly perturbed energy spectrum and it is much less clear how to design such systems for general continuous pumping schemes.

The controllers, that we presented in this Chapter is distinct from these in that both the Kerr resonator and the flip-flop device is designed to work in a modular fashion, such that they can be separated and optimized independent from the qubits they are designed to control. It is also easy to see how the prensented components may apply more generally [195] in superconducting microwave systems.

Chapter 6

Implementing controllable couplings

Although the field of circuit QED has shown great progress, all challenges of circuit QED have not been solved. A few very successful approaches are used to encode and manipulate quantum information (see Sec. 2.2) and to apply quantum gates (see Sec. 2.5), but an open question still remains on how to move forward in terms of scalable high-fidelity control. Do we need to incrementally improve the current approaches or do we need to step back and take a new path? In particular, a robust and scalable way to couple multiple quantum systems is still highly desired. One of the biggest obstacles towards multi-quantum operations is the fact that all experientially built circuits will be sightly different. System frequencies must therefore be tunable or approaches for circumventing the difficulties of frequency differences must be applied.

Many approaches to improve current multi-qubit gates exist, and the first part of this chapter will concentrate on a proposal to use a flux-modulated resonator to apply controllable gates between transmon qubits. While this gate does not suggest to replace the dominating strategy of using resonator-coupled tranmons, the flux modulation of resonators adds a new approach. The theory is presented in [6] but due to recent development in high coherence transmons with fixed frequency [133], we present here numerical simulations with more optimistic parameters than used in [6]. While transmons are natural components for encoded quantum information, the second part will focus on an alternative encoding scheme and present the engineering of a four-body interaction partly included in [14] relevant for adiabatic quantum computing using Kerr resonators [222].

(a)

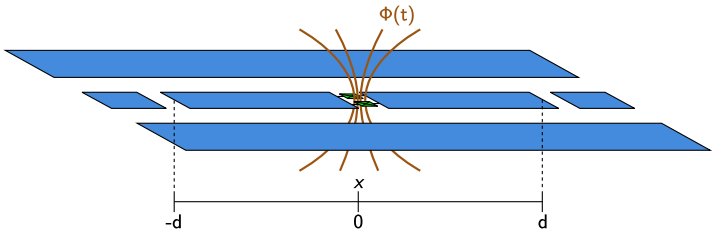

(b)

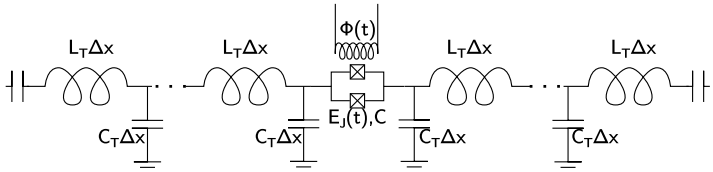

Figure 6.1: (a) A superconducting resonator, interupted by a SQUID at $x = 0$. The SQUID is modulated by an external magnetic flux $\Phi(t)$ yielding a time dependent Josephson energy $E_J(t)$. (b) Circuit diagram of a resonator interrupted by an inline-SQUID. L_T and C_T denote the inductance and capacitance per length of the waveguide, such that each inductor (capacitor) has the inductance (capacitance) $L_T\Delta x$ ($C_T\Delta x$). The resonator is described in the limit of $\Delta x \to 0$. The inline-SQUID is characterized by the time-dependent Josephson energy, $E_J(t)$, and its capacitance, C.

6.1 Bridging frequency gaps in off-resonant couplings

To control the interaction between the resonator mode of circuit QED and other physical systems such as qubits, one may use the ability to tune the frequencies of the resonator mode using an in-line SQUID [220, 223–225]. On a related, periodic modulation of SQUID parameters is used in parametric amplifiers [86, 87], as presented in Sec. 2.4, and interactions may appear between the modes of the resonator [141]. While changing the frequency of a resonator allows tuning of the photon energies to match energy differences in other systems, the quantized field does not necessarily

adiabatically adjust to the change in frequency and the associated change in mode function. Indeed, rapid motion of an optical mirror has been predicted to lead to the creation of photons by the so-called dynamical Casimir effect [226], and experiments in circuit QED have addressed the microwave equivalent by rapid modulation of a SQUID, altering the boundary conditions of a waveguide with half open boundary conditions [166, 227].

In this section we study a periodically modulated SQUID (see Fig. 1 (a)) in a finite size waveguide with a discrete frequency spectrum. The goal is to investigate how this driving leads to new, multi-frequency modes and to characterize their frequency content. Then it is determined how such modes can be used to bridge frequency gaps and coherently couple different physical systems. In particular the new time-dependent modes are used to couple two transmon qubits.

6.1.1 Multi-frequency resonance modes

To analyze the dynamics of a superconducting resonator modulated by an inline-SQUID, a similar approach to Sec. 2.1 is following with the circuit diagram in Fig. 6.1 (b). Here, we have represented the waveguide by a series of LC-circuits. Each waveguide segment of length Δx is associated with an inductor with inductance $L_T\Delta x$ and a capacitor with capacitance of $C_T\Delta x$, with L_T and C_T are defined as the inductance and capacitance per length of the waveguide. In the limit of $\Delta x \to 0$, the function $\phi(x,t)$ describes the flux in the resonator. At the center of the waveguide we introduce the inline-SQUID, which contributes a non-linear inductance set by the Josephson energy, $E_J(t)$, and a capacitance set by C.

The Lagrangian of the circuit is given by the expression,

$$\begin{aligned}\mathcal{L} = &\int_{-d}^{d}\left\{\frac{C_T}{2}\left(\partial_t\phi(x,t)\right)^2 - \frac{1}{2L_T}\left(\partial_x\phi(x,t)\right)^2\right\}dx \\ &+ \frac{C}{2}(\partial_t\Delta\phi(x_J,t))^2 + E_J(t)\cos\frac{2\pi\Delta\phi(x_J,t)}{\Phi_0},\end{aligned} \tag{6.1}$$

where $\Delta\phi(x_J,t) = \phi(x_{J+},t) - \phi(x_{J-},t)$ denotes the change in the flux variable, $\phi(x,t)$, imposed by the discrete boundary conditions at the inline-SQUID [141]. In the following the cosine term is expanded to second order in $\Delta\phi$ and, as usual (see Chapter 3), the higher order terms can as usual be reintroduced as a perturbation [141].

The Euler-Lagrange equation,

$$\partial_x\frac{\partial\mathcal{L}}{\partial(\partial_x(\phi(x,t))} + \partial_t\frac{\partial\mathcal{L}}{\partial(\partial_t(\phi(x,t))} - \frac{\partial\mathcal{L}}{\partial\phi(x,t)} = 0, \tag{6.2}$$

yields the wave-equation for the phase variable along the waveguide resonator

$$-v^2\partial_x^2\phi(x,t)+\partial_t^2\phi(x,t)=0, \tag{6.3}$$

where $v=1/\sqrt{C_T L_T}$ denotes the propagation speed of the wave. We assume that our resonator obeys open boundary conditions at its ends at $x=\pm d$, while at $x_J=0$ the SQUID defines boundary conditions, parametrized by the time-dependent Josephson energy, $E_J(t)$, and the capacitance, C, of the SQUID,

$$\frac{\partial\phi(x,t)}{\partial x}\Big|_{x=\pm d}=0 \tag{6.4}$$

$$\frac{1}{L_T}\frac{\partial\phi(x,t)}{\partial x}\Big|_{x=0\pm}=C\frac{\partial^2\Delta\phi(0,t)}{\partial t^2}+\frac{(2\pi)^2E_J(t)}{\Phi_0^2}\Delta\phi(0,t). \tag{6.5}$$

Equations (6.3)–(6.5) define the time-dependent mode functions of the circuit that we shall first calculate and then use as basis for the quantum interaction with additional circuit elements.

The magnetic flux, $\Phi(t)$, through the SQUID is here assumed to be modulated periodically around a non-zero value, leading to a harmonically varying Josephson energy,

$$E_J(t)=E_{J,0}+\delta E_J\cos\omega_d t. \tag{6.6}$$

For the linearized problem with the time-dependent boundary condition, the periodicity of the driving is used when transforming the resonator fields into frequency space,

$$\phi(x,\omega)=\frac{1}{\sqrt{2\pi}}\int_{-\infty}^{\infty}\phi(x,t)\,e^{-i\omega t}dt. \tag{6.7}$$

We rewrite the wave-equation as

$$v^2\partial_x^2\phi(x,\omega)+\omega^2\phi(x,\omega)=0. \tag{6.8}$$

while the boundary conditions in frequency space become:

$$\frac{\partial\phi(x,\omega)}{\partial x}\Big|_{x=0\pm}=L_TC\omega^2\Delta\phi(0,\omega)+L_T\frac{(2\pi)^2}{\Phi_0^2}\frac{E_J(\omega)\otimes\Delta\phi(0,\omega)}{\sqrt{2\pi}}, \tag{6.9}$$

$$\frac{\partial\phi(x,\omega)}{\partial x}\Big|_{x=\pm d}=0. \tag{6.10}$$

In Eq. (6.9), $E_J(\omega) \otimes \Delta\phi(0,\omega)$ denotes the convolution product, which is readily calculated since $E_J(\omega) = E_{J,0}\delta(\omega) + \frac{\delta E_J}{2}(\delta(\omega+\omega_d) + \delta(\omega-\omega_d))$,

$$E_J(\omega) \otimes \Delta\phi(0,\omega) = \\ E_{J,0}\Delta\phi(0,\omega) + \frac{\delta E_J}{2}(\Delta\phi(0,\omega+\omega_d) + \Delta\phi(0,\omega-\omega_d)). \tag{6.11}$$

Since the coupling to the SQUID in Eq. (6.1) cancels for even modes ($\Delta\phi(x_J,t)=0$), we consider only odd solutions to Eqs. (6.8) and (6.10), i.e., solutions in the form

$$\phi(x,\omega) = \begin{cases} \phi(\omega)\cos\left(\omega/v\ (d-x)\right) & \text{for } x>0, \\ -\phi(\omega)\cos\left(\omega/v\ (-d-x)\right) & \text{for } x<0. \end{cases} \tag{6.12}$$

These functions display the discrete jump at $x = x_J = 0$ necessary to fulfil the boundary condition (6.9), which leads to the equation

$$\begin{aligned} \frac{\omega}{v}d\,\sin\Big(\frac{\omega}{v}d\Big)\phi(\omega) &= 2\frac{L_T d}{L_J}\cos\Big(\frac{\omega}{v}d\Big)\phi(\omega) \\ &+ 2\frac{L_T d}{\delta L_J}\cos\Big(\frac{\omega+\omega_d}{v}d\Big)\phi(\omega+\omega_d) \\ &+ 2\frac{L_T d}{\delta L_J}\cos\Big(\frac{\omega-\omega_d}{v}d\Big)\phi(\omega-\omega_d), \end{aligned} \tag{6.13}$$

where we have defined $L_J = \sqrt{2\pi}\Phi_0^2/(4\pi^2 E_J)$ and $\delta L_J = 2\sqrt{2\pi}\Phi_0^2/(4\pi^2\delta E_J)$. We have neglected contributions from the Josephson capacitance, assuming typical values obeying $C\omega^2 \ll L_T/L_J$ [227].

Equation (6.13) can be solved numerically for the allowed discrete values of ω and the corresponding vector of amplitude strengths $\phi(\omega + m\omega_d)$. For our purpose it is sufficient to approximate the system and restrict ourselves to a dominant frequency component, ω, and two sidebands, $\omega\pm\omega_d$, and ignore coupling to further frequency components $\omega \pm 2\omega_d, \ldots$. With this approximation the carrier and sideband components of the system eigenmodes have wave numbers that obey

$$\begin{aligned} kd = &\frac{2L_T d}{L_J}\frac{\cos kd}{\sin kd} + \frac{\left(\frac{2L_T d}{\delta L_J}\right)^2\frac{\cos kd}{\sin kd}\cos k_- d}{\frac{2L_T d}{L_J}\cos k_- d + k_- d\sin k_- d} \\ &+ \frac{\left(\frac{2L_T d}{\delta L_J}\right)^2\frac{\cos kd}{\sin kd}\cos k_+ d}{\frac{2L_T d}{L_J}\cos k_+ d + k_+ d\sin k_+ d}. \end{aligned} \tag{6.14}$$

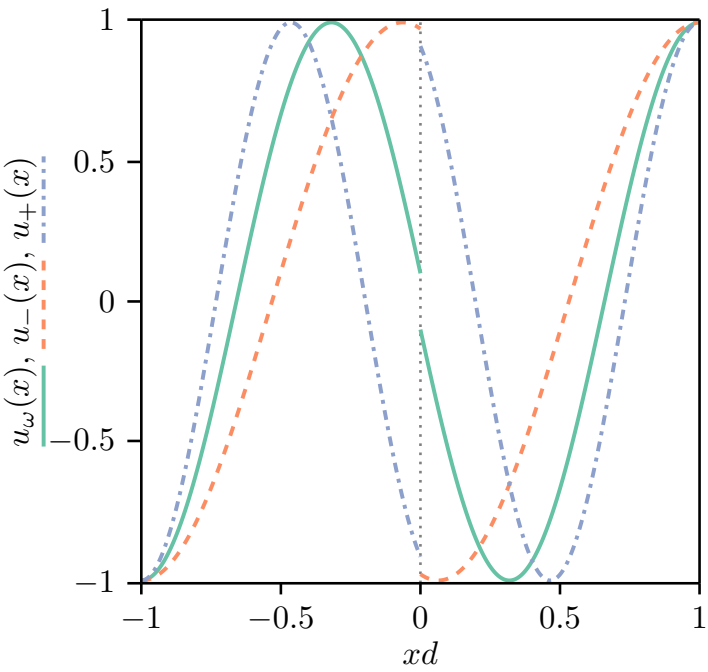

Figure 6.2: The mode-functions when we modulate the SQUID with a frequency $\omega_d = 2\pi \times 2.0$ GHz and $\delta E_J/E_{J,0} = 0.4$ for a mode with $kd = 4.614$ ($\omega = 2\pi \times 7.343$ GHz). The green solid line shows the central frequency component $u_\omega(x)$ while the orange dashed and the blue dash-dotted lines show the sideband components $u_-(x)$ and $u_+(x)$ respectively. The parameters of the resonator are $d = 1.2$ cm, $E_{J,0}/\hbar = 2\pi \times 715$ GHz, $v = 1.2 \times 10^8$ m/s and $L_T = 416\,\mathrm{nH/m}$ (corresponding to $Z_0 = \sqrt{L_T/C_T} = 50\,\Omega$).

where $k = \omega/v$ and $k_\pm = (\omega \pm \omega_d)/v$. The amplitudes of the sidebands are given by

$$\phi(\omega \pm \omega_d) = \frac{\frac{2L_T d}{\delta L_J}\cos kd}{\frac{2L_T d}{L_J}\cos k_\pm d + k_\pm d \sin k_\pm d}\phi(\omega) \equiv A_\pm \phi(\omega). \tag{6.15}$$

We notice that to first order, the amplitude of the sidebands are inversely proportional to δL_J and hence proportional to the driving amplitude δE_J.

Now we transform our solution back into the time-domain where the solution to the wave equation attains the form:

$$\begin{aligned}\phi(x,t) &= \operatorname{sign}(x)\cos\big(k(\operatorname{sign}(x)d-x)\big)\cos(\omega t)\phi_\omega \\ &\quad + \operatorname{sign}(x)\cos\big(k_+(\operatorname{sign}(x)d-x)\big)\cos(\omega_+ t)\phi_+ \\ &\quad + \operatorname{sign}(x)\cos\big(k_-(\operatorname{sign}(x)d-x)\big)\cos(\omega_- t)\phi_- \qquad (6.16)\\ &= u_\omega(x)\phi_\omega(t) + u_+(x)\phi_+(t) + u_-(x)\phi_-(t). \qquad (6.17)\end{aligned}$$

In the last line we have separated the terms into space-dependent $u_j(x)$ with values exploring the range $[-1,1]$, while the amplitudes governed by (6.15) are included in the time-dependent functions $\phi_j(t) = \cos(\omega_j t)\phi_j$.

We show an example of the mode-structure in Fig. 6.2, where the solid line shows the carrier function $u_\omega(x)$ and the dashed curves show the two associated side band mode functions $u_\pm(x)$. The solutions have three nodes and correspond to the 3rd mode of the resonator. Only odd modes acquire sidebands due to the coupling to the SQUID, and in Fig. 6.3 we show how the solution of Eq. (6.14) for the 1st, 3rd and 5th mode leads to eigenfrequencies that vary with the modulation strength, $\delta E_J/E_{J,0}$. In Fig. 6.3 we notice a frequency shift of the order of 10 MHz, which is much larger than typical bandwidths of superconducting resonators and cannot be predicted without taking the full dynamics into account.

To reach the solution (6.17), we assumed that the sidebands at $\omega \pm \omega_d$ in (6.13) are present and that the coupling to further components at $\omega \pm 2\omega_d$ is negligible. This assumption is fulfilled for applications in this section, where we deal with $A_\pm \sim 10^{-2}$, significantly limiting higher sideband exitation. When the system is externally driven on resonance with the values of ω shown, or at the sidebands $\omega \pm \omega_d$, the modulation of the SQUID at ω_d causes the effective excitation of the multi-frequency solution (6.17). While (6.17) is derived under the assumption of periodic driving, it also holds during transient excitation of the system or coupling to other systems, as long as the resulting evolution is slow with respect to the natural frequencies, i.e., $\omega_\pm, \omega \gg G_{max}$, where G_{max} is the maximal interaction strength and hence rate of change of the excitation amplitude.

6.1.2 Quantization of the multi-frequency modes

To treat the time dependent modes derived above quantum mechanically, we observe that the central frequency amplitude $\phi_\omega(t)$ oscillates at frequency

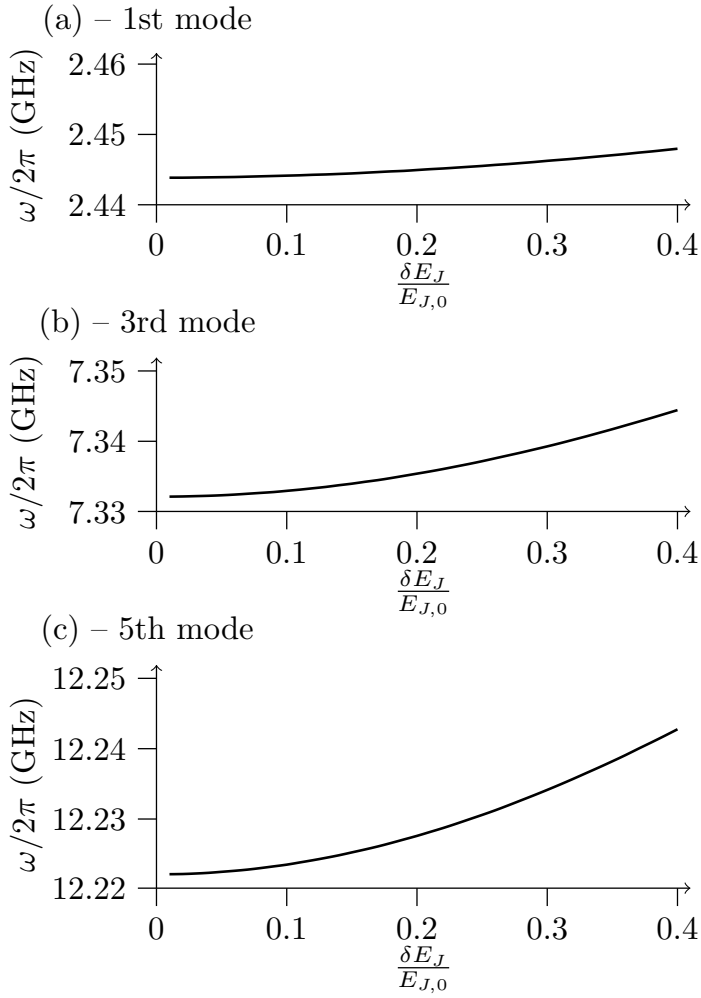

Figure 6.3: Classical resonances for the odd modes of a resonator calculated by Eq. (6.14) with the same parameters as in Fig. 6.2. We modulate the SQUID with varying strengths at a frequency $\omega_d = 2\pi \times 2.0$ GHz . In (a) we show the variation of the central frequency of the 1st mode, in (b) the 3rd mode and in (c) the 5th mode. The even modes are not considered, since they do not experience the modulation of the SQUID.

ω, consistent with the quadratic Lagrangian,

$$\mathcal{L} = \frac{C_\omega}{2}\dot{\phi}_\omega(t)^2 - \frac{1}{2L_\omega}\phi_\omega(t)^2 \tag{6.18}$$

where C_ω is conveniently represented by the parts of (6.1) that depend on $\dot{\phi}_\omega(t)$

$$\begin{aligned} C_\omega &= 2\int_0^d C_T \cos^2 k(d-x)\, dx + C\cos^2 kd \\ &= C_T d\Big(1 + \frac{\sin 2kd}{2kd}\Big) + C\cos^2 kd. \end{aligned} \tag{6.19}$$

The full Lagrangian, indeed, depends on $\dot{\phi}_\omega(t)$ also via the sideband components, but by setting $L_\omega = 1/(C_\omega\omega^2)$ in (6.18), we ensure the right evolution frequency of the amplitude variable. The error that we make by assigning the approximate values of C_ω and L_ω will only cause relative changes of order $A_\pm$ or $A_\pm^2$ in the coupling strengths used later in the article.

Introducing the canonical conjugate pair of variables, $\phi = \phi_\omega(t)$, $q = \partial\mathcal{L}/\partial\dot{\phi}_\omega(t) = C_\omega\dot{\phi}_\omega(t)$, we obtain the effective harmonic oscillator Hamiltonian for the mode

$$H = \frac{1}{2C_\omega}q^2 + \frac{1}{2L_\omega}\phi^2. \tag{6.20}$$

Applying usual canonical quantization, we impose $[\phi, q] = i\hbar$, and define annihilation and creation operators as in Sec. 2.1,

$$q = i\sqrt{\frac{\hbar C_\omega\omega}{2}}(a^\dagger - a), \tag{6.21}$$

$$\phi = \sqrt{\frac{\hbar}{2C_\omega\omega}}(a^\dagger + a), \tag{6.22}$$

which obey $[a, a^\dagger] = 1$ and allow rewriting of the quantum mechanical Hamiltonian in the well known form

$$H = \hbar\omega\Big(a^\dagger a + \frac{1}{2}\Big). \tag{6.23}$$

By construction, this Hamiltonian yields the dynamics of the amplitude of the central frequency component of the driven ω-mode, and Eqs. (6.15,6.17) account for the physical circuit observables that oscillate at ω and $\omega_\pm$.

Coupling physical systems across frequency gaps

Our quantization of the multi-frequency mode suggests the operator form of the positive and negative frequency parts,

$$\hat{\phi}(x,t) = \frac{1}{2}\sqrt{\frac{\hbar}{2C_\omega\omega}}\, a(t)\left(u_\omega(x) + A_+ e^{-i\omega_d t}u_+(x) + A_- e^{i\omega_d t}u_-(x)\right) + \text{h.c.}, \tag{6.24}$$

where $a(t)$ is given in the Heisenberg picture, and therefore $\hat{\phi}(x,t)$, due to (6.23), acquires oscillations at the frequencies ω and $\omega \pm \omega_d$. From $\hat{\phi}(x,t)$ we can express all other variable of interest like the voltage, charge distribution etc. As an example we can consider the voltage operator

$$\hat{V}(x,t) = \frac{\partial\hat{\phi}(x,t)}{\partial t} \tag{6.25}$$

$$= -\frac{i}{2}\sqrt{\frac{\hbar}{2C_\omega\omega}}\, a(t)\left(\omega u_\omega(x) + \omega_+ A_+ e^{-i\omega_d t}u_+(x) + \omega_- A_- e^{i\omega_d t}u_-(x)\right) + \text{h.c.}. \tag{6.26}$$

Electric charges and dipoles couple to the voltage along the waveguide, and the expression (6.26) implies that the driving of the in-line SQUID allows to bridge the frequency gap between the quantized circuit degrees of freedom and auxiliary quantum systems if they have transition frequencies equal to any one of the frequencies ω and $\omega \pm \omega_d$ - in the same way as a pump laser field may assist a quantized optical probe in the driving of atomic Raman transitions and optomechanical motion.

The coupling may have different forms, but if a quantum system $\mathcal{S}$ is detuned by a small amount δ, from one of the multimode frequency components, the joint system dynamics is given by a Hamiltonian, which in the interaction picture takes the form,

$$H = \hbar\delta\, a^\dagger a + \hbar G(a^\dagger b + b^\dagger a), \tag{6.27}$$

where the coupling strength G depends on the physical coupling mechanism and b ($b^\dagger$) is the lowering (raising) operator of excitations in $\mathcal{S}$. This Hamiltonian is known as a beam-splitter interaction, which adiabatically transfers the quantum state of $\mathcal{S}$ to the resonator. For the application of the resonator as a quantum bus this is the desired interaction. For a physical component with excitation frequency $\omega_S \sim \omega \pm \omega_d$, situated at $x = x_t$ and

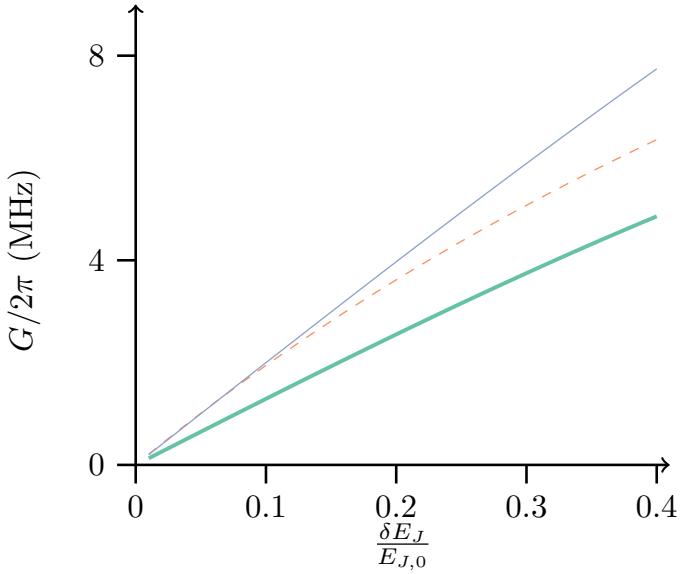

Figure 6.4: (Color Online) Coupling strength of the two lowest states of a transmon to the resonator mode. The frequencies are such that $\omega_{10} = \omega_- = \omega - \omega_d$, where ω is the frequency of the 1st mode in a resonator with $d = 0.25$ cm and $\omega = 2\pi \times 10.82$ GHz in the absence of modulation. The transmon is located at $x_t = 0.1d$ and it has $E_J/E_C = 80$ and $\beta = 2/3$. The thick (green) line is calculated by Eq. (6.28) for the modulation frequency set to $\omega_d = 2\pi \times 6$ GHz while the thin (blue) line shows Eq. (6.28) for $\omega_d = 2\pi \times 0.5$ GHz. The dashed (orange) line shows the result of a quasi-static aspproximation independent of the modulation frequency [6].

coupled to the local value of $\hat{V}(x,t)$, we obtain $G_\pm \propto (\omega \pm \omega_d) A_\pm u_\pm(x_t)$, while the value $G_\omega \propto \omega u_\omega(x_t)$ is obtained when $\omega_S \sim \omega$. We will write this coupling for the former case as

$$G_\pm = \frac{g\,\omega_\pm A_\pm}{4\sqrt{\hbar C_\omega \omega}} u_\pm(x_t), \tag{6.28}$$

where g is determined by the auxiliary system observables.

As a simple example we consider a transmon capacitively coupled to the resonator [42] at position x_t. The transmon has quantized charge and phase variables $\hat{n}$ and $\hat{\psi}$, such that its Hamiltonian is given by the standard transmon Hamiltonian $H_t = 4E_C(\hat{n} - n_g)^2 - E_{J,t}\cos\hat{\psi}$ (see Sec. 2.2), while it couples to the resonator with

$$H_I = 2e\beta\hat{n}\,\hat{V}(x_t) \tag{6.29}$$

where $\beta = C_c/C_\Sigma$ denotes the ratio between the coupling capacitor and the total capacitance of the transmon. In the limit of $E_{J,t} \gg E_C$, the transmon can be approximated as a two-level system with the charge operator given by Pauli transition operators between its eigenstates

$$\hat{n} = i\Big(\frac{E_{J,t}}{8E_C}\Big)^{1/4}\frac{1}{\sqrt{2}}(\sigma^\dagger - \sigma). \tag{6.30}$$

The coupling constant g between the system states in (6.28) thus becomes [42] (see also Sec. 2.3)

$$g = 2e\beta\langle 1|\hat{n}|0\rangle = \sqrt{2}e\beta\Big(\frac{E_{J,t}}{8E_C}\Big)^{1/4}. \tag{6.31}$$

For realistic transmon and resonator parameters, the coupling strength G_- to the lower sideband of the first mode of a short resonator is shown in Fig. 6.4 for different values of ω_d. Characteristic resonant coupling strengths of transmon qubits to coplanar waveguides are a few hundred MHz [43], and we expect, within the validity of our approximations, to obtain few MHz coupling strengths between transmons and waveguides when a GHz of frequency separation is bridged by the modulated SQUID. We, indeed, observe such values in the figure, and we also observe the expected increase of the coupling strength with the modulation amplitude δE_J. Due to the factor of ω_- in the expression for G we obtain a lower value when we modulate with a higher frequency. In the figure we have also included a simplified calculation using a quasi-static approximation [6]. This quasi-static approach yields a coupling that is independent of the modulation frequency and in the regime of small modulation frequency and amplitude it matches well to our more accurate calculation.

We have chosen parameters to ensure a large free spectral range for the transmon qubits, since close to a resonance a dispersive coupling between the transmon and the resonator mode of strength (see also Sec. 2.2)

$$\chi = G_\omega^2\frac{\alpha}{\hbar\Delta(\hbar\Delta + \alpha)}, \tag{6.32}$$

may alter the dynamics. In Eq.(6.32), $\Delta = \omega_{10} - \omega$, G_ω is the coupling strength to the center frequency and $\alpha = -E_C$ is the anharmonicity of the transmon [42]. For the parameters used for the thick green line in Fig. 6.4 the small value $\chi \approx 2\pi \times 0.2$ MHz is obtained, and it is independent of the modulation frequency amplitude.

The multi-frequency modes were calculated using a linearized Lagrangian. Treating the non-linearity of the Josephson Hamiltonian as a perturbation on the single mode Hamiltonian, we obtain the Kerr-nonlinearity [81, 141],

$$H_{NL} = -\frac{E_{J,0}}{4}\left(\frac{2\pi\sqrt{\hbar/2C_\omega\omega}}{\Phi_0}\right)\cos^4 kd\; a^\dagger a^\dagger aa. \tag{6.33}$$

This term is small for the parameters used in this paper, but in combination with the ability to couple systems at very different frequencies, its application, e.g., for the generation of non-classical states of the oscillator mode may be useful.

6.1.3 Multi-frequency modulation and Multi-Qubit gates

A drive at the inline-SQUID may not only couple systems resonantly, but it may also be at off-resonant frequencies and thus establish sidebands, which can interact selectively with different systems. The multi-frequency mode can therefore couple to two different transmon qubits and obtain a bichromatic two-qubit entangling gate, similar to gates applied in ion traps. Trapped ions, in contrast to superconducting qubits, can be excited by laser fields at a frequency sideband that excites their collective vibrational motion, and a bichromatic scheme, using laser frequencies detuned symmetrically around the internal state transition frequency, can be used to entangle the internal state of two or more ions [228–230]. An analogous scheme for circuit QED uses the multi-frequency resonator modes to accomplish a similar entangling operation among transmon qubits. If the central frequency component of the quantized field has frequency ω, and the qubits have frequency Ω_i, driving the SQUID at $\omega_{t,i} = \omega - \Omega_i$ makes the transfer of excitation between the qubit i and the lower multi-frequency sideband almost resonant. If, at the same time, the SQUID is driven at $\omega_{p,i} = \omega + \Omega_i$, a parametric interaction, leading to the joint excitation (and deexcitation) of the resonator mode and the transmon, becomes resonant. Detuning of these two driving terms by a small amount δ and having two transmons, leads in the interaction picture with respect to the transmons and single

(a)

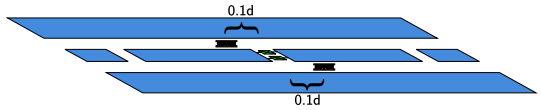

(b)

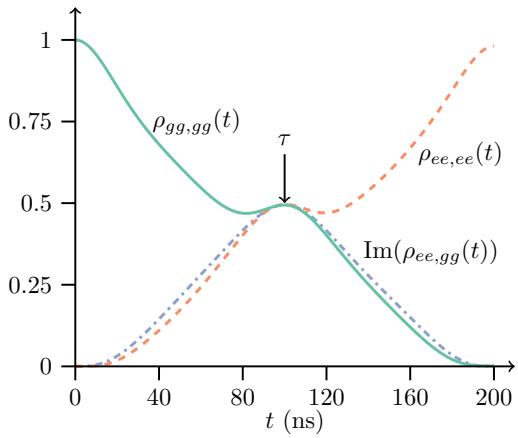

Figure 6.5: (a) Setup with two transmon qubits placed at $x_I = 0.1d$ and $x_I = -0.1d$. (b) Time evolution of two-qubit density matrix elements obtained by a simulation of the master-equation with the Hamiltonian in Eq. (6.34), a resonator decay-rate of $\kappa = 2\pi \times 50$ kHz, and transmon decay and dephasing lifetimes $T_1 = 55$ μs (Q-factor of 2M) and a puse dephasing time, $T_\phi = 55$ μs. The transmon qubits have different excitation frequencies $\Omega_1 = 2\pi \times 6.0$ GHz and $\Omega_2 = 2\pi \times 6.5$ GHz and the resonator frequency is $2\pi \times 10.82$GHz. For parameters described in the text we obtain the Hamiltonian (6.34) with $G = 2\pi \times 2.5$ MHz and $\delta = 2\pi \times 10$ MHz. In the simulation we have also included a kerr-term with magnitude given in Eq. (6.32).

mode Hamiltonian to the near resonant coupling of the transmons and resonator field operators,

$$H_I = \hbar G \sum_{n=1,2} (a e^{-i\delta t} + a^\dagger e^{i\delta t})(\sigma_{+,n} + \sigma_{-,n}). \tag{6.34}$$

Unlike the ion trap implementation, where laser frequencies differing by a relatively small amount are applied to the ion qubits, our driving fields are applied to the resonator system and their frequencies differ strongly (by twice the qubit transition frequency, $\omega_p - \omega_t \sim 2\Omega$). The interaction Hamiltonian, however, is the same, and the analysis in [230] applies for both the trapped ions and for the superconducting qubit system. We can hence use the scheme to accomplish a two-qubit entangling gate as part of a universal gate set and with more transmon qubits, we may also prepare multi-qubit entangled states.

For two transmons well separated in frequency, we merely have to modulate the in-line SQUID by separate pairs of modulation frequencies, $\omega_{t,n} = \omega - \delta - \Omega_n$, $\omega_{p,n} = \omega - \delta + \Omega_n$ and strengths, to recover Eq. (6.34). In Fig. 5 we illustrate a coplanar waveguide resonator coupled to two transmon qubits with different transition frequencies, $\Omega_1 = 2\pi \times 6.0$ GHz and $\Omega_2 = 2\pi \times 6.5$ GHz. We modulate the SQUID at frequencies $\{\omega_{t,1}, \omega_{p,1}, \omega_{t,2}, \omega_{p,2}\} = 2\pi \times \{4.366, 17.366, 4.866, 16.866\}$ GHz and with the amplitudes $\{\delta E_{J,t1}, \delta E_{J,p1}, \delta E_{J,t2}, \delta E_{J,p2}\}/E_{J,0} = \{0.1581, -0.1584, 0.1682, -0.1687\}$, leading to the Hamiltonian (6.34), with $G = 2\pi \times 2.5$ MHz and $\delta = 2\pi \times 10$ MHz. With these parameters, an entangling gate has the duration $\tau = 2\pi/\delta = 100$ ns [230], as indicated in Fig. 5 (b) by the time evolution of the two-qubit density matrix elements. The three matrix elements shown in Fig. 6.5 are, in the ideal case, the only non-zero matrix elements of the two-qubit density matrix and thus the concurrence can be expressed as $2\,\mathrm{Im}(\rho_{ee,gg})$. In the calculation, we have taken the finite coherence and excitation lifetimes of the qubit and of the resonator into account, and we obtain a maximally entangled state with a fidelity $F = 98.9\%$, which is completely limited by decoherence.

Since the rapid modification of SQUID parameters is already routinely accomplished for rapid tuning in laboratories and the harmonic driving is used in parametric amplifiers [86, 87], the current proposal can be implemented with devices that can be readily constructed. The analysis presented here also readily generalizes to multi-qubit systems, where the frequency control of the SQUID modulation may be used to control one and two-qubit gates as well as multi-qubit entanglement operations on any qubits in the resonator.

6.2 Implementing a four-body interaction term

An alternative approach to quantum computing is the technique of adiabatic quantum computing (AQC), which was formulated with the hopes of achieving quantum speedups in finding the solution to, among other things, the Ising problem [231]. In AQC, the "quantum computer" is slowly evolved from the ground state of a trivial initial Ising Hamiltonian to that of the final Ising Hamiltonian encoding an optimization problem. Since the state of the system will then always be close to ground state of the instantaneous Hamiltonian, the system will not decohere and therefore the quality of the individual qubits are not detrimental as long as precise control is available [232].

To successfully perform AQC, several conditions must be met: (i) The Ising spins must be implemented in an appropriate physical system, where control and readout of each individual spin is possible. Typically a qubit, such as superconducting qubits [233–236], is used to represent the Ising spin. (ii) The evolution must be sufficiently slow to avoid non-adiabatic evolution. (iii) The system must have full connectivity to be able to encode any problem. This challenge has in particular been addressed by embedding long-range interactions in system with only local connectivity. Recently, a new embedding scheme was proposed by Lechner, Hauke and Zoller (LHZ) [237] in which N logical Ising spins are encoded in $M = N(N-1)/2$ physical spins along with $M - N + 1$ constraint couplings. The physical spins represent the relative configuration of two logical spins. An all-to-all connected Ising problem in the logical spins is realized by mapping the logical couplings onto the local fields of the physical spins and a problem independent four-body coupling to enforce the constraints.

Despite great efforts in solving these challenges, there is still a long way before a general purpose AQC algorithm can be implemented and it is imperative to search for novel ideas for implementation of AQC that promise great controllability, connectivity and, as a result, improved computational abilities. In [14] we propose to encode the Ising problem in a network of two-photon driven Kerr nonlinear resonators (KNR). In this scheme, a single Ising spin is mapped onto the phase of a coherent state, $|\pm\alpha\rangle$, which constitutes a two-fold degenerate steady state of the two-photon-driven KNR in the rotating frame of the drive [222]. While the primary concern of [14] is the evaluation of the performance of AQC algorithms, this section will focus on the physical implementation of a four-body interaction necessary to implement the LHZ scheme, when Ising spins are encoded as coherent states of a KNR. For this purpose we need

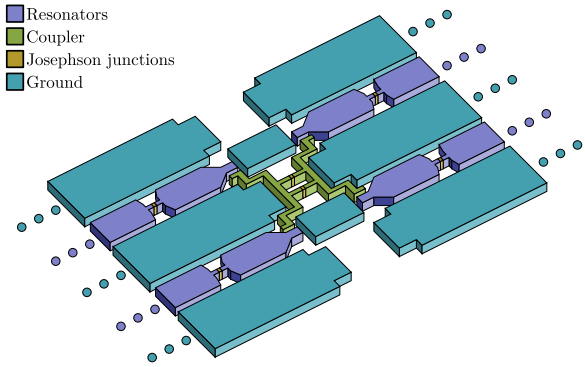

Figure 6.6: A four-body interaction is created using a single SQUID. The coupling can be either static or it can be driven by an external flux.

a four-body interaction of the form

$$H_c = -\mathcal{F}(\alpha_1\alpha_2\alpha_3\alpha_4 + \text{h.c}), \tag{6.35}$$

where $\alpha_i = \hat{a}_i$ or $\hat{a}_i^\dagger$ and $\hat{a}_i$ is the mode operator for resonator i. Because we choose the coherent phase α to be real, the hermitian conjugate can be applied to any number of the resonator operators. To implement this four-body interaction, some amount of non-linearity is needed as otherwise only several two-body interactions between pairs of resonators will be present. One problem that may occur is, however, that a given implementation often comes along with lower order coupling as well, which will often be of a much larger magnitude. Therefore, it is necessary to engineer the coupling such that only the four-body term is resonant.

The non-linearity of a SQUID (or just a single Josephson junction) is one possibility to implement this four-body interaction, see a sketch in Fig. 6.6. The potential for a SQUID with a phase-difference, Φ,

$$U(\Phi) = -E_J \cos(\Phi_x)\cos(\Phi/\phi_0) \tag{6.36}$$

$$\approx -E_J \cos(\Phi_x)\left(1 - \frac{1}{2\phi_0^2}\Phi^2 + \frac{1}{24\phi_0}\Phi^4\right), \tag{6.37}$$

with $\phi_0 = \hbar/(2e)$ being the reduced flux quantum and Φ_x being the external flux through the SQUID loop that can be used to tune the effective coupling.

We see from the expansion that we indeed get a fourth order term, which is exactly what we intend to use to implement the desired coupling.

The challenge is now to design an appropriate circuit such that we obtain a phase difference on the form

$$\Phi = \hat{\Phi}_1 + \hat{\Phi}_2 + \hat{\Phi}_3 + \hat{\Phi}_4 \tag{6.38}$$

where we have

$$\hat{\Phi}_i = \Phi_i^0(\hat{a}_i + \hat{a}_i^\dagger). \tag{6.39}$$

Going to a frame rotating at each resonator frequency, ω_i, for each resonator, we have

$$\hat{a}_i \to \hat{a}_i\, e^{-i\omega_i t} \tag{6.40}$$

Applying this transformation directly yields all terms off-resonant unless the rotation frequency of each term cancels. Furthermore, we can drive the external field with a time-dependent flux of frequency ω_d. Therefore we get the condition for the four-body interaction to be resonant

$$\omega_1 \pm \omega_2 \pm \omega_3 \pm \omega_4 - \omega_d = 0. \tag{6.41}$$

Here the sign $\pm$ in front of ω_i decides whether α_i in Eq. (6.35) is $\hat{a}_i$ or $\hat{a}_i^\dagger$ such that the term is resonant with drive. Therefore, the simplest implementation can be achieved by choosing $\omega_d = 0$ and $\omega_1 + \omega_2 = \omega_3 + \omega_4$, which will create the static SQUID interaction

$$H_c = -\mathcal{F}(\hat{a}_1\hat{a}_2\hat{a}_3^\dagger\hat{a}_4^\dagger + \text{h.c}). \tag{6.42}$$

6.2.1 Calculating the coupling

We consider the general coupling Lagrangian given by

$$\mathcal{L}_c = \sum_{j=1}^{4} \frac{C}{2}(\dot{\phi}_j - \dot{\phi}_{c,j})^2 + \mathcal{L}_c \tag{6.43}$$

with the four resonator phases, ϕ_j, which map onto the operators $\hat{a}_j + \hat{a}_j^\dagger$ in the quantum regime. Similarly we have $\phi_{c,j}$ as the phase variables of the inner coupling circuit that each couple to ϕ_j. Notice that $\phi_{c,j}$ may be identical depending on the specific implementation. Finally we have the coupling Lagrangian, $\mathcal{L}_c$, that includes the SQUIDs of the coupling circuit.

The coupling circuit will typically consist of several normal modes, each of which may couple to the resonators. We will focus on only one mode, $\hat{a}_c$ of the coupling circuit, in other words, we require that only one mode is relevant (near resonant) with the four resonators. Therefore we can write the Hamiltonian for the combined system as

$$H = \omega_c \hat{a}_c^\dagger \hat{a}_c + \sum_{j=1}^{4} \left(\omega_j \hat{a}_j^\dagger \hat{a}_j + g_j (\hat{a}_j \hat{a}_c^\dagger + \hat{a}_j^\dagger \hat{a}_c) \right) + H_{nl}, \tag{6.44}$$

where H_{nl} include all non-linear terms.

Our goal is to obtain a non-linear coupling between all a_j, but H_{nl} contains only terms including $\hat{a}_c$. Moreover, the coupling mode, $\hat{a}_c$, is expected to be only weakly perturbed by the resonator fields, $\hat{a}_j$. Therefore, we express the $\hat{a}_c$-mode in terms of the dressed modes of the system by writing the bilinear Hamiltonian part of the Hamiltonian as

$$H' = \vec{a}^\dagger \begin{pmatrix} 0 & g_1 & g_2 & g_3 & g_4 \\ g_1 & \Delta_1 & 0 & 0 & 0 \\ g_2 & 0 & \Delta_2 & 0 & 0 \\ g_3 & 0 & 0 & \Delta_3 & 0 \\ g_4 & 0 & 0 & 0 & \Delta_4 \end{pmatrix} \vec{a} = \vec{a}^\dagger G \vec{a} \tag{6.45}$$

with $\Delta_j = \omega_j - \omega_c$ and $\vec{a} = (a_c, a_1, a_2, a_3, a_4)^T$. The matrix G can be diagonalized such that the Hamiltonian is given as $H' = \tilde{a}^\dagger D \tilde{a}$. In order to obtain a new Hamiltonian that contains the four-body interaction, we first express the linear Hamiltonian in the dressed modes $\tilde{a}_i$. The bare mode, $\hat{a}_c$, can then be expressed in terms of the diagonal modes $\tilde{a}_i$ such that

$$\hat{a}_c = \sum_{i=0}^{4} p_i \tilde{a}_i, \tag{6.46}$$

with $\tilde{a}_j$ being the renomalized resonator modes, $\hat{a}_j$, (with $0 \equiv c$) and $\sum |p_i|^2 = 1$ in order to preserve the commutator relations. Similarly, a transformation of the non-linear part of the Hamiltonian, H'_{nl} can be expressed in the dressed modes and will then couple then couple each of the modes, $\tilde{a}_j$. The mode $\tilde{a}_c$ is then far off-resonant and we neglect contributions for this such that we have $H = H' + H'_{nl}$ as the Hamiltonian, which ideally should contain resonant terms of the type in Eq. (6.35) but for the dressed modes.

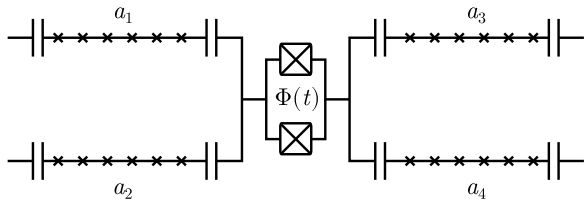

Figure 6.7: Four resonators coupled via a SQUID. The SQUID may be driven by an AC-flux, $\Phi(t)$.

6.2.2 Static SQUID coupling

The simplest implementation of the desired four-body interaction is by a single static SQUID. Lets draw a circuit of such a system, see Fig. 6.7 with $\Phi(t) = 0$. We can write the Lagrangian for the SQUID as,

$$\begin{aligned}\mathcal{L} = \frac{C}{2}\Big[&(\dot{\phi}_l - \dot{\phi}_1)^2 + (\dot{\phi}_l - \dot{\phi}_2)^2 \\ &+ (\dot{\varphi}_r - \dot{\phi}_3)^2 + (\dot{\phi}_r - \dot{\phi}_4)^2\Big] \\ &+ \frac{C_J}{2}(\dot{\phi}_l - \dot{\phi}_r)^2 + E_J \cos((\phi_l - \phi_r)/\phi_0).\end{aligned} \tag{6.47}$$

with ϕ_r and ϕ_l being the phase variable on the right and left side of the SQUID respectively. We now consider the two variables $\phi_c = \phi_l - \phi_r$ and $\phi_\Sigma = \phi_l + \phi_r$ and notice that ϕ_Σ does not have any potential energy, so we will ignore this mode. Now the Lagrangian reads

$$\begin{aligned}\mathcal{L} = \frac{C}{2}\Big[&(\dot{\phi}_c/2 - \dot{\phi}_1)^2 + (\dot{\phi}_c/2 - \dot{\phi}_2)^2 \\ &+ (\dot{\phi}_c/2 + \dot{\phi}_3)^2 + (\dot{\phi}_c/2 + \dot{\phi}_4)^2\Big] \\ &+ \frac{C_J}{2}(\dot{\phi}_c)^2 + E_J \cos(\phi_c/\phi_0),\end{aligned} \tag{6.48}$$

and from the Euler-Lagrange equation we directly identify the normal frequency of the coupling mode using a small angle approximation for the cos-term

$$\omega_c = \sqrt{\frac{E_J}{\phi_0^2(C + C_J)}}, \tag{6.49}$$

and similarly we find the coupling strengths

$$g_j = (-1)^{f(j)} \frac{C}{2} \omega_j \omega_c \phi_j^0 \phi_c^0 \tag{6.50}$$

with ϕ_j^0 being the phase variable zero-point fluctuation of the $\hat{a}_j$-mode $\phi_j^0 = \sqrt{\hbar Z_0/2}$ with Z_0 the impedance of the mode. We also have ϕ_c^0 as the coupling mode's zero-point fluctuations given by

$$\phi_c^0 = \sqrt{\frac{\hbar}{2(C + C_J)\omega_c}}. \tag{6.51}$$

The function $f(j)$ sets the sign of the coupling by $f(1,2) = 1$ and $f(3,4) = 0$. Now, we can obtain each modes contribution to the coupling mode, p_j, as in Eq. (6.46) such that we have

$$\hat{\phi}_c = \sum_{j=1}^{4} \phi_c^0 p_j (\hat{a}_j^\dagger + \hat{a}_j). \tag{6.52}$$

Choosing the frequencies $\omega_1 + \omega_2 = \omega_3 + \omega_4$ yields the term $\hat{a}_1 \hat{a}_2 \hat{a}_3^\dagger \hat{a}_4^\dagger$ (and its Hermitian conjugate) resonant and we obtain the coupling strength

$$\mathcal{F}_{ss} = \frac{E_J \, p_1 p_2 p_3 p_4}{4} \left(\frac{\phi_c^0}{\phi_0} \right)^4. \tag{6.53}$$

Now taking realistic number as $C = 10$ fF, $C_J = 20$ fF, $E_J = 2\pi \times 15$ GHz which yield $\omega_c = 2\pi \times 8.76$ GHz, and using $(\omega_1, \omega_2, \omega_3, \omega_4) = 2\pi \times (7.8, 8.0, 8.2, 8.4)$ GHz the coupling becomes $\mathcal{F}_{ss} \approx 2\pi \times 1$ MHz.

6.2.3 Flux-driven SQUID coupling

The downside of the static coupling is that is will be on at all times, which may not always be optimal, although in simple AQC problems it does not seem to be a big issue [14]. Nevertheless, a time-dependent flux can be applied to the SQUID leading to the replacement $E_J \to E_J(t)$, which makes the coupling tunable. While this already allows for tunability, the change in E_J will also change the couplings and detunings g_i and Δ_i. It turns out to be advantageous instead to choose $\Phi(t) = \Phi_0 + \Phi_d \cos(\omega_d t)$, which leads to $E_J(t) = E_{J,0} + \delta E_J \cos(\omega_d t)$ as in Sec. 6.1. The Euler-Lagrange

equation for the coupling mode in frequency space therefore reads

$$\left(\frac{E_{J,0}}{\phi_0^2} - (C + C_J)\omega^2\right)\tilde{\phi}_c(\omega)$$
$$= -\frac{\delta E_J}{2\phi_0^2}\Big(\tilde{\phi}_c(\omega + \omega_d) + \tilde{\phi}_c(\omega - \omega_d)\Big) - \frac{C}{2}\sum_{j=1}^{4}\omega^2\tilde{\phi}_j(\omega). \tag{6.54}$$

This lead to flux dependent coupling mode frequency

$$\omega_c = \sqrt{\frac{E_{J,0}}{\phi_0^2(C + C_J)}} + \Delta\omega(\delta E_J) \tag{6.55}$$

with $\Delta\omega(x)/\omega_c \ll 1$ for typical parameters. We can now directly repeat the calculations in Sec. 6.1. We set $\omega_d = \omega_1 + \omega_2 - \omega_3 - \omega_4$ and from Eq. (6.54), we observe the $\hat{a}_c$-mode has sidebands from the modulation, thus, the phase-operator should be written as

$$\hat{\varphi}_c = \varphi_c^0\,\hat{a}_c(1 + A_+e^{-i\omega_d t} + A_-e^{i\omega_d t}) + \text{h.c.} \tag{6.56}$$

with

$$A_\pm = \frac{\delta E_J/2}{E_J^0 - \left(\frac{\phi_0}{2\pi}\right)^2(C + C_J)(\omega_\delta \pm \omega_D)}, \tag{6.57}$$

which we get from evaluating Eq. (6.54) in $\omega_\delta \pm \omega_d$. Collecting all the relevant terms we arrive at the the interaction Hamiltonian

$$H_{c,fd} = -\mathcal{F}_{fd}(a^\dagger b^\dagger cd + abc^\dagger d^\dagger) \tag{6.58}$$

and we find

$$\tilde{F} = \frac{p_1p_2p_3p_4}{4}\left(\frac{\phi_c^0}{\phi_0}\right)^4\Big(\frac{\delta E_J}{2} + 4E_{J,0}A_-\Big) \tag{6.59}$$

to first order in $A_\pm$.

To find the value of δE_J we notice that the potential of a SQUID given as

$$-E_J\big|\cos(\Phi(t))\big|\cos(\varphi_\delta/\phi_0) \tag{6.60}$$

so to bring it on the form used above we have

$$\Phi(t) = -\Phi_0 + \Phi_d\cos(\omega_d t). \tag{6.61}$$

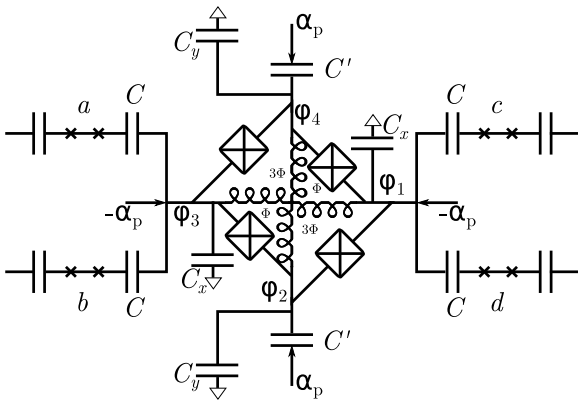

Figure 6.8: Circuit for implementing a microwave driven four-body interaction using a Josephson ring modulator.

Ideally we would like Φ_X to be as close to $\pi/2$ as possible, but this will lower ω_c. Inspired by recent experiments [166] we choose $\Phi_X = 0.42\pi$ and $\Phi_d = 0.06\pi$. This can put $E_{J,0}$ in the same order of magnitude as in the static case using a large SQUID and we directly evaluate $\delta E_J = 0.7E_{J,0}$. We can with this method control the coupling by changing Φ_d as a function of time.

6.2.4 Josephson ring modulator coupling

Another problem in the above description is the fact that the coupling mode was treated as an harmonic oscillator. This is not entirely true as the anharmonicity for the parameters used in the example becomes around $2\pi \times 50$ MHz. A means to circumvent this is to replace the single SQUID by a series of M SQUIDs. This will decrease the anharmonicity by M^2, but this is also true for the coupling strength. Again, this is not a major issue, since the population of the coupling mode is still very small due to the adiabatic condition [14, 222]. However, when increasing the amplitude of the coherent states, α, the non-linearity will become an increasing problem.

Therefore we seek an alternative where we can decrease the anharmonicity but increase the coupling, for instance by microwave pumping. For this purpose, we focus on the imbalanced shunted Josephson Ring Modulator (JRM) as displayed in Fig. 6.8 [60, 238], which is the main component also used for the JPC discussed in Sec. 2.4. This way of cou-

pling has the advantage that the coupling internal mode frequencies is set by the capacitances C_x and C_y and the inductance L, which allows us to boost the coupling significantly by using a large Josephson junction with $E_J \gtrsim 2\pi \times 1000$ GHz without affecting the coupling mode inductance. Furthermore, with such a large junction, we have a large critical current, which allows a a very strong classical pump field. The JRM consists of 4 orthogonal modes

$$\phi_x = \phi_1 - \phi_3 \tag{6.62}$$
$$\phi_y = \phi_2 - \phi_4 \tag{6.63}$$
$$\phi_z = \phi_1 + \phi_2 - \phi_3 - \phi_4 \tag{6.64}$$
$$\phi_w = \phi_1 + \phi_2 + \phi_3 + \phi_4, \tag{6.65}$$

where the mode ϕ_w is a free mode and only couples to the rest by the capacitances, so we neglect this mode, and we have the Hamiltonian for the 3 coupled modes as

$$\begin{aligned} H = &\frac{q_x^2}{2(C + \frac{C_x}{2})} + \frac{q_y^2}{2(C' + \frac{C_y}{2})} + \frac{4q_z^2}{2(C + C' + \frac{C_x}{2} + \frac{C_y}{2})} \\ &+ \frac{1}{2L}(\phi_x^2 + \phi_y^2 + \frac{1}{2}\phi_z^2) + U_J(\phi_x, \phi_y, \phi_z) \end{aligned} \tag{6.66}$$

with U_J being the potential from the four Josephson junctions, which will include the external fluxes. We write this potential as

$$\begin{aligned} U_J = &-E_J\big[\cos(\varphi_2 - \varphi_1 + 3\Phi) + \cos(\varphi_3 - \varphi_2 + \Phi) \\ &+ \cos(\varphi_4 - \varphi_3 + 3\Phi) + \cos(\varphi_1 - \varphi_4 + \Phi)\big] \end{aligned} \tag{6.67}$$

$$\begin{aligned} = &-E_J\Big(\cos\big[\frac{1}{2}(\varphi_x - \varphi_y + \varphi_z) + 3\Phi\big] \\ &+ \cos\big[\frac{1}{2}(\varphi_x + \varphi_y - \varphi_z) + \Phi\big] \\ &+ \cos\big[\frac{1}{2}(-\varphi_x + \varphi_y + \varphi_z) + 3\Phi\big] \\ &+ \cos\big[\frac{1}{2}(-\varphi_x - \varphi_y - \varphi_z) + \Phi\big]\Big) \end{aligned} \tag{6.68}$$

$$\begin{aligned} = &-E_J\Big(2\cos\big[(\varphi_x - \varphi_y)/2\big]\cos\big[\varphi_z + 3\Phi\big] \\ &+ 2\cos\big[(\varphi_x + \varphi_y)/2\big]\cos\big[-\varphi_z + \Phi\big]\Big), \end{aligned} \tag{6.69}$$

with $\varphi_i = \phi_i/\phi_0$ and Φ being the unit-less phases. We now choose $\Phi = \pi/2$, so we get

$$\begin{aligned} U_J &= -E_J\Big(2\cos\left[(\varphi_x - \varphi_y)/2\right]\sin\left[\varphi_z\right] \\ &\quad + 2\cos\left[(\varphi_x + \varphi_y)/2\right]\sin\left[\varphi_z\right]\Big) \qquad (6.70) \\ &= -4E_J\cos\frac{\varphi_x}{2}\cos\frac{\varphi_y}{2}\sin\varphi_z. \qquad (6.71) \end{aligned}$$

The x-mode will now couple to the four resonators as can be seen from Fig. 6.8, while the z-mode is far detuned and only used for pumping the four-body term. This leaves the y-mode neglectable. We then write the Hamiltonian as

$$\begin{aligned} H = &\sum_{i=1,2,3,4,x,z} \omega_i a_i^\dagger a_i + \sum_{i=1}^{4} K a_i^\dagger a_i a_i^\dagger a_i \\ &+ \sum_{i=1}^{4} g_i^x (a_i^\dagger a_x + a_x^\dagger a_i) + g_i^z (a_i^\dagger a_z + a_z^\dagger a_i) \\ &+ 2E_J \frac{(2\pi)^3 \phi_x^2}{\phi_0^3}\phi_z - E_J \frac{(2\pi)^5 \phi_x^4}{6\phi_0^5}\phi_z + \alpha_p(t)\, q_z, \end{aligned} \qquad (6.72)$$

where α_p is the drive applied to directly couple the z-mode as indicated in Fig. 6.8. We assume that the applied field can be written as

$$\alpha_p(t) = \alpha_d \sin(\omega_d t) \qquad (6.73)$$

so we can perform the rotating wave approximation and write the Heisenberg equation for a_z in frame rotating at ω_z

$$\dot{a}_z = \epsilon_d e^{i\Delta_d t} - \frac{\kappa}{2} a_z - i \sum_{j=1}^{4} g_j^z a_j e^{i(\omega_j - \omega_z)t} + f(t) \qquad (6.74)$$

with $\Delta_d = \omega_d - \omega_z$, $\epsilon_d \propto \alpha_d$ and $f(t)$ containing the noise operators for the decay channels with combined decay rate κ. If we assume that ϵ_d is sufficiently large and that $g_j^z/(\omega_j - \omega_z)$ is small, we will approximate the mode with a c-number

$$a_z \to \alpha_z = \frac{\epsilon_d e^{-i\omega_d t}}{\Delta_i + i\kappa/2}, \qquad (6.75)$$

where ϵ_d is directly proportional to the amplitude α applied in Fig. 6.8. The x-mode is not driven by any external fields and is, thus, only weakly

perturbed by the non-linear resonators, a, b, c and d. Therefore, we can adiabatically eliminate the x-mode as

$$a_x = \sum_{i=1}^{j} p_i \tilde{a}_i, \tag{6.76}$$

Now if $\omega_d = \omega_a + \omega_b + \omega_c - \omega_d$, we obtain the interaction Hamiltonian as the only resonant term.

$$H = -\tilde{F} abcd^\dagger - \tilde{F}^* a^\dagger b^\dagger c^\dagger d \tag{6.77}$$

with

$$\tilde{F} = E_J \frac{(2\pi)^5 \phi_x^4 \phi_z}{\phi_0^5} p_1 p_2 p_3 p_4 \frac{\epsilon_d}{\Delta_d + i\kappa/2}. \tag{6.78}$$

Now by choosing a moderately large impedance for the JRM modes ($Z = \sqrt{L/(C + C_x)} \sim 100\ \Omega$), which can easily be realized with Josephson junction arrays (see Chapter 3), we can obtain a very large tunable coupling $\mathcal{F}_{jrm} \sim 2\pi \times 2$ MHz. This was obtained with parameters ($C = 15$ fF, $C_x = 160$ fF, $C_y = 20$ fF, $C' = 18$ fF) such that $\omega_x = 2\pi \times 9$ GHz and ω_z resonant with ω_d. Notice also that for the JRM, both the coupling mode, x, and the drive mode, z, is purely harmonic and as such, we can increase the coupling by increasing the drive, ϵ_d.

Chapter 7

Conclusion, outlook and some final thoughts

The field of circuit QED is actively being developed with the aim of building the quantum technology of the future. Several milestones have been reached in the pursuit of solving the challenges listed in Chapter 2. Some of these are the transmon qubit [42], which defines a high coherence qubit, the coupling of the transmon to a transmission line resonator enables high fidelity readout of the qubit states and microwave signals can control the state of the qubit. A number of methods also exist for performing multi-qubit gates and scaling up chips to many qubits are currently being realized [121, 133]. However, more efficient approaches for multi-qubit gates and for scaling are still required before a fully operational quantum computer is developed. Moreover, it is not clear if the fidelity of present readout protocols are sufficient. While scaling of circuit QED may, to some extent, be solved by improved microwave engineering, this thesis argues that the solution should rely on the continuous development of physically motived devices implemented in a modular approach and optimized separately [32].

This final part of the thesis aims at giving a perspective on the challenges in circuit QED that are to come in the near future on the basis of the chapters of the thesis. This perspective will be given in four parts; the first part will consider the challenge of engineering devices that can be integrated in large scale devices, the second part will shed light on the challenge of readout and will also draw on publications not covered in the thesis, part three will discuss control and scalability and part four will

take one step back compared to standard approaches for multi-qubit gates and consider the couplings presented in Chapter 6.

(i) Chapter 3 discusses the use of Josephson arrays as a probe of quantum optics effects and shows how a semi-classical description of the quantum dynamics was insufficient. This is important knowledge for future designs and motivates devices that actively use non-classical effects for control or readout of quantum systems [53, 83, 137, 138, 168]. It was also shown in Chapter 3, how the array can be used to implement ultrastrong coupling dynamics in a manner that allows for efficient readout of this dynamics. Since quantum computers ideally should be as fast as possible, it is imperative to investigate the ultrastrong coupling regime and how it can be used for quantum information processing [239–241]. In conclusion, we argue that arrays of Josephson junction are versatile devices and focus should be put on how to integrate them in current technology and take advantageous of their properties.

(ii) A module already implemented in many current circuit QED experiments is the readout resonator associated with each qubit and possibly also with a Purcell filter. This enables, as mentioned (see Sec. 2.4), high fidelity qubit readout [102]. The full readout process is however still much slower than the time needed for qubit gates, which limits quantum protocols requiring subsequent measurements and gates such as the surface code implementation of quantum error correction [136].

In Chapter 4 we proposed new device for detection of microwave photons. While current technology does not allow for this new device to perform a faster qubit readout, the strategy presented here may prove better in measuring higher order correlation functions, which can be used for certain quantum simulation protocols [242, 243].

Another downside of the current dispersive readout method is the down time after a measurement due to the photons in the readout resonator. This disables the possibility for a new readout and it also complicates subsequent gates, since the photons dispersively change the qubit frequency. In [11] (see also [244, 245]) it is proposed to employ optimal control theory to reset the readout resonator as fast as possible.

Finally, some quantum protocols may be improved by carefully considering the readout signal in a more complete analysis. Such an example is presented in [12], where a quantum teleportation scheme is simplified but requires a full Bayesian analysis [246, 247] of the readout for high fidelity operations. As such, we conclude that while readout of quantum systems is possible with high fidelity there are still challenges that needs attention and the pursuit for future development should be inspired by approaches

in Chapter 4 and in [11, 12].

(iii) The scaling to many qubit systems is the motivation for Chapter 5, as many qubits requires a proportionally large overhead of classical operations. For example, the surface code [136] requires classical operations that scales as the number of physical qubits squared (although the operations are parallizable) [248]. This creates a huge overhead of classical operations and strategies for how to performed these operation in an optimal way is needed. The approach taken in Chapter 5 is that many classical operations can be performed in parallel within the cryogenic environment and a few possible control elements are proposed. Together with optimized classical microwave control [134], the classical overhead may be performed more efficiently. As already alluded to, parts of the surface code may be implemented in this way in a completely autonomous manner.

(iv) The challenge of high fidelity multi-qubit operation is also touched upon in Chapter 6. Many other approach exist and aims either at improving already known gates [125, 249, 250] or by implementing new approaches [126, 127]. In Chapter 6, an alternative approach to couple different quantum systems with large differences in transition frequencies is proposed. The idea of this gate is to couple the qubit via a parametrically pumped resonator. The approach is very similar to the gate already experimentally implemented in [127], however the gate in Chapter 6 does not add phase noise to the same extent as [127]. The physical implementation in [127] encourages a similar experimental realization of the gate proposed Chapter 6 and in particular it encourages more effort to be put into flux-driven gates.

While most this thesis is considering quantum information encoded in transmon qubits, there is also a growing awareness of using the large Hilbert spaces of resonator fields as quantum memories [61]. Chapter 6 also considered this new path by encoding quantum states into the degenerate steady states of a two-photon driven Kerr-resonator [222] and performing adiabatic quantum computing with these [14]. In contrast to [61], the approach in [14] does not rely on dynamically corrected quantum states [60]. We extend the model of [222] using the LHZ scheme [237] which allows for the encoding of general Ising problems. The main prerequisite for this approach to solve large scale optimization problems in the implementation of a controllable four-body interaction, which we propose the implementation of in Chapter 6.

With these final remarks, it is argued that the research presented in this thesis contributes to solving the challenges listed in Chapter 2. While these challenges will persist long into the future, quantum technologies

may already emerge in a near future and the results in this thesis open new avenues in making this possible. In conclusion this thesis presents a number of quantum devices that can be implemented with current technology and serve to open further research in the field of circuit QED.

Bibliography

[1] C. K. Andersen and K. Mølmer, *Squeezing of collective excitations in spin ensembles*, Phys. Rev. A **86**, 043831 (2012).

[2] C. K. Andersen and K. Mølmer, *Effective description of tunneling in a time-dependent potential with applications to voltage switching in josephson junctions*, Phys. Rev. A **87**, 052119 (2013).

[3] C. K. Andersen, G. Oelsner, E. Il'ichev, and K. Mølmer, *Quantized resonator field coupled to a current-biased josephson junction in circuit qed*, Phys. Rev. A **89**, 033853 (2014).

[4] M. C. Tichy and C. K. Andersen, *Comment on "contextuality in bosonic bunching"*, Phys. Rev. Lett. **113**, 138901 (2014).

[5] C. K. Andersen and K. Mølmer, *Circuit qed flip-flop memory with all-microwave switching*, Phys. Rev. Applied **3**, 024002 (2015).

[6] C. K. Andersen and K. Mølmer, *Multifrequency modes in superconducting resonators: Bridging frequency gaps in off-resonant couplings*, Phys. Rev. A **91**, 023828 (2015).

[7] C. K. Andersen, J. Kerckhoff, K. W. Lehnert, B. J. Chapman, and K. Mølmer, *Closing a quantum feedback loop inside a cryostat: Autonomous state preparation and long-time memory of a superconducting qubit*, Phys. Rev. A **93**, 012346 (2016).

[8] G. Oelsner, C. Andersen, M. Rehák, M. Schmelz, S. Anders, M. Grajcar, U. Hübner, K. Mølmer, and E. Il'ichev, *Detection of weak microwave fields with an underdamped josephson junction*, arXiv preprint arXiv:1605.05935 (2016).

[9] C. K. Andersen and A. Blais, *Ultrastrong coupling dynamics with a transmon qubit*, arXiv preprint arXiv:1607.03770 (2016).

[10] C. K. Andersen, A. Kamal, M. H. Devoret, and A. Blais, *Quantum versus classical switching dynamics of driven-dissipative kerr resonators*, in preparation (2016).

[11] S. Boutin, C. K. Andersen, J. Venkatraman, and A. Blais, *Resonator reset in circuit qed by optimal control for large open quantum systems*, in preparation (2016).

[12] E. Greplova, K. Mølmer, and C. K. Andersen, *Quantum teleportaion with continous measurements*, in preparation (2016).

[13] H. L. Mortensen, K. Mølmer, and C. K. Andersen, *Normal modes of a superconducting transmission-line resonator with embedded lumped element circuit components*, arXiv preprint arXiv:1607.04416 (2016).

[14] S. Puri, C. K. Andersen, A. Grimsmo, and A. Blais, *Adiabatic quantum computing with parametrically driven kerr resonator*, in preparation (2016).

[15] C. K. Andersen and A. C. J. Wade, *Bohr vs. einstein: Fortolkning af kvantemekanikken*, Kvant (2013).

[16] A. Einstein, B. Podolsky, and N. Rosen, *Can quantum-mechanical description of physical reality be considered complete?*, Phys. Rev. **47**, 777 (1935).

[17] N. Bohr, *Can quantum-mechanical description of physical reality be considered complete?*, Phys. Rev. **48**, 696 (1935).

[18] W. K. Wootters and W. H. Zurek, *A single quantum cannot be cloned*, Nature **299**, 802 (1982).

[19] D. Deutsch, in *Proceedings of the Royal Society of London A: Mathematical, Physical and Engineering Sciences* (The Royal Society, 1985), vol. 400, pp. 97–117.

[20] D. Deutsch and R. Jozsa, in *Proceedings of the Royal Society of London A: Mathematical, Physical and Engineering Sciences* (The Royal Society, 1992), vol. 439, pp. 553–558.

[21] P. W. Shor, in *Foundations of Computer Science, 1994 Proceedings., 35th Annual Symposium on* (IEEE, 1994), pp. 124–134.

[22] A. d. Touzalin, C. Marcus, F. Heijman, I. Cirac, R. Murray, and T. Calarco, *Quantum manifesto: A new era of technology* (2016).

[23] L. M. Vandersypen, M. Steffen, G. Breyta, C. S. Yannoni, M. H. Sherwood, and I. L. Chuang, *Experimental realization of shor's quantum factoring algorithm using nuclear magnetic resonance*, Nature **414**, 883 (2001).

[24] J. I. Cirac and P. Zoller, *Quantum computations with cold trapped ions*, Phys. Rev. Lett. **74**, 4091 (1995).

[25] T. Monz, D. Nigg, E. A. Martinez, M. F. Brandl, P. Schindler, R. Rines, S. X. Wang, I. L. Chuang, and R. Blatt, *Realization of a scalable shor algorithm*, Science **351**, 1068 (2016).

[26] M. Saffman, T. G. Walker, and K. Mølmer, *Quantum information with rydberg atoms*, Rev. Mod. Phys. **82**, 2313 (2010).

[27] I. Bloch, J. Dalibard, and S. Nascimbène, *Quantum simulations with ultracold quantum gases*, Nature Physics **8**, 267 (2012).

[28] D. Loss and D. P. DiVincenzo, *Quantum computation with quantum dots*, Phys. Rev. A **57**, 120 (1998).

[29] A. Wallraff, D. I. Schuster, A. Blais, L. Frunzio, R.-S. Huang, J. Majer, S. Kumar, S. M. Girvin, and R. J. Schoelkopf, *Strong coupling of a single photon to a superconducting qubit using circuit quantum electrodynamics*, Nature **431**, 162 (2004).

[30] A. Blais, R.-S. Huang, A. Wallraff, S. M. Girvin, and R. J. Schoelkopf, *Cavity quantum electrodynamics for superconducting electrical circuits: An architecture for quantum computation*, Phys. Rev. A **69**, 062320 (2004).

[31] A. Blais, J. Gambetta, A. Wallraff, D. I. Schuster, S. M. Girvin, M. H. Devoret, and R. J. Schoelkopf, *Quantum-information processing with circuit quantum electrodynamics*, Phys. Rev. A **75**, 032329 (2007).

[32] M. H. Devoret and R. J. Schoelkopf, *Superconducting circuits for quantum information: an outlook*, Science **339**, 1169 (2013).

[33] M. A. Nielsen and I. L. Chuang, *Quantum computation and quantum information* (Cambridge university press, 2010).

[34] D. P. DiVincenzo et al., *The physical implementation of quantum computation*, arXiv preprint quant-ph/0002077 (2000).

[35] J. M. Martinis, *Qubit metrology for building a fault-tolerant quantum computer*, arXiv preprint arXiv:1510.01406 (2015).

[36] J. M. Gambetta, J. M. Chow, and M. Steffen, *Building logical qubits in a superconducting quantum computing system*, arXiv preprint arXiv:1510.04375 (2015).

[37] M. H. Devoret, *Quantum fluctuations in electrical circuits* (Les Houches, Session LXIII, 1995).

[38] J. D. Jackson, *Classical electrodynamics* (Wiley, 1999), 3rd ed.

[39] Y. Nakamura, Y. A. Pashkin, and J. Tsai, *Coherent control of macroscopic quantum states in a single-cooper-pair box*, Nature **398**, 786 (1999).

[40] S. Girvin, M. Devoret, and R. Schoelkopf, *Circuit qed and engineering charge-based superconducting qubits*, Physica Scripta **2009**, 014012 (2009).

[41] D. Vion, A. Aassime, A. Cottet, P. Joyez, H. Pothier, C. Urbina, D. Esteve, and M. H. Devoret, *Manipulating the quantum state of an electrical circuit*, Science **296**, 886 (2002).

[42] J. Koch, T. M. Yu, J. Gambetta, A. A. Houck, D. I. Schuster, J. Majer, A. Blais, M. H. Devoret, S. M. Girvin, and R. J. Schoelkopf, *Charge-insensitive qubit design derived from the cooper pair box*, Phys. Rev. A **76**, 042319 (2007).

[43] J. A. Schreier, A. A. Houck, J. Koch, D. I. Schuster, B. R. Johnson, J. M. Chow, J. M. Gambetta, J. Majer, L. Frunzio, M. H. Devoret, et al., *Suppressing charge noise decoherence in superconducting charge qubits*, Phys. Rev. B **77**, 180502 (2008).

[44] A. Houck, D. Schuster, J. Gambetta, J. Schreier, B. Johnson, J. Chow, L. Frunzio, J. Majer, M. Devoret, S. Girvin, et al., *Generating single microwave photons in a circuit*, Nature **449**, 328 (2007).

[45] R. Barends, J. Kelly, A. Megrant, D. Sank, E. Jeffrey, Y. Chen, Y. Yin, B. Chiaro, J. Mutus, C. Neill, et al., *Coherent josephson qubit suitable for scalable quantum integrated circuits*, Phys. Rev. Lett. **111**, 080502 (2013).

[46] H. Paik, D. I. Schuster, L. S. Bishop, G. Kirchmair, G. Catelani, A. P. Sears, B. R. Johnson, M. J. Reagor, L. Frunzio, L. I. Glazman, et al., *Observation of high coherence in josephson junction qubits measured in a three-dimensional circuit qed architecture*, Phys. Rev. Lett. **107**, 240501 (2011).

[47] J. Mooij, T. Orlando, L. Levitov, L. Tian, C. H. Van der Wal, and S. Lloyd, *Josephson persistent-current qubit*, Science **285**, 1036 (1999).

[48] C. H. Van der Wal, A. Ter Haar, F. Wilhelm, R. Schouten, C. Harmans, T. Orlando, S. Lloyd, and J. Mooij, *Quantum superposition of macroscopic persistent-current states*, Science **290**, 773 (2000).

[49] I. Chiorescu, Y. Nakamura, C. M. Harmans, and J. Mooij, *Coherent quantum dynamics of a superconducting flux qubit*, Science **299**, 1869 (2003).

[50] J. Bourassa, J. M. Gambetta, A. A. Abdumalikov, O. Astafiev, Y. Nakamura, and A. Blais, *Ultrastrong coupling regime of cavity qed with phase-biased flux qubits*, Phys. Rev. A **80**, 032109 (2009).

[51] T. Orlando, J. Mooij, L. Tian, C. H. van der Wal, L. Levitov, S. Lloyd, and J. Mazo, *Superconducting persistent-current qubit*, Physical Review B **60**, 15398 (1999).

[52] V. E. Manucharyan, J. Koch, L. I. Glazman, and M. H. Devoret, *Fluxonium: Single cooper-pair circuit free of charge offsets*, Science **326**, 113 (2009).

[53] U. Vool, I. M. Pop, K. Sliwa, B. Abdo, C. Wang, T. Brecht, Y. Y. Gao, S. Shankar, M. Hatridge, G. Catelani, et al., *Non-poissonian quantum jumps of a fluxonium qubit due to quasiparticle excitations*, Phys. Rev. Lett. **113**, 247001 (2014).

[54] M. T. Bell, I. A. Sadovskyy, L. B. Ioffe, A. Y. Kitaev, and M. E. Gershenson, *Quantum superinductor with tunable nonlinearity*, Phys. Rev. Lett. **109**, 137003 (2012).

[55] N. A. Masluk, I. M. Pop, A. Kamal, Z. K. Minev, and M. H. Devoret, *Microwave characterization of josephson junction arrays: Implementing a low loss superinductance*, Phys. Rev. Lett. **109**, 137002 (2012).

[56] I. M. Pop, K. Geerlings, G. Catelani, R. J. Schoelkopf, L. I. Glazman, and M. H. Devoret, *Coherent suppression of electromagnetic dissipation due to superconducting quasiparticles*, Nature **508**, 369 (2014).

[57] J. M. Martinis, S. Nam, J. Aumentado, and C. Urbina, *Rabi oscillations in a large josephson-junction qubit*, Phys. Rev. Lett. **89**, 117901 (2002).

[58] A. Berkley, H. Xu, R. Ramos, M. Gubrud, F. Strauch, P. Johnson, J. Anderson, A. Dragt, C. Lobb, and F. Wellstood, *Entangled macroscopic quantum states in two superconducting qubits*, Science **300**, 1548 (2003).

[59] B. Vlastakis, G. Kirchmair, Z. Leghtas, S. E. Nigg, L. Frunzio, S. M. Girvin, M. Mirrahimi, M. H. Devoret, and R. J. Schoelkopf, *Deterministically encoding quantum information using 100-photon schrödinger cat states*, Science **342**, 607 (2013).

[60] M. Mirrahimi, Z. Leghtas, V. V. Albert, S. Touzard, R. J. Schoelkopf, L. Jiang, and M. H. Devoret, *Dynamically protected cat-qubits: a new paradigm for universal quantum computation*, New Journal of Physics **16**, 045014 (2014).

[61] N. Ofek, A. Petrenko, R. Heeres, P. Reinhold, Z. Leghtas, B. Vlastakis, Y. Liu, L. Frunzio, S. Girvin, L. Jiang, et al., *Extending the lifetime of a quantum bit with error correction in superconducting circuits*, Nature (2016).

[62] S. Haroche and J. M. Raimond, *Exploring the quantum* (Oxford Univ. Press, 2006).

[63] A. Fedorov, A. Feofanov, P. Macha, P. Forn-Díaz, C. Harmans, and J. Mooij, *Strong coupling of a quantum oscillator to a flux qubit at its symmetry point*, Physical review letters **105**, 060503 (2010).

[64] M. Hofheinz, E. Weig, M. Ansmann, R. C. Bialczak, E. Lucero, M. Neeley, A. O'connell, H. Wang, J. M. Martinis, and A. Cleland, *Generation of fock states in a superconducting quantum circuit*, Nature **454**, 310 (2008).

[65] J. Fink, M. Göppl, M. Baur, R. Bianchetti, P. Leek, A. Blais, and A. Wallraff, *Climbing the jaynes–cummings ladder and observing its nonlinearity in a cavity qed system*, Nature **454**, 315 (2008).

[66] J. Mlynek, A. Abdumalikov, C. Eichler, and A. Wallraff, *Observation of dicke superradiance for two artificial atoms in a cavity with high decay rate*, Nature communications **5** (2014).

[67] S. E. Nigg, H. Paik, B. Vlastakis, G. Kirchmair, S. Shankar, L. Frunzio, M. H. Devoret, R. J. Schoelkopf, and S. M. Girvin, *Black-box superconducting circuit quantization*, Phys. Rev. Lett. **108**, 240502 (2012).

[68] G. Kirchmair, B. Vlastakis, Z. Leghtas, S. E. Nigg, H. Paik, E. Ginossar, M. Mirrahimi, L. Frunzio, S. M. Girvin, and R. J. Schoelkopf, *Observation of quantum state collapse and revival due to the single-photon kerr effect*, Nature **495**, 205 (2013).

[69] D. I. Schuster, A. Wallraff, A. Blais, L. Frunzio, R.-S. Huang, J. Majer, S. M. Girvin, and R. J. Schoelkopf, *ac stark shift and dephasing of a superconducting qubit strongly coupled to a cavity field*, Phys. Rev. Lett. **94**, 123602 (2005).

[70] M. Boissonneault, J. M. Gambetta, and A. Blais, *Dispersive regime of circuit qed: Photon-dependent qubit dephasing and relaxation rates*, Phys. Rev. A **79**, 013819 (2009).

[71] M. Boissonneault, J. M. Gambetta, and A. Blais, *Nonlinear dispersive regime of cavity qed: The dressed dephasing model*, Phys. Rev. A **77**, 060305 (2008).

[72] C. Gardiner and P. Zoller, *Quantum noise* (Springer, 2004), 3rd ed.

[73] M. P. da Silva, D. Bozyigit, A. Wallraff, and A. Blais, *Schemes for the observation of photon correlation functions in circuit qed with linear detectors*, Phys. Rev. A **82**, 043804 (2010).

[74] A. Wallraff, D. I. Schuster, A. Blais, L. Frunzio, J. Majer, M. H. Devoret, S. M. Girvin, and R. J. Schoelkopf, *Approaching unit visibility for control of a superconducting qubit with dispersive readout*, Phys. Rev. Lett. **95**, 060501 (2005).

[75] J. Gambetta, A. Blais, M. Boissonneault, A. A. Houck, D. I. Schuster, and S. M. Girvin, *Quantum trajectory approach to circuit qed: Quantum jumps and the zeno effect*, Phys. Rev. A **77**, 012112 (2008).

[76] C. M. Caves, *Quantum limits on noise in linear amplifiers*, Phys. Rev. D **26**, 1817 (1982).

[77] A. A. Clerk, M. H. Devoret, S. M. Girvin, F. Marquardt, and R. J. Schoelkopf, *Introduction to quantum noise, measurement, and amplification*, Rev. Mod. Phys. **82**, 1155 (2010).

[78] C. M. Caves, J. Combes, Z. Jiang, and S. Pandey, *Quantum limits on phase-preserving linear amplifiers*, Phys. Rev. A **86**, 063802 (2012).

[79] B. Yurke, P. G. Kaminsky, R. E. Miller, E. A. Whittaker, A. D. Smith, A. H. Silver, and R. W. Simon, *Observation of 4.2-k equilibrium-noise squeezing via a josephson-parametric amplifier*, Phys. Rev. Lett. **60**, 764 (1988).

[80] M. Castellanos-Beltran, K. Irwin, G. Hilton, L. Vale, and K. Lehnert, *Amplification and squeezing of quantum noise with a tunable josephson metamaterial*, Nature Physics **4**, 929 (2008).

[81] C. Eichler and A. Wallraff, *Controlling the dynamic range of a josephson parametric amplifier*, EPJ Quantum Technology **1**, 1 (2014).

[82] C. Eichler, D. Bozyigit, and A. Wallraff, *Characterizing quantum microwave radiation and its entanglement with superconducting qubits using linear detectors*, Phys. Rev. A **86**, 032106 (2012).

[83] C. Eichler, Y. Salathe, J. Mlynek, S. Schmidt, and A. Wallraff, *Quantum-limited amplification and entanglement in coupled nonlinear resonators*, Phys. Rev. Lett. **113**, 110502 (2014).

[84] R. Vijay, C. Macklin, D. Slichter, S. Weber, K. Murch, R. Naik, A. N. Korotkov, and I. Siddiqi, *Stabilizing rabi oscillations in a superconducting qubit using quantum feedback*, Nature **490**, 77 (2012).

[85] R. Vijay, D. H. Slichter, and I. Siddiqi, *Observation of quantum jumps in a superconducting artificial atom*, Phys. Rev. Lett. **106**, 110502 (2011).

[86] T. Yamamoto, K. Inomata, M. Watanabe, K. Matsuba, T. Miyazaki, W. Oliver, Y. Nakamura, and J. Tsai, *Flux-driven josephson parametric amplifier*, Appl. Phys. Lett. p. 042510 (2008).

[87] M. Hatridge, R. Vijay, D. H. Slichter, J. Clarke, and I. Siddiqi, *Dispersive magnetometry with a quantum limited squid parametric amplifier*, Phys. Rev. B **83**, 134501 (2011).

[88] N. Bergeal, R. Vijay, V. Manucharyan, I. Siddiqi, R. Schoelkopf, S. Girvin, and M. Devoret, *Analog information processing at the quantum limit with a josephson ring modulator*, Nature Physics **6**, 296 (2010).

[89] N. Bergeal, F. Schackert, M. Metcalfe, R. Vijay, V. Manucharyan, L. Frunzio, D. Prober, R. Schoelkopf, S. Girvin, and M. Devoret, *Phase-preserving amplification near the quantum limit with a josephson ring modulator*, Nature **465**, 64 (2010).

[90] P. Campagne-Ibarcq, P. Six, L. Bretheau, A. Sarlette, M. Mirrahimi, P. Rouchon, and B. Huard, *Observing quantum state diffusion by heterodyne detection of fluorescence*, Phys. Rev. X **6**, 011002 (2016).

[91] K. O'Brien, C. Macklin, I. Siddiqi, and X. Zhang, *Resonant phase matching of josephson junction traveling wave parametric amplifiers*, Phys. Rev. Lett. **113**, 157001 (2014).

[92] C. Macklin, K. O'Brien, D. Hover, M. Schwartz, V. Bolkhovsky, X. Zhang, W. Oliver, and I. Siddiqi, *A near–quantum-limited josephson traveling-wave parametric amplifier*, Science **350**, 307 (2015).

[93] T. White, J. Mutus, I.-C. Hoi, R. Barends, B. Campbell, Y. Chen, Z. Chen, B. Chiaro, A. Dunsworth, E. Jeffrey, et al., *Traveling wave parametric amplifier with josephson junctions using minimal resonator phase matching*, Applied Physics Letters **106**, 242601 (2015).

[94] K. Inomata, Z. Lin, K. Koshino, W. D. Oliver, J.-S. Tsai, T. Yamamoto, and Y. Nakamura, *Single microwave-photon detector using an artificial λ-type three-level system*, arXiv preprint arXiv:1601.05513 (2016).

[95] B. Fan, A. F. Kockum, J. Combes, G. Johansson, I.-c. Hoi, C. M. Wilson, P. Delsing, G. J. Milburn, and T. M. Stace, *Breakdown of the cross-kerr scheme for photon counting*, Phys. Rev. Lett. **110**, 053601 (2013).

[96] S. R. Sathyamoorthy, L. Tornberg, A. F. Kockum, B. Q. Baragiola, J. Combes, C. M. Wilson, T. M. Stace, and G. Johansson, *Quantum nondemolition detection of a propagating microwave photon*, Phys. Rev. Lett. **112**, 093601 (2014).

[97] G. Romero, J. J. García-Ripoll, and E. Solano, *Microwave photon detector in circuit qed*, Phys. Rev. Lett. **102**, 173602 (2009).

[98] B. Peropadre, G. Romero, G. Johansson, C. M. Wilson, E. Solano, and J. J. García-Ripoll, *Approaching perfect microwave photodetection in circuit qed*, Phys. Rev. A **84**, 063834 (2011).

[99] Y.-F. Chen, D. Hover, S. Sendelbach, L. Maurer, S. T. Merkel, E. J. Pritchett, F. K. Wilhelm, and R. McDermott, *Microwave photon counter based on josephson junctions*, Phys. Rev. Lett. **107**, 217401 (2011).

[100] A. Poudel, R. McDermott, and M. G. Vavilov, *Quantum efficiency of a microwave photon detector based on a current-biased josephson junction*, Phys. Rev. B **86**, 174506 (2012).

[101] H. M. Wiseman and G. J. Milburn, *Quantum measurement and control* (Cambridge University Press, 2009).

[102] E. Jeffrey, D. Sank, J. Y. Mutus, T. C. White, J. Kelly, R. Barends, Y. Chen, Z. Chen, B. Chiaro, A. Dunsworth, et al., *Fast accurate state measurement with superconducting qubits*, Phys. Rev. Lett. **112**, 190504 (2014).

[103] M. Reed, B. Johnson, A. Houck, L. DiCarlo, J. Chow, D. Schuster, L. Frunzio, and R. Schoelkopf, *Fast reset and suppressing spontaneous emission of a superconducting qubit*, Applied Physics Letters **96**, 203110 (2010).

[104] N. T. Bronn, E. Magesan, N. A. Masluk, J. M. Chow, J. M. Gambetta, and M. Steffen, *Reducing spontaneous emission in circuit quantum electrodynamics by a combined readout/filter technique*, Applied Superconductivity, IEEE Transactions on **25**, 1 (2015).

[105] E. A. Sete, J. M. Martinis, and A. N. Korotkov, *Quantum theory of a bandpass purcell filter for qubit readout*, Physical Review A **92**, 012325 (2015).

[106] D. M. Pozar, *Microwave engineering* (John Wiley & Sons, 2009).

[107] F. Mallet, F. R. Ong, A. Palacios-Laloy, F. Nguyen, P. Bertet, D. Vion, and D. Esteve, *Single-shot qubit readout in circuit quantum electrodynamics*, Nature Physics **5**, 791 (2009).

[108] R. Vijay, M. Devoret, and I. Siddiqi, *Invited review article: The josephson bifurcation amplifier*, Review of Scientific Instruments **80**, 111101 (2009).

[109] M. D. Reed, L. DiCarlo, B. R. Johnson, L. Sun, D. I. Schuster, L. Frunzio, and R. J. Schoelkopf, *High-fidelity readout in circuit quantum electrodynamics using the jaynes-cummings nonlinearity*, Phys. Rev. Lett. **105**, 173601 (2010).

[110] M. Boissonneault, J. M. Gambetta, and A. Blais, *Improved superconducting qubit readout by qubit-induced nonlinearities*, Phys. Rev. Lett. **105**, 100504 (2010).

[111] N. Didier, J. Bourassa, and A. Blais, *Fast quantum nondemolition readout by parametric modulation of longitudinal qubit-oscillator interaction*, Phys. Rev. Lett. **115**, 203601 (2015).

[112] N. Didier, A. Kamal, W. D. Oliver, A. Blais, and A. A. Clerk, *Heisenberg-limited qubit read-out with two-mode squeezed light*, Phys. Rev. Lett. **115**, 093604 (2015).

[113] M. Steffen, J. M. Martinis, and I. L. Chuang, *Accurate control of josephson phase qubits*, Phys. Rev. B **68**, 224518 (2003).

[114] E. Lucero, M. Hofheinz, M. Ansmann, R. C. Bialczak, N. Katz, M. Neeley, A. D. O'Connell, H. Wang, A. N. Cleland, and J. M. Martinis, *High-fidelity gates in a single josephson qubit*, Phys. Rev. Lett. **100**, 247001 (2008).

[115] F. Motzoi, J. M. Gambetta, P. Rebentrost, and F. K. Wilhelm, *Simple pulses for elimination of leakage in weakly nonlinear qubits*, Phys. Rev. Lett. **103**, 110501 (2009).

[116] J. M. Chow, L. DiCarlo, J. M. Gambetta, F. Motzoi, L. Frunzio, S. M. Girvin, and R. J. Schoelkopf, *Optimized driving of superconducting artificial atoms for improved single-qubit gates*, Phys. Rev. A **82**, 040305 (2010).

[117] E. Lucero, J. Kelly, R. C. Bialczak, M. Lenander, M. Mariantoni, M. Neeley, A. D. O'Connell, D. Sank, H. Wang, M. Weides, et al., *Reduced phase error through optimized control of a superconducting qubit*, Phys. Rev. A **82**, 042339 (2010).

[118] J. Majer, J. Chow, J. Gambetta, J. Koch, B. Johnson, J. Schreier, L. Frunzio, D. Schuster, A. Houck, A. Wallraff, et al., *Coupling superconducting qubits via a cavity bus*, Nature **449**, 443 (2007).

[119] Y. Salathé, M. Mondal, M. Oppliger, J. Heinsoo, P. Kurpiers, A. Potočnik, A. Mezzacapo, U. Las Heras, L. Lamata, E. Solano, et al., *Digital quantum simulation of spin models with circuit quantum electrodynamics*, Phys. Rev. X **5**, 021027 (2015).

[120] L. DiCarlo, J. Chow, J. Gambetta, L. S. Bishop, B. Johnson, D. Schuster, J. Majer, A. Blais, L. Frunzio, S. Girvin, et al., *Demonstration of two-qubit algorithms with a superconducting quantum processor*, Nature **460**, 240 (2009).

[121] R. Barends, J. Kelly, A. Megrant, A. Veitia, D. Sank, E. Jeffrey, T. White, J. Mutus, A. Fowler, B. Campbell, et al., *Superconducting quantum circuits at the surface code threshold for fault tolerance*, Nature **508**, 500 (2014).

[122] C. Rigetti and M. Devoret, *Fully microwave-tunable universal gates in superconducting qubits with linear couplings and fixed transition frequencies*, Phys. Rev. B **81**, 134507 (2010).

[123] J. M. Chow, J. M. Gambetta, E. Magesan, D. W. Abraham, A. W. Cross, B. Johnson, N. A. Masluk, C. A. Ryan, J. A. Smolin, S. J. Srinivasan, et al., *Implementing a strand of a scalable fault-tolerant quantum computing fabric*, Nature communications **5** (2014).

[124] A. W. Cross and J. M. Gambetta, *Optimized pulse shapes for a resonator-induced phase gate*, Phys. Rev. A **91**, 032325 (2015).

[125] S. Puri and A. Blais, *High-fidelity resonator-induced phase gate with single-mode squeezing*, Phys. Rev. Lett. **116**, 180501 (2016).

[126] B. Royer, A. L. Grimsmo, N. Didier, and A. Blais, *Fast and high-fidelity entangling gate through parametrically modulated longitudinal coupling*, arXiv preprint arXiv:1603.04424 (2016).

[127] D. C. McKay, S. Filipp, A. Mezzacapo, E. Magesan, J. M. Chow, and J. M. Gambetta, *A universal gate for fixed-frequency qubits via a tunable bus*, arXiv preprint arXiv:1604.03076 (2016).

[128] J. E. Johnson, C. Macklin, D. H. Slichter, R. Vijay, E. B. Weingarten, J. Clarke, and I. Siddiqi, *Heralded state preparation in a superconducting qubit*, Phys. Rev. Lett. **109**, 050506 (2012).

[129] D. Ristè, J. G. van Leeuwen, H.-S. Ku, K. W. Lehnert, and L. DiCarlo, *Initialization by measurement of a superconducting quantum bit circuit*, Phys. Rev. Lett. **109**, 050507 (2012).

[130] K. Geerlings, Z. Leghtas, I. M. Pop, S. Shankar, L. Frunzio, R. J. Schoelkopf, M. Mirrahimi, and M. H. Devoret, *Demonstrating a driven reset protocol for a superconducting qubit*, Phys. Rev. Lett. **110**, 120501 (2013).

[131] P. Campagne-Ibarcq, E. Flurin, N. Roch, D. Darson, P. Morfin, M. Mirrahimi, M. H. Devoret, F. Mallet, and B. Huard, *Persistent control of a superconducting qubit by stroboscopic measurement feedback*, Phys. Rev. X **3**, 021008 (2013).

[132] D. Riste, M. Dukalski, C. Watson, G. De Lange, M. Tiggelman, Y. M. Blanter, K. Lehnert, R. Schouten, and L. DiCarlo, *Deterministic entanglement of superconducting qubits by parity measurement and feedback*, Nature **502**, 350 (2013).

[133] A. Córcoles, E. Magesan, S. J. Srinivasan, A. W. Cross, M. Steffen, J. M. Gambetta, and J. M. Chow, *Demonstration of a quantum error detection code using a square lattice of four superconducting qubits*, Nature communications **6** (2015).

[134] S. Asaad, C. Dickel, S. Poletto, A. Bruno, N. Langford, M. Rol, D. Deurloo, and L. DiCarlo, *Independent, extensible control of same-frequency superconducting qubits by selective broadcasting*, arXiv preprint arXiv:1508.06676 (2015).

[135] D. A. Lidar and T. A. Brun, *Quantum error correction* (Cambridge University Press, 2013).

[136] A. G. Fowler, M. Mariantoni, J. M. Martinis, and A. N. Cleland, *Surface codes: Towards practical large-scale quantum computation*, Phys. Rev. A **86**, 032324 (2012).

[137] K. M. Sliwa, M. Hatridge, A. Narla, S. Shankar, L. Frunzio, R. J. Schoelkopf, and M. H. Devoret, *Reconfigurable josephson circulator/directional amplifier*, Phys. Rev. X **5**, 041020 (2015).

[138] J. Kerckhoff, K. Lalumière, B. J. Chapman, A. Blais, and K. W. Lehnert, *On-chip superconducting microwave circulator from synthetic rotation*, Phys. Rev. Applied **4**, 034002 (2015).

[139] B. J. Chapman, B. A. Moores, E. I. Rosenthal, J. Kerckhoff, and K. Lehnert, *General purpose multiplexing device for cryogenic microwave systems*, Applied Physics Letters **108**, 222602 (2016).

[140] M. Pechal, J.-C. Besse, M. Mondal, M. Oppliger, S. Gasparinetti, and A. Wallraff, *Superconducting switch for fast on-chip routing of quantum microwave fields*, arXiv preprint arXiv:1606.01031 (2016).

[141] J. Bourassa, F. Beaudoin, J. M. Gambetta, and A. Blais, *Josephson-junction-embedded transmission-line resonators: From kerr medium to in-line transmon*, Phys. Rev. A **86**, 013814 (2012).

[142] T. Weißl, B. Küng, E. Dumur, A. K. Feofanov, I. Matei, C. Naud, O. Buisson, F. W. J. Hekking, and W. Guichard, *Kerr coefficients of plasma resonances in josephson junction chains*, Phys. Rev. B **92**, 104508 (2015).

[143] J. Kerckhoff and K. W. Lehnert, *Superconducting microwave multivibrator produced by coherent feedback*, Phys. Rev. Lett. **109**, 153602 (2012).

[144] M. A. Armen and H. Mabuchi, *Low-lying bifurcations in cavity quantum electrodynamics*, Phys. Rev. A **73**, 063801 (2006).

[145] C. Santori, J. S. Pelc, R. G. Beausoleil, N. Tezak, R. Hamerly, and H. Mabuchi, *Quantum noise in large-scale coherent nonlinear photonic circuits*, Phys. Rev. Applied **1**, 054005 (2014).

[146] J. Kerckhoff, M. A. Armen, and H. Mabuchi, *Remnants of semiclassical bistability in the few-photon regime of cavity qed*, Optics express **19**, 24468 (2011).

[147] H. Risken, C. Savage, F. Haake, and D. F. Walls, *Quantum tunneling in dispersive optical bistability*, Phys. Rev. A **35**, 1729 (1987).

[148] M. Dykman and M. Krivoglaz, *Fluctuations in nonlinear systems near bifurcations corresponding to the appearance of new stable states*, Physica A: Statistical Mechanics and its Applications **104**, 480 (1980).

[149] R. Vijay, Ph.D. thesis, Ph. D. thesis, Yale University (2008).

[150] H. A. Kramers, *Brownian motion in a field of force and the diffusion model of chemical reactions*, Physica **7**, 284 (1940).

[151] P. Hänggi, P. Talkner, and M. Borkovec, *Reaction-rate theory: fifty years after kramers*, Rev. Mod. Phys. **62**, 251 (1990).

[152] C. Ciuti and I. Carusotto, *Input-output theory of cavities in the ultrastrong coupling regime: The case of time-independent cavity parameters*, Physical Review A **74**, 033811 (2006).

[153] D. Braak, *Integrability of the rabi model*, Phys. Rev. Lett. **107**, 100401 (2011).

[154] J. Hausinger and M. Grifoni, *Qubit-oscillator system: An analytical treatment of the ultrastrong coupling regime*, Phys. Rev. A **82**, 062320 (2010).

[155] B. Peropadre, P. Forn-Díaz, E. Solano, and J. J. García-Ripoll, *Switchable ultrastrong coupling in circuit qed*, Phys. Rev. Lett. **105**, 023601 (2010).

[156] J. Casanova, G. Romero, I. Lizuain, J. J. García-Ripoll, and E. Solano, *Deep strong coupling regime of the jaynes-cummings model*, Phys. Rev. Lett. **105**, 263603 (2010).

[157] X. Cao, J. You, H. Zheng, and F. Nori, *A qubit strongly coupled to a resonant cavity: asymmetry of the spontaneous emission spectrum beyond the rotating wave approximation*, New Journal of Physics **13**, 073002 (2011).

[158] Z.-J. Ying, M. Liu, H.-G. Luo, H.-Q. Lin, and J. Q. You, *Ground-state phase diagram of the quantum rabi model*, Phys. Rev. A **92**, 053823 (2015).

[159] J. Lolli, A. Baksic, D. Nagy, V. E. Manucharyan, and C. Ciuti, *Ancillary qubit spectroscopy of vacua in cavity and circuit quantum electrodynamics*, Phys. Rev. Lett. **114**, 183601 (2015).

[160] T. Niemczyk, F. Deppe, H. Huebl, E. Menzel, F. Hocke, M. Schwarz, J. Garcia-Ripoll, D. Zueco, T. Hümmer, E. Solano, et al., *Circuit quantum electrodynamics in the ultrastrong-coupling regime*, Nature Physics **6**, 772 (2010).

[161] P. Forn-Díaz, J. Lisenfeld, D. Marcos, J. J. García-Ripoll, E. Solano, C. Harmans, and J. Mooij, *Observation of the bloch-siegert shift in a qubit-oscillator system in the ultrastrong coupling regime*, Physical review letters **105**, 237001 (2010).

[162] P. Forn-Díaz, J. García-Ripoll, B. Peropadre, M. Yurtalan, J.-L. Orgiazzi, R. Belyansky, C. Wilson, and A. Lupascu, *Ultrastrong coupling of a single artificial atom to an electromagnetic continuum*, arXiv preprint arXiv:1602.00416 (2016).

[163] F. Yoshihara, T. Fuse, S. Ashhab, K. Kakuyanagi, S. Saito, and K. Semba, *Superconducting qubit-oscillator circuit beyond the ultrastrong-coupling regime*, arXiv preprint arXiv:1602.00415 (2016).

[164] N. Samkharadze, A. Bruno, P. Scarlino, G. Zheng, D. DiVincenzo, L. DiCarlo, and L. Vandersypen, *High kinetic inductance superconducting nanowire resonators for circuit qed in a magnetic field*, arXiv preprint arXiv:1511.01760 (2015).

[165] F. Beaudoin, J. M. Gambetta, and A. Blais, *Dissipation and ultrastrong coupling in circuit qed*, Phys. Rev. A **84**, 043832 (2011).

[166] C. Wilson, G. Johansson, A. Pourkabirian, M. Simoen, J. Johansson, T. Duty, F. Nori, and P. Delsing, *Observation of the dynamical casimir effect in a superconducting circuit*, Nature **479**, 376 (2011).

[167] S. Shevchenko, S. Ashhab, and F. Nori, *Landau–zener–stückelberg interferometry*, Physics Reports **492**, 1 (2010).

[168] V. Schmitt, X. Zhou, K. Juliusson, B. Royer, A. Blais, P. Bertet, D. Vion, and D. Esteve, *Multiplexed readout of transmon qubits with josephson bifurcation amplifiers*, Phys. Rev. A **90**, 062333 (2014).

[169] G. Kurizki, P. Bertet, Y. Kubo, K. Mølmer, D. Petrosyan, P. Rabl, and J. Schmiedmayer, *Quantum technologies with hybrid systems*, Proceedings of the National Academy of Sciences **112**, 3866 (2015).

[170] A. Stockklauser, V. F. Maisi, J. Basset, K. Cujia, C. Reichl, W. Wegscheider, T. Ihn, A. Wallraff, and K. Ensslin, *Microwave emission from hybridized states in a semiconductor charge qubit*, Phys. Rev. Lett. **115**, 046802 (2015).

[171] A. Narla, S. Shankar, M. Hatridge, Z. Leghtas, K. Sliwa, E. Zalys-Geller, S. Mundhada, W. Pfaff, L. Frunzio, R. Schoelkopf, et al., *Robust concurrent remote entanglement between two superconducting qubits*, arXiv preprint arXiv:1603.03742 (2016).

[172] N. Grønbech-Jensen, M. G. Castellano, F. Chiarello, M. Cirillo, C. Cosmelli, L. V. Filippenko, R. Russo, and G. Torrioli, *Microwave-induced thermal escape in josephson junctions*, Phys. Rev. Lett. **93**, 107002 (2004).

[173] M. H. Devoret, J. M. Martinis, and J. Clarke, *Measurements of macroscopic quantum tunneling out of the zero-voltage state of a current-biased josephson junction*, Phys. Rev. Lett. **55**, 1908 (1985).

[174] M. Razavy, *Quantum theory of tunneling*, vol. 1222445599 (World Scientific, 2003).

[175] Y. Yu, S. Han, X. Chu, S.-I. Chu, and Z. Wang, *Coherent temporal oscillations of macroscopic quantum states in a josephson junction*, Science **296**, 889 (2002).

[176] R. De La Madrid and M. Gadella, *A pedestrian introduction to gamow vectors*, American Journal of Physics **70**, 626 (2002).

[177] O. Civitarese and M. Gadella, *Physical and mathematical aspects of gamow states*, Physics Reports **396**, 41 (2004).

[178] J. Dalibard, Y. Castin, and K. Mølmer, *Wave-function approach to dissipative processes in quantum optics*, Phys. Rev. Lett. **68**, 580 (1992).

[179] J. G. Muga, J. Palao, B. Navarro, and I. Egusquiza, *Complex absorbing potentials*, Physics reports **395**, 357 (2004).

[180] G. S. Paraoanu, *Running-phase state in a josephson washboard potential*, Phys. Rev. B **72**, 134528 (2005).

[181] A. O. Caldeira and A. J. Leggett, *Influence of dissipation on quantum tunneling in macroscopic systems*, Phys. Rev. Lett. **46**, 211 (1981).

[182] A. Caldeira and A. J. Leggett, *Quantum tunnelling in a dissipative system*, Annals of Physics **149**, 374 (1983).

[183] P. Macha, S. van Der Ploeg, G. Oelsner, E. Il'ichev, H.-G. Meyer, S. Wünsch, and M. Siegel, *Losses in coplanar waveguide resonators at millikelvin temperatures*, Applied Physics Letters **96**, 062503 (2010).

[184] G. Oelsner, L. Revin, E. Il'Ichev, A. Pankratov, H.-G. Meyer, L. Grönberg, J. Hassel, and L. Kuzmin, *Underdamped josephson junction as a switching current detector*, Applied Physics Letters **103**, 142605 (2013).

[185] H. F. Yu, X. B. Zhu, Z. H. Peng, W. H. Cao, D. J. Cui, Y. Tian, G. H. Chen, D. N. Zheng, X. N. Jing, L. Lu, et al., *Quantum and classical resonant escapes of a strongly driven josephson junction*, Phys. Rev. B **81**, 144518 (2010).

[186] M. V. Fistul, A. Wallraff, and A. V. Ustinov, *Quantum escape of the phase in a strongly driven josephson junction*, Phys. Rev. B **68**, 060504 (2003).

[187] S. Guozhu, W. Yiwen, C. Junyu, C. Jian, J. Zhengming, K. Lin, X. Weiwei, Y. Yang, H. Siyuan, and W. Peiheng, *Microwave-induced phase escape in a josephson tunnel junction*, Phys. Rev. B **77**, 104531 (2008).

[188] H. J. Carmichael, *Statistical Methods in Quantum Optics 2: Non-Classical Fields* (Springer Science & Business Media, 2009).

[189] S. Anders, M. Schmelz, L. Fritzsch, R. Stolz, V. Zakosarenko, T. Schönau, and H. Meyer, *Sub-micrometer-sized, cross-type nb–alox–nb tunnel junctions with low parasitic capacitance*, Superconductor Science and Technology **22**, 064012 (2009).

[190] S. N. Shevchenko, G. Oelsner, Y. S. Greenberg, P. Macha, D. S. Karpov, M. Grajcar, U. Hübner, A. N. Omelyanchouk, and E. Il'ichev, *Amplification and attenuation of a probe signal by doubly dressed states*, Phys. Rev. B **89**, 184504 (2014).

[191] A. O. Caldeira and A. J. Leggett, *Influence of dissipation on quantum tunneling in macroscopic systems*, Physical Review Letters **46**, 211 (1981).

[192] R. H. Brown and R. Q. Twiss, *Correlation between photons in two coherent beams of light*, Nature **177**, 27 (1956).

[193] D. Bozyigit, C. Lang, L. Steffen, J. Fink, C. Eichler, M. Baur, R. Bianchetti, P. Leek, S. Filipp, M. Da Silva, et al., *Antibunching of microwave-frequency photons observed in correlation measurements using linear detectors*, Nature Physics **7**, 154 (2011).

[194] H. Mabuchi, *Cavity-qed models of switches for attojoule-scale nanophotonic logic*, Phys. Rev. A **80**, 045802 (2009).

[195] J. Kerckhoff, H. I. Nurdin, D. S. Pavlichin, and H. Mabuchi, *Designing quantum memories with embedded control: Photonic circuits for autonomous quantum error correction*, Phys. Rev. Lett. **105**, 040502 (2010).

[196] A. E. B. Nielsen and J. Kerckhoff, *Efficient all-optical switch using a Λ atom in a cavity qed system*, Phys. Rev. A **84**, 043821 (2011).

[197] R. Bose, D. Sridharan, H. Kim, G. S. Solomon, and E. Waks, *Low-photon-number optical switching with a single quantum dot coupled to a photonic crystal cavity*, Phys. Rev. Lett. **108**, 227402 (2012).

[198] W. Chen, K. M. Beck, R. Bücker, M. Gullans, M. D. Lukin, H. Tanji-Suzuki, and V. Vuletić, *All-optical switch and transistor gated by one stored photon*, Science p. 1237242 (2013).

[199] Y.-D. Kwon, M. A. Armen, and H. Mabuchi, *Femtojoule-scale all-optical latching and modulation via cavity nonlinear optics*, Phys. Rev. Lett. **111**, 203002 (2013).

[200] B. Zou, Z. Tan, M. Musa, and Y. Zhu, *Interaction-free all-optical switching at low light intensities in a multiatom cavity-qed system*, Phys. Rev. A **89**, 023806 (2014).

[201] M. Mariantoni, F. Deppe, A. Marx, R. Gross, F. K. Wilhelm, and E. Solano, *Two-resonator circuit quantum electrodynamics: A superconducting quantum switch*, Phys. Rev. B **78**, 104508 (2008).

[202] J.-Q. Liao, J.-F. Huang, Y.-x. Liu, L.-M. Kuang, and C. P. Sun, *Quantum switch for single-photon transport in a coupled superconducting transmission-line-resonator array*, Phys. Rev. A **80**, 014301 (2009).

[203] L. Neumeier, M. Leib, and M. J. Hartmann, *Single-photon transistor in circuit quantum electrodynamics*, Phys. Rev. Lett. **111**, 063601 (2013).

[204] M. T. Manzoni, F. Reiter, J. M. Taylor, and A. S. Sørensen, *Single-photon transistor based on superconducting systems*, Phys. Rev. B **89**, 180502 (2014).

[205] D. Ristè, S. Poletto, M.-Z. Huang, A. Bruno, V. Vesterinen, O.-P. Saira, and L. DiCarlo, *Detecting bit-flip errors in a logical qubit using stabilizer measurements*, Nature communications **6** (2015).

[206] K. W. Murch, U. Vool, D. Zhou, S. J. Weber, S. M. Girvin, and I. Siddiqi, *Cavity-assisted quantum bath engineering*, Phys. Rev. Lett. **109**, 183602 (2012).

[207] S. Shankar, M. Hatridge, Z. Leghtas, K. Sliwa, A. Narla, U. Vool, S. M. Girvin, L. Frunzio, M. Mirrahimi, and M. H. Devoret, *Autonomously stabilized entanglement between two superconducting quantum bits*, Nature **504**, 419 (2013).

[208] E. T. Holland, B. Vlastakis, R. W. Heeres, M. J. Reagor, U. Vool, Z. Leghtas, L. Frunzio, G. Kirchmair, M. H. Devoret, M. Mirrahimi, et al., *Single-photon-resolved cross-kerr interaction for autonomous stabilization of photon-number states*, Phys. Rev. Lett. **115**, 180501 (2015).

[209] B. Peropadre, J. Lindkvist, I.-C. Hoi, C. Wilson, J. J. García-Ripoll, P. Delsing, and G. Johansson, *Scattering of coherent states on a single artificial atom*, New Journal of Physics **15**, 035009 (2013).

[210] K. Lalumière, B. C. Sanders, A. F. van Loo, A. Fedorov, A. Wallraff, and A. Blais, *Input-output theory for waveguide qed with an ensemble of inhomogeneous atoms*, Physical Review A **88**, 043806 (2013).

[211] M. Boissonneault, J. M. Gambetta, and A. Blais, *Dispersive regime of circuit qed: Photon-dependent qubit dephasing and relaxation rates*, Physical Review A **79**, 013819 (2009).

[212] J. Dalibard, Y. Castin, and K. Mølmer, *Wave-function approach to dissipative processes in quantum optics*, Physical review letters **68**, 580 (1992).

[213] S. Montangero, T. Calarco, and R. Fazio, *Robust optimal quantum gates for josephson charge qubits*, Phys. Rev. Lett. **99**, 170501 (2007).

[214] X. Y. Jin, A. Kamal, A. P. Sears, T. Gudmundsen, D. Hover, J. Miloshi, R. Slattery, F. Yan, J. Yoder, T. P. Orlando, et al., *Thermal and residual excited-state population in a 3d transmon qubit*, Phys. Rev. Lett. **114**, 240501 (2015).

[215] D. E. Chang, A. S. Sørensen, E. A. Demler, and M. D. Lukin, *A single-photon transistor using nanoscale surface plasmons*, Nature Physics **3**, 807 (2007).

[216] M. Pechal, L. Huthmacher, C. Eichler, S. Zeytinoğlu, A. A. Abdumalikov, S. Berger, A. Wallraff, and S. Filipp, *Microwave-controlled generation of shaped single photons in circuit quantum electrodynamics*, Phys. Rev. X **4**, 041010 (2014).

[217] A. N. Korotkov, *Flying microwave qubits with nearly perfect transfer efficiency*, Phys. Rev. B **84**, 014510 (2011).

[218] Y. Yin, Y. Chen, D. Sank, P. J. J. O'Malley, T. C. White, R. Barends, J. Kelly, E. Lucero, M. Mariantoni, A. Megrant, et al., *Catch and release of microwave photon states*, Phys. Rev. Lett. **110**, 107001 (2013).

[219] A. Palacios-Laloy, F. Nguyen, F. Mallet, P. Bertet, D. Vion, and D. Esteve, *Tunable resonators for quantum circuits*, Journal of Low Temperature Physics **151**, 1034 (2008).

[220] M. Sandberg, C. Wilson, F. Persson, T. Bauch, G. Johansson, V. Shumeiko, T. Duty, and P. Delsing, *Tuning the field in a microwave resonator faster than the photon lifetime*, Applied Physics Letters **92**, 203501 (2008).

[221] S. Y. Kilin and T. Krinitskaya, *Single-atom phase bistability in a fundamental model of quantum optics*, JOSA B **8**, 2289 (1991).

[222] S. Puri and A. Blais, *Engineering the quantum states of light in a kerr-nonlinear resonator by two-photon driving*, arXiv preprint arXiv:1605.09408 (2016).

[223] Y. Kubo, C. Grezes, A. Dewes, T. Umeda, J. Isoya, H. Sumiya, N. Morishita, H. Abe, S. Onoda, T. Ohshima, et al., *Hybrid quantum circuit with a superconducting qubit coupled to a spin ensemble*, Phys. Rev. Lett. **107**, 220501 (2011).

[224] O. Buisson, F. Balestro, J. P. Pekola, and F. W. J. Hekking, *One-shot quantum measurement using a hysteretic dc squid*, Phys. Rev. Lett. **90**, 238304 (2003).

[225] M. Wallquist, V. S. Shumeiko, and G. Wendin, *Selective coupling of superconducting charge qubits mediated by a tunable stripline cavity*, Phys. Rev. B **74**, 224506 (2006).

[226] G. T. Moore, *Quantum theory of the electromagnetic field in a variable-length one-dimensional cavity*, Journal of Mathematical Physics **11**, 2679 (1970).

[227] J. R. Johansson, G. Johansson, C. M. Wilson, and F. Nori, *Dynamical casimir effect in a superconducting coplanar waveguide*, Phys. Rev. Lett. **103**, 147003 (2009).

[228] A. Sørensen and K. Mølmer, *Quantum computation with ions in thermal motion*, Phys. Rev. Lett. **82**, 1971 (1999).

[229] C. Sackett, D. Kielpinski, B. King, C. Langer, V. Meyer, C. Myatt, M. Rowe, Q. Turchette, W. Itano, D. Wineland, et al., *Experimental entanglement of four particles*, Nature **404**, 256 (2000).

[230] A. Sørensen and K. Mølmer, *Entanglement and quantum computation with ions in thermal motion*, Phys. Rev. A **62**, 022311 (2000).

[231] E. Farhi, J. Goldstone, S. Gutmann, J. Lapan, A. Lundgren, and D. Preda, *A quantum adiabatic evolution algorithm applied to random instances of an np-complete problem*, Science **292**, 472 (2001).

[232] T. Albash and D. A. Lidar, *Decoherence in adiabatic quantum computation*, Phys. Rev. A **91**, 062320 (2015).

[233] M. Johnson, M. Amin, S. Gildert, T. Lanting, F. Hamze, N. Dickson, R. Harris, A. Berkley, J. Johansson, P. Bunyk, et al., *Quantum annealing with manufactured spins*, Nature **473**, 194 (2011).

[234] S. Boixo, T. F. Rønnow, S. V. Isakov, Z. Wang, D. Wecker, D. A. Lidar, J. M. Martinis, and M. Troyer, *Evidence for quantum annealing with more than one hundred qubits*, Nature Physics **10**, 218 (2014).

[235] R. Barends, A. Shabani, L. Lamata, J. Kelly, A. Mezzacapo, U. Las Heras, R. Babbush, A. Fowler, B. Campbell, Y. Chen, et al., *Digitized adiabatic quantum computing with a superconducting circuit*, Nature **534**, 222 (2016).

[236] M. Leib, P. Zoller, and W. Lechner, *A transmon quantum annealer: Decomposing many-body ising constraints into pair interactions*, arXiv preprint arXiv:1604.02359 (2016).

[237] W. Lechner, P. Hauke, and P. Zoller, *A quantum annealing architecture with all-to-all connectivity from local interactions*, Science advances **1**, e1500838 (2015).

[238] B. Abdo, A. Kamal, and M. Devoret, *Nondegenerate three-wave mixing with the josephson ring modulator*, Phys. Rev. B **87**, 014508 (2013).

[239] G. Romero, D. Ballester, Y. M. Wang, V. Scarani, and E. Solano, *Ultrafast quantum gates in circuit qed*, Phys. Rev. Lett. **108**, 120501 (2012).

[240] T. H. Kyaw, D. A. Herrera-Martí, E. Solano, G. Romero, and L.-C. Kwek, *Creation of quantum error correcting codes in the ultrastrong coupling regime*, Phys. Rev. B **91**, 064503 (2015).

[241] S. Felicetti, T. Douce, G. Romero, P. Milman, and E. Solano, *Parity-dependent state engineering and tomography in the ultrastrong coupling regime*, Scientific reports **5** (2015).

[242] S. Barrett, K. Hammerer, S. Harrison, T. E. Northup, and T. J. Osborne, *Simulating quantum fields with cavity qed*, Phys. Rev. Lett. **110**, 090501 (2013).

[243] C. Eichler, J. Mlynek, J. Butscher, P. Kurpiers, K. Hammerer, T. J. Osborne, and A. Wallraff, *Exploring interacting quantum many-body systems by experimentally creating continuous matrix product states in superconducting circuits*, Phys. Rev. X **5**, 041044 (2015).

[244] D. T. McClure, H. Paik, L. S. Bishop, M. Steffen, J. M. Chow, and J. M. Gambetta, *Rapid driven reset of a qubit readout resonator*, Phys. Rev. Applied **5**, 011001 (2016).

[245] C. Bultink, M. Rol, T. O'Brien, X. Fu, B. Dikken, R. Vermeulen, J. de Sterke, A. Bruno, R. Schouten, and L. DiCarlo, *Active resonator reset in the nonlinear dispersive regime of circuit qed*, arXiv preprint arXiv:1604.00916 (2016).

[246] S. Gammelmark, B. Julsgaard, and K. Mølmer, *Past quantum states of a monitored system*, Phys. Rev. Lett. **111**, 160401 (2013).

[247] Q. Xu, E. Greplova, B. Julsgaard, and K. Mølmer, *Correlation functions and conditioned quantum dynamics in photodetection theory*, Physica Scripta **90**, 128004 (2015).

[248] A. G. Fowler, A. C. Whiteside, and L. C. L. Hollenberg, *Towards practical classical processing for the surface code*, Phys. Rev. Lett. **108**, 180501 (2012).

[249] Y. Chen, C. Neill, P. Roushan, N. Leung, M. Fang, R. Barends, J. Kelly, B. Campbell, Z. Chen, B. Chiaro, et al., *Qubit architecture with high coherence and fast tunable coupling*, Phys. Rev. Lett. **113**, 220502 (2014).

[250] S. Sheldon, E. Magesan, J. M. Chow, and J. M. Gambetta, *Procedure for systematically tuning up crosstalk in the cross resonance gate*, arXiv preprint arXiv:1603.04821 (2016).